SANDIA REPORT

SAND86—0286 • UC—70
Unlimited Release
Printed March 1987

Nevada Nuclear Waste Storage Investigations Project

An Evaluation of the Use of Mercury Porosimetry in Calculating Hydrologic Properties of Tuffs From Yucca Mountain, Nevada

E. A. Klavetter, R. R. Peters

Prepared by
Sandia National Laboratories
Albuquerque, New Mexico 87185 and Livermore, California 94550
for the United States Department of Energy
under Contract DE-AC04-76DP00789

HYDROLOGY DOCUMENT NUMBER 125

SF2900Q(8-81)

"Prepared by Nevada Nuclear Waste Storage Investigations (NNWSI) Project participants as part of the Civilian Radioactive Waste Management Program (CRWM). The NNWSI Project is managed by the Waste Management Project Office (WMPO) of the U. S. Department of Energy, Nevada Operations Office (DOE/NV). NNWSI Project work is sponsored by the Office of Geologic Repositories (OGR) of the DOE Office of Civilian Radioactive Waste Management (OCRWM)."

Issued by Sandia National Laboratories, operated for the United States Department of Energy by Sandia Corporation.

NOTICE: This report was prepared as an account of work sponsored by an agency of the United States Government. Neither the United States Government nor any agency thereof, nor any of their employees, nor any of their contractors, subcontractors, or their employees, makes any warranty, express or implied, or assumes any legal liability or responsibility for the accuracy, completeness, or usefulness of any information, apparatus, product, or process disclosed, or represents that its use would not infringe privately owned rights. Reference herein to any specific commercial product, process, or service by trade name, trademark, manufacturer, or otherwise, does not necessarily constitute or imply its endorsement, recommendation, or favoring by the United States Government, any agency thereof or any of their contractors or subcontractors. The views and opinions expressed herein do not necessarily state or reflect those of the United States Government, any agency thereof or any of their contractors or subcontractors.

Printed in the United States of America
Available from
National Technical Information Service
U.S. Department of Commerce
5285 Port Royal Road
Springfield, VA 22161

NTIS price codes
Printed copy: A07
Microfiche copy: A01

Distribution
Category UC-70

SAND86-0286
Unlimited Release

AN EVALUATION OF THE USE OF MERCURY POROSIMETRY IN CALCULATING HYDROLOGIC PROPERTIES OF TUFFS FROM YUCCA MOUNTAIN, NEVADA

by

E. A. Klavetter and R. R. Peters
Nevada Nuclear Waste Storage Investigations Project Department
Sandia National Laboratories
Albuquerque, NM 87185

ABSTRACT

The geologic formations in the unsaturated zone at Yucca Mountain, on and adjacent to the Nevada Test Site (NTS), are currently being studied for consideration as the host rock for a radioactive-waste repository. Under the direction of the U.S. Department of Energy, the Nevada Nuclear Waste Storage Investigations project is carrying out these studies. The formations are composed of tuffaceous materials, the hydrologic properties of which must be characterized to support analyses of the potential for water and radionuclide movement from the waste canisters to the accessible environment. Pore-size distributions have been determined for tuff samples by means of mercury porosimetry. These pore-size distributions are used in conjunction with capillary-bundle theory to calculate saturated hydraulic conductivities and water saturations as a function of pressure head for tuff matrix materials. The results are compared with those of more direct methods of measurement of these hydrologic properties to investigate the usefulness of employing pore-size distributions, as determined from mercury-intrusion testing, for estimating hydrologic properties of tuffs. The comparisons indicate that pore-size distributions can be useful in estimating saturated hydraulic conductivity values for tuffs from Yucca Mountain, but do not yield good comparisons with data on saturations as a function of pressure head obtained from more direct experimental measurements.

This work, performed at Sandia National Laboratories, was supported by the U. S. Department of Energy under contract number DE-AC02-76DP00789.

TABLE OF CONTENTS

		Page
	NOMENCLATURE	viii
I.	INTRODUCTION	1
	A. Purpose of the Report	1
	B. Description of the Hydrogeologic Units at Yucca Mountain	5
II.	EXPERIMENTAL METHODS	10
	A. Mercury Intrusion	10
	B. Thermocouple Psychrometry	11
	C. Permeametry (Constant-Head Method)	13
	D. Advantages and Disadvantages of the Methods	13
	1. Mercury Intrusion	13
	2. Thermocouple Psychrometry	24
	3. Permeametry	25
III.	RESULTS	25
	A. Estimation of the Water-Saturation Curve	27
	B. Estimation of the Saturated Hydraulic Conductivity	40
IV.	CONCLUSIONS	50
	REFERENCES	53
	APPENDICES	
	A. Results of Mercury-Intrusion Tests	A.1
	B. Comparison of Results of Mercury-Intrusion and Thermocouple-Psychrometer Test Results	B.1
	DISTRIBUTION LIST	D-1

FIGURES

Number		Page
1a	Simulation of Pore Saturation as a Function of Increasing Intrusion Pressure -- Simulation #1	19
1b	Simulation of Pore Saturation as a Function of Increasing Intrusion Pressure -- Simulation #2	20
2	Actual and Simulated Pore-Size Distributions	22
3	Saturation Curves from Mercury-Intrusion Simulation	23
4	Psychrometer and Mercury-Intrusion Saturation Curves for Units TSw1 and TSw2	31
5	Psychrometer and Mercury-Intrusion Saturation Curves for Unit CHnv	32
6	Psychrometer and Mercury-Intrusion Saturation Curves for Unit CHnz	33
	Unit TCw	
B.1	Saturation as a Function of Pressure Head for Sample GU3-82	B.2
B.2	Saturation as a Function of Pressure Head for Sample GU3-121	B.3
B.3	Saturation as a Function of Pressure Head for Sample GU3-155	B.4
B.4	Saturation as a Function of Pressure Head for Sample GU3-257	B.5
B.5	Saturation as a Function of Pressure Head for Sample GU3-316	B.6
B.6	Saturation as a Function of Pressure Head for Sample G4-43	B.7
	Unit PTn	
B.7	Saturation as a Function of Pressure Head for Sample GU3-374	B.8
B.8	Saturation as a Function of Pressure Head for Sample GU3-378	B.9
B.9	Saturation as a Function of Pressure Head for Sample GU3-397	B.10
B.10	Saturation as a Function of Pressure Head for Sample G4-124	B.11
B.11	Saturation as a Function of Pressure Head for Sample G4-136	B.12
B.12	Saturation as a Function of Pressure Head for Sample G4-172	B.13
B.13	Saturation as a Function of Pressure Head for Sample G4-208	B.14
	Unit TSw1	
B.14	Saturation as a Function of Pressure Head for Sample G1-389	B.15
B.15	Saturation as a Function of Pressure Head for Sample G1-616	B.16
B.16	Saturation as a Function of Pressure Head for Sample G1-752	B.17
B.17	Saturation as a Function of Pressure Head for Sample GU3-585	B.18
B.18	Saturation as a Function of Pressure Head for Sample GU3-687	B.19
B.19	Saturation as a Function of Pressure Head for Sample G4-247 (Psychrometer Only)	B.20

FIGURES (continued)

Number		Page
	Unit TSw2	
B.20	Saturation as a Function of Pressure Head for Sample G1-1102	B.21
B.21	Saturation as a Function of Pressure Head for Sample G1-1111 (Mercury Intrusion Only)	B.22
B.22	Saturation as a Function of Pressure Head for Sample G1-1198	B.23
B.23	Saturation as a Function of Pressure Head for Sample G1-1211 (Mercury Intrusion Only)	B.24
B.24	Saturation as a Function of Pressure Head for Sample GU3-884	B.25
B.25	Saturation as a Function of Pressure Head for Sample GU3-1132	B.26
B.26	Saturation as a Function of Pressure Head for Sample G4-864L	B.27
B.27	Saturation as a Function of Pressure Head for Sample G4-864D	B.28
B.28	Saturation as a Function of Pressure Head for Sample G4-1158 (Mercury-Intrusion Test Results from G4-1159 Added.)	B.29
B.29	Saturation as a Function of Pressure Head for Sample G4-1215 (Psychrometer Only)	B.30
B.30	Saturation as a Function of Pressure Head for Sample G4-1256	B.31
B.31	Saturation as a Function of Pressure Head for Sample G4-1278 (Psychrometer Only)	B.32
B.32	Saturation as a Function of Pressure Head for Sample B.B. #10	B.33
	Unit TSw3	
B.33	Saturation as a Function of Pressure Head for Sample G1-1306	B.34
B.34	Saturation as a Function of Pressure Head for Sample GU3-1197	B.35
B.35	Saturation as a Function of Pressure Head for Sample GU3-1246	B.36
B.36	Saturation as a Function of Pressure Head for Sample G4-1299	B.37
B.37	Saturation as a Function of Pressure Head for Sample G4-1324 (Psychrometer Only)	B.38
	Unit CHnv	
B.38	Saturation as a Function of Pressure Head for Sample G1-1359	B.39
B.39	Saturation as a Function of Pressure Head for Sample G1-1362 (Mercury Intrusion Only)	B.40
B.40	Saturation as a Function of Pressure Head for Sample G1-1387	B.41
B.41	Saturation as a Function of Pressure Head for Sample G1-1392 (Mercury Intrusion Only)	B.42
B.42	Saturation as a Function of Pressure Head for Sample GU3-1311	B.43
B.43	Saturation as a Function of Pressure Head for Sample GU3-1331	B.44
B.44	Saturation as a Function of Pressure Head for Sample GU3-1440	B.45
B.45	Saturation as a Function of Pressure Head for Sample GU3-1499	B.46
B.46	Saturation as a Function of Pressure Head for Sample GU3-1555	B.47
B.47	Saturation as a Function of Pressure Head for Sample G4-1359 (Psychrometer Only)	B.48

FIGURES (continued)

Number		Page
	Unit CHnz	
B.48	Saturation as a Function of Pressure Head for Sample G1-1500	B.49
B.49	Saturation as a Function of Pressure Head for Sample G1-1637	B.50
B.50	Saturation as a Function of Pressure Head for Sample G1-1753	B.51
B.51	Saturation as a Function of Pressure Head for Sample G1-1780	B.52
B.52	Saturation as a Function of Pressure Head for Sample G1-1790	B.53
B.53	Saturation as a Function of Pressure Head for Sample G1-1821	B.54
B.54	Saturation as a Function of Pressure Head for Sample G1-1841	B.55
B.55	Saturation as a Function of Pressure Head for Sample G4-1405	B.56
B.56	Saturation as a Function of Pressure Head for Sample G4-1548 (Mercury-Intrusion Test Results from G4-1547 Added.)	B.57
B.57	Saturation as a Function of Pressure Head for Sample G4-1551 (Psychrometer Only)	B.58
B.58	Saturation as a Function of Pressure Head for Sample G4-1686	B.59
B.59	Saturation as a Function of Pressure Head for Sample G4-1728	B.60
B.60	Saturation as a Function of Pressure Head for Sample G4-1737 (Mercury-Intrusion Test Results from G4-1736 Added.)	B.61
B.61	Saturation as a Function of Pressure Head for Sample G4-1769	B.62
B.62	Saturation as a Function of Pressure Head for Sample G4-1778 (Thermocouple-Psychrometer Curve-Fit from G4-1778-F Added.)	B.63
B.63	Saturation as a Function of Pressure Head for Sample G4-1778-F (Thermocouple-Psychrometer Curve-Fit from G4-1778 Added.)	B.64
B.64	Saturation as a Function of Pressure Head for Sample G4-1787	B.65
	Unit PPw	
B.65	Saturation as a Function of Pressure Head for Sample G1-1917	B.66
B.66	Saturation as a Function of Pressure Head for Sample GU3-1628	B.67
B.67	Saturation as a Function of Pressure Head for Sample GU3-1680	B.68
B.68	Saturation as a Function of Pressure Head for Sample GU3-1730	B.69
B.69	Saturation as a Function of Pressure Head for Sample G4-1899	B.70
	Unit CFUn	
B.70	Saturation as a Function of Pressure Head for Sample G4-2006	B.71
B.71	Saturation as a Function of Pressure Head for Sample G4-2101	B.72
	Unit BFw	
B.72	Saturation as a Function of Pressure Head for Sample G4-2401	B.73
B.73	Saturation as a Function of Pressure Head for Sample G4-2407	B.74

TABLES

Number		Page
1	Description of Hydrogeologic Units at Yucca Mountain	6
2	Data for and Results from the Mercury-Intrusion Simulations	17
3	Statistical Comparison of Thermocouple-Psychrometer Data and Mercury-Intrusion Data	35
4	Comparison of Measured and Calculated Saturated Hydraulic Conductivities	43
A.1	Location of Samples Tested	A.2

NOMENCLATURE

A	- cross-sectional area
a	- slope, fitting parameter (Eq. 6a)
b	- intercept, fitting parameter (Eq. 6a)
c	- constant (Eq. 8 and 9)
g	- acceleration of gravity
h	- pressure head across a sample (Eq. 3)
K	- hydraulic conductivity
k	- permeability
L	- length
n	- porosity
P	- pressure
q	- flow
r	- pore radius; correlation coefficient
R	- ideal gas constant
RH	- relative humidity (0-100%)
S	- saturation
SA	- surface area (Eq. 8)
T	- absolute temperature
t	- time
$\bar{x}$	- mean value
V	- volume of a mole of water

Greek Symbols

α - curve fit parameter (van Genuchten, 1978) in Appendix B

β - curve fit parameter (van Genuchten, 1978) in Appendix B

γ - surface tension

μ - viscosity

ρ - fluid density

σ - standard deviation

ϕ - contact angle

ψ - pressure head

Superscripts

^ - estimate of variable

* - value of pressure head at which the saturation was measured (Eq. 6a)

Subscripts

ave - average

i - i^{th} quantity

psy - psychrometer (psychrometry method)

Hg - mercury

H_2O - water

r - residual

I. INTRODUCTION

The geologic formations in the unsaturated zone at Yucca Mountain, on and adjacent to the Nevada Test Site (NTS), are currently under consideration as the host rock for a radioactive-waste repository. Under the direction of the U.S. Department of Energy the Nevada Nuclear Waste Storage Investigations (NNWSI) project is carrying out technical studies of their feasibility as a medium for radioactive-waste disposal. Because water flow through unsaturated rock is a principal mechanism for the transport of soluble radionuclides and other contaminants from a repository to the biosphere, the determination of the hydrologic properties of the system is an essential part of the analysis of radionuclide transport. An understanding of the hydrologic properties of both saturated and unsaturated tuffs underlying Yucca Mountain are required for this analysis.

A. Purpose of the Report

Laboratory hydrologic data for both welded and nonwelded tuffs from Yucca Mountain have been previously acquired and documented by various researchers (e.g., see Weeks and Wilson, 1984; Peters et al., 1984; and Peters et al., 1985). In both documents by Peters et al., data on saturated hydraulic conductivity (permeability)[1] were acquired using a standard permeametry

---

[1] The saturated hydraulic conductivity, K, is related to the permeability, k, by the following relationship: $K = \rho g k/\mu$. The permeability is theoretically dependent only upon the structure and properties of the rock, whereas the saturated hydraulic conductivity is dependent upon both the fluid and rock properties. Because we are interested in the permeability of tuffs to water and because we will restrict the discussion to ambient temperature, each of the terms "permeability" and "saturated hydraulic conductivity" may be used to refer to the same characteristic of the system.

(Footnote continues on next page)

technique, and data on saturation as a function of water pressure head were obtained using a thermocouple-psychrometry technique. These parameters can also be determined indirectly using information on the pore structure of the matrix material (e.g., pore-size distributions) and theoretical models. Pore-size distributions can be estimated using the mercury-porosimetry (mercury-intrusion) technique. These distributions can be used to estimate not only the saturated conductivity and saturation versus pressure-head relationship, but also to estimate the porosity and the hydraulic conductivity versus pressure-head relationship.

Because of the large scale of the system that must be characterized ($\approx 10^9$ m^3) by the NNWSI project, extensive hydrologic data may be required to adequately predict water paths and fluxes. Therefore, the determination of hydrologic parameters through the use of mercury-intrusion data is a convenient alternative to direct measurement, which is usually more expensive and time consuming. The hydrologic parameters for which data are needed include saturated hydraulic conductivity, saturation as a function of pressure head, and relative conductivity as a function of pressure head. This report deals with the first two of these parameters; its purpose is to present estimates of their values calculated from pore-size distributions and to compare these estimates with the values determined from more direct experimental measurements on tuff samples from Yucca Mountain. The report describes the experimental methods used to obtain the data required for the determination of the two specified hydrologic parameters, presents the methods of analysis used to convert the data into those hydrologic parameters, and compares the hydrologic values determined from pore-size

---

(Footnote continued from previous page)

At room temperature, the conversion from permeability to saturated hydraulic conductivity is approximately 1 m^2 = 10^7 m/s.

distributions to the values determined from more direct measurement techniques.

Pore-size distributions for the tuffs were determined by using the results of mercury intrusion (mercury porosimetry) tests. These tests were performed by Micromeritics, Inc.[1] for tuff samples obtained from approximately the same locations as those tested by Peters et al. (1984 and 1985). The samples tested by mercury intrusion were subsamples taken from a larger drill core and were either identical to those subsamples tested by Peters et al. or samples taken nearby from the same core sample and location (drill hole and depth). The saturated hydraulic conductivity measured by using a permeameter may be compared with that estimated by using pore-size distribution information obtained from the mercury-intrusion data. The saturation versus pressure-head data obtained using the thermocouple psychrometer may be compared with that estimated from mercury-intrusion test data. Therefore, estimates of the two hydrologic parameters can be made using at least two different methods. Using several methods to estimate hydrologic parameters may provide additional verification for and confidence in the estimates of the hydrologic properties of interest.

Using pore-size distributions based on mercury-intrusion testing to determine hydrologic parameters, places a substantial emphasis on capillary-bundle theory (see, e.g., Hillel, 1971) -- a theory based on the assumption that a large group of interconnected pores having a wide range of radii can be considered analogous to and represented by a bundle of capillary tubes similarly having a wide range of radii. The lengths of the tubes can be assumed, with the pore radius for each tube remaining constant along the length of the tube. Capillary-bundle theory provides a simplified tool for describing the pore geometry and pore interconnections. The theory often provides a very simplistic view of a very complicated system. However, if the theory can be applied successfully to tuffs for estimating

---

[1] Micromeritics Instrument Corp., Norcross, Georgia 30093. Tests performed on an Auto-Pore 9200 Porosimeter to 60,000 psi.

hydrologic properties, mercury-intrusion tests can be run quickly and inexpensively to obtain a large quantity of data. If capillary-bundle theory and mercury-intrusion testing are unable to provide sufficiently accurate results, then the more time-consuming, direct testing methods (such as thermocouple psychrometry and permeametry) must be employed.

An important hydrologic parameter not compared here is relative conductivity as a function of pressure head (or saturation). For the low-permeability tuffs under investigation in the NNWSI project, the complete determination of the relative conductivity curves ranges from difficult to impossible using current standard techniques (Johnson et al., 1959). Even for the relatively high-permeability samples of tuff (e.g., vitric nonwelded tuffs), the direct determination of the relative conductivity curves using standard steady-state or unsteady-state, gas-drive techniques is both time-consuming and expensive. The relative conductivity curves can be calculated from the pore-size distributions; however, these calculations would generally be more sensitive to errors in the pore-size distribution and calculational method used, than calculations of the saturated hydraulic conductivity or the saturation versus pressure-head curves. For the samples tested by Peters et al. (1984 and 1985), no relative conductivity values are available, and comparisons with curves generated from pore-size distributions could not be made. If pore-size distributions determined from mercury-intrusion tests can in the future be shown to provide a basis for adequately estimating the relative hydraulic conductivity values, large quantities of data can be efficiently determined. If strong correlations can be made between the saturation versus pressure-head curves determined from pore-size distributions and from thermocouple psychrometry measurements, they would be a favorable indication that pore-size distributions can adequately provide reliable estimates of the relative conductivity curves for tuffs.

B. Description of the Hydrogeologic Units at Yucca Mountain

Yucca Mountain is made up predominantly of ash-flow and ash-fall tuffs. These can be organized into formal geologic units or into functional stratigraphic units. The major difference between these two methods of organization is that a formal geologic unit may contain two or more lithologies, each of which may have very different hydrologic properties, whereas the functional grouping strives to identify units that have a minimum of internal variability of these properties within each unit. Table 1 gives a brief description of the hydrogeologic units at Yucca Mountain. Thicknesses of the various units have been given (in terms of ranges of depth) for drill hole USW G-4 on Yucca Mountain, for illustrative purposes. A more complete discussion of the definition of the hydrogeologic (functional) units and the methods for selecting their boundaries may be found in the compilation by Ortiz et al. (1985).

Table 1.
Description of Hydrogeologic Units at Yucca Mountain

Unit	USW G-4 Depth[1] (ft)	Hydrogeologic Unit	Description[2]
TCw	30- 118	Tiva Canyon welded unit	Moderately to densely welded, devitrified ash-flow tuff in the Tiva Canyon Member of the Paintbrush Tuff.
PTn	118- 243	Paintbrush nonwelded unit	Partially welded to nonwelded, vitric and occasionally devitrified tuffs of the Tiva Canyon, Yucca Mountain, Pah Canyon, and Topopah Spring Members of the Paintbrush Tuff.
TSwl	243- 670	Topopah Spring welded unit	Moderately to densely welded, devitrified ashflow zone in the Topopah Spring Member of the Paintbrush Tuff that contains more than approximately 10% by volume of vugs.

[1] Information from Ortiz et al. (1985).

[2] The hydrogeologic unit description includes their location in terms of formal geologic units.

Table 1. (continued)
Description of Hydrogeologic Units at Yucca Mountain

Unit	USW G-4 Depth[1] (ft)	Hydrogeologic Unit	Description[2]
TSw2	670-1293	Topopah Spring welded unit	Moderately to densely welded, devitrified ashflow zone in the Topopah Spring Member of the Paintbrush Tuff that contains less than approximately 10% by volume of vugs. This is the potential repository unit.
TSw3	1293-1345	Basal Vitrophyre of Topopah Spring welded unit	Basal vitrophyre of the Topopah Spring Member of the Paintbrush Tuff.
CHnlv[3]	1345-1363	Vitric Calico Hills nonwelded unit	Nonwelded ashflows, bedded and reworked tuffs, vitric and primarily nonzeolitized from the Topopah Spring Member and/or the Calico Hills.

[1] Information from Ortiz et al. (1985).

[2] The hydrogeologic unit description includes their location in terms of formal geologic units.

[3] The lower case "v" or "z" in a unit number (e.g., Chnlv) indicates that the unit is vitric (v) or that it has altered, and is primarily zeolitized (z).

Table 1. (continued)
Description of Hydrogeologic Units at Yucca Mountain

Unit	USW G-4 Depth[1] (ft)	Hydrogeologic Unit	Description[2]
CHn2v	Absent	Vitric Calico Hills nonwelded unit	Basal bedded and reworked zone of the vitric tuffs and tuffaceous sandstones of the Calico Hills
CHn3v	Absent	Vitric Calico Hills nonwelded unit	Upper vitric zone of the Prow Pass Member of the Crater Flat Tuff
CHn1z	1360-1705	Zeolitized Calico Hills nonwelded unit	Nonwelded ashflows, bedded and reworked tuffs, vitric and primarily zeolitized, from the Topopah Spring Member and/or the Calico Hills.
CHn2z	1705-1761	Zeolitized Calico Hills nonwelded unit	Basal Bedded and reworked zone of the zeolitized tuffs and tuffaceous sandstones of the Calico Hills
CHn3z	1761-1792	Zeolitized Calico Hills nonwelded unit	Upper zeolitized zone of the Prow Pass Member of the Crater Flat Tuff

[1] Information from Ortiz et al. (1985).

[2] The hydrogeologic unit description includes their location in terms of formal geologic units.

Table 1. (continued)
Description of Hydrogeologic Units at Yucca Mountain

Unit	USW G-4 Depth[1] (ft)	Hydrogeologic Unit	Description[2]
PPw	1792-1960	Prow Pass welded unit	Moderately welded, devitrified zone of the Prow Pass Member of the Crater Flat Tuff.
CFUn	1960-2258	Upper Crater Flat nonwelded unit	Zeolitic nonwelded to partially welded ashflows and bedded, reworked portions of the lower Prow Pass Member and upper Bullfrog Member of the Crater Flat Tuff.
BFw	2258-2682	Bullfrog welded unit	Moderately to densely welded ashflows of the Bullfrog Member of the Crater Flat Tuff.

[1] Information from Ortiz et al. (1985).

[2] The hydrogeologic unit description includes their location in terms of formal geologic units.

II. EXPERIMENTAL METHODS

Three experimental methods will be discussed in this section. The first, mercury porosimetry, is used for obtaining pore-size distributions from which hydrologic properties may be calculated using various theoretical models. The second, thermocouple psychrometry, is used for obtaining data that can be used to calculate water saturations as a function of pressure head. The third, permeametry, is used to obtain values of saturated hydraulic conductivities. The latter is the simplest and most standard technique.

It should be noted that the use of a centrifuge technique for determining data on saturations as a function of pressure head for tuffs also will be investigated within the NNWSI Project by the U. S. Geological Survey (Hammermeister, personal communication). Because no published hydrologic data on Yucca Mountain tuffs have been obtained by this technique, it was not considered in this document.

A. Mercury Intrusion

The mercury-intrusion technique is based on the principle that the surface tension of a nonwetting liquid will oppose the entry of the liquid into a small pore of a solid. The nonwetting liquid is characterized by having a contact angle greater than 90 degrees. Washburn (1921) determined that this opposition could be overcome by external pressure and that the external pressure that was required to intrude the nonwetting fluid into the pore was inversely proportional to the pore radius. Assuming a cylindrical pore, a momentum balance can show this relation to be

$$P = 2\gamma \cos(\phi)/r \qquad (1)$$

where P is the absolute pressure required, γ is the surface tension of the nonwetting fluid, ϕ is the contact angle between the solid and the liquid, and r is the pore radius. The contact angle for a wetting fluid is less than 90 degrees and for a nonwetting fluid, greater than 90 degrees. For

many solids, mercury is a nonwetting fluid, with its contact angle commonly in the range of 130-140 degrees.

The experimental sample is initially evacuated to remove all fluid and then put in the porosimeter and surrounded by mercury. The pressure is raised in small increments, with the subsequent volume of mercury penetrating the sample recorded after each pressure increase. It is assumed that each pressure increment forces mercury into the accessible pores with a diameter larger than or equal to that calculated by Equation 1 for the given pressure. In this manner, the volume of pore space between pressure increments, and thus diameter decrements, is recorded, generating a pore-size distribution.

The volume of interconnected porosity may be calculated from the volume of mercury that is forced into the sample and the volume of the sample tested. This assumes that all the pores have been intruded by mercury. For materials (like the tuffs from Yucca Mountain) with very small pore sizes, it is, therefore, necessary to use very large intrusion pressures to access all of the available pore space. From the mercury-intrusion data presented in Appendix A (in microfiche), it can be seen that the intrusion pressure must exceed 50,000 psi to access the available pore space.

From the cumulative volume distribution as a function of intrusion pressure, data on mercury saturation as a function of intrusion pressure (also referred to as capillary pressure) may be calculated. As will be shown later, data on water saturation as a function of capillary pressure may be estimated from the mercury-intrusion data (e.g., see Purcell, 1949). The cumulative volume distribution, or pore-size distribution, may also be used to calculate relative hydraulic conductivity relationships as well as the permeability, or saturated hydraulic conductivity, of the material (e.g., see Burdine, 1953; Burdine et al., 1950; Purcell, 1949; and Garcia-Bengochea et al., 1979).

B. Thermocouple Psychrometry

For a system in equilibrium, there is a relationship between pressure head (moisture potential) and equilibrium relative humidity of the air

surrounding a sample in a closed container. This relationship is described by the following equation (Edlefsen and Anderson, 1943):

$$\psi = (RT/V) \ln (RH/100) \qquad (2)$$

where ψ is the pressure head (or negative suction head), R is the ideal gas constant, T is the absolute temperature, V is the volume of a mole of water, and RH is the relative humidity. A thermocouple psychrometer is an electronic probe that measures relative humidity by either determining the temperature depression associated with the evaporation of water from the wet surface of the measuring thermocouple or by determining the compensation needed to maintain the temperature of the wet thermocouple at the dew point corresponding to the ambient relative humidity. A stationary thermocouple, with measuring and reference junctions, is provided in the psychrometer. The measuring junction is moistened, while the reference junction remains dry. As evaporation proceeds at the measuring junction, the electromotive force (emf), or voltage, that is generated by the thermocouple is measured. This voltage is an indication of the difference between the wet and dry-bulb temperatures of the air. After being calibrated by measuring the humidity over a salt solution of a known concentration, this voltage is used to determine the relative humidity, and from Eq. 2, the pressure head, for a material under the temperature and pressure conditions of the measurement.

Depending upon the resolution of the instrumentation used in thermocouple psychrometry, the general sensitivity of the thermocouple psychrometer is about -10 m of water pressure head. The upper bound of useful water pressure heads is therefore no more than about -20 or -30 m. For the type of psychrometer used by Peters et al. (1984 and 1985), there is no theoretically-limiting lower bound. (Psychrometers used in the field are generally regarded as having a limit of about -800 m (Daniels et al., 1981), while those used in the lab appear to be useful to lower pressure heads (see Peters et al. (1984 and 1985)). Daniels et al. noted that their experience indicates that laboratory measurements with psychrometers in the range of -20 to -800 m of water pressure head are generally reproducible to within about 10 to 30 percent or better, provided there are no serious problems with corrosion. The saturation data at a pressure head of -30,000 m cited in Peters et al. (1985) were obtained by placing samples in an airtight vessel, the humidity of which was controlled by a salt solution.)

The pressure head (or moisture potential) determined by thermocouple psychrometers includes both matric and osmotic components. For the psychrometry-derived data, it was assumed that the matric potential was much larger than the osmotic potential because of the low concentration of solutes in the working fluid (water). Thus, the pressure head is assumed to be equal to the matric potential.

C. Permeametry (Constant-Head Method)

This method measures the hydraulic conductivity of saturated samples by determining the time necessary for a given volume of liquid at some temperature to pass through a sample of constant cross-sectional area under a fixed pressure gradient. The saturated hydraulic conductivity is calculated from Darcy's law for laminar flow in a right circular cylinder as follows:

$$K = (q/At)(L/\Delta h) \qquad (3)$$

where K (m/s) is the saturated hydraulic conductivity, q (m^3) is the volume of water passing through the sample in time t (s), A (m^2) is the cross-sectional area of the sample, L (m) is the length of the sample, and Δh (m) is the pressure head difference. The lower bound on the conductivity is determined by the equipment (how leak-tight it is and how stable the operation is) and by time constraints. The range of conductivity values reported by various authors is quite large; e.g., Peters et al. (1984 and 1985) report values of from 10^{-6} to 10^{-14} m/s. The method has no theoretical upper bound; its practical upper limit is dependent on the equipment available.

D. Advantages and Disadvantages of the Methods

1. Mercury Intrusion

The mercury-intrusion method appears to have both significant advantages and disadvantages. A major advantage is that the data required (the pore-size distribution) for estimating the entire saturation curve, the

relative conductivity curve, and the saturated conductivity may be obtained in a relatively short time -- a pore-size distribution curve with 60 points ranging from 0 up to a maximum intrusion pressure of 60,000 psi takes approximately one hour to obtain. Also, the range of pressures observed may be considerably higher than other methods. It may also be possible to retest samples after a regeneration process is accomplished for removing the intruded mercury from the tested material. Retesting the sample could determine whether mercury-intrusion testing and regeneration had altered the sample and, if unaltered, the precision of the method for determining the pore-size distribution. The regeneration process can be accomplished by vacuum distillation (see Burdine et al., 1950). It should be noted that this regeneration process may be expensive and may not completely return the sample to its condition prior to the intrusion of mercury.

There are also some serious disadvantages in using the technique. One needs a porous medium in which the character of the interstitial spaces is unrelated to the physico-chemical properties of the saturating fluids. For example, clayey material may swell when saturated with water and thus may have a different pore-size distribution from the distribution estimated using mercury as the saturating fluid. Also, using the mercury intrusion method, no irreducible minimum wetting-phase saturation, or residual saturation, can be attained, so that a piece of data required to numerically estimate the relative conductivity curve is unavailable. This error can usually be mitigated through other testing to obtain the residual saturation.

There may also be effects resulting from the sample size and its relation to the surface area exposed. Wardlaw and Taylor (1976) state that

> Pores are accessible through throats and, on the exterior surface of the sample, there are many random intersections of pores which act as artificially enlarged throats. Thus, the pore system at the surface of the sample is not representative of the infinite pore system away from the surface. Sample size and shape influence surface area to volume ratios and therefore can be expected to affect the form of the capillary pressure curves.

These effects would be expected to be more significant in the mercury-intrusion method than the psychrometer method, because the mercury-intrusion method makes several assumptions concerning the pore structure and pore interactions within the sample while the psychrometer method makes no assumptions about the pore structure. There may also be effects resulting from the rate of mercury intrusion. However, this type of non-equilibrium effect may be present, to some degree, in any measurement.

The effects discussed above are not an all inclusive list of the difficulties present that may prevent the mercury-intrusion technique from yielding an accurate portrayal of the pore-size distribution. More important, perhaps, than the experimental difficulties, are the problems associated with the interpretation of the data used to determine the pore-size distribution for the material tested. In order to calculate the pore-size distribution using Eq. 1, it is assumed (with the mercury-intrusion technique) that the pore space can be thought of as being composed of a bundle of cylindrical tubes. Fatt, commenting on Burdine (1953), noted that

> The model, a bundle of parallel tubes, is so very much over-simplified that calculated and measured relative permeability often do not agree. To bring these into better agreement, the concept of tortuosity has been introduced. Tortuosity, being difficult to evaluate experimentally, is empirically adjusted to improve the fit of calculated data to measured data. An improvement of fit by such empirical adjustment cannot be accepted as making the parallel tube model more valid nor the tortuosity concept more sound.

Burdine (1953) agreed as to the simplicity of the model and to the frequent disagreement observed, but pointed to the significant number of cases in which really remarkable agreement is observed.

Other effects related to the surface may also be present to the extent that they may significantly affect the determination of the pore size. For example, in Eq. 1, the contact angle is generally assumed to have a constant value when, in fact, it may vary significantly because of surface inhomogeneities or the presence of polar molecular monolayers on the pore walls. The complexities of fluid movement in the void space of a porous material make it extremely difficult in many circumstances to accurately

determine the pore structure through such a simple model assumed by mercury intrusion.

In general, as pointed out by Rose [in a comment on the paper by W. R. Purcell (1949)], "it must be emphasized that exact equivalence between conventional capillary pressure data and that obtained by the mercury penetration method is not to be expected as a common result."

As mentioned above, one of the most significant aspects of using mercury-intrusion data for predicting hydrologic properties is the use of capillary-bundle theory in the data-reduction procedure. Capillary-bundle theory assumes that, for a nonwetting fluid, a larger pore fills before a smaller pore does, with the smallest pore filling last. This can be seen by using Eq. 1 to determine the pressures that pores of different radii are in equilibrium with. Therefore, when the mercury is intruded into the sample, the volume of mercury intruded is attributed to a single pore size related to the intrusion pressure. The mercury intrusion data are reduced to a pore-size distribution as though the mercury intruding the outer part of the material filled all of, and only, the largest pores first, and subsequently filled the next largest pores and finally the smallest pores. Representing pores as a bundle of capillary tubes therefore assumes a very orderly arrangement of pores (or at least pore filling) in the material. If, as is more likely in a real material, a large pore is often shielded from penetration by smaller pores, the large pore will not be penetrated until the smaller pores have been. The resulting intrusion volume will be the sum of the larger and smaller pores, but the volume will be assumed to correspond <u>only</u> to the smaller pores. Therefore, it is probable that mercury intrusion might yield a valid pore-size distribution function for a material with a unimodal pore-size distribution but could be in error for a material with a very heterogeneous distribution. In the former case, there is little "shielding" of large pores by small pores because all pores are essentially the same size. In the latter case, because of the random distribution of pores, small pores could often completely shield large pores. In this case, the mercury intrusion method would give an erroneous pore-size distribution. The subsequent calculation of hydrologic properties from such a distribution could yield significant errors.

The simple example that follows shows how errors in pore-size distributions derived from mercury-intrusion data can occur if the pores are distributed randomly instead of by the orderly arrangement assumed by capillary-bundle theory. The example takes what is assumed to be an actual or real pore-size distribution of a tuff sample and randomly distributes the pores (assumed to be of equal length) in a two-dimensional matrix. Mercury intrusion is simulated by a process described below, and the resulting intrusion-derived pore-size distribution is compared with the real pore-size distribution. Hydrologic data on water saturation as a function of pressure head are generated from both the actual pore-size distribution and the intrusion-derived distribution. These hydrologic property data are then compared.

The actual pore-size distribution (pore volume as a function of pore radius) was a distribution estimated from data on water saturation as a function of water pressure head obtained on a tuff sample using thermocouple psychrometry. The distribution was estimated using Eq. 1 and the data on water saturation as a function of pressure head listed in Table 2. The estimated pore-size distribution (given as the number of pores of a particular pore radius) is also shown in Table 2. For the purposes of this example, it was assumed that these data were representative of the real pore-size distribution of the sample.

Table 2.

Data for and Results from the Mercury-Intrusion Simulations

						Simulation # 1		Simulation # 2	
ID Number	Water Saturation	Pressure Head (m of H_2O)	Hg Intrusion Pressure (psi)	Pore Radius i (μm)	Actual No. of Pores of Size i	Apparent No. of Pores of Size i	Water Saturation	Apparent No. of Pores of Size i	Water Saturation
1	0.87	-81	517	0.35	3	0	1.00	0	1.00
2	0.79	-189	1,203	0.15	4	0	1.00	0	1.00
3	0.59	-360	2,289	0.079	11	0	1.00	0	1.00
4	0.48	-630	4,012	0.045	40	4	0.96	5	0.97
5	0.17	-1283	8,169	0.022	120	33	0.86	28	0.84
6	0.07	-2638	16,800	0.011	80	202	0.17	202	0.19
7	0.03	-4690	29,870	0.0061	56	75	0.03	73	0.06
8	0.00	-9376	59,720	0.0030	85	85	0.00	91	0.00

In the simulations, each pore in the matrix is connected vertically or horizontally to four other pores of random sizes. For simplicity, eight distinct pore radii, corresponding to eight distinct mercury-intrusion pressures (as related through Eq. 1), were used. The identification (ID) numbers in Table 2 designate each of these eight pore sizes; the table also lists the eight corresponding intrusion pressures. A residual saturation of zero was assumed. Using the actual data on pore volume for each of the 8 pore sizes (note that the volume is actually averaged over a range of pore sizes), 399 pores comprising the 8 different pore sizes were randomly arranged, in a 20 x 20 (approximately) grid configuration. The pore sizes were placed in each grid location using a random-number generator to select the pore size. Two separate random simulations were run.

In each simulation, mercury intruded into the lower face of the two-dimensional matrix, first at the lowest mercury-intrusion pressure in Table 2 (ID number 1) and then at each of the other seven pressures in increasing order. At each mercury-intrusion pressure, only the pore sizes with an absolute value of capillary pressure (as specified by Eq. 1) less than or equal to the applied intrusion pressure were filled. Figures 1a and 1b show which pores were filled at each particular intrusion pressure in the two simulations. The pore sizes are designated by their ID numbers from Table 2. In both simulations, the lower face of the material contained no pores equal to or larger than pore size 3 (pore radius of 0.0790 μm); figures for the two lowest intrusion pressures (corresponding to ID numbers 1 and 2) are therefore not shown. At a mercury-intrusion pressure of 4012 psi, corresponding to pore size 4 (pore radius of 0.045 μm), all pores of size 1 through 4 that are connected to the lower face are filled. In the first simulation (Figure 1a), five size 4 pores are filled; in the second simulation (Figure 1b), two size 4 pores are filled, one size 3 pore is filled, and one size 2 pore is filled. In both simulations, the total pore volume intruded at the pressure of 4012 psi is taken to be that volume which corresponds to a pore radius of 0.045 μm. Therefore, in the second simulation, the volume of the pores of radius of 0.079 μm (size 2) and the pores of radius 0.15 μm (size 3) is lumped with the volume of pores of 0.045 μm (size 4). This yields and erroneous pore-size distribution.

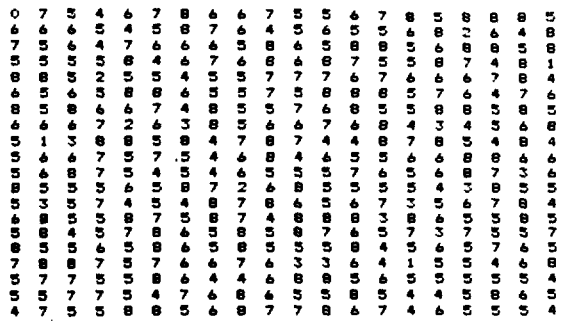

(3) P_{Hg} = 2,289 psi

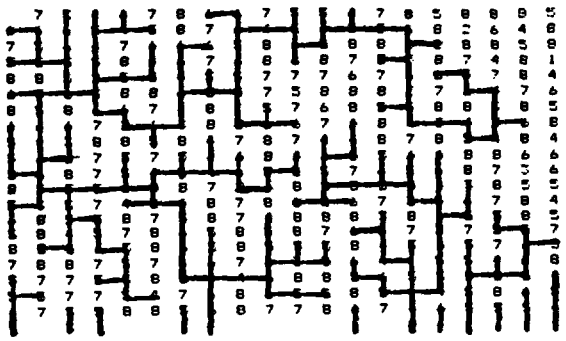

(6) P_{Hg} = 16,800 psi

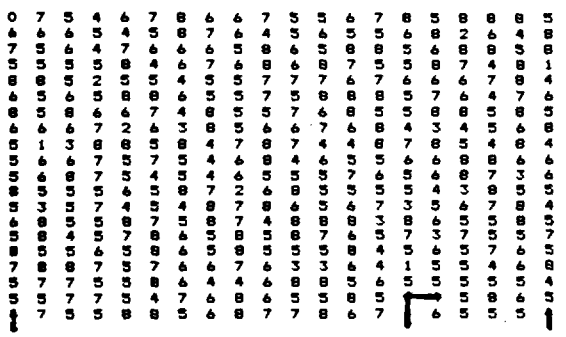

(4) P_{Hg} = 4,012 psi

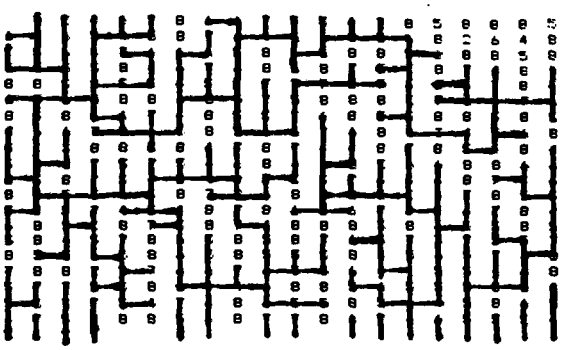

(7) P_{Hg} = 29,870 psi

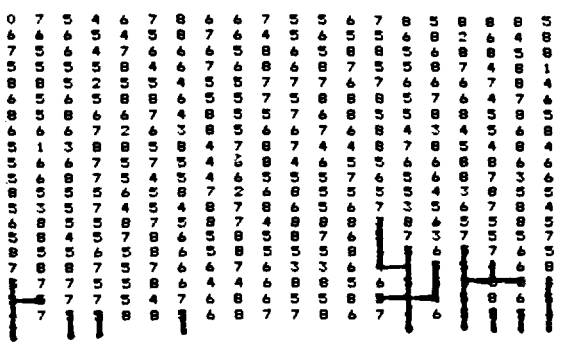

(5) P_{Hg} = 8,169 psi

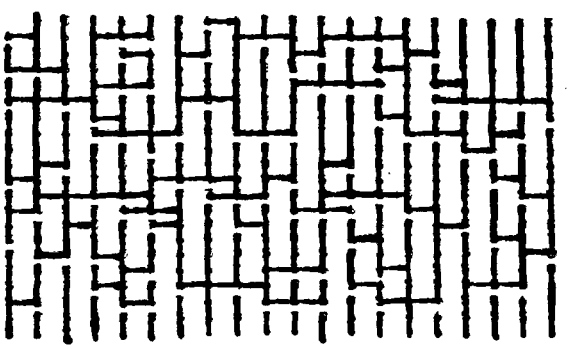

(8) P_{Hg} = 59,720 psi

Figure 1a. Simulation of Pore Saturation as a Function of Increasing Intrusion Pressure -- Simulation #1. Mercury is assumed to penetrate the block of material from the lower face.

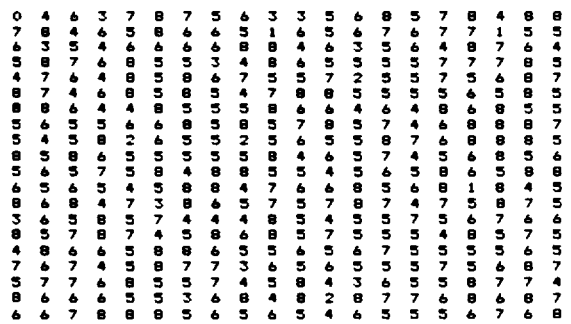

(3) P_{Hg} = 2,289 psi

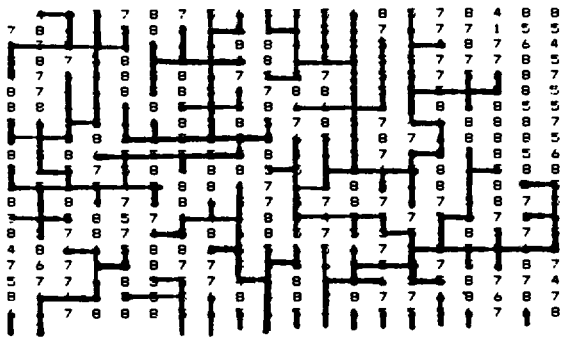

(6) P_{Hg} = 16,800 psi

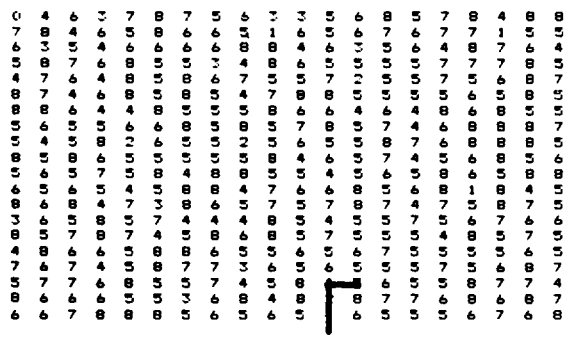

(4) P_{Hg} = 4,012 psi

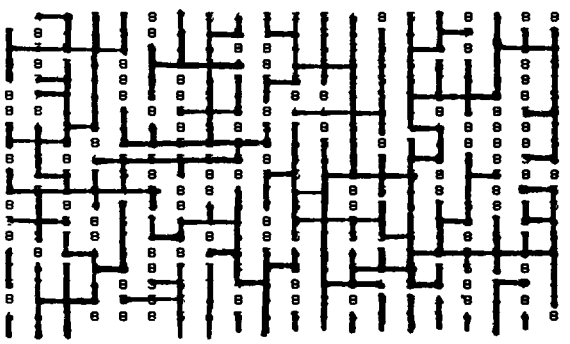

(7) P_{Hg} = 29,870 psi

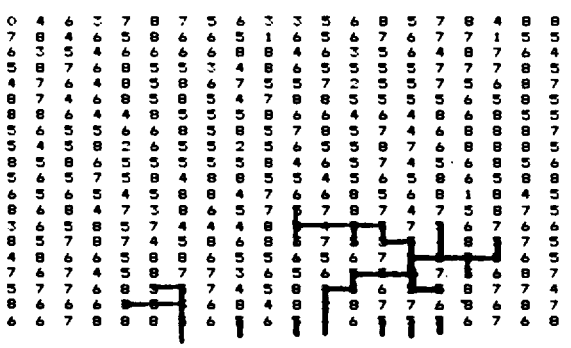

(5) P_{Hg} = 8,169 psi

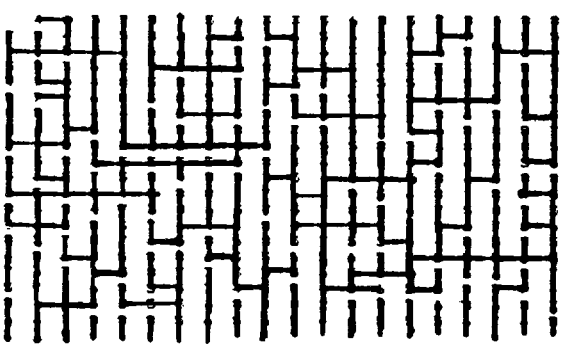

(8) P_{Hg} = 59,720 psi

Figure 1b. Simulation of Pore Saturation as a Function of Increasing Intrusion Pressure -- Simulation #2. Mercury is assumed to penetrate the block of material from the lower face.

In the next step, the mercury-intrusion pressure is raised to 8169 psi (corresponding to pore size 5), and all connected pores with sizes in the range of 1 through 5 are filled. The process of stepwise increasing the mercury-intrusion pressure continues until all of the pores are filled.

Table 2 shows results of the two simulations, giving the apparent number of pores in each pore-radius group filled at each intrusion pressure. The apparent pore-size distributions from these two simulations are shown in Figure 2, together with the "actual" (assumed) pore-size distribution. Both simulations yield very similar results but are very different from the actual pore-size distribution.

The pore-size distributions are used to calculate water saturation as a function of pressure head. The saturation curves based on the pore-size distributions from the mercury-intrusion simulations are compared with the psychrometer saturation curve (with the corresponding actual pore-size distribution) in Figure 3. (The method used to calculate the saturation curves from the pore-size distributions is shown later in this report.) Because some of the larger pores were shielded by smaller pores in the two simulations with the randomly distributed pores, the corresponding curve of water saturation as a function of water pressure head shifted significantly to more negative pressure heads. The curve is also much steeper.

These simulations provide an indication of how mercury-intrusion testing of a heterogeneous pore-size distribution can yield erroneous results. Because the pore-size distribution is used to calculate saturated hydraulic conductivities, relative hydraulic conductivity curves, and saturation (drainage) curves, errors in the distribution will yield errors in the calculated hydrologic parameters.

Although the above discussion does not cover all the difficulties involved in using mercury intrusion data to obtain true pore-size distributions and to calculate hydrologic parameters, it gives an indication of the variety of experimental and theoretical problems that can and do occur. Whether the incurred errors are significant depends on the characteristics of the material under consideration and on the degree of accuracy desired for a particular set of investigations.

INTRUSION PRESSURE AND PORE RADIUS SIZE NUMBER	1	2	3	4	5	6	7	8
PORE RADIUS (micrometers)	0.35	0.15	0.079	0.045	0.022	0.011	0.0061	0.0030
INTRUSION PRESSURE (psi)	517	1203	2289	4012	8169	16,800	29,870	59,720

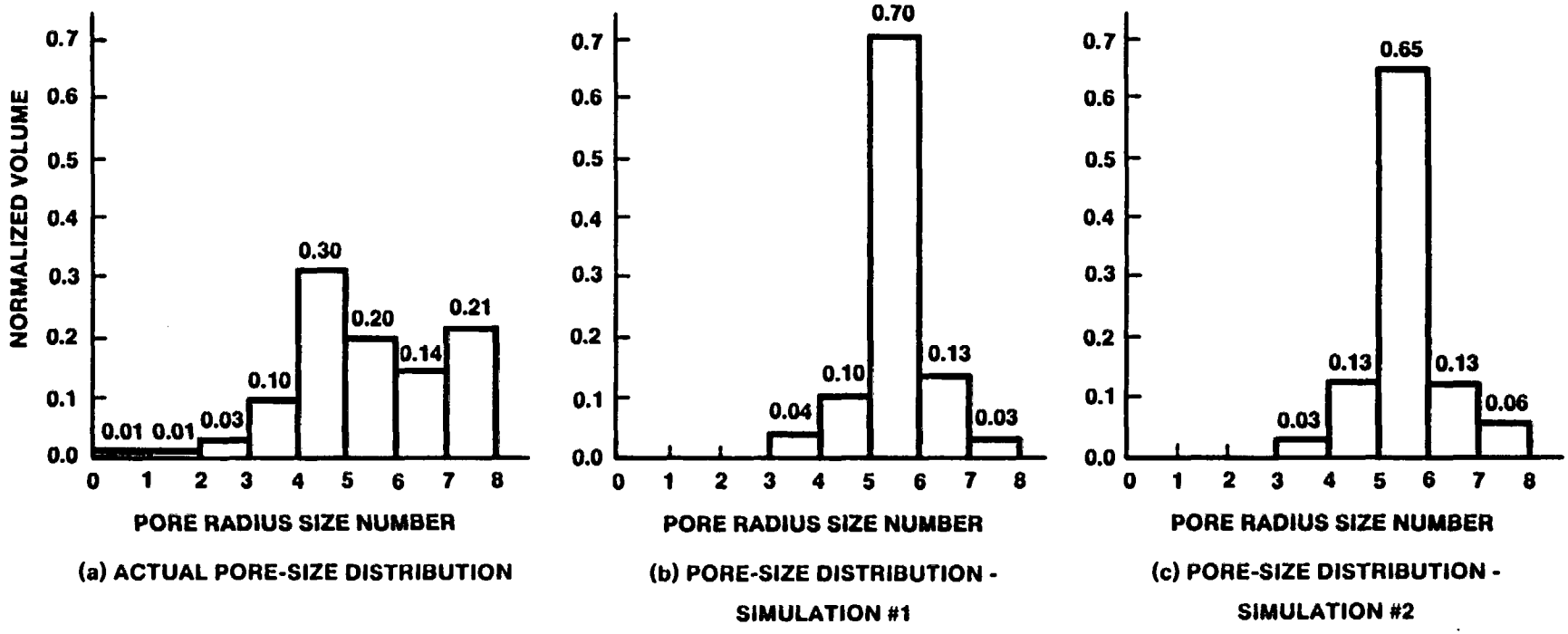

Figure 2. Actual and Simulated Pore-Size Distributions

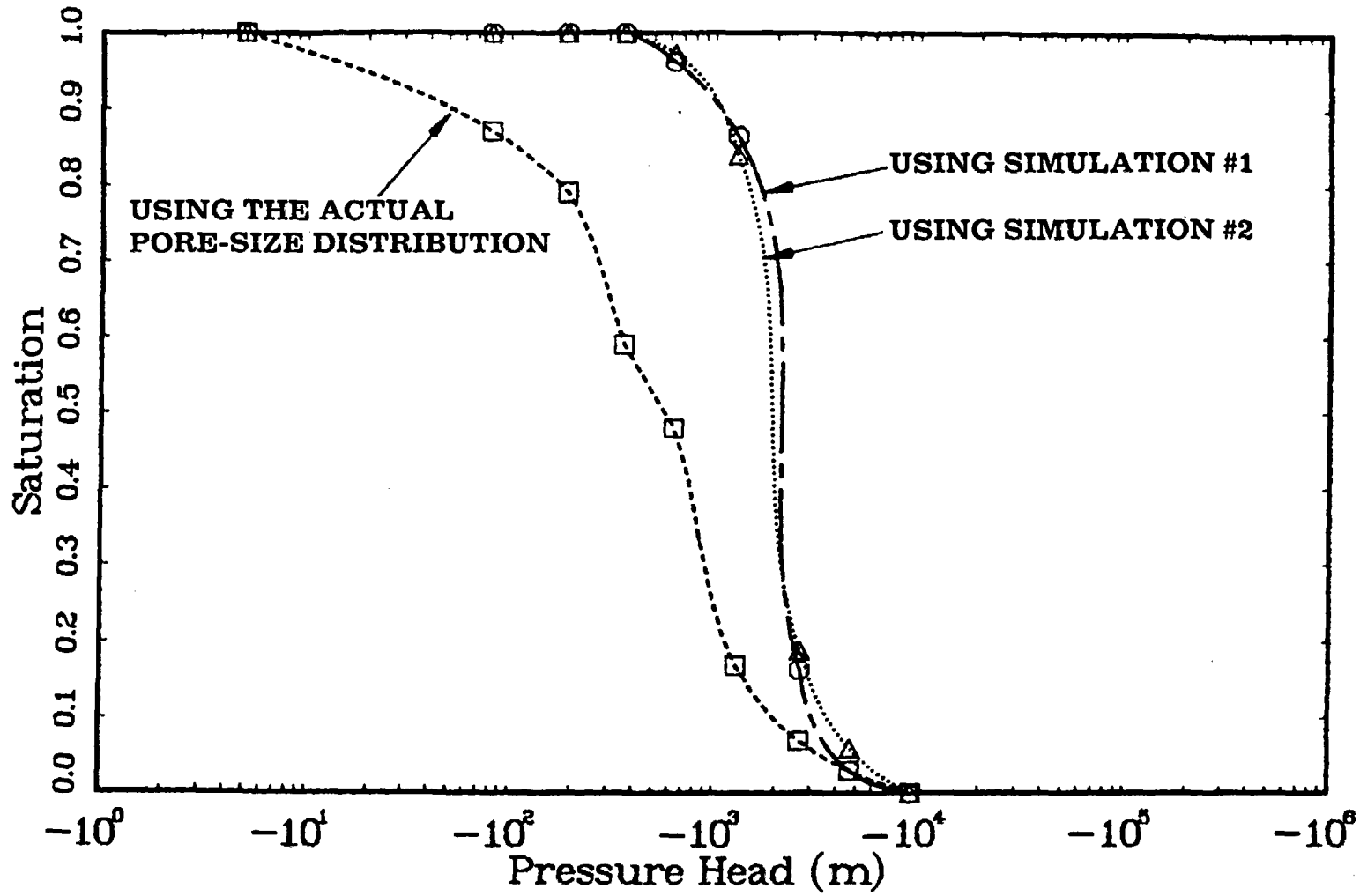

Figure 3. Saturation Curves from Mercury-Intrusion Simulation

2. Thermocouple Psychrometry

There are also significant advantages and disadvantages in using the thermocouple-psychrometry technique to determine the saturation curves. Although mercury porosimetry relates only one pore size to a particular pressure head, psychrometric data results from the effects of all of the pores and the interactions between the pores to produce a certain potential at any particular saturation. The method is not excessively slow, requiring on the order of one to several days to obtain the complete saturation curve. The time required to obtain data measurements, of course, depends on the time estimated to achieve saturation equilibrium and how many different saturation and humidity measurements one desires to represent the curve. The method is also suitable for both field and laboratory use. As shown in Peters et al. (1984 and 1985), it also gives repeatable and consistent results. However, the psychrometry method is more sensitive to environmental conditions than mercury-intrusion testing, and the temperature must be fairly well controlled. The thermocouple psychrometer and the mercury-intrusion methods both suffer the disadvantage that only relatively small samples are generally tested. Daniels et al. (1981), in studying the applicability of thermocouple psychrometers for use in measuring pressure heads in partially saturated soils, note that "the thermocouple psychrometer is one of the best devices now available for measuring suctions in relatively dry, unsaturated soils." However, it is relatively more expensive and time-consuming than mercury intrusion.

The psychrometry method has a sensitivity of only about -10 m of water pressure head and is not accurate above approximately -20 to -30 m of pressure head, where large pores may have an effect. This may be a significant disadvantage in the determination of the pressure head versus saturation relationship for some of the tuffs at Yucca Mountain. Scanning electron microscope (SEM) results (Connolly, 1986) indicate that nonwelded vitric tuffs at Yucca Mountain have a large fraction (over half) of pores of radii greater than a few μm. The corresponding pressure heads for pore radii greater than a few μm are greater than -30 m; therefore, the psychrometry method may not detect the effects of the presence of these large pores. Pores of radii greater than a few μm may also be present to a smaller extent in other welded and nonwelded tuffs at Yucca Mountain. The

lack of data at low negative pressure heads can be supplemented by pressure-plate measurements [see, e.g., Hillel, 1971]. However, data for tuffs from Yucca Mountain on saturation as a function of pressure heads are not available from measurement techniques other than thermocouple psychrometry. It is therefore recognized that the psychrometry results shown in this report are not accurate above pressure heads of approximately -20 to -30 m.

3. Permeametry

The constant-head method for determining saturated hydraulic conductivity is simple, accurate, and relatively inexpensive. For low conductivity samples, the test can be time-consuming under the low hydraulic-head gradients generally used. Sample size is limited by the apparatus used, but in general is relatively flexible. The accuracy is limited primarily by the accuracy of the measurement of the liquid flow rate and the pressure drop across the sample. The disadvantages are relatively minor.

III. RESULTS

Mercury-intrusion data were acquired on samples from 68 different locations at Yucca Mountain and are tabulated in Appendix A (data sheets on microfiche). The data include values for intruded mercury volume as a function of mercury-intrusion pressure and corresponding pore radius. Saturated conductivities and intrusion-derived curves of saturation as a function of pressure head are calculated from these data. The data sheets in Appendix A also include estimates of average pore diameter, median pore diameter, total pore surface area, and bulk and skeletal density for each sample. The average pore diameter and surface area values were calculated based on the assumption that the pores were cylindrical in geometry and that their diameters and volumes were specified by the pore-size distribution. The data are in the format provided to the authors by Micromeritics Instrument Corporation, who made the mercury-intrusion measurements.

Capillary-bundle theory is used to convert the mercury-intrusion data into a pore-size distribution, which is then used to estimate hydrologic parameters for the material. As mentioned previously, mercury-intrusion

data (mercury volume intruded as a function of mercury-intrusion pressure) can be converted into a pore-size distribution (pore volume as a function of pore radius) by assuming that the pores of the material are bundles of circular (capillary) tubes. Equation 1 and the mercury-intrusion pressure were used to derive the radii of the pores corresponding to the incremental mercury volumes intruded.

Values for saturated hydraulic conductivity obtained from permeametry testing and values for saturation as a function of pressure head obtained from thermocouple psychrometry testing have been previously documented for tuff samples from Yucca Mountain. These values are reported in Peters et al. (1984 and 1985) and reproduced here for comparison with the mercury-intrusion-derived values. The samples tested by mercury intrusion were subsamples taken from a larger drill core and were either the identical subsamples tested by Peters et al. or nearby samples taken from the same core sample from the same location (drill hole and depth).

The mercury-intrusion data in Appendix A show that most pores in welded tuffs and some nonwelded zeolitized tuffs appear to be less than a few μm in radius, with the average pore radius for the majority of the samples (calculated from the ratio of the total volume of mercury intruded to the total surface area of the pores) being generally less than 0.05 μm. For nonwelded vitric tuffs, the mercury-intrusion data indicate that often a significant fraction of pore volume is from pores of greater than 1 μm, with an average pore radius for the vitric tuffs generally under 0.1 μm. The mercury-intrusion data also suggest that many of the tuff samples possess a bimodal pore-size distribution. In general, the pore-size distribution results obtained using mercury porosimetry qualitatively concur with results from SEM analysis of the pore-size distributions for both the nonwelded and welded tuffs (Connolly, 1985 and 1986).

Using the relationship between capillary pressure and the surface tension of the fluid of interest, data on mercury saturations as a function of mercury-intrusion pressure can be converted to curves of water saturation as a function of capillary pressure. These data are compared below with the more direct calculation of these curves by means of data obtained through thermocouple-psychrometry testing. Capillary-bundle theory may also be used to calculate the permeability; several alternative methods are available.

For this document, four methods are used to calculate the permeability of the tuffs under study using pore-size distributions derived from mercury-intrusion data. These values are compared with values from direct measurements of permeability (or saturated hydraulic conductivity) using the standard permeametry technique.

A. Estimation of the Water-Saturation Curve

In comparing the capillary pressure curves determined by the two methods described here, it must be recalled that the magnitudes of the capillary pressures are proportional to the product of the surface tension of the liquid being used and the cosine of the angle of contact against the solid. Although the surface tensions of the liquids involved can be measured with a reasonable level of accuracy, there can be significant uncertainty in the values of the contact angle. For comparison purposes, a first approximation of the values can be assumed as follows:

γ_{Hg} = 484 dynes/cm $\qquad$ γ_{H_2O} = 72 dynes/cm

ϕ_{Hg} = 130 degrees $\qquad$ ϕ_{H_2O} = 15 degrees

Both contact angles are assumed, using published values for other materials as guidance (see, e.g. Purcell, 1949; Micromeritics Instrument Corp., 1985).

The adjustment for the differences in the liquid properties of mercury and water for the capillary pressure can then be calculated as follows (Purcell, 1949):

$$P_{H_2O} = (\rho gh)_{H_2O} = P_{Hg} \frac{\gamma_{H_2O} \cos(\phi_{H_2O})}{\gamma_{Hg} \cos(\phi_{Hg})} \qquad (4)$$

Because mercury is regarded as a nonwetting fluid and water a wetting fluid, the water saturation corresponding to this adjusted pressure is 1 minus the mercury saturation determined by the intrusion tests. Thus, at zero intrusion pressure, the mercury saturation of the sample is zero and the corresponding water saturation is 100%. At the maximum recorded intrusion pressure of approximately 60,000 psi (4080 bars), corresponding to a pressure head of about -1.0×10^4 m of water, the mercury saturation of the sample is assumed to be 100% and the corresponding water saturation is zero.

Data on water saturation as a function of capillary pressure are available for the samples from Yucca Mountain as listed in Table A.1. The samples are grouped by hydrogeologic unit, descending from the Tiva Canyon welded (TCw) unit nearest the ground surface to the Bullfrog welded (BFw) unit. The samples are identified by drill hole and depth from the surface expressed in feet. In this report, a shorthand notation is used for sample identification, consisting of the (USW) geologic drill hole from which the sample was obtained (G1, GU3, or G4) followed by the sample depth (expressed in feet). For example, sample ID GU3-82 indicates the sample was obtained from drill hole USW GU-3, from a depth of 82 feet. B. B. #10 indicates that the sample was obtained from the Busted Butte Outcrop, Rock #10.

Both thermocouple-psychrometer data and mercury-intrusion data are available for most of the samples listed in Table A.1; those samples which have had only thermocouple-psychrometer or mercury-intrusion tests are noted in Table A.1. The mercury-intrusion data were converted into water saturation-capillary pressure data using the method described above and compared with the data available from thermocouple-psychrometry testing. The results are shown in Figures B.1 to B.73 in Appendix B for the 81 samples tested. For each depth in Appendix B, the top figure represents the thermocouple-psychrometry data with a curve fit through the data using a formulation by van Genuchten (1978). The bottom figure shows the comparison of the saturation curve derived from the mercury-intrusion data with the saturation curve-fit of the psychrometry data. [Note that the bottom figures have a larger pressure-head range than the top figures.] The functional (or hydrogeologic) unit associated with each sample is noted on the figures. The vertically-directed arrows at a pressure head of -20 m

indicate the approximate upper limit of the accuracy of the thermocouple psychrometer.

A qualitative comparison between the curves determined from the two methods shows substantial differences between the results for many of the samples. Although for some samples the comparisons are very good (e.g., samples G1-1359 (Fig. B.38), G1-1387 (Fig. B.40), GU3-884 (Fig. B.24), GU3-1680 (Fig. B.67), GU3-1730 (Fig. B.68), G4-1256 (Fig. B.30), G4-1299 (Fig. B.36), and G4-2407 (Fig. B.73)), many of the samples do not even show a qualitatively similar curve shape (e.g., G1-1306 (Fig. B.33), GU3-121 (Fig. B.2), GU3-397 (Fig. B.9), and GU3-1555 (Fig. B.46)). The comparisons are relatively good for the two "double-humped" curves for samples G1-1359 and G1-1387 (Figures B.38 and B.40). These curves indicate a bimodal pore-size distribution. The mercury-intrusion method would be expected to easily detect two different major groupings of pore sizes.

As is also visually evident, there are a number of samples (e.g., G1-616 (Fig. B.15), G1-1780 (Fig. B.51), G1-1917 (Fig. B.65), GU3-374 (Fig. B.7), GU3-585 (Fig. B.17), GU3-1197 (Fig. B.34), and G4-1728 (Fig. B.59)) for which the saturation curves resulting from the two methods are similar in shape but are located at different points along the pressure-head axis (x-axis). The offset is as much as three orders of magnitude (see GU3-1197; Fig. B.34). The offset may be due, in part, because of the inherent differences in the fluids used (mercury and water) in the two methods. The saturation curve determined from thermocouple psychrometry is a drying curve for a wetting fluid (water); the curve determined from mercury-intrusion data is an imbibition curve for a nonwetting fluid. A quick calculation can be performed to indicate whether the psychrometry data or the intrusion-derived data are more indicative of the true nature of the pore structure and material characteristics.

First, consider sample GU3-1197 (Fig. B.34) for which the curves are offset by about three orders of magnitude in pressure head. The curves are approximately the same shape, decreasing from 100% saturation to about 40% over a short distance on the logarithmic pressure-head scale. However, most of the apparent mobile-fluid saturation occurs at less than approximately 0.3 m of negative pressure head for the intrusion-derived data and at less than approximately 500 m of negative pressure head for the psychrometry

data. For simplicity, capillary-bundle theory is assumed, with a representative (volume-averaged) pore radius, r, used for all pores in the material. The volume-averaged pore radius from the mercury-intrusion data is approximately 34 μm and about 0.045 μm from the thermocouple psychrometry data (using Eq. 1 to convert from pressure head to pore radius). The permeability of the sample is calculated as

$$k = n\, r^2/8 \tag{5}$$

From the intrusion-derived volume-averaged pore radius (with the porosity, n, as calculated from the mercury-intrusion data, equal to 0.069) the permeability is calculated as 1×10^{-11} m^2; from the psychrometer-derived radius, the permeability is calculated as 2×10^{-17} m^2. The experimentally measured value (Peters et al., 1985) is given as 1.5×10^{-18} m^2. Even with this simple calculation, it can be seen that the saturation curve derived from the mercury-intrusion pore-size distribution would appear to be physically unrealistic.

A similar judgement can be made from a sample (e.g., G1-1780; Fig. B.51) for which the curves are offset only slightly. For the intrusion-derived curve, the volume-averaged pore radius is approximately 15 μm; for the psychrometer curve, the volume-averaged pore radius is approximately 0.039 μm. The corresponding permeabilities calculated from Eq. 5 (with n = 0.25) are 7×10^{-12} m^2 and 7×10^{-17} m^2, respectively. From Peters et al. (1985), the measured permeability is 2×10^{-19} m^2. Again, the psychrometer data appear to be the more physically realistic.

The psychrometer saturation curves and the mercury-intrusion saturation curves are compared for units TSw1 and TSw2, CHnv, and CHnz in Figures 4 to 6. According to these figures, the mercury-intrusion data indicate that there are some large pores that desaturate in the pressure-head range of -0.1 m to -10 m, whereas the psychrometer data indicate that desaturation begins in the range of -10 to -100 m. (Note: the accuracy of the psychrometer technique is of the order of ± 10 m.) The vertically-directed arrows on the figures at a pressure head of -20 m indicate the approximate upper limit of the accuracy of the thermocouple psychrometer. The psychrometer saturation curves for units TSw1 and TSw2 form a fairly

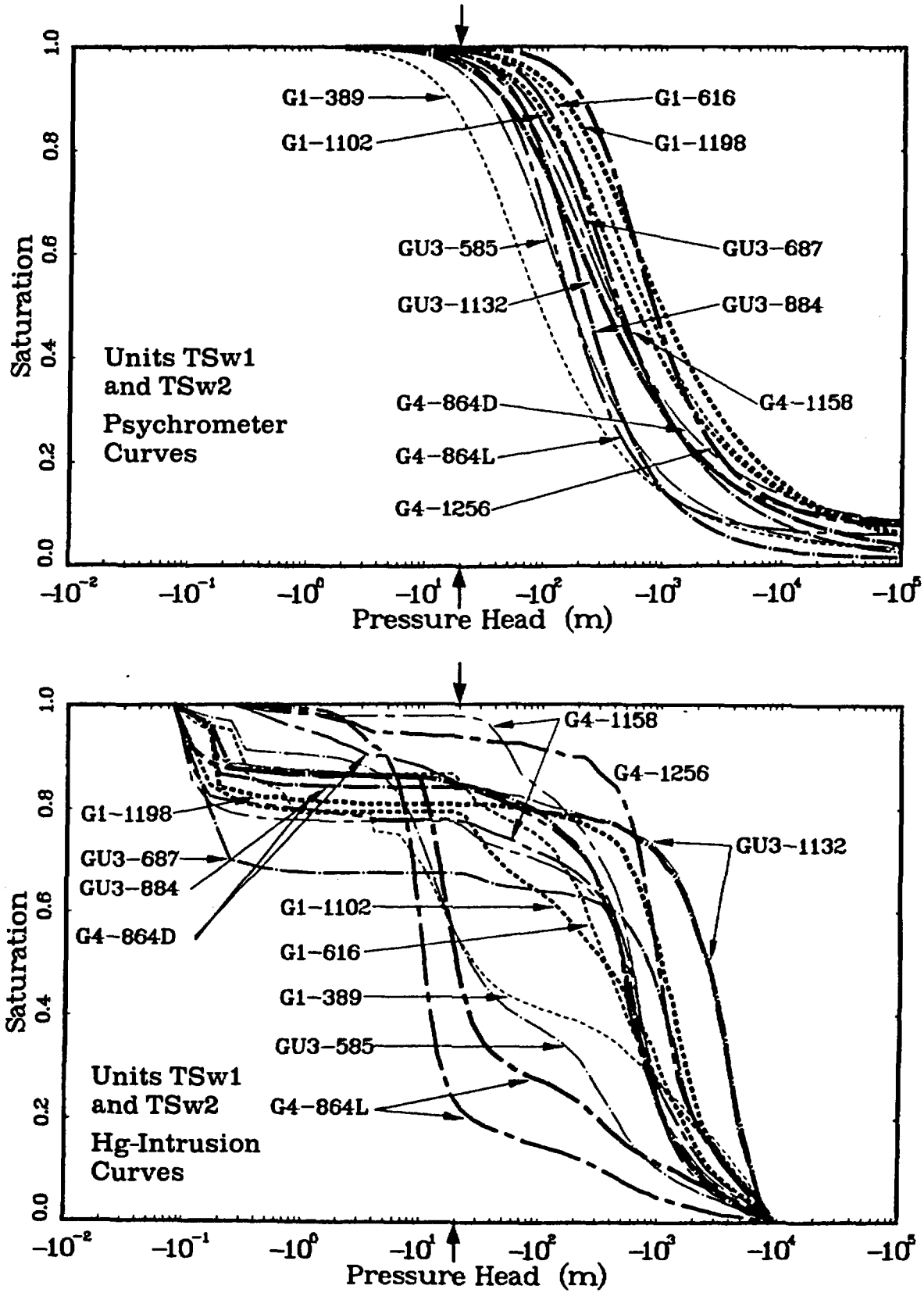

Figure 4. Psychrometer and Mercury-Intrusion Saturation Curves for Units TSw1 and TSw2

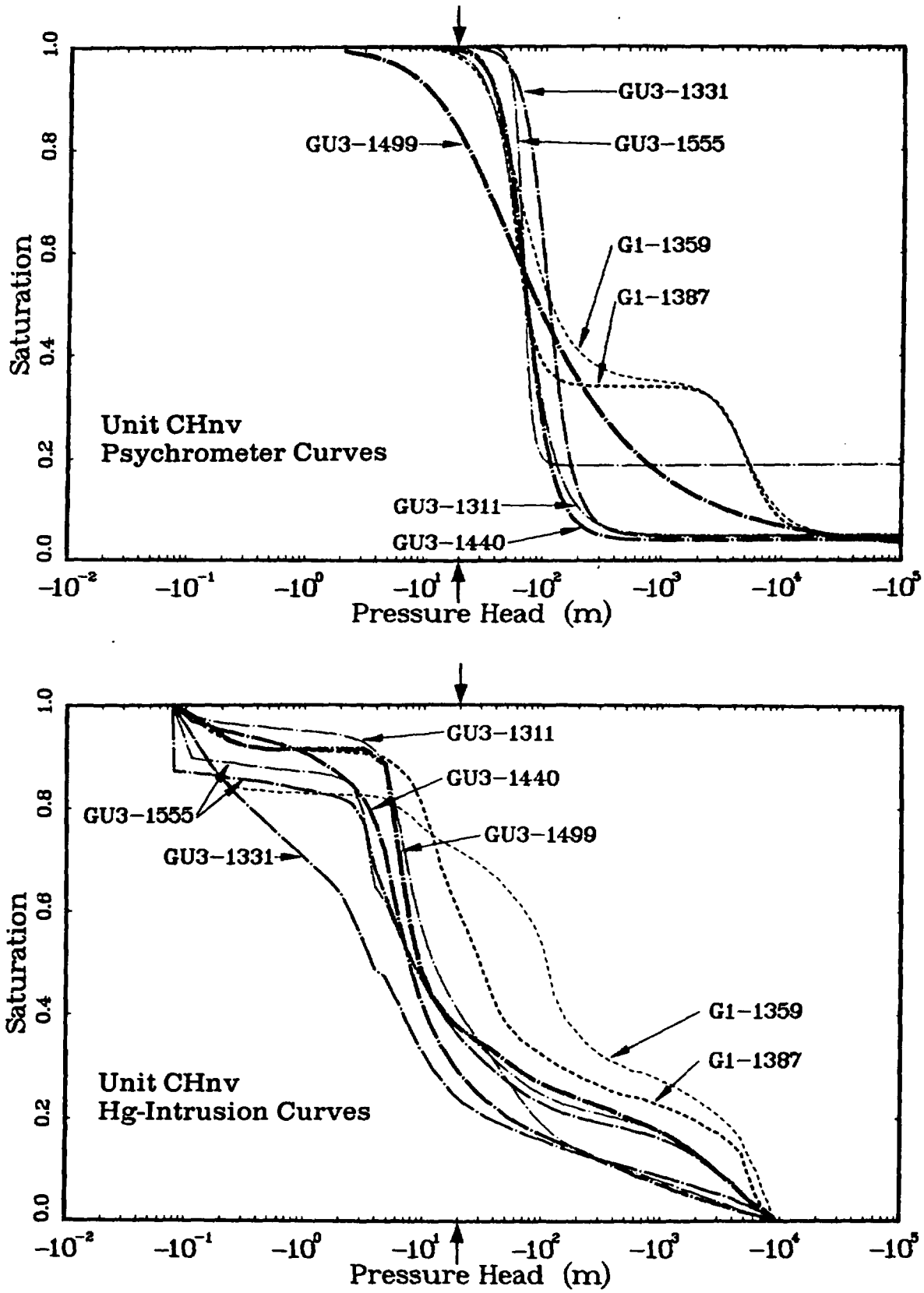

Figure 5. Psychrometer and Mercury-Intrusion Saturation Curves for Unit CHnv

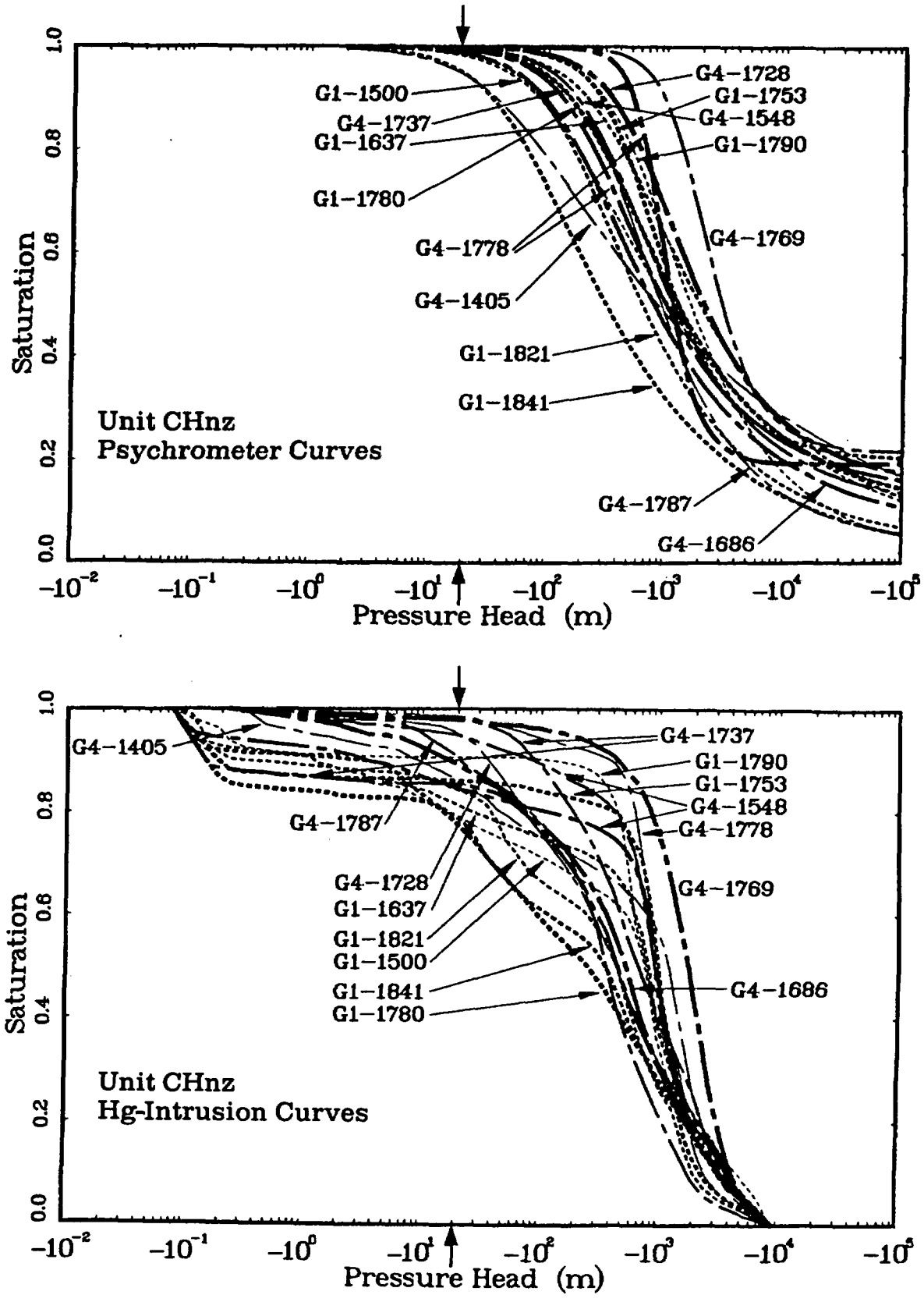

Figure 6. Psychrometer and Mercury-Intrusion Saturation Curves for Unit CHnz

coherent group, which is what might be expected from a densely welded tuff that has fairly uniform properties (Nimick et al., in preparation). However, the mercury-intrusion saturation curves are quite variable. For a certain saturation (e.g., 50%), the pressure-head range of the psychrometer saturation curves is about one order of magnitude (at 50% saturation from -10^2 to -10^3 m), whereas the pressure-head range for the mercury-intrusion saturation curves can be almost three orders of magnitude (at 50% saturation from -10^1 to -10^4 m). Figures 5 and 6 for units CHnv and CHnz show similar results. The major conclusion to be drawn from these three figures is that the psychrometer saturation curves form a much less variable group than the mercury-intrusion saturation curves.

The saturation data derived from the mercury-intrusion data and from the psychrometer data may be linked in some manner. The specific form of linkage that was investigated is a linear relation between the two values.

$$\hat{S}_{psy}(\psi^*) = a * S_{Hg}(\psi^*) + b \qquad (6a)$$

where:

$$-20 \text{ m} > \psi^* \qquad (6b)$$

Equation 6a expresses an estimate of the value of the saturation determined by the psychrometer ($\hat{S}_{psy}$) in terms of the saturation value resulting from the mercury-intrusion test results (S_{Hg}) at a pressure head ψ^*. This relationship might be expected to hold (see 6b above) for all pressure heads less than approximately -20 m of pressure head (the accuracy of the pressure head determined by the thermocouple psychrometer is approximately ± 10 m). The calculations for determining the parameters "a" and "b" used the measured values of the saturation and pressure head obtained in the thermocouple-psychrometer tests ($\hat{S}_{psy}$ and ψ^*) and a mercury-intrusion value (S_{Hg}) at ψ^* that was obtained by interpolation of the mercury-intrusion data.

The results of calculations of fitting the data by Eq. 6a are listed in Table 3. The correlation coefficient is high (ranging from 0.00 to 0.99, with most values above 0.8) indicating that the psychrometer curve can be fit with an equation of the form of Eq. 6a. However, the values of the variables "a" and "b" have quite a range. For example, for unit CHnv the slope variable "a" ranges from 1.1 to 5.4 and the intercept variable "b"

Table 3.
Statistical Comparison of Thermocouple-Psychrometer Data and Mercury-Intrusion Data

Sample Identifier	Number of Psychrometer Data Points	Number of Points Meeting Criteria	Corr. Coef.[1]	a[1]	b[1]
		Unit TCw			
GU3-82	23	20	0.9373	1.0665	-0.1032
GU3-121	18	16	0.8051	1.8482	0.0286
GU3-155	13	11	0.8872	1.2831	-0.1675
GU3-257	18	14	0.7449	0.8046	-0.0534
GU3-316	23	20	0.9899	1.1770	-0.0266
G4-43	29	20	0.8754	0.9010	-0.1624
			Mean	1.180	-0.081
			Standard Deviation	0.371	0.078
		Unit PTn			
GU3-374	16	14	0.7602	2.7895	-0.1650
GU3-378	16	14	0.8208	3.5617	-0.2787
GU3-397	16	13	0.6727	1.3208	-0.0409
G4-124	27	20	0.9376	0.5542	0.3056
G4-136	21	15	0.8623	2.0953	-0.1317
G4-172	16	11	0.3916	21.0083	-0.2273
G4-208	20	17	0.9328	4.0568	-0.0389
G4-208	20	17	0.8501	4.3832	-0.1997
			Mean	4.971	-0.097
			Standard Deviation	6.614	0.183
		Unit TSwl			
G1-389	30	23	0.9284	2.1261	-0.3886
G1-616	31	25	0.9653	1.0455	0.1279
G1-752	21	19	0.8712	0.7844	0.1037
GU3-585	27	21	0.9619	1.7432	-0.0054
GU3-687	27	20	0.8439	1.0063	-0.0302
			Mean	1.341	-0.039
			Standard Deviation	0.567	0.207

[1] The thermocouple-psychrometer saturation data are estimated from the mercury-intrusion saturation data using Equation 6a ($S_{psy} = a * S_{Hg} + b$).

The correlation coefficient is the statistical measure of the goodness of fit.

Table 3. (continued)
Statistical Comparison of Thermocouple-Psychrometer Data
and Mercury-Intrusion Data

Sample Identifier	Number of Psychrometer Data Points	Number of Points Meeting Criteria	Corr. Coef.[1]	a[1]	b[1]
		Unit TSw2			
G1-1102	33	27	0.9886	1.0966	0.1029
G1-1198	29	23	0.9041	0.8145	0.1387
GU3-884	28	22	0.9056	0.9544	-0.0568
GU3-1132	22	18	0.6150	0.6466	-0.0528
GU3-1132	22	18	0.6100	0.6381	-0.0513
G4-864L[2]	36	30	0.9193	4.0368	-0.0435
G4-864L[2]	36	30	0.9009	2.3322	-0.0907
G4-864D	29	20	0.9048	0.7299	0.1323
G4-864D	29	20	0.8636	0.8274	0.0943
G4-1158	37	33	0.9164	0.7505	0.1020
G4-1159	37	33	0.8916	0.9217	0.0494
G4-1256	28	21	0.8927	0.8213	0.0610
B. B. #10	23	21	0.9389	1.1768	-0.1708
			Mean	0.853	0.032
			Standard Deviation	0.172	0.100
		Unit TSw3			
G1-1306	26	19	0.9525	3.3335	-0.4549
GU3-1197	19	17	0.7558	1.7002	0.1955
GU3-1246	20	16	0.8265	1.8243	-0.0643
G4-1299	34	28	0.9232	0.7377	0.1096
G4-1299	34	28	0.8999	0.8587	0.0447
			Mean	1.691	-0.034
			Standard Deviation	1.039	0.254

[1] The thermocouple-psychrometer saturation data are estimated from the mercury-intrusion saturation data using Equation 6a ($S_{psy} = a * S_{Hg} + b$).

The correlation coefficient is the statistical measure of the goodness of fit.

[2] This sample was not included in the calculation of the mean and standard deviation of the parameters "a" and "b" because it had such extreme values of these parameters. Including this sample would significantly bias the calculated means and standard deviation, indicating a much worse comparison.

Table 3. (continued)
Statistical Comparison of Thermocouple-Psychrometer Data
and Mercury-Intrusion Data

Sample Identifier	Number of Psychrometer Data Points	Number of Points Meeting Criteria	Corr. Coef.[1]	a[1]	b[1]
		Unit CHnv			
G1-1359	28	20	0.9650	1.1017	0.0518
G1-1387	26	18	0.8955	1.7674	-0.0275
GU3-1311	17	14	0.9182	2.5367	-0.1169
GU3-1331	10	8	0.9129	4.7368	-0.1755
GU3-1440	18	16	0.8763	3.6117	-0.1916
GU3-1499	17	13	0.8947	1.5541	-0.0337
GU3-1555	11	8	0.9041	5.0937	-0.7725
GU3-1555	11	8	0.9034	5.4161	-0.7552
			Mean	3.227	-0.253
			Standard Deviation	1.717	0.326
		Unit CHnz			
G1-1500	34	26	0.9680	0.7904	0.2340
G1-1637	33	25	0.9396	0.7548	0.3120
G1-1753	29	23	0.9610	0.7588	0.2413
G1-1780	30	24	0.9934	1.0236	0.2663
G1-1790	26	20	0.9840	0.7620	0.2825
G1-1821	31	23	0.9934	0.9453	0.1609
G1-1841	28	21	0.9432	0.9487	0.0814
G4-1405	30	25	0.8961	0.7437	0.1641
G4-1547	30	21	0.9320	0.6655	0.2385
G4-1548	30	21	0.9424	0.6010	0.2638
G4-1686	38	34	0.9812	0.8879	0.1707
G4-1728	29	24	0.8560	0.7639	0.3928
G4-1736	28	19	0.9752	0.9009	0.2626
G4-1737	28	19	0.9757	0.7444	0.2484
G4-1769	22	19	0.9852	0.7577	0.3016
G4-1778	39	33	0.9572	0.5519	0.2479
G4-1778-F	39	33	0.9847	0.8407	0.1617
G4-1787	29	20	0.8619	0.9115	0.2671
			Mean	0.797	0.239
			Standard Deviation	0.123	0.071

[1] The thermocouple-psychrometer saturation data are estimated from the mercury-intrusion saturation data using Equation 6a ($S_{psy} = a * S_{Hg} + b$).

The correlation coefficient is the statistical measure of the goodness of fit.

Table 3. (continued)
Statistical Comparison of Thermocouple-Psychrometer Data
and Mercury-Intrusion Data

Sample Identifier	Number of Psychrometer Data Points	Number of Points Meeting Criteria	Corr. Coef.[1]	a[1]	b[1]
		Unit PPw			
G1-1917	30	22	0.0000	0.8283	-0.0182
GU3-1628[2]	18	16	0.9034	8.6132	-0.2159
GU3-1680	22	18	0.9228	2.1579	-0.0611
GU3-1730	21	19	0.9932	1.2577	-0.0701
G4-1899	35	29	0.8623	1.7475	-0.2209
			Mean	1.498	-0.093
			Standard Deviation	0.578	0.088
		Unit CFUn			
G4-2006	35	29	0.9812	0.9322	0.1585
G4-2101	35	31	0.9328	0.6813	0.3500
			Mean	0.807	0.254
			Standard Deviation	0.177	0.135
		Unit BFw			
G4-2401	34	30	0.8993	1.5921	-0.0283
G4-2407	30	24	0.9694	1.1307	0.0145
			Mean	1.361	-0.007
			Standard Deviation	0.326	0.030

[1] The thermocouple-psychrometer saturation data are estimated from the mercury-intrusion saturation data using Equation 6a ($S_{psy} = a * S_{Hg} + b$).

The correlation coefficient is the statistical measure of the goodness of fit.

[2] This sample was not included in the calculation of the mean and standard deviation of the parameters "a" and "b" because it had such extreme values of these parameters. Including this sample would significantly bias the calculated means and standard deviation, indicating a much worse comparison.

ranges from -0.77 to 0.05. The variability of the slope and intercept variables for a hydrogeologic unit was characterized by calculating their mean and standard deviation, which are listed in the table. The mean value of the slope variable "a" for unit CHnv is 3.2, and the standard deviation is 1.7. The mean value of the intercept variable "b" for unit CHnv is -0.25, and the standard deviation is 0.33. The variability of the samples is so great that single values for the slope and intercept variables for a unit cannot be chosen. Thus, it appears that it is not possible to use this method to convert mercury-intrusion saturation curves into psychrometer saturation curves without individually testing each sample using both methods. Testing using both methods, of course, is not practical. The comparatively large amount of variability in the mercury-intrusion saturation curves will probably make it very difficult to devise any simple transform function, with constant variables for each unit, that can accurately correlate the mercury-intrusion-derived saturation curve with the actual saturation curve for the material. Other transform functions, such as one that slides the mercury-intrusion saturation curve along the pressure-head axis, might be tested. But it appears that the mercury-intrusion saturation curves are fundamentally different from the psychrometer saturation curves.

It might be expected that the curves of hydraulic conductivity as a function of pressure head are, in general, more sensitive to pore interactions and the two-phase interactions of fluids within the distributions of pores than the curves for saturation as a function of pressure head. Therefore, it is the opinion of the authors that a comparison of measured relative hydraulic conductivities with relative hydraulic conductivities derived from pore-size distributions would be even less favorable than the saturation-curve comparisons shown here.

B. Estimation of the Saturated Hydraulic Conductivity

One of the most basic hydrologic properties of a material is its permeability. Therefore, comparisons were also made between measured permeabilities (or saturated hydraulic conductivities) and estimated permeabilities calculated by several formulations from the pore-size distributions derived from mercury-intrusion data. The four formulations used to estimate the permeability, drawn from sources discussed below, are as follows:

$$k = c \frac{n}{8} r_{ave}^2 \tag{7a}$$

where $r_{ave} = 4V/(SA)$

$$k = c \frac{n}{8} r_{ave}^2 \tag{7b}$$

where $r_{ave} = \frac{\Sigma\, v(r_i) r_i}{\Sigma\, v(r_i)}$

$$k = n / [c\ (SA/V)^2] \tag{8}$$

$$k = c\ n \int_0^1 dS/(P_c^2) \tag{9}$$

where k is permeability, n is porosity, r_i is the radius of pore i, $v(r_i)$ is the incremental volume fraction of pores of radius r_i, c is some constant related to the structure of the matrix material, SA is the surface area, S is saturation, P_c is capillary pressure, and V is the total volume of mercury intruded, or the total pore volume.

The constants in the formulations generally include such effects as pore tortuosity, length distribution, surface characteristics, pore-geometry

variations, connectiveness, etc. None of the formulations are expected to yield accurate predictions without scaling them to account for some of these effects. What is generally hoped for is that for a particular rock type, approximately the same scaling factor will hold for different samples. For purposes of comparison with the measured saturated hydraulic conductivity (permeability), the constant was set equal to unity for all samples.

The formulations are based on capillary theory and might, therefore, be expected to yield somewhat similar prediction capabilities. Because permeability has units of area and is generally related to the size of the opening in which a fluid flows, the formulations can usually be related to some characteristic length of the pore. This length is usually a characteristic, or average radius. The first two formulations (see, e.g., Amyx et al., 1960) assume that all of the pores are of cylindrical shape and can be thought of as discrete volumes. The permeability for a single cylindrical capillary tube is simply calculated by squaring the value for the size of the tube radius and dividing by eight. Therefore, the permeability of a bundle of tubes is the sum of all of the individual permeability values of the tubes, and the permeability of a rock matrix is that sum multiplied by the matrix porosity. The two formulations (Eq. 7a and 7b) differ in the manner in which the pore radii are weighted in order to yield a value for the size of the average radius. For Eq. 7a, the value for the average pore radius is calculated using the value for the total volume of mercury intruded in conjunction with that of the calculated size of the surface area of the pores ($r = 4V/SA$). The calculated size of the total surface area of the pores is listed in Appendix A for each sample tested. Calculations of the total area assumed the pores were cylindrical and summed the individual calculated pore surface areas over the pore-size distribution. For Eq. 7b, a volume-averaged pore radius length is calculated.

The third formulation (Eq. 8) is the familiar Kozeny-Carman equation (see, e.g., Amyx et al., 1960) for estimating permeability. The surface area can be determined in more than one manner, but the permeability again becomes proportional to the square of the pore radius. In this formulation, the value for the size of the total surface area of the bundle of cylindrical capillaries is divided by that of the total pore volume. The ratio of the surface area of the pores to the pore volume is referred to as

the specific surface area. For a bundle of cylinders, this is simply $\Sigma\ (2\pi rL)/\Sigma\ (\pi r^2 L)$, which is proportional to $1/r$. Therefore, because the permeability is proportional to the inverse square of the specific surface area, it is also proportional to the radius squared. The constant in the formulation includes the constants from the geometric ratio of area to volume, as well as the less quantifiable effects of pore tortuosity, length distribution, surface characteristics, pore-geometry variations, connectiveness, etc. For purposes of comparison with the measured saturated hydraulic conductivity (permeability), the constant was set equal to unity for all samples.

The fourth formulation (Eq. 9) follows from the work of Purcell (1949). He equated the flow as defined by Darcy's law of fluid flow in a porous medium with the flow through a bundle of tubes as defined using Poiseuille's derivation, by substituting the capillary pressure for the pore radius, as defined in Eq. 1. This yielded a formulation for the permeability in terms of the square of the capillary pressure, rather than that of the pore radius. The constant takes into account value for the fluid surface tension, value of the contact angle between the fluid and the solid, unit conversion factors, and a lithology factor that reflects such characteristics as tortuosity, pore shape, etc. as mentioned earlier. This constant was set to a value of unity for purposes of comparison, as it was for the previous formulation.

Table 4 shows the samples grouped by hydrogeologic unit, the measured saturated hydraulic conductivities obtained from Peters et al. (1984 and 1985), and the ratio of the experimentally measured conductivity to the calculated conductivity for each sample, using the samples' pore-size distributions for calculations in conjunction with Eqs. 7a, 7b, 8, and 9. For each hydrogeologic unit, a mean and sample standard deviation of these ratios were calculated. [Units TSw1 and TSw2 were grouped together because available information shows no significant difference in the rock matrix physical structure and mineralogy; the units were separated only on the basis of the percentage of lithophysae in the units (Nimick et al., in preparation).] The standard deviations of the ratios, using the calculated conductivities, are generally somewhat greater than those of the experimentally determined conductivities. The large deviations may be

Table 4.
Comparison of Measured and Calculated Saturated Hydraulic Conductivities

Sample	Unit	K_{expt}(m/s)	K_{expt}/K_{calc} Ratio Using Eq. 7a	Eq. 7b	Eq. 8	Eq. 9
GU3-82	TCw	1.50×10^{-12}	1.47×10^{-02}	4.39×10^{-08}	2.93×10^{-01}	1.33×10^{-08}
GU3-121	TCw	7.00×10^{-12}	4.34×10^{-03}	3.93×10^{-08}	8.69×10^{-02}	2.74×10^{-08}
GU3-155	TCw	2.66×10^{-12}	8.96×10^{-02}	2.39×10^{-07}	1.79	6.03×10^{-08}
GU3-316	TCw	1.50×10^{-12}	3.07×10^{-02}	1.28×10^{-07}	6.13×10^{-01}	4.64×10^{-08}
G4-43	TCw	9.68×10^{-12}	2.34×10^{-01}	7.41×10^{-05}	4.68	6.28×10^{-06}
$\log_{10}$ mean[1]		-11.5	-1.5	-6.5	-0.2	-7.0
std. dev.[2]		0.4	0.7	1.4	0.7	1.1
GU3-374	PTn	1.63×10^{-06}	$4.27 \times 10^{+02}$	1.70×10^{-02}	$8.51 \times 10^{+03}$	5.39×10^{-03}
GU3-378	PTn	3.90×10^{-07}	$3.19 \times 10^{+02}$	7.01×10^{-03}	$6.37 \times 10^{+03}$	1.06×10^{-03}
GU3-397	PTn	3.52×10^{-07}	$2.33 \times 10^{+03}$	4.65×10^{-04}	$4.67 \times 10^{+04}$	4.08×10^{-04}
G4-136	PTn	2.80×10^{-07}	$1.95 \times 10^{+02}$	3.16×10^{-03}	$3.90 \times 10^{+03}$	9.20×10^{-04}
G4-208	PTn	2.35×10^{-06}	$7.16 \times 10^{+02}$	1.78×10^{-02}	$1.43 \times 10^{+04}$	1.96×10^{-03}
G4-208[3]	PTn	2.35×10^{-06}	$7.16 \times 10^{+01}$	6.28×10^{-01}	$1.43 \times 10^{+03}$	3.30×10^{-01}
$\log_{10}$ mean		-6.1	2.6	-2.0	3.9	-2.5
std. dev.		0.4	0.5	1.0	0.5	1.0
G1-389	TSw1	4.00×10^{-11}	3.08×10^{-01}	9.48×10^{-07}	6.16	3.35×10^{-07}
G1-616	TSw1	1.70×10^{-12}	2.08×10^{-02}	1.41×10^{-07}	4.16×10^{-01}	2.88×10^{-08}
G1-752	TSw1	1.09×10^{-11}	4.60×10^{-01}	6.24×10^{-07}	9.20	2.20×10^{-07}
G1-1102	TSw2	9.20×10^{-12}	8.15×10^{-02}	2.05×10^{-07}	1.63	2.79×10^{-08}
G1-1198	TSw2	1.50×10^{-12}	4.34×10^{-02}	6.53×10^{-08}	8.68×10^{-01}	3.12×10^{-08}
GU3-585	TSw1	1.40×10^{-11}	1.88×10^{-02}	1.51×10^{-06}	3.76×10^{-01}	3.14×10^{-07}

[1] $\log_{10}$ mean x = $\Sigma \log_{10}(x_i)/n$

[2] std. dev. = $\Sigma \{\log_{10} x_i - [\log_{10} \text{mean } x]\}^2 /(n-1)$

[3] A different subsample of a larger sample of core from that depth.

Table 4. (continued)
Comparison of Measured and Calculated Saturated Hydraulic Conductivities

Sample	Unit	K_{expt}(m/s)	K_{expt}/K_{calc} Ratio Using Eq. 7a	Eq. 7b	Eq. 8	Eq. 9
GU3-687	TSw1	1.20×10^{-12}	2.43×10^{-02}	1.59×10^{-08}	4.87×10^{-01}	3.65×10^{-09}
GU3-884	TSw2	7.20×10^{-11}	5.23×10^{-01}	3.69×10^{-06}	$1.05 \times 10^{+01}$	1.54×10^{-06}
GU3-1132	TSw2	1.50×10^{-12}	1.18×10^{-01}	1.57×10^{-07}	2.37	1.84×10^{-08}
GU3-1132	TSw2	1.50×10^{-12}	1.16×10^{-01}	1.81×10^{-07}	2.32	2.09×10^{-08}
G4-864	TSw2	1.90×10^{-11}	1.48×10^{-01}	2.13×10^{-07}	2.95	9.16×10^{-08}
G4-864[1]	TSw2	3.90×10^{-11}	4.39×10^{-02}	5.72×10^{-07}	8.78×10^{-01}	1.40×10^{-07}
G4-864[1]	TSw2	3.90×10^{-11}	6.59×10^{-03}	4.29×10^{-05}	1.32×10^{-01}	2.41×10^{-05}
G4-864[1]	TSw2	1.87×10^{-11}	1.53×10^{-01}	4.60×10^{-05}	3.07	7.01×10^{-06}
G4-1158	TSw2	1.86×10^{-11}	1.45×10^{-01}	3.13×10^{-04}	2.90	1.35×10^{-05}
G4-1159	TSw2	1.90×10^{-11}	1.65×10^{-01}	2.58×10^{-07}	3.30	9.02×10^{-08}
G4-1256	TSw2	1.31×10^{-11}	3.95×10^{-01}	2.76×10^{-04}	7.90	2.13×10^{-05}
B. B. #10	TSw2	5.30×10^{-12}	7.19×10^{-02}	4.57×10^{-07}	1.44	1.30×10^{-07}
$\log_{10}$ mean[2]		-11.0	-1.0	-6.0	0.3	-6.6
std. dev.[3]		0.6	0.5	1.2	0.5	1.1
G1-1306	TSw3	3.70×10^{-11}	1.81	3.04×10^{-07}	$3.62 \times 10^{+01}$	2.90×10^{-07}
GU3-1197	TSw3	1.50×10^{-11}	1.42×10^{-01}	1.53×10^{-07}	2.85	2.16×10^{-07}
GU3-1246	TSw3	1.50×10^{-12}	4.60×10^{-02}	1.15×10^{-08}	9.21×10^{-01}	1.26×10^{-08}
G4-1299	TSw3	4.47×10^{-10}	$1.13 \times 10^{+01}$	4.84×10^{-03}	$2.26 \times 10^{+02}$	3.48×10^{-04}
G4-1299[1]	TSw3	4.47×10^{-10}	$1.45 \times 10^{+01}$	3.85×10^{-03}	$2.90 \times 10^{+02}$	3.58×10^{-04}
$\log_{10}$ mean		-10.4	0.06	-5.2	1.4	-5.6
std. dev.		1.0	1.1	2.6	1.1	2.0

[1] A different subsample of a larger sample of core from that depth.

[2] $\log_{10}$ mean x = $\Sigma \log_{10}(x_i)/n$

[3] std. dev. = $\Sigma (\log_{10} x_i - [\log_{10} \text{mean } x])^2 /(n-1)$

Table 4. (continued)
Comparison of Measured and Calculated Saturated Hydraulic Conductivities

Sample	Unit	K_{expt}(m/s)	K_{expt}/K_{calc} Ratio Using Eq. 7a	Eq. 7b	Eq. 8	Eq. 9
G1-1359	CHnv	2.40×10^{-11}	2.64×10^{-01}	5.39×10^{-07}	5.28	6.37×10^{-08}
G1-1387	CHnv	7.80×10^{-10}	3.15	3.18×10^{-05}	$6.29 \times 10^{+01}$	5.86×10^{-06}
GU3-1311	CHnv	3.15×10^{-09}	1.11	2.58×10^{-04}	$2.23 \times 10^{+01}$	3.47×10^{-05}
GU3-1331	CHnv	2.92×10^{-07}	$1.12 \times 10^{+02}$	1.48×10^{-03}	$2.23 \times 10^{+03}$	3.15×10^{-04}
GU3-1440	CHnv	2.68×10^{-07}	$5.49 \times 10^{+01}$	6.89×10^{-03}	$1.10 \times 10^{+03}$	1.40×10^{-03}
GU3-1499	CHnv	2.57×10^{-08}	$3.83 \times 10^{+01}$	1.14×10^{-03}	$7.65 \times 10^{+02}$	9.97×10^{-05}
GU3-1555	CHnv	7.90×10^{-08}	$1.15 \times 10^{+02}$	7.18×10^{-04}	$2.29 \times 10^{+03}$	1.90×10^{-04}
GU3-1555[1]	CHnv	7.90×10^{-08}	$9.48 \times 10^{+01}$	2.47×10^{-04}	$1.90 \times 10^{+03}$	6.27×10^{-04}
$\log_{10}$ mean[2]		-7.9	1.2	-3.6	2.5	-4.3
std. dev.[3]		1.4	1.0	1.3	1.0	1.4

[1] A different subsample of a larger sample of core from that depth.

[2] $\log_{10}$ mean x = $\Sigma \log_{10}(x_i)/n$

[3] std. dev. = $\Sigma \{\log_{10} x_i - [\log_{10} \text{mean } x]\}^2 /(n-1)$

Table 4. (continued)
Comparison of Measured and Calculated Saturated Hydraulic Conductivities

Sample	Unit	K_{expt}(m/s)	K_{expt}/K_{calc} Ratio Using Eq. 7a	Eq. 7b	Eq. 8	Eq. 9
G1-1500	CHnz	1.50×10^{-11}	1.06×10^{-01}	2.41×10^{-07}	2.12	6.16×10^{-08}
G1-1637	CHnz	1.30×10^{-11}	1.04×10^{-01}	6.30×10^{-07}	2.08	1.20×10^{-07}
G1-1753	CHnz	1.40×10^{-11}	1.18×10^{-01}	4.41×10^{-07}	2.37	3.90×10^{-08}
G1-1780	CHnz	2.10×10^{-12}	1.02×10^{-02}	2.95×10^{-08}	2.04×10^{-01}	8.71×10^{-09}
G1-1790	CHnz	5.20×10^{-12}	5.03×10^{-02}	4.73×10^{-07}	1.01	7.80×10^{-08}
G1-1821	CHnz	4.30×10^{-11}	1.04×10^{-01}	1.44×10^{-06}	2.08	1.02×10^{-07}
G1-1841	CHnz	1.60×10^{-10}	4.38×10^{-01}	4.04×10^{-06}	8.75	6.76×10^{-07}
G4-1405	CHnz	2.99×10^{-12}	2.75×10^{-02}	3.47×10^{-06}	5.51×10^{-01}	4.29×10^{-07}
G4-1547	CHnz	1.40×10^{-11}	1.23×10^{-01}	7.49×10^{-07}	2.46	9.29×10^{-08}
G4-1548	CHnz	1.40×10^{-12}	1.16×10^{-02}	1.56×10^{-05}	2.32×10^{-01}	9.06×10^{-07}
G4-1686	CHnz	4.24×10^{-12}	2.56×10^{-02}	1.75×10^{-05}	5.13×10^{-01}	1.52×10^{-06}
G4-1728	CHnz	4.53×10^{-12}	2.87×10^{-02}	5.40×10^{-05}	5.74×10^{-01}	2.66×10^{-06}
G4-1736	CHnz	2.60×10^{-12}	1.63×10^{-02}	7.74×10^{-08}	3.25×10^{-01}	6.42×10^{-09}
G4-1737	CHnz	2.63×10^{-12}	2.71×10^{-02}	4.87×10^{-05}	5.42×10^{-01}	1.52×10^{-06}
G4-1769	CHnz	2.30×10^{-12}	5.98×10^{-02}	9.01×10^{-05}	1.20	2.11×10^{-06}
G4-1778	CHnz	1.16×10^{-11}	8.43×10^{-02}	3.47×10^{-04}	1.69	7.04×10^{-06}
G4-1787	CHnz	2.85×10^{-11}	5.65×10^{-02}	5.60×10^{-04}	1.13	2.75×10^{-05}
$\log_{10}$ mean[1]		-11.1	-1.3	-5.4	0.009	-6.5
std. dev.[2]		0.5	0.4	1.3	0.4	1.0

[1] $\log_{10}$ mean x = $\Sigma \log_{10}(x_i)/n$

[2] std. dev. = $\Sigma \{\log_{10} x_i - [\log_{10} \text{mean } x]\}^2 /(n-1)$

Table 4. (continued)
Comparison of Measured and Calculated Saturated Hydraulic Conductivities

Sample	Unit	K_{expt}(m/s)	K_{expt}/K_{calc} Ratio Using Eq. 7a	Eq. 7b	Eq. 8	Eq. 9
G1-1917	PPw	1.60×10^{-09}	$1.63 \times 10^{+01}$	6.60×10^{-05}	$3.27 \times 10^{+02}$	1.09×10^{-05}
GU3-1628	PPw	6.92×10^{-09}	9.18×10^{-01}	4.76×10^{-05}	$1.84 \times 10^{+01}$	1.36×10^{-05}
GU3-1680	PPw	1.28×10^{-09}	3.05×10^{-01}	7.58×10^{-06}	6.09	3.04×10^{-06}
GU3-1730	PPw	1.18×10^{-09}	2.41	4.24×10^{-05}	$4.81 \times 10^{+01}$	9.37×10^{-06}
G4-1899	PPw	3.88×10^{-09}	$1.55 \times 10^{+01}$	1.36×10^{-02}	$3.10 \times 10^{+02}$	1.43×10^{-03}
$\log_{10}$ mean[1]		-8.6	0.4	-4.0	1.7	-4.6
std. dev.[2]		0.3	0.8	1.2	0.8	1.0
G4-2006	CFUn	2.03×10^{-11}	4.79×10^{-02}	2.65×10^{-04}	9.58×10^{-01}	1.04×10^{-05}
G4-2101	CFUn	4.36×10^{-10}	2.28	3.03×10^{-02}	$4.55 \times 10^{+01}$	6.06×10^{-04}
$\log_{10}$ mean		-10.0	-0.5	-2.5	0.8	-4.0
std. dev.		0.9	1.2	1.5	1.2	1.2
G4-2401	BFw	2.31×10^{-09}	6.17×10^{-01}	1.02×10^{-02}	$1.23 \times 10^{+01}$	1.05×10^{-03}
G4-2407	BFw	6.26×10^{-09}	1.05	2.83×10^{-02}	$2.11 \times 10^{+01}$	3.48×10^{-03}
$\log_{10}$ mean		-8.4	-0.09	-1.8	1.2	-2.7
std. dev.		0.3	0.2	0.3	0.2	0.4

[1] $\log_{10}$ mean x = $\Sigma \log_{10}(x_i)/n$

[2] std. dev. = $\Sigma (\log_{10} x_i - [\log_{10} \text{mean } x])^2 /(n-1)$

because of errors in the pore-size distribution as determined from the mercury-intrusion testing or because of the inadequacy of the model used in the calculations. It would appear, however, that if suitable mean tortuosity or lithology factors could be calculated, the methods used would generally provide predictions of saturated conductivities to within, approximately, an order of magnitude. If predictions of saturated hydraulic conductivities within an order of magnitude are all that is required, these results indicate that mercury-intrusion data would be adequate. As usual, the adequacy of the method depends upon the accuracy that is required.

No direct comparison of predicted values can be made because little or no information is available about tortuosity factors for the different tuffs. Nevertheless, the values of the standard deviations indicate that Eqs. 7a and 8 do a better job of predicting conductivity values than the other two methods. The standard deviations predicted by the two methods are equivalent for each unit. They are equivalent because the method used to calculate the surface area, from the intrusion data in Eq. 8, is equivalent to the method used to calculate the average pore radius in Eq. 7a. However, other methods exist for determining the specific surface area and may yield significantly better or worse results.

It is interesting to note that the simplest formulation (Eq. 7a) yields results at least as good as those of the other formulations. A comparison of results using Eqs. 7a and 7b indicates that the results are very sensitive to the manner in which the value of the average pore radius is calculated. This might be expected because there are indications that the pore-size distributions of the tuff samples are often very heterogeneous. Different methods of calculating the value of the average pore radii could therefore yield significantly different values and different standard deviations in their predictions. It should be remembered that the accuracy of the predictions by the tested formulations depends on either a "tortuosity" factor or some lithology factor. The variation in these factors between the different units emphasizes the variation in the structure of the porous tuff matrix. It is probable that the tortuosity factor is an acceptable constant if the features of the pore structures within a particular type of rock are similar.

It can also be noted that, although the samples were divided into nine hydrogeologic units for comparison, fewer groupings could have been made if desired. For example, Units TCw, TSw1, and TSw2 could have been grouped all together because they consist of densely welded tuffs, and Units PTn and CHnv, which are nonwelded vitric tuff units, similarly could have been grouped together. They have similar pore-size distributions and hydrologic characteristics, and grouping them would not have significantly changed the standard deviation of the conductivity ratios listed for the individual groupings. Unit CHnz, although nonwelded, has hydrologic properties and pore sizes similar to the densely welded units and also could have been grouped with those tuffs. Fewer groupings might be more practical in order to limit the number of structural factors for the tuffs that need to be determined.

These results show that the results of mercury-intrusion tests can be used to make estimates of the saturated conductivity that are usually within an order of magnitude of the experimental value. Often, the calculated values are within a factor of three of the experimental value. Perhaps it should not be surprising that the comparison between the calculated and experimentally derived saturated-conductivity values is better than the comparison between the calculated and experimentally derived saturation curves. For the calculation of the saturation curve, such things as contact angle (and whether it varies with saturation and position), distribution of the two fluids, and pore interactions at various levels of saturation have to be accounted for. The calculation of the saturated conductivity generally includes an empirically determined constant (a lithology factor or tortuosity factor) to yield better predictions. The theoretical or physical relationship of this factor to known characteristics of the physical structure of the material is sometimes nebulous, but it does aid in yielding better predictions.

The results also suggest that better correlations between the saturated hydraulic conductivity and the intrusion-determined pore-size distribution (and perhaps surface-area distribution) might be found. It would appear from these results, however, that, if pore-size distribution data are to be used to calculate accurate saturated-conductivity values, more intrusion testing and analyses to determine better empirical relationships should be done.

IV. CONCLUSIONS

To assess the feasibility of disposal of high-level waste at Yucca Mountain, it is necessary to determine major hydrologic properties of the site -- the saturated hydraulic conductivity, and saturation and relative conductivities as a function of pressure head -- for a large number of tuff matrix samples. It is generally recognized that it is always preferable to use experimentally determined values instead of calculated values if that option is available. However, defining these hydrologic properties can be very time-consuming and expensive for the tuffs under investigation. Mercury-intrusion testing can provide estimates of pore-size distributions that can be used for calculating the above-mentioned hydrologic properties. The method is attractive with regard to both cost and the time required for testing, but, as comparisons with more direct measurements and other physical considerations show, hydrologic values calculated from mercury intrusion may not be sufficiently accurate for many performance-assessment applications.

This report provides estimates of both saturation versus pressure-head values and saturated hydraulic conductivities using the mercury-intrusion test results and compares them to experimentally determined values. Although there is, in general, a favorable comparison between the calculated and experimental values for saturated hydraulic conductivity, there is poor correlation between the saturation curves determined from thermocouple-psychrometry data and the curves calculated from the mercury-intrusion-derived pore-size distributions. The saturation curves determined using the thermocouple psychrometer form a fairly coherent group; however, the saturation curves determined from the mercury porosimetry results are quite variable. The results suggest that the saturation curves determined from thermocouple psychrometry are more indicative of the true hydrologic characteristics of the tuff samples (although the psychrometer data is not considered valid at pressure heads above approximately -20 m).

The results suggest that mercury-intrusion data could be used to predict the experimental conductivity values within an order of magnitude (and perhaps better, if more data become available to determine the empirical constants in the formulations used to calculate the saturated conductivity).

The requirements for assessing the performance of the site will determine the accuracy that is required, but the use of mercury-intrusion data to calculate saturation curves is questionable, at best.

The saturation curves often compare reasonably well qualitatively; they only sometimes compare well quantitatively. Sometimes, however, they do not compare well either qualitatively or quantitatively. Even when the methods yield curves of similar shape, the mercury-intrusion-derived curve is often shifted along the pressure-head axis to larger pressure head values to such a degree that it may misrepresent the dominant pore sizes in the sample. There are some major problems in using pore-size distributions to determine the saturation curves, including difficulties in 1) determining the pore-size distribution, 2) interpreting the distribution with respect to pore shapes, lengths, and interactions, and 3) calculating the saturation curve for water from the derived pore-size distribution. The differences that are found to exist between the mercury-intrusion-derived saturation curves and the psychrometer curves are understandable when the complexity of the problem is examined. The results of the statistical comparison of the mercury-intrusion-derived curves and psychrometer curves indicate a general lack of correlation of the mercury-intrusion-derived curves with the psychrometer curves and the lack of consistency of the fitting parameters within a particular rock type. Even a quick visual inspection indicates that the saturation curves, calculated from mercury-intrusion-derived pore-size distributions, can not be relied upon to give predictions, within an order of magnitude, of the pressure head associated with a certain saturation. Although the accuracy needed depends upon the ultimate use of the data, it is doubtful that any analyses that require data on saturation as a function of pressure head could reliably depend on the intrusion-derived saturation curves.

Calculation of relative-conductivity curves using mercury-intrusion-derived pore-size distributions uses basic concepts similar to those for calculating the saturation curves, neglecting two-phase flow interactions. Many techniques, in fact, provide equations for calculating relative-conductivity values that only use data on saturation as a function of pressure head. Therefore, the comparison of relative-conductivity values calculated from the mercury-porosimetry data with experimentally measured relative-conductivity values is expected to be no better than the comparison

of the saturation curves calculated from the mercury-porosimetry data to experimental results obtained from thermocouple-psychrometer data. The comparison would probably be worse.

The results in this report indicate that, depending upon the accuracy and precision required by the NNWSI project for the hydrologic properties to meet its goals, it may be feasible to use mercury-intrusion data to calculate saturated hydraulic conductivity values for tuffs (assuming proper lithology or tortuosity factors are determined). The poor comparison of the mercury-intrusion-derived saturation curves with the psychrometry-derived curves suggests that the curves (both saturation and relative conductivity) determined from mercury-intrusion-derived pore-size distributions could not reliably be used in performance-assessment calculations. It is suggested that experimental data (e.g., psychrometer and pressure-plate data) be used to determine the saturation curves until other more accurate methods are established.

REFERENCES

Amyx, J. W., Bass, D. M., and R. L. Whiting, Petroleum Reservoir Engineering, McGraw-Hill Book Company, New York, NY, 1960.

Burdine, N. T., L. S. Gournay, and P. P. Reichertz, "Pore Size Distribution of Petroleum Rocks," Petroleum Transactions, AIME, Vol. 189, T.P. 2893, 195-204, 1950.

Burdine, N. T., "Relative Permeability Calculations from Pore Size Distribution Data," Petroleum Transactions, AIME, Vol. 198, T.P. 3519, 71-78, 1953.

Connolly, J., "Petrologic Properties of Nonlithophysal Topopah Spring Member Welded Tuff from Rock #10, Busted Butte, Nevada Test Site," Summary Report from Jim Connolly, Institute of Meteoritics, University of New Mexico, Albuquerque, NM to F. B. Nimick, Sandia National Laboratories, Albuquerque, NM, July 8, 1985.

Connolly, J., written communication, 1986.

Daniels, D. E., Hamilton, J. M., and R. E. Olson, "Suitability of Thermocouple Psychrometers for Studying Moisture Movement in Unsaturated Soils," Permeability and Groundwater Contaminant Transport, ASTM STP 746, T. F. Zimmie and C. O. Riggs, Eds., Amer. Soc. for Testing and Materials, 84-100, 1981.

Edlefsen, N. E., and A. B. C. Anderson, "Thermodynamics of Soil Moisture," Hilgardia, Vol. 15, No. 2, 31-298, 1943.

García-Bengochea, I., Lovell, C. W., and L. E. Wood, "The Use of Pore Size Distribution Parameters to Predict Permeability," Proceedings of the Seventh European Conference on Soil Mechanics and Foundation Engineering, Brighton, England, Vol. 2, Paper C8, 49-56, 1979.

Hammermeister, D. P., U. S. Geological Survey, personal communication, July 1985.

Hillel, D., Soil and Water, Academic Press, New York, NY., 1971.

Johnson, E. F., D. P. Bossler, and V. O. Naumann, "Calculation of Relative Permeability from Displacement Experiments," Petroleum Trans., Vol. 216, T.N. 2027, 370-372, 1959.

Micromeritics Materials Analysis Lab, Micromeritics Instrument Corp., Norcross, GA, personal communication, October 29, 1985.

Nimick, F. B., B. M. Schwartz, and R. H. Price, "Bulk, Thermal and Mechanical Properties of the Topopah Spring Member of the Paintbrush Tuff, Yucca Mountain, Nevada," SAND85-0762, Sandia National Laboratories, Albuquerque, NM, In preparation.

Ortiz, T. S., R. L. Williams, F. B. Nimick, B. C. Whittet, and D. L. South, "A Three-Dimensional Model of Reference Thermal/Mechanical and Hydrological Stratigraphy at Yucca Mountain, Southern Nevada," SAND84-1076, Sandia National Laboratories, Albuquerque, NM, 1985.

Peters, R. R., E. A. Klavetter, I. J. Hall, S. C. Blair, P. R. Heller, and G. W. Gee, "Fracture and Matrix Hydrologic Characteristics of Tuffaceous Materials from Yucca Mountain, Nye County, Nevada,", SAND84-1471, Sandia National Laboratories, Albuquerque, NM, 1984.

Peters, R. R., E. A. Klavetter, and P. R. Heller, "Water Retention Characteristics and Saturated Hydraulic Conductivities for Tuffaceous Material from Yucca Mountain - FY85 Results," Keystone Doc. 6310-85-10, Sandia National Laboratories, Albuquerque, NM, 1985.

Purcell, W. R., "Capillary Pressures-Their Measurement Using Mercury and the Calculation of Permeability Therefrom," Petroleum Transactions, AIME, T.P. 2544, 39-48, 1949.

van Genuchten, R., "Calculating the Unsaturated Hydraulic Conductivity with a New Closed Form Analytical Model," Water Resources Bulletin, Princeton University Press, Princeton University, Princeton, NJ, 1978.

Wardlaw, N. C., and R. P. Taylor, "Mercury Capillary Pressure Curves and the Interpretation of Pore Structure and Capillary Behavior in Reservoir Rocks," Bulletin of Canadian Petroleum Geology, Vol. 24, No. 2, 225-262, 1976.

Washburn, E. W., "Note on a Method of Determining the Distribution of Pore Sizes in a Porous Material," National Academy of Science Proceedings, Vol. 7, 115, 1921.

Weeks, E. P., and W. E. Wilson, "Preliminary Evaluation of Hydrologic Properties of Cores of Unsaturated Tuff, Test Well USW H-1, Yucca Mountain, Nevada," U. S. Geological Survey, Water-Resources Investigations Report 84-4193, 1984.

Wyllie, M. R. J., and G. H. F. Gardner, "The Generalized Kozeny-Carman Equation," World Oil, Vol. 146, 210-228, 1958.

APPENDIX A

Results of Mercury-Intrusion Tests

The mercury-intrusion tests were conducted by Micromeritics Instrument Corporation, Norcross, Georgia. A complete list of the samples tested by the mercury-intrusion method and by the thermocouple-psychrometer method is included in this appendix shown in Table A.1. The microfiche attached to this report contains the mercury-intrusion test results provided by Micromeritics Instrument Corporation.

TABLE A.1

Location of Samples Tested

Drill Hole	Depth (feet)	Unit	Tests Performed[1]
USW GU-3	82	TCw	T M
USW GU-3	121	TCw	T M
USW GU-3	155	TCw	T M
USW GU-3	257	TCw	T M
USW GU-3	316	TCw	T M
USW G-4	43	TCw	T M
USW GU-3	374	PTn	T M
USW GU-3	378	PTn	T M
USW GU-3	397	PTn	T M
USW G-4	124	PTn	T M
USW G-4	136	PTn	T M
USW G-4	172	PTn	T M
USW G-4	208	PTn	T M2

[1] The code used to indicate the types of tests performed on each sample follows.

T - Thermocouple-Psychrometer test with 2 to 3 subsamples tested. The number of different symbols used in the upper plots in the figures in Appendix B indicates the number of subsamples tested.

M - Mercury-Intrusion test; 1 subsample only

M2 - Mercury-Intrusion test; 2 subsamples

TABLE A.1 (continued)
Location of Samples Tested

Drill Hole	Depth (feet)	Unit	Tests Performed[1]
USW G-1	389	TSw1	T M
USW G-1	616	TSw1	T M
USW G-1	752	TSw1	T M
USW GU-3	585	TSw1	T M
USW GU-3	687	TSw1	T M
USW G-4	247	TSw1	T
USW G-1	1102	TSw2	T M
USW G-1	1111	TSw2	M
USW G-1	1198	TSw2	T M
USW G-1	1211	TSw2	M

[1] The code used to indicate the types of tests performed on each sample follows.

T - Thermocouple-Psychrometer test with 2 to 3 subsamples tested. The number of different symbols used in the upper plots in the figures in Appendix B indicates the number of subsamples tested.

M - Mercury-Intrusion test; 1 subsample only

M2 - Mercury-Intrusion test; 2 subsamples

TABLE A.1 (continued)
Location of Samples Tested

Drill Hole	Depth (feet)	Unit	Tests Performed[1]
USW GU-3	884	TSw2	T M
USW GU-3	1132	TSw2	T M2
USW G-4	864L (altered)	TSw2	T M2
USW G-4	864D (welded)	TSw2	T M2
USW G-4	1158	TSw2	T M
USW G-4	1159	TSw2	M
USW G-4	1215	TSw2	T
USW G-4	1256	TSw2	T M
USW G-4	1278	TSw2	T
B. B. #10	N/A	TSw2	T M
USW G-1	1306	TSw3	T M
USW GU-3	1197	TSw3	T M
USW GU-3	1246	TSw3	T M
USW G-4	1299	TSw3	T M2
USW G-4	1324	TSw3	T

[1] The code used to indicate the types of tests performed on each sample follows.

T - Thermocouple-Psychrometer test with 2 to 3 subsamples tested. The number of different symbols used in the upper plots in the figures in Appendix B indicates the number of subsamples tested.

M - Mercury-Intrusion test; 1 subsample only

M2 - Mercury-Intrusion test; 2 subsamples

TABLE A.1 (continued)
Location of Samples Tested

Drill Hole	Depth (feet)	Unit	Tests Performed[1]
USW G-1	1359	CHnv	T M
USW G-1	1362	CHnv	M
USW G-1	1387	CHnv	T M
USW G-1	1392	CHnv	M
USW GU-3	1311	CHnv	T M
USW GU-3	1331	CHnv	T M
USW GU-3	1440	CHnv	T M
USW GU-3	1499	CHnv	T M
USW GU-3	1555	CHnv	T M2
USW G-4	1359	CHnv	T

[1] The code used to indicate the types of tests performed on each sample follows.

T - Thermocouple-Psychrometer test with 2 to 3 subsamples tested. The number of different symbols used in the upper plots in the figures in Appendix B indicates the number of subsamples tested.

M - Mercury-Intrusion test; 1 subsample only

M2 - Mercury-Intrusion test; 2 subsamples

TABLE A.1 (continued)
Location of Samples Tested

Drill Hole	Depth (feet)	Unit	Tests Performed[1]
USW G-1	1500	CHnz	T M
USW G-1	1637	CHnz	T M
USW G-1	1753	CHnz	T M
USW G-1	1780	CHnz	T M
USW G-1	1790	CHnz	T M
USW G-1	1821	CHnz	T M
USW G-1	1841	CHnz	T M
USW G-4	1405	CHnz	T M
USW G-4	1547	CHnz	M
USW G-4	1548	CHnz	T M
USW G-4	1551	CHnz	T
USW G-4	1686	CHnz	T M
USW G-4	1728	CHnz	T M
USW G-4	1736	CHnz	M
USW G-4	1737	CHnz	T M

[1] The code used to indicate the types of tests performed on each sample follows.

T - Thermocouple-Psychrometer test with 2 to 3 subsamples tested. The number of different symbols used in the upper plots in the figures in Appendix B indicates the number of subsamples tested.

M - Mercury-Intrusion test; 1 subsample only

M2 - Mercury-Intrusion test; 2 subsamples

TABLE A.1 (continued)
Location of Samples Tested

Drill Hole	Depth (feet)	Unit	Tests Performed[1]
USW G-4	1769	CHnz	T M
USW G-4	1778	CHnz	T M
USW G-4	1787	CHnz	T M
USW G-1	1917	PPw	T M
USW GU-3	1628	PPw	T M
USW GU-3	1680	PPw	T M
USW GU-3	1730	PPw	T M
USW G-4	1899	PPw	T M
USW G-4	2006	CFUn	T M
USW G-4	2101	CFUn	T M
USW G-4	2401	BFw	T M
USW G-4	2407	BFw	T M

[1] The code used to indicate the types of tests performed on each sample follows.

T - Thermocouple-Psychrometer test with 2 to 3 subsamples tested. The number of different symbols used in the upper plots in the figures in Appendix B indicates the number of subsamples tested.

M - Mercury-Intrusion test; 1 subsample only

M2 - Mercury-Intrusion test; 2 subsamples

APPENDIX B

Comparison of Results of Mercury-Intrusion and Thermocouple-Psychrometer Test Results

The mercury-intrusion and the thermocouple-psychrometer test results are plotted in this section. Information regarding sample locations and tests performed may be found in Table A.1. The upper curve for each sample shows the thermocouple-psychrometer data and the curve fit of the data. The curve fit used is that suggested by van Genuchten (1978). The parameters α, β, and S_r are parameters in that curve fit. The lower curve shows the thermocouple-psychrometer curve-fit and the mercury-intrusion data converted in the manner suggested in Section III.A, entitled "Estimation of the Water-Saturation Curve." Note that the bottom figures have a larger pressure-head range than the top figures. The vertically-directed arrows on the figures at a pressure head of -20 m indicate the approximate upper limit of the accuracy of the thermocouple psychrometer.

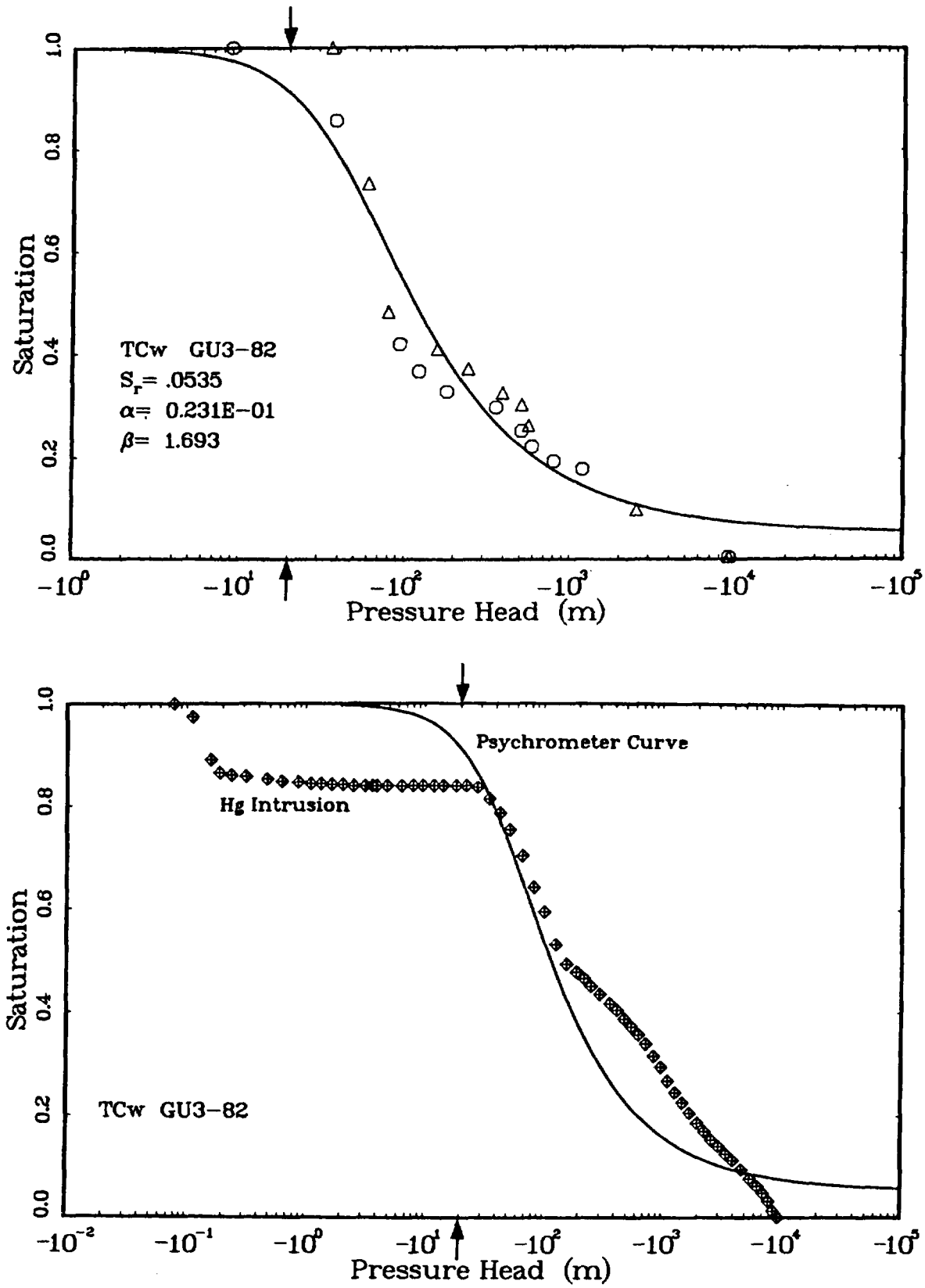

Figure B.1 Saturation as a Function of Pressure Head for Sample GU3-82

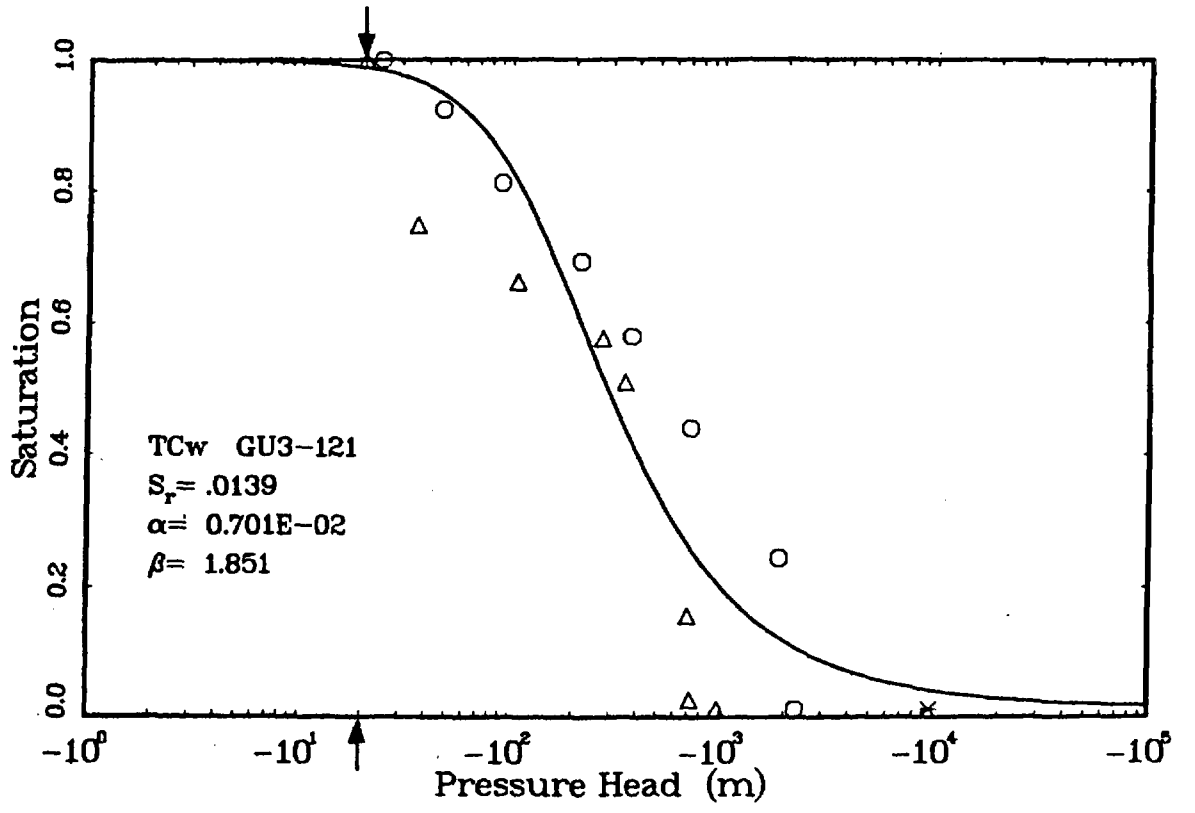

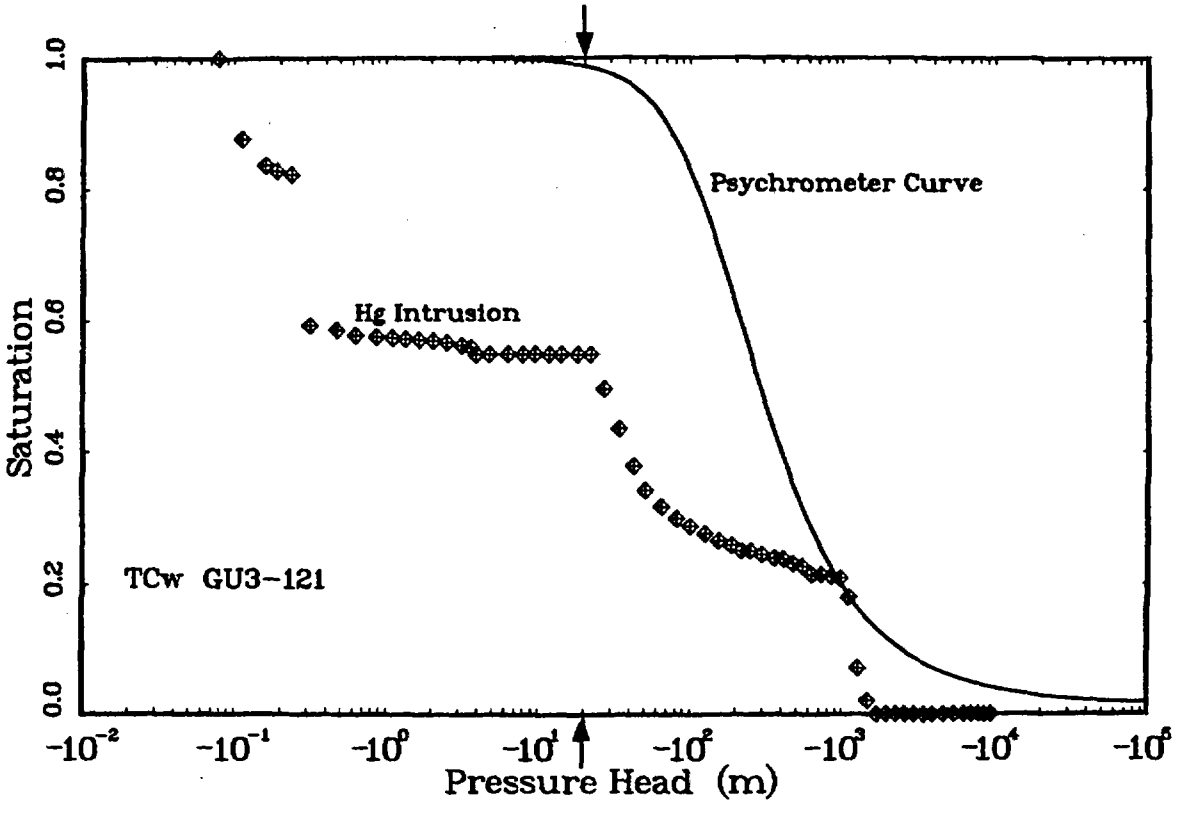

Figure B.2 Saturation as a Function of Pressure Head for Sample GU3-121

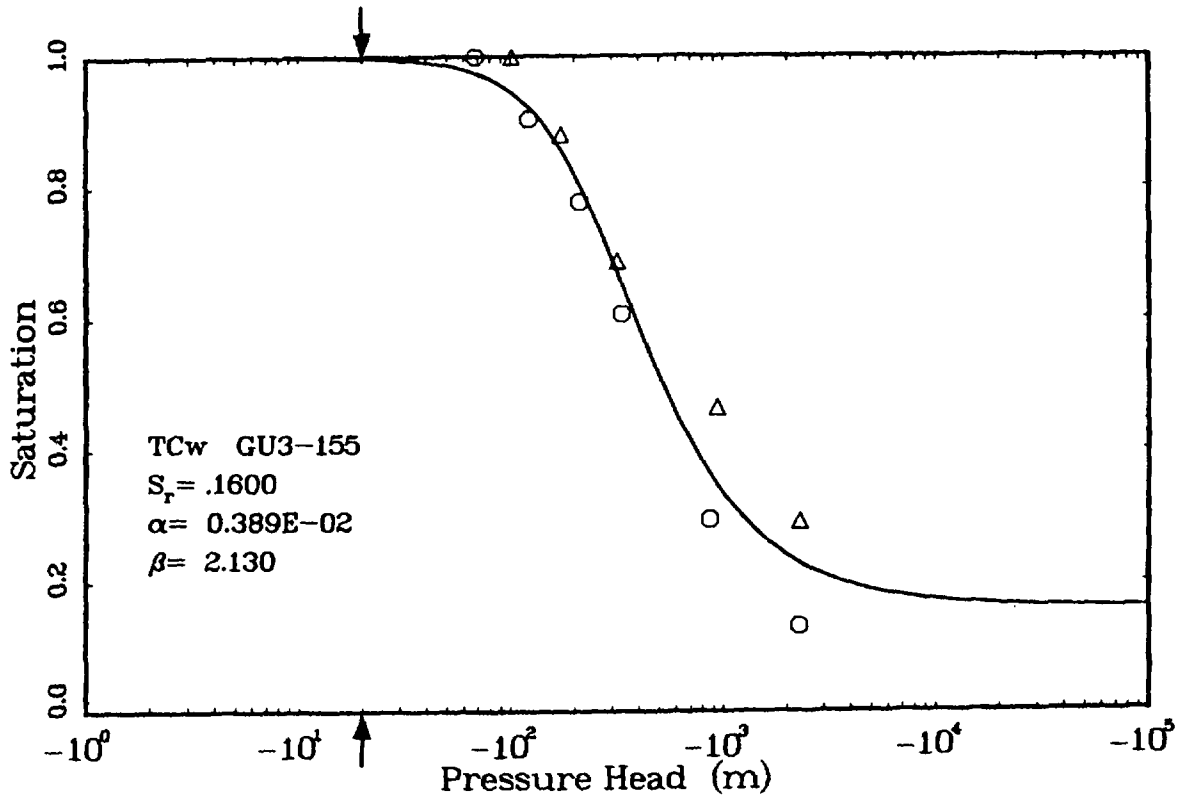

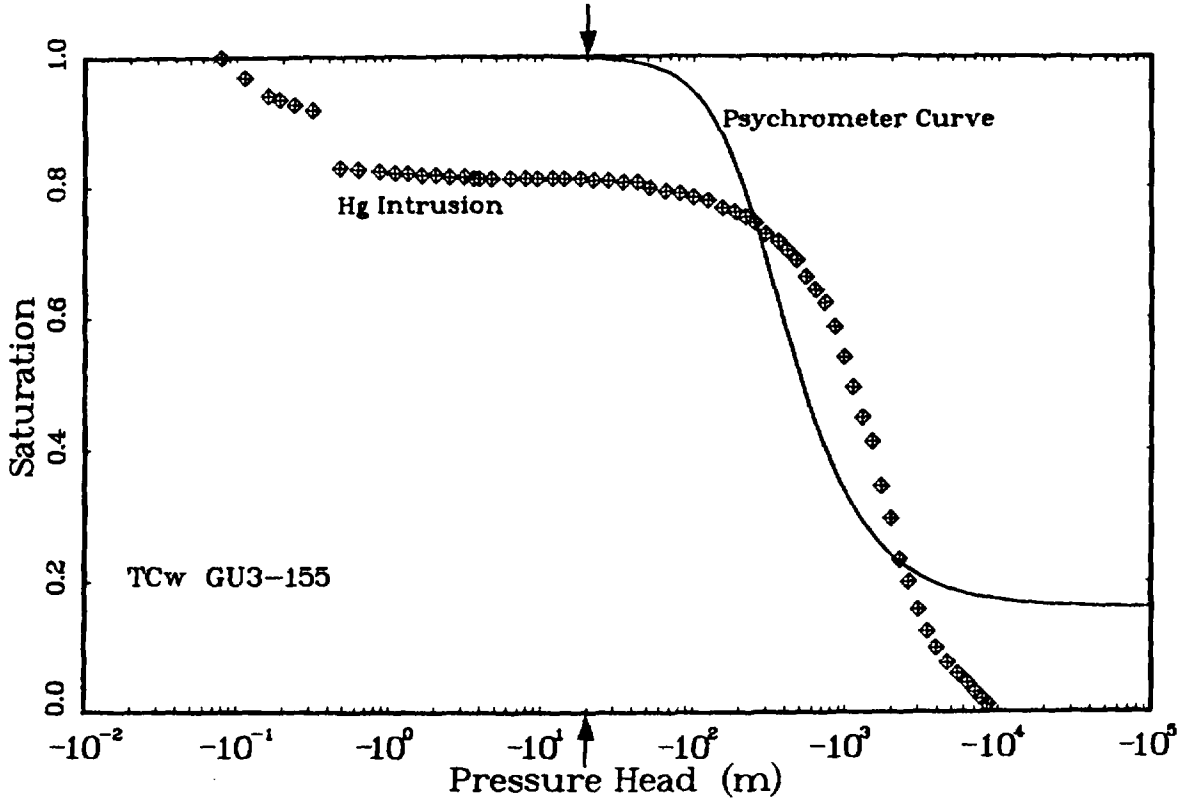

Figure B.3 Saturation as a Function of Pressure Head for Sample GU3-155

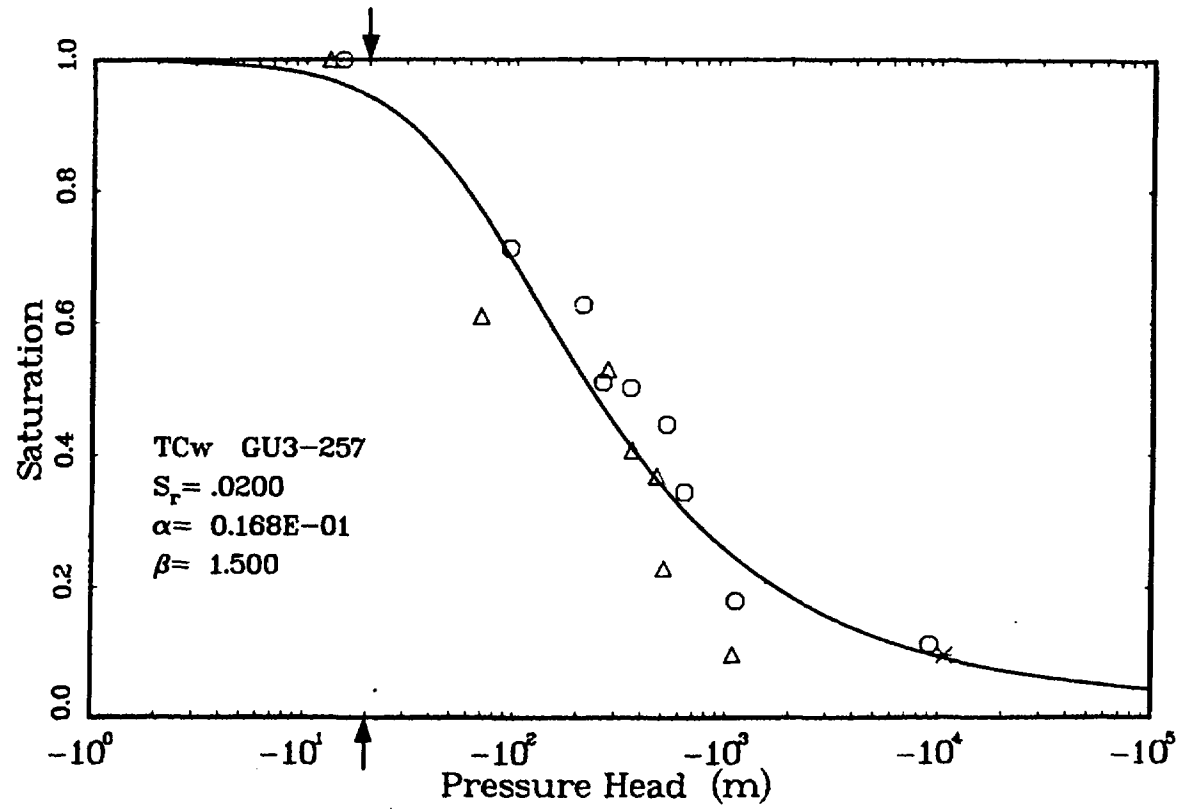

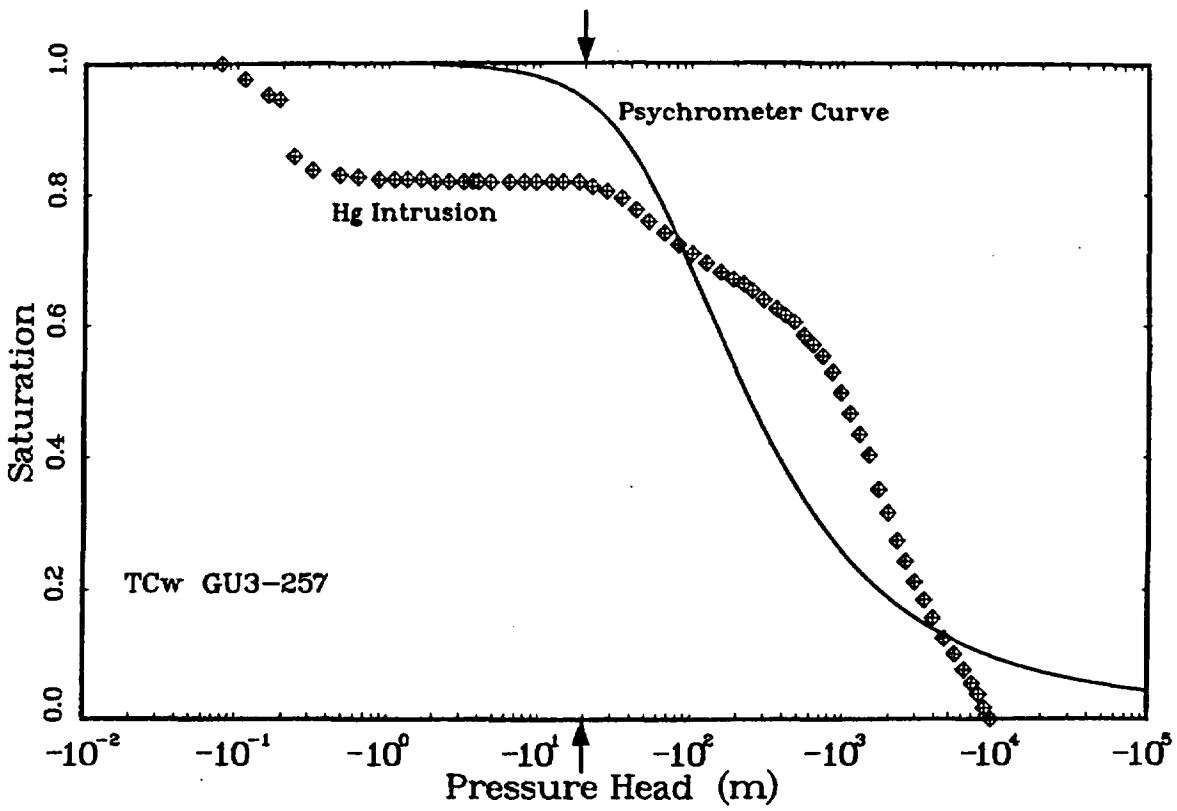

Figure B.4 Saturation as a Function of Pressure Head for Sample GU3-257

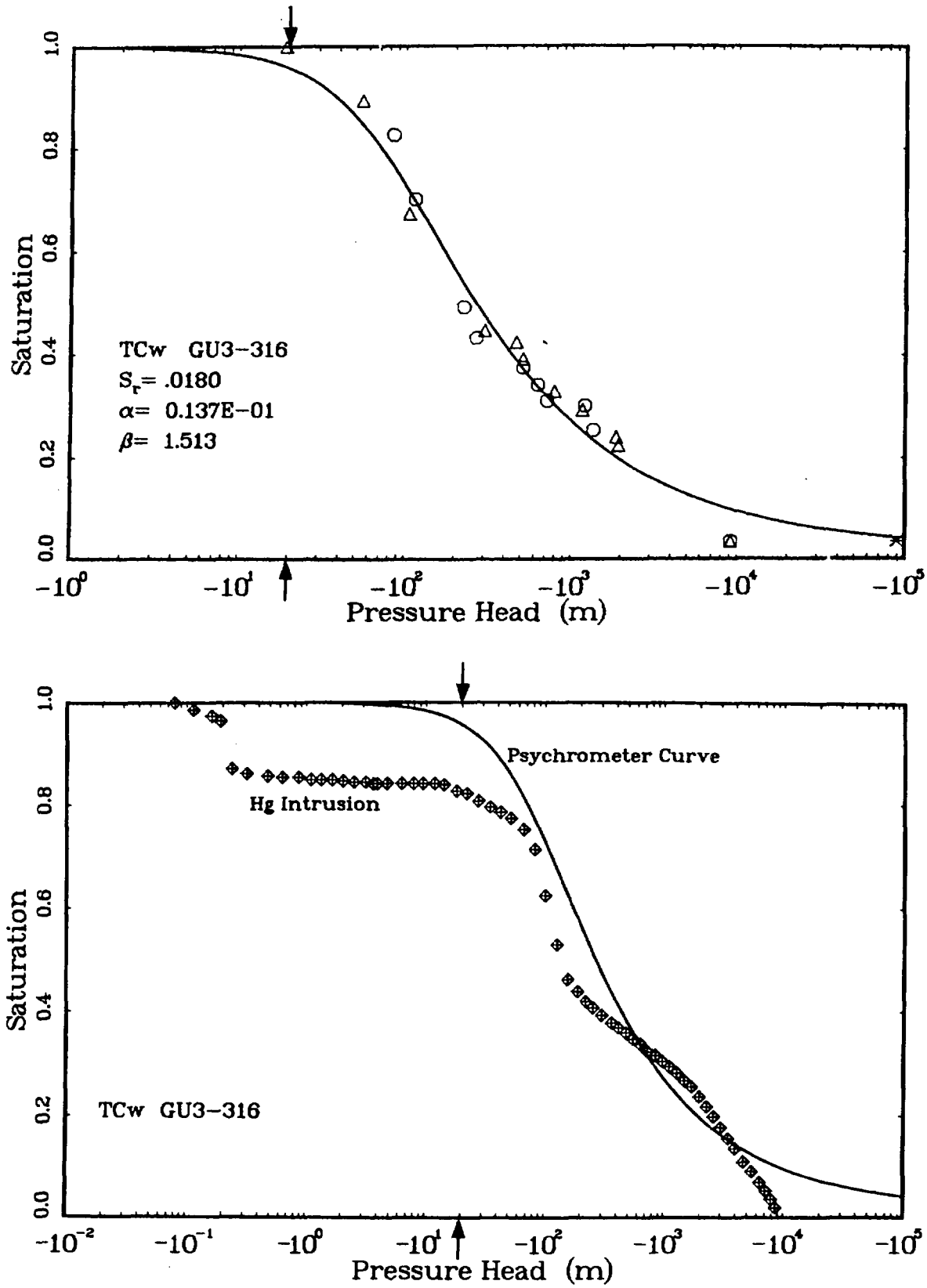

Figure B.5 Saturation as a Function of Pressure Head for Sample GU3-316

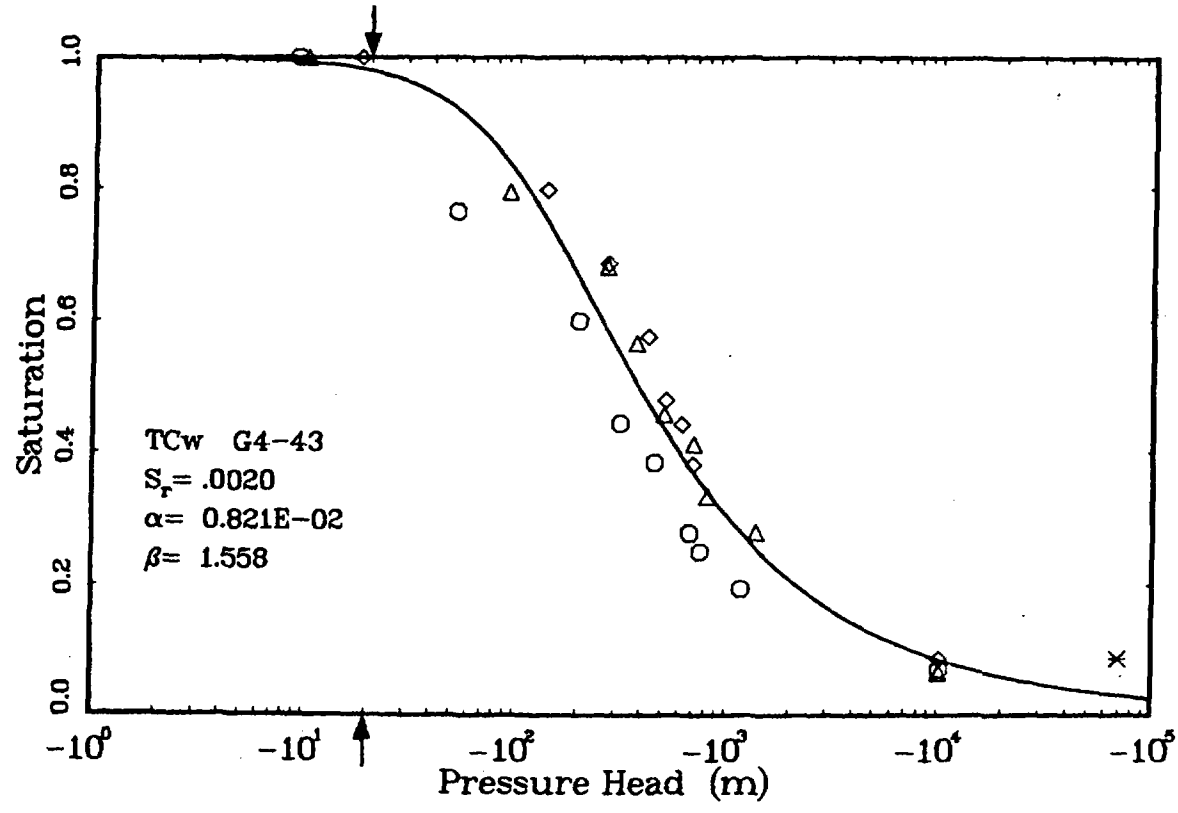

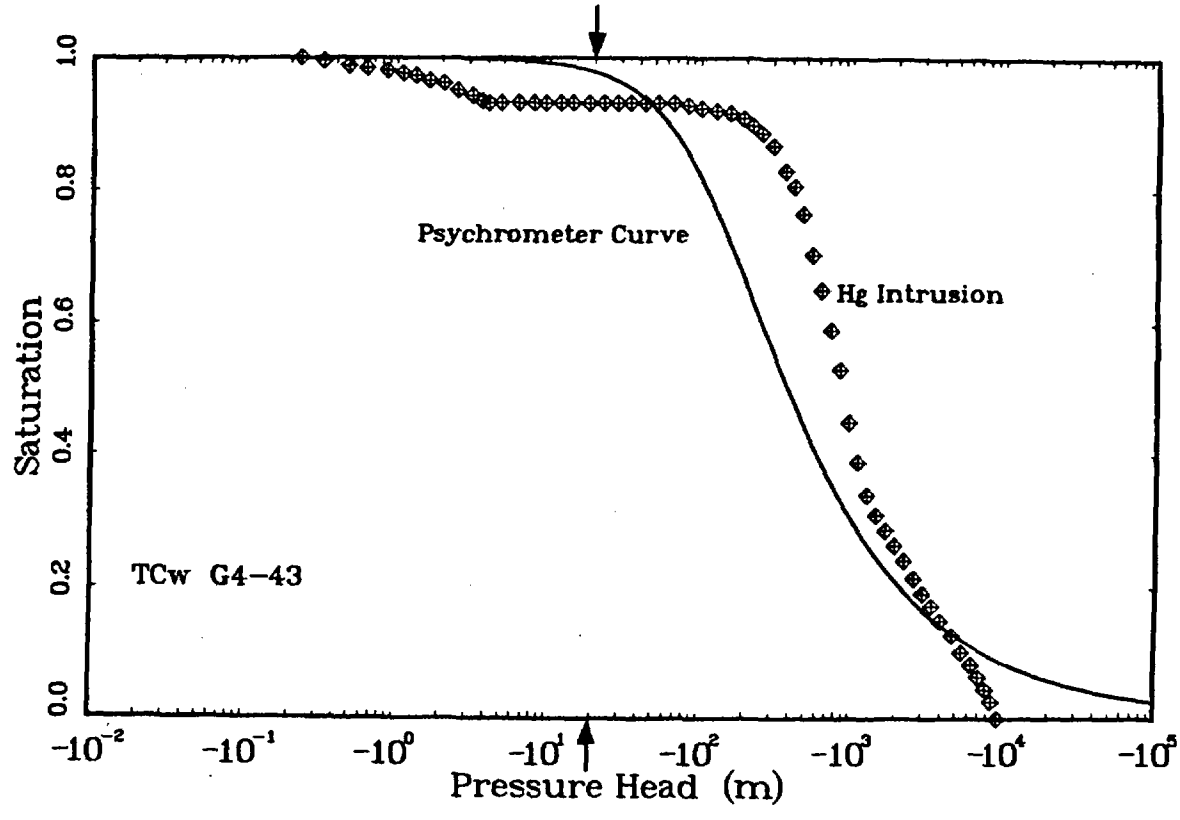

Figure B.6 Saturation as a Function of Pressure Head for Sample G4-43

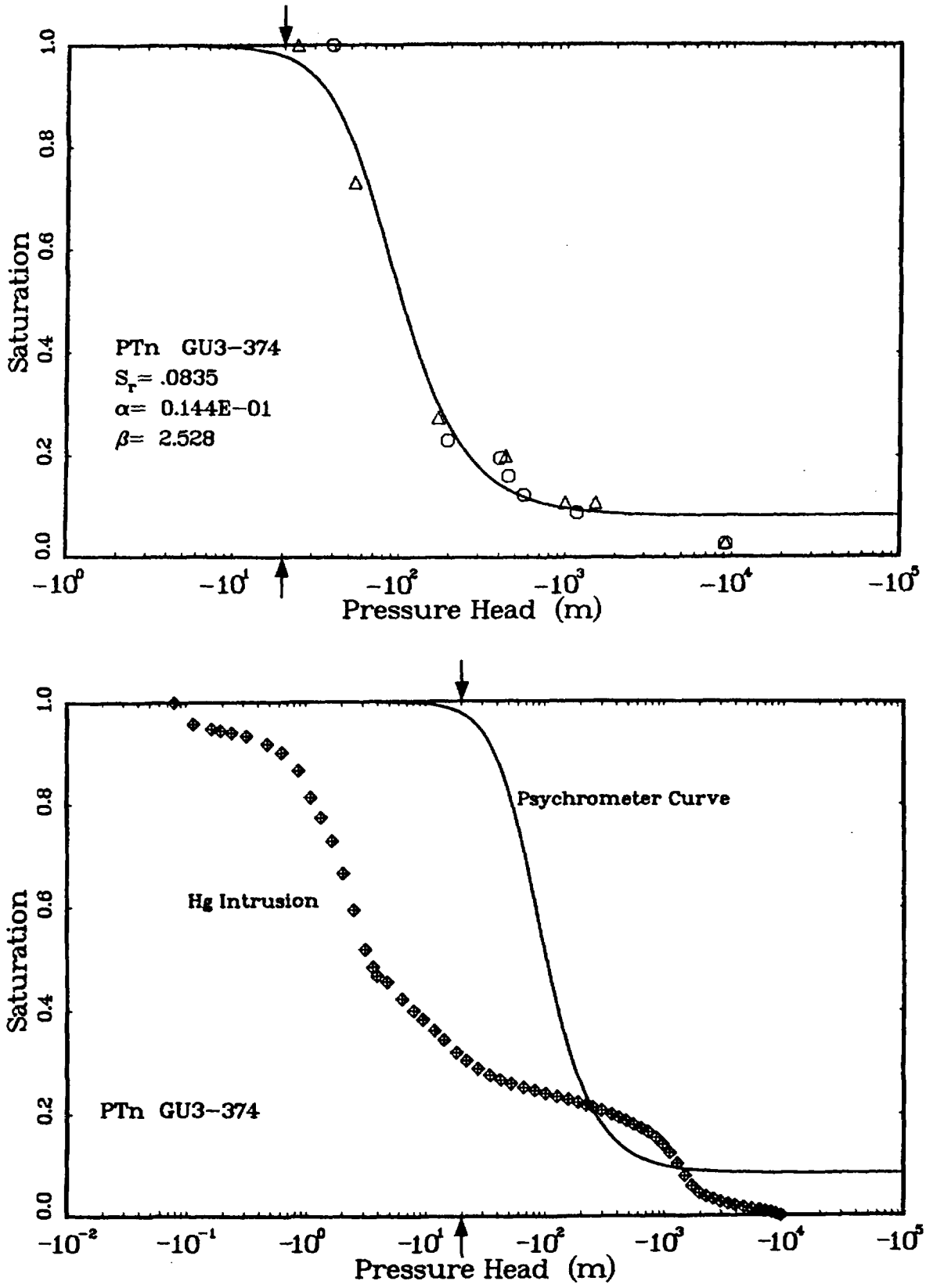

Figure B.7 Saturation as a Function of Pressure Head for Sample GU3-374

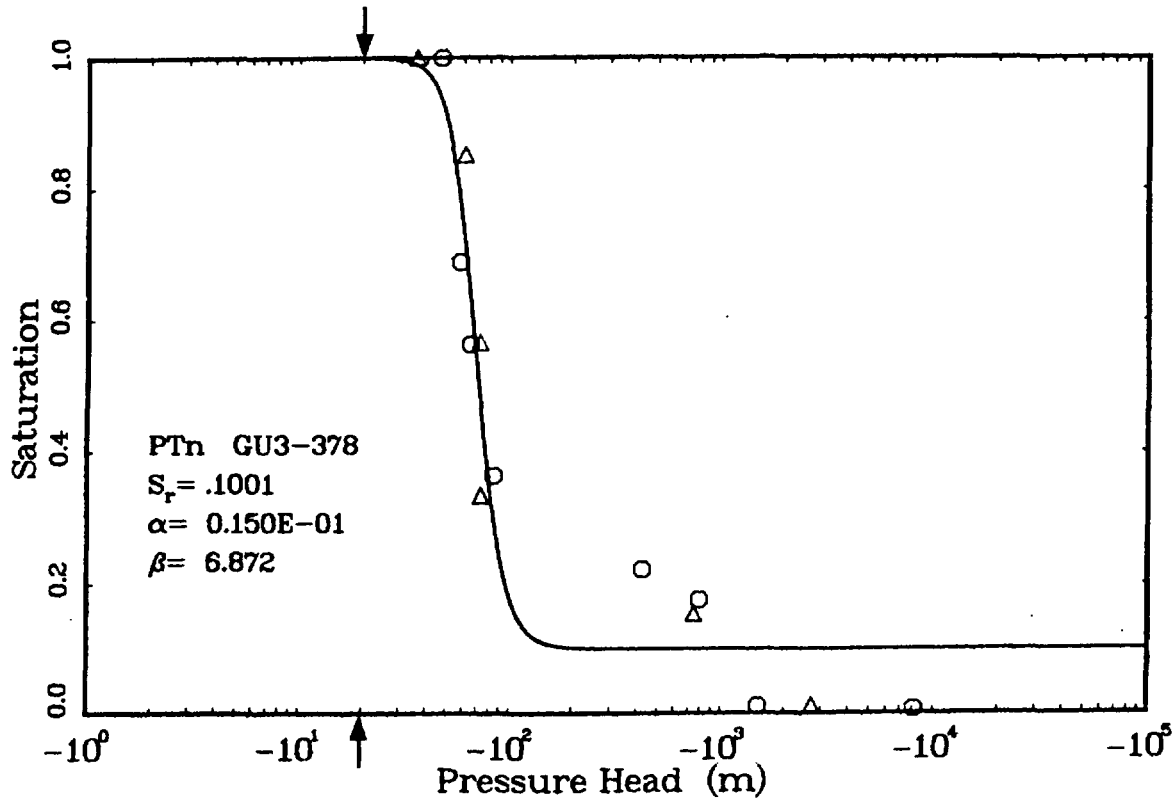

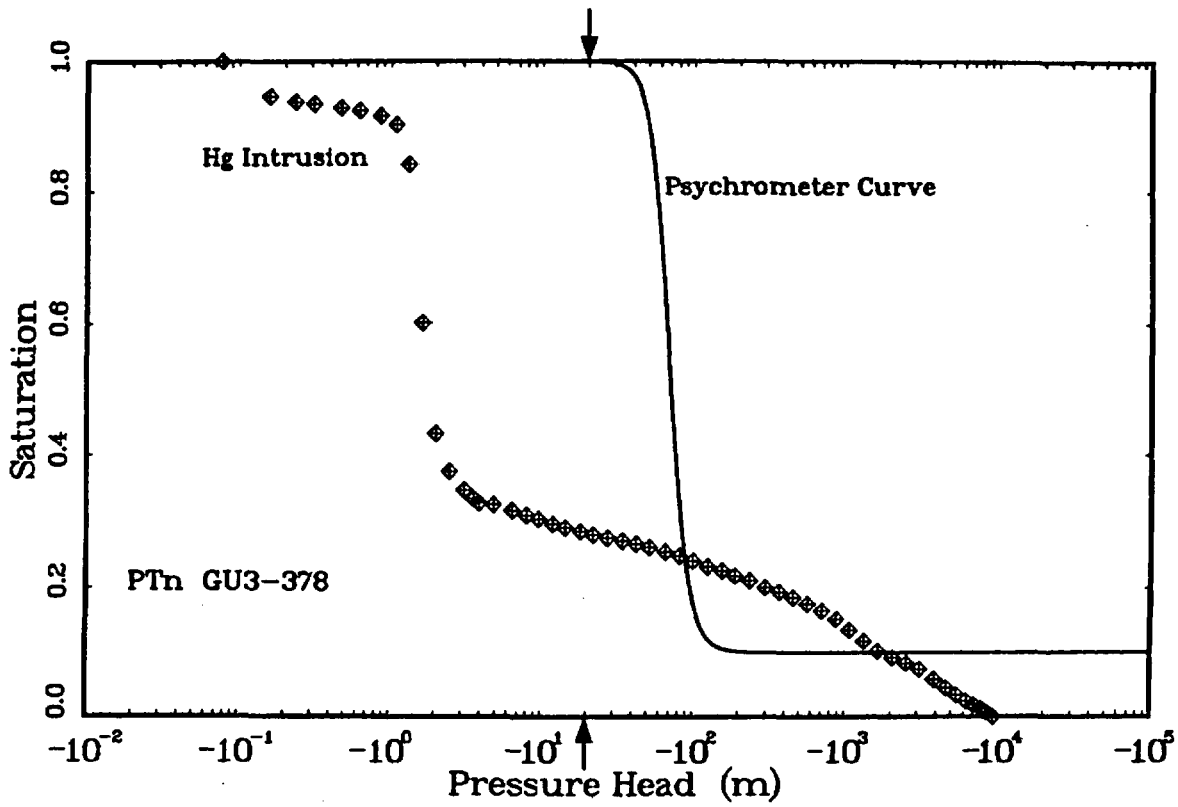

Figure B.8 Saturation as a Function of Pressure Head for Sample GU3-378

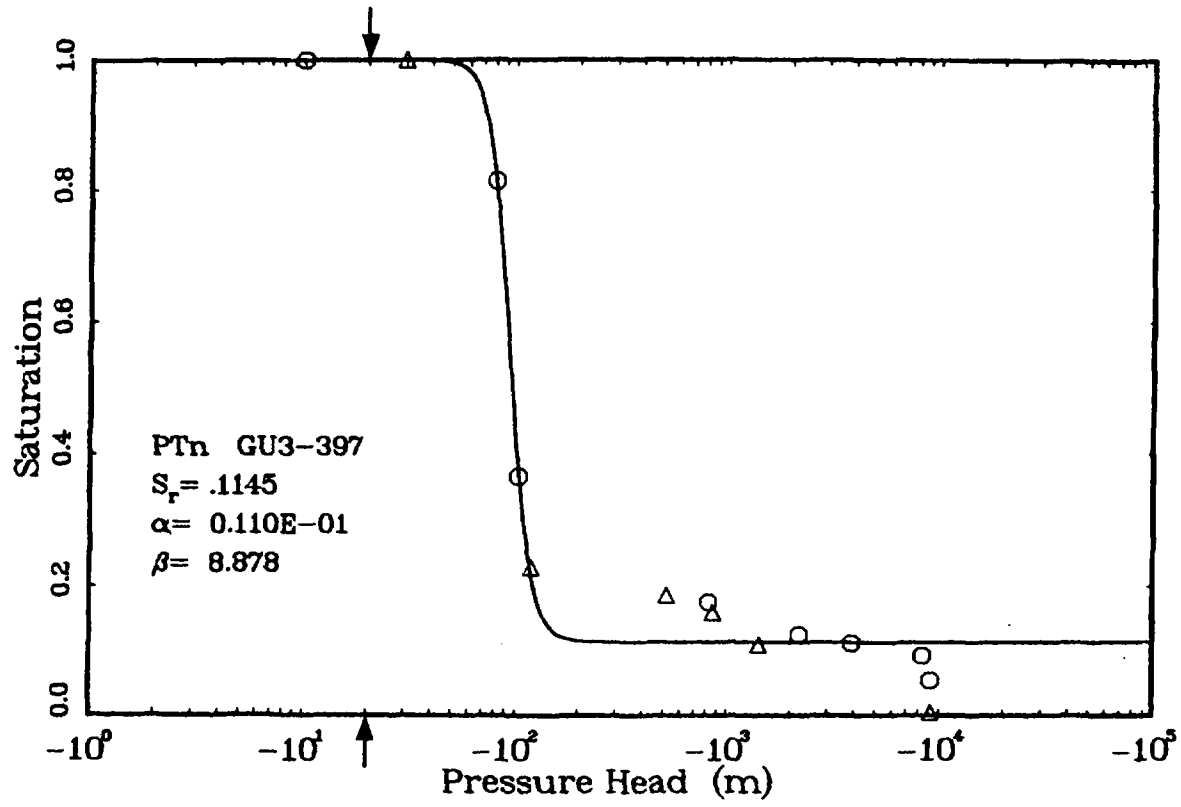

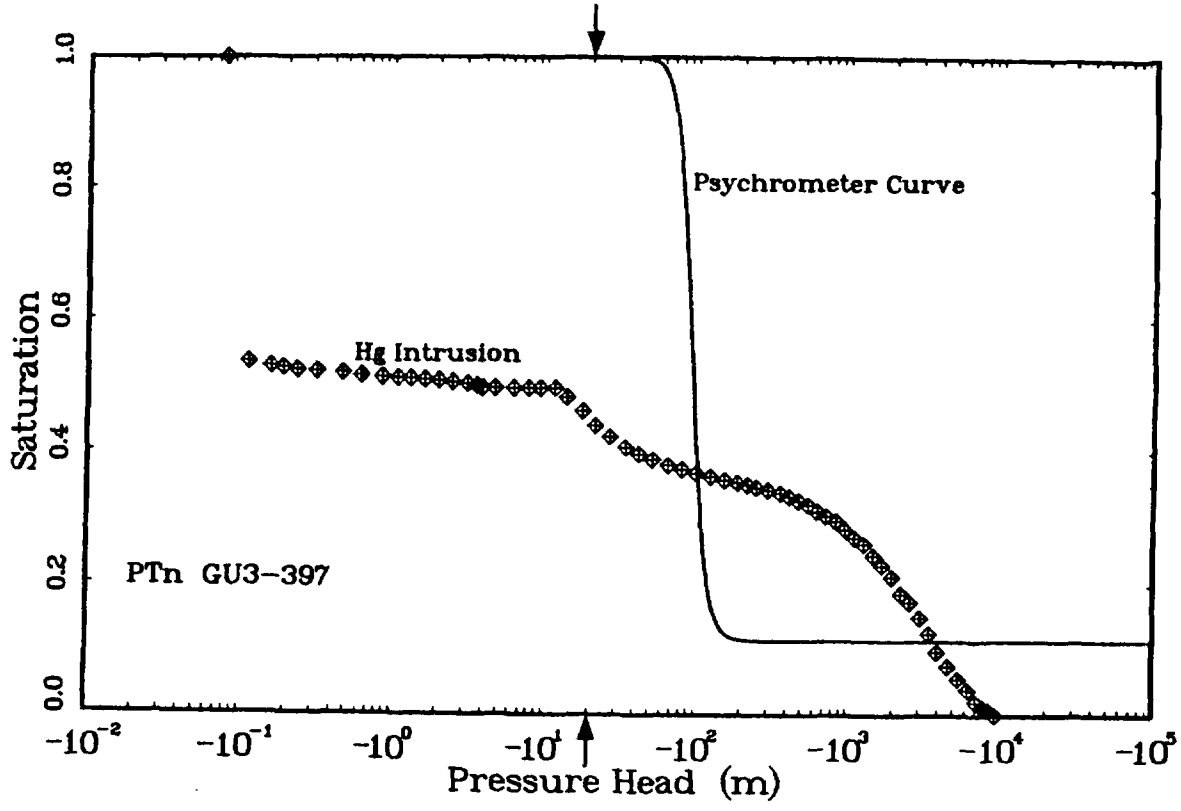

Figure B.9 Saturation as a Function of Pressure Head for Sample GU3-397

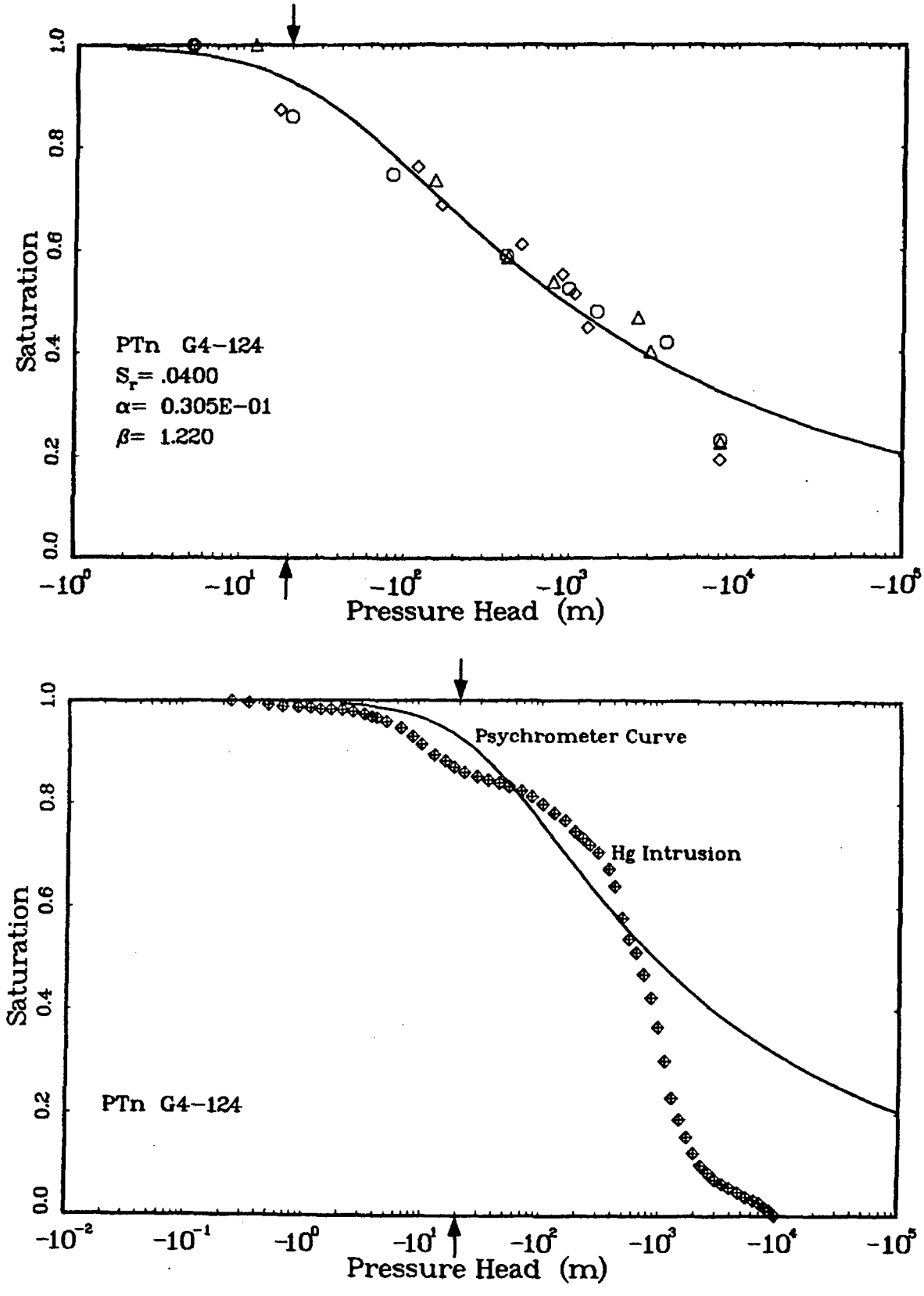

Figure B.10 Saturation as a Function of Pressure Head for Sample G4-124

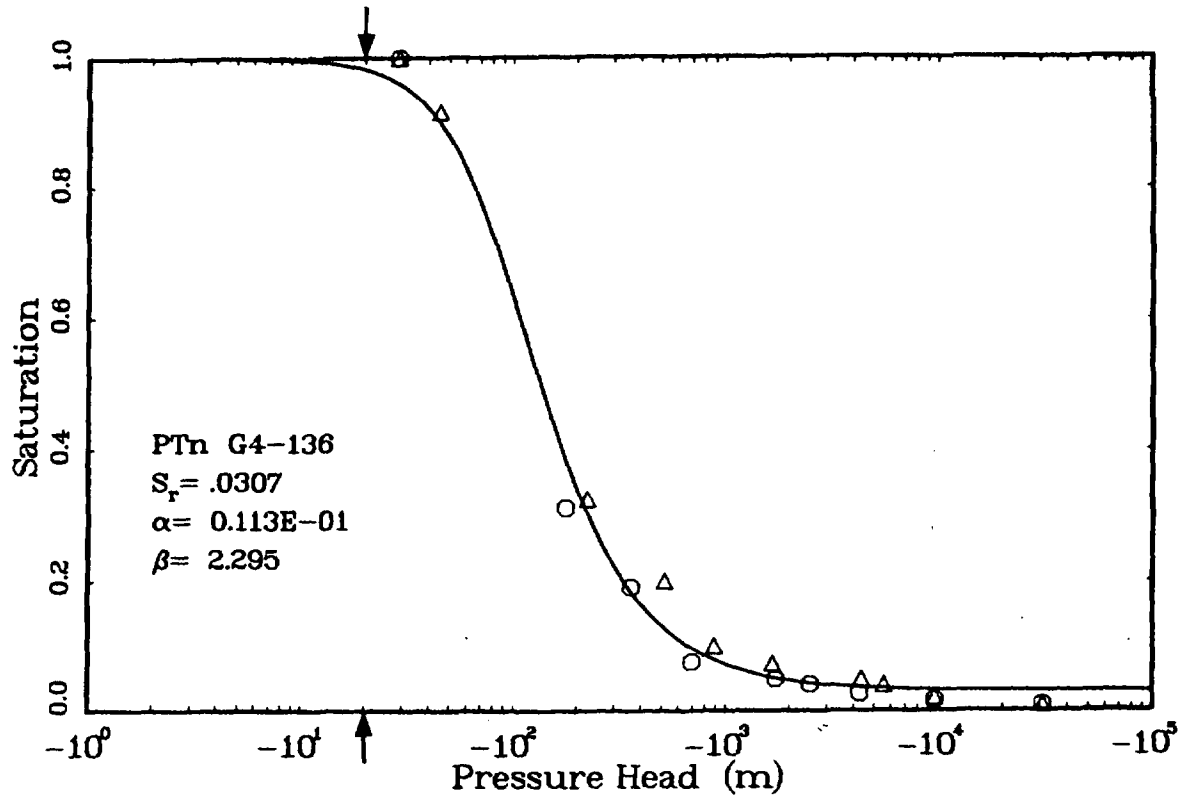

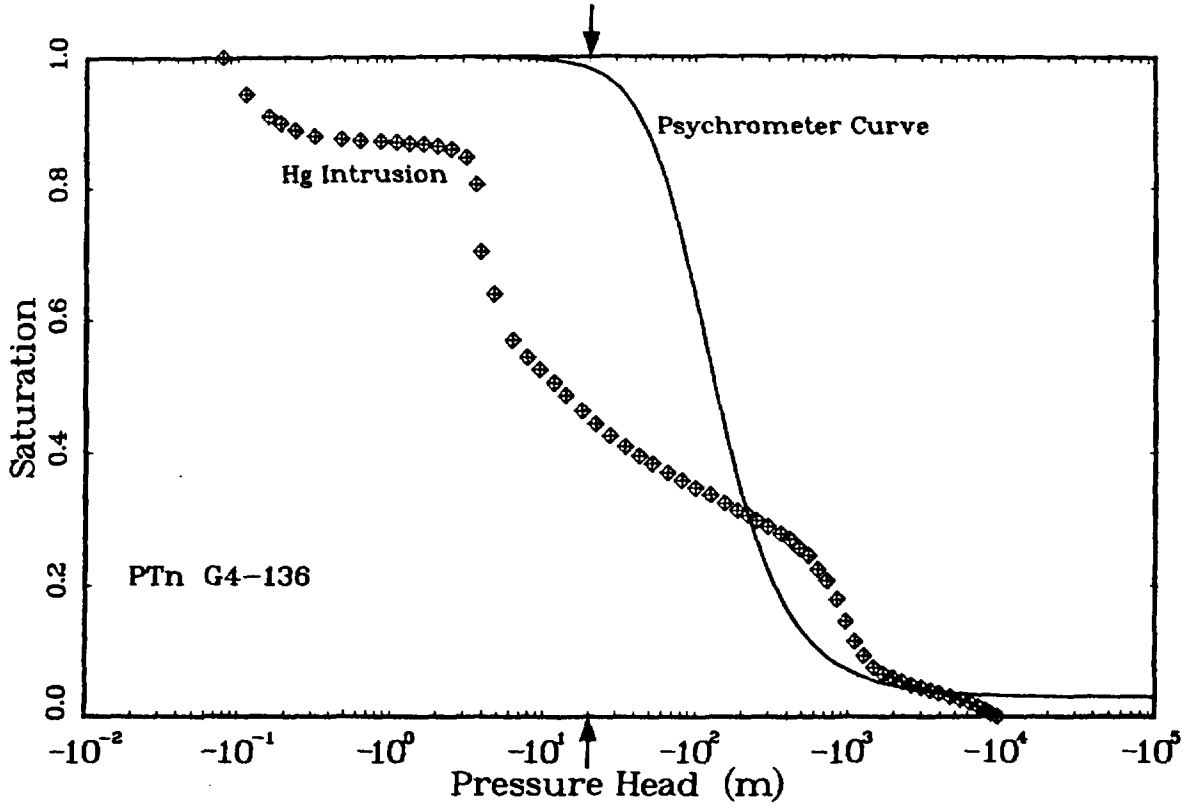

Figure B.11 Saturation as a Function of Pressure Head for Sample G4-136

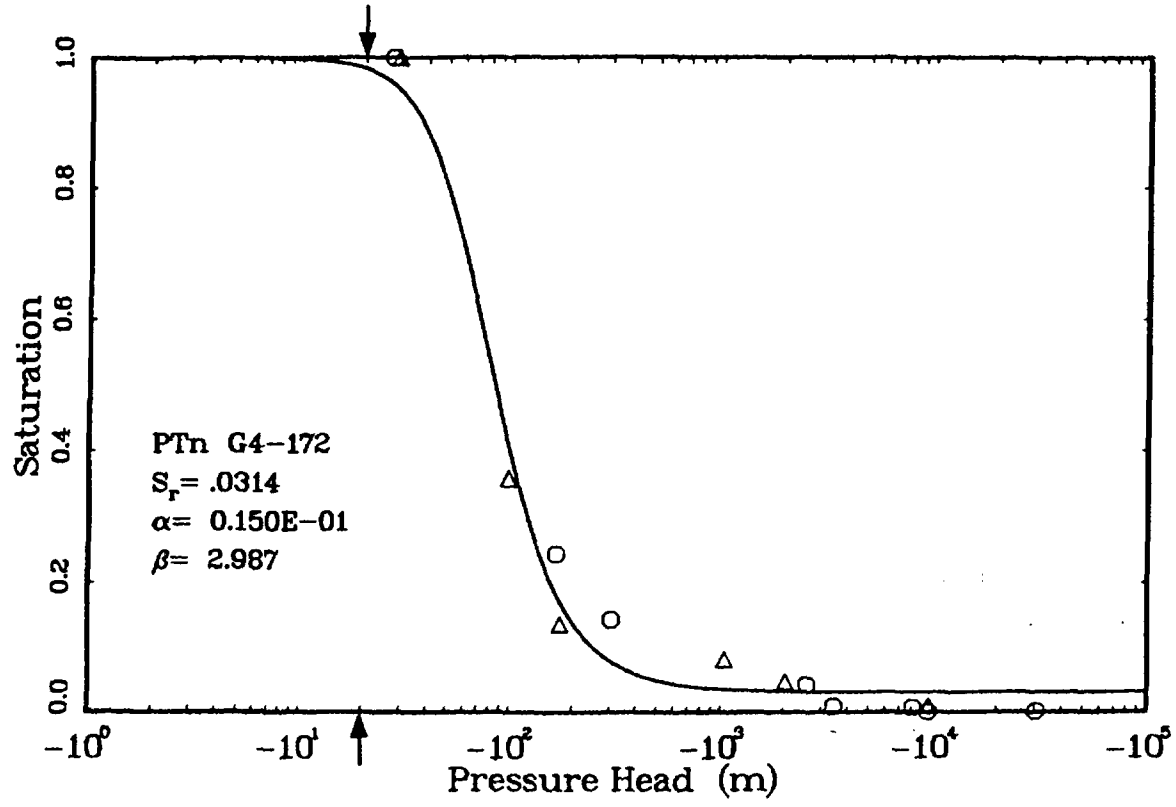

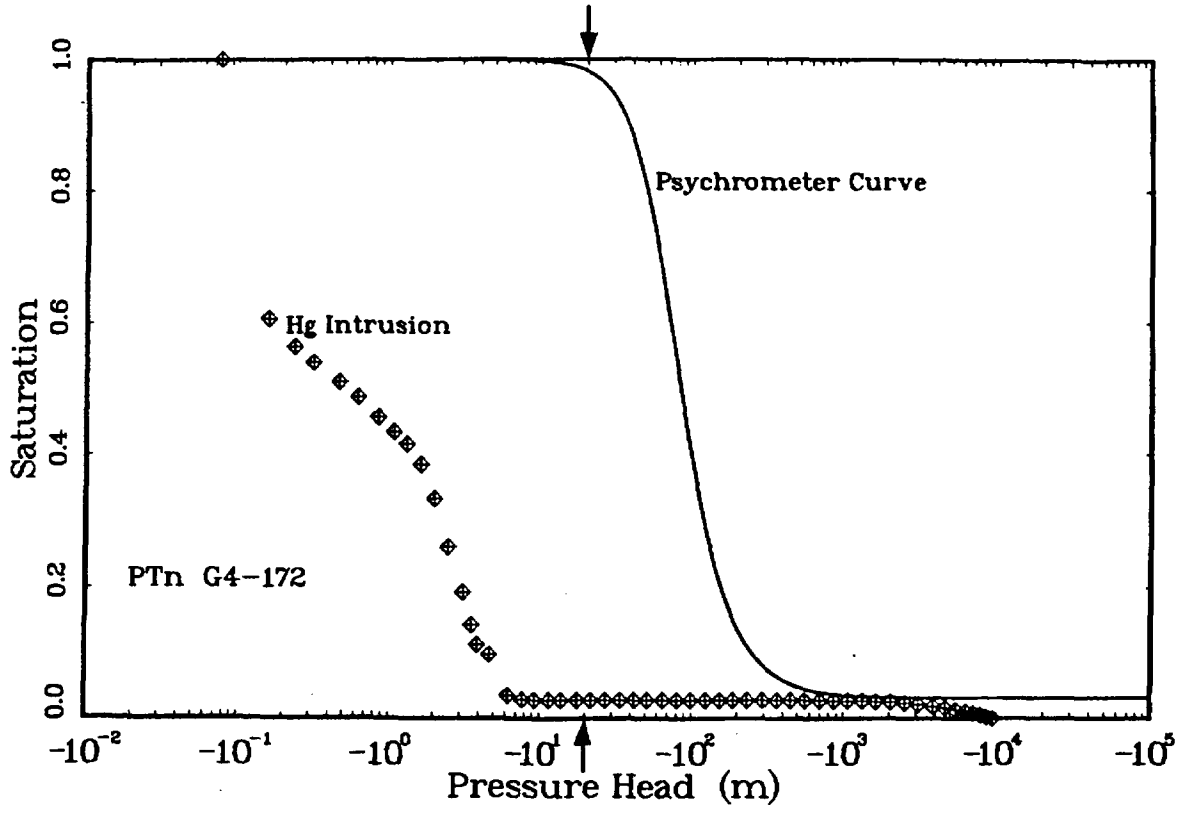

Figure B.12 Saturation as a Function of Pressure Head for Sample G4-172

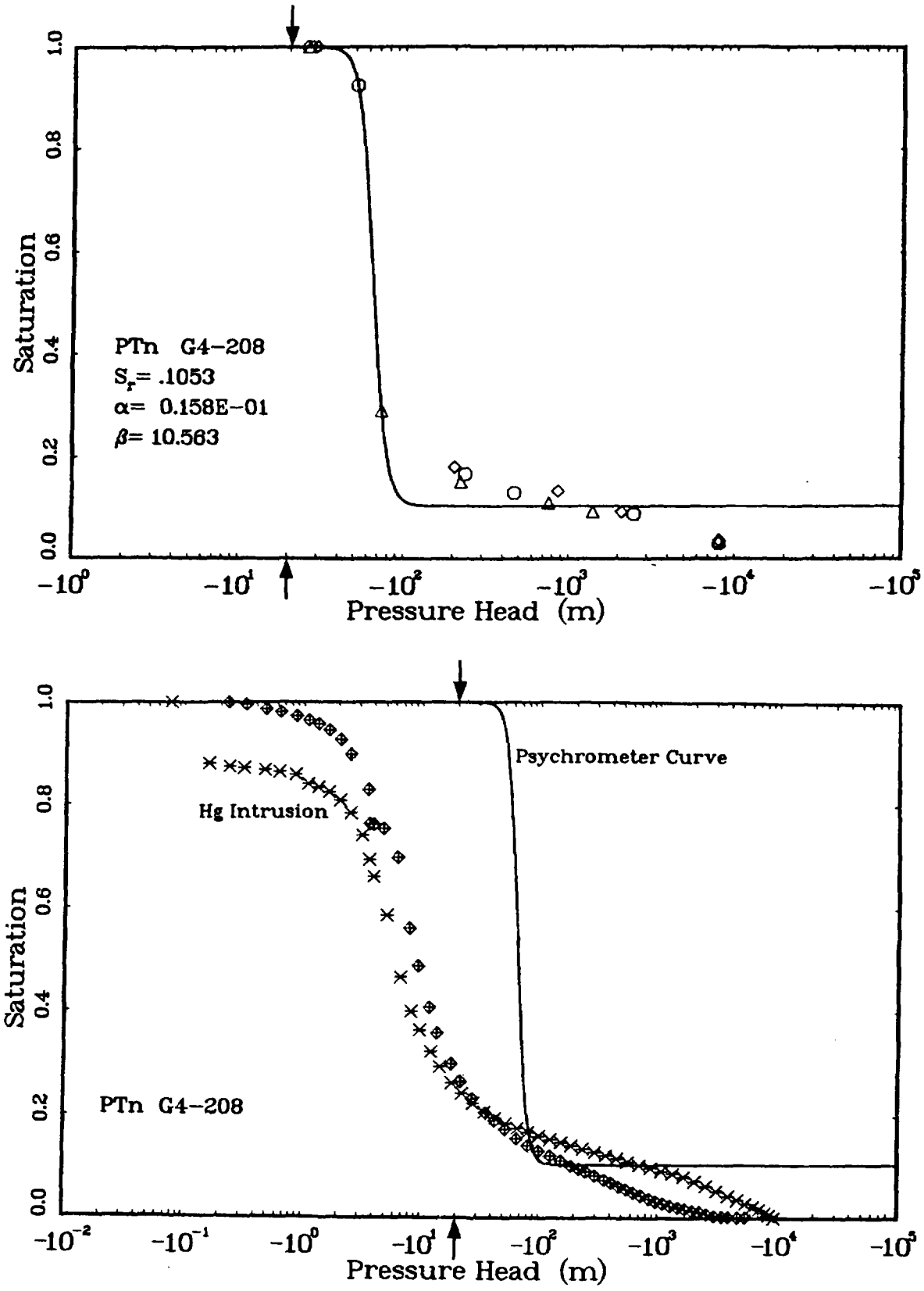

Figure B.13 Saturation as a Function of Pressure Head for Sample G4-208

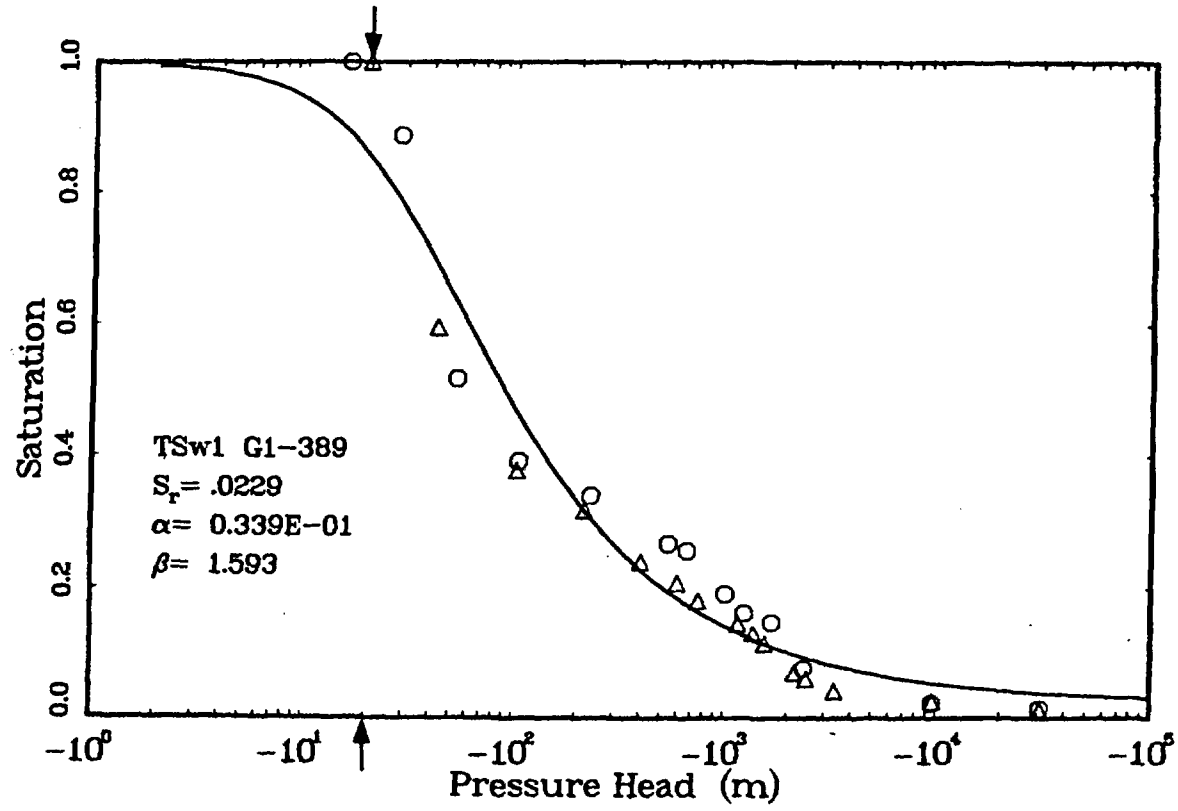

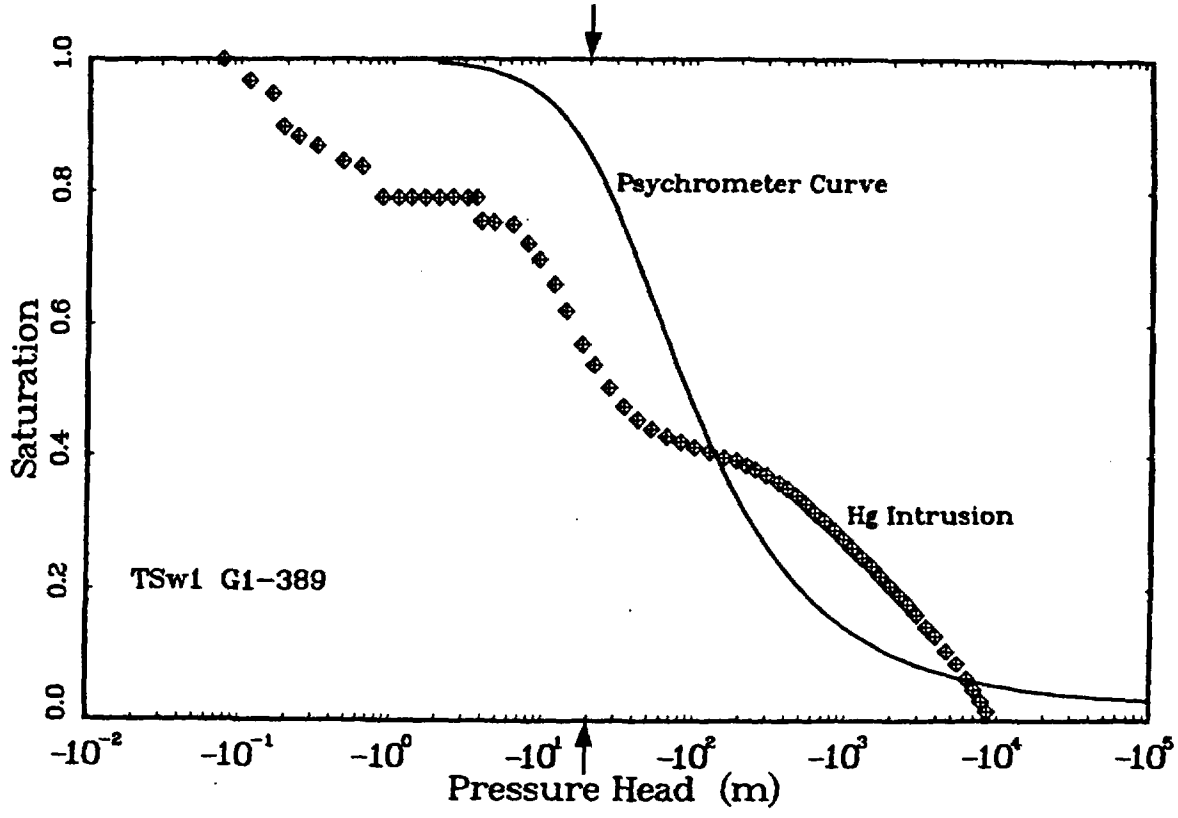

Figure B.14 Saturation as a Function of Pressure Head for Sample G1-389

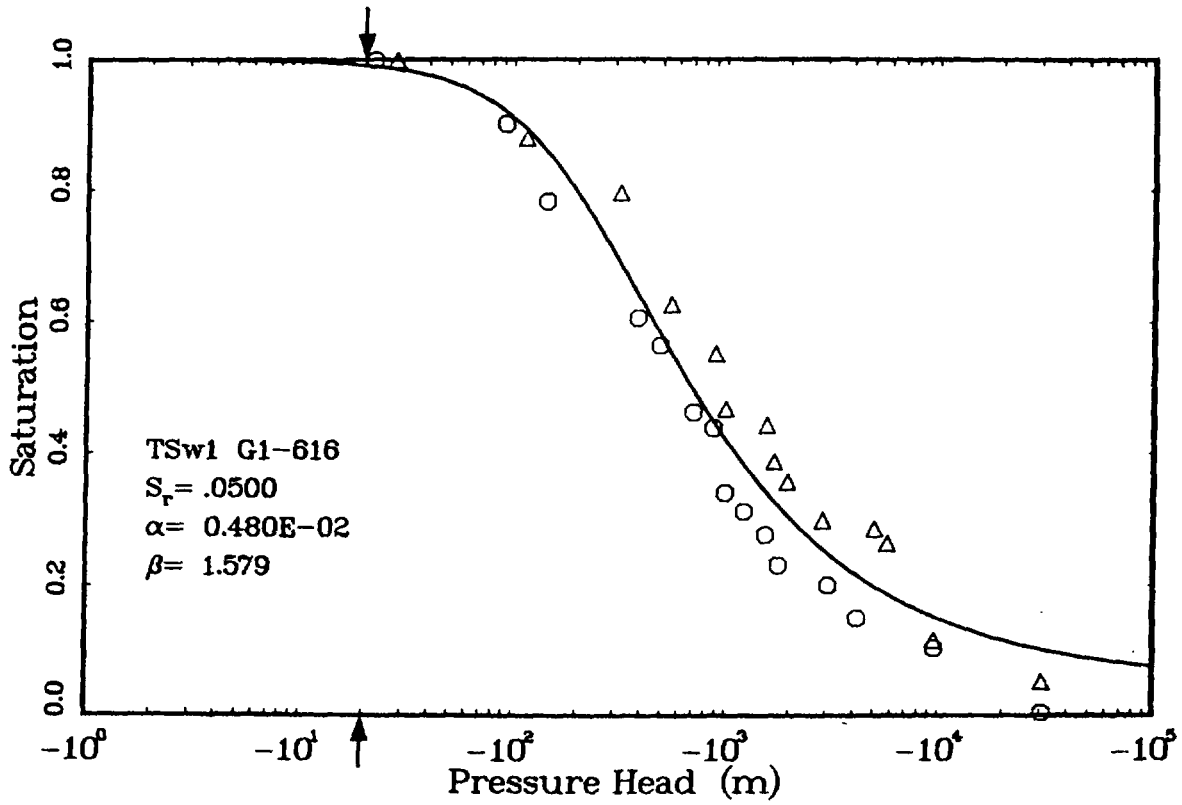

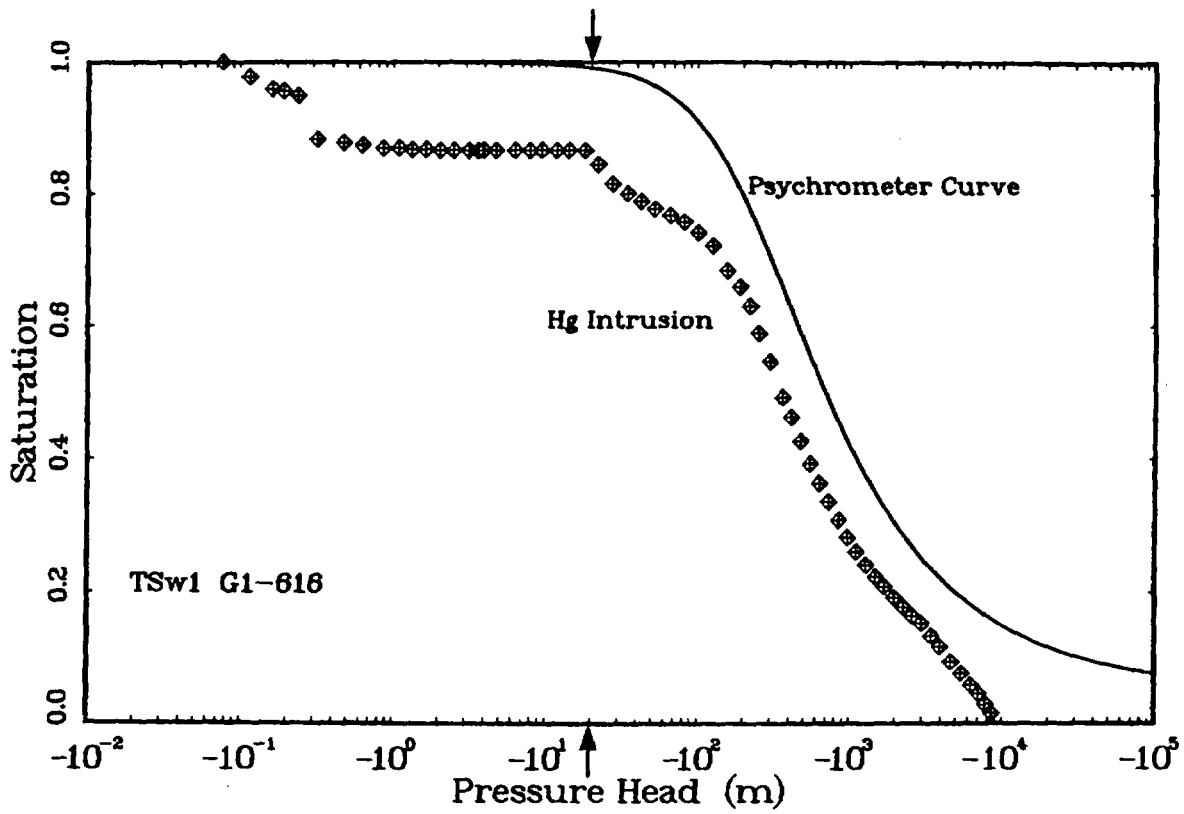

Figure B.15 Saturation as a Function of Pressure Head for Sample G1-616

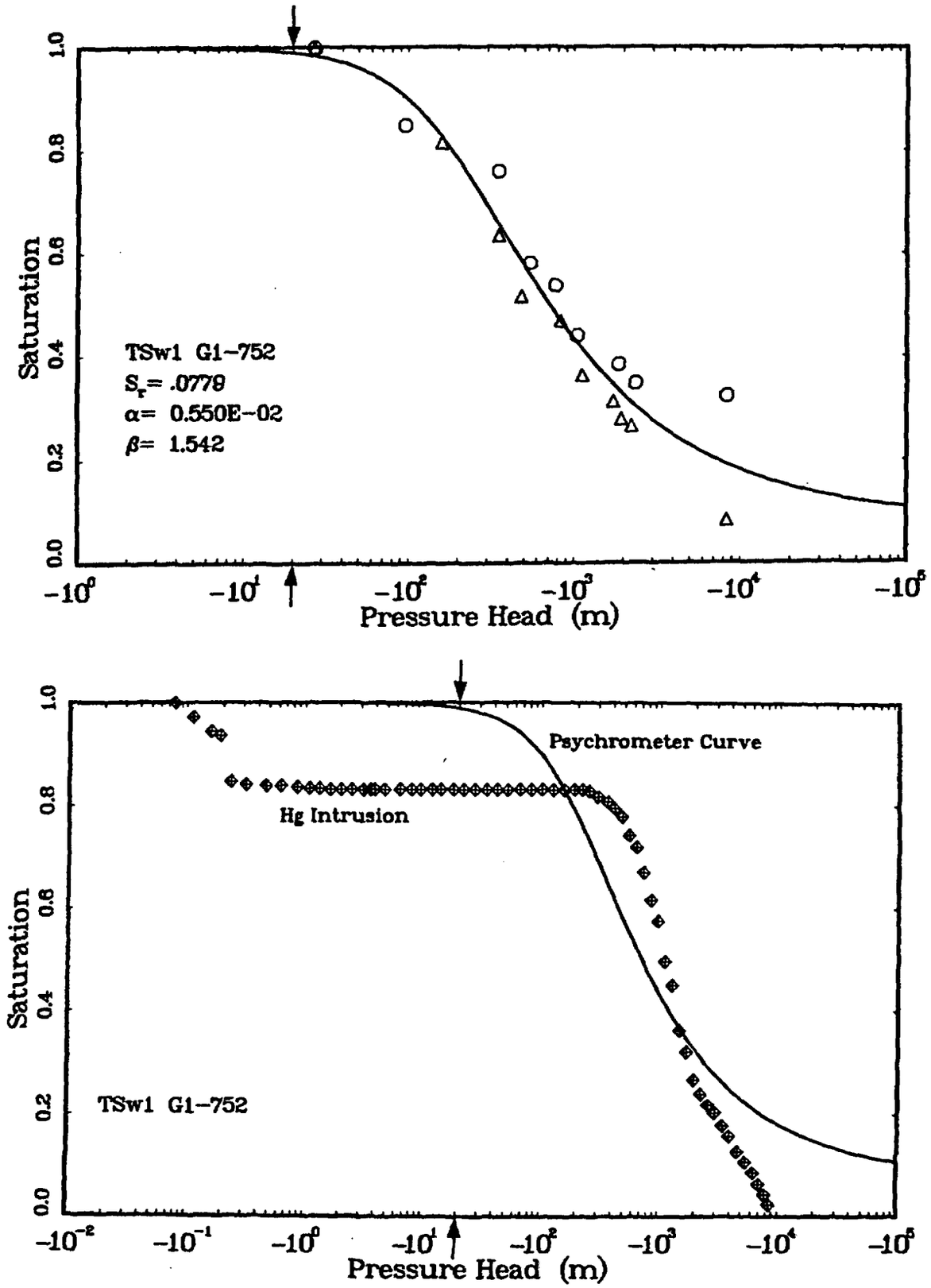

Figure B.16 Saturation as a Function of Pressure Head for Sample G1-752

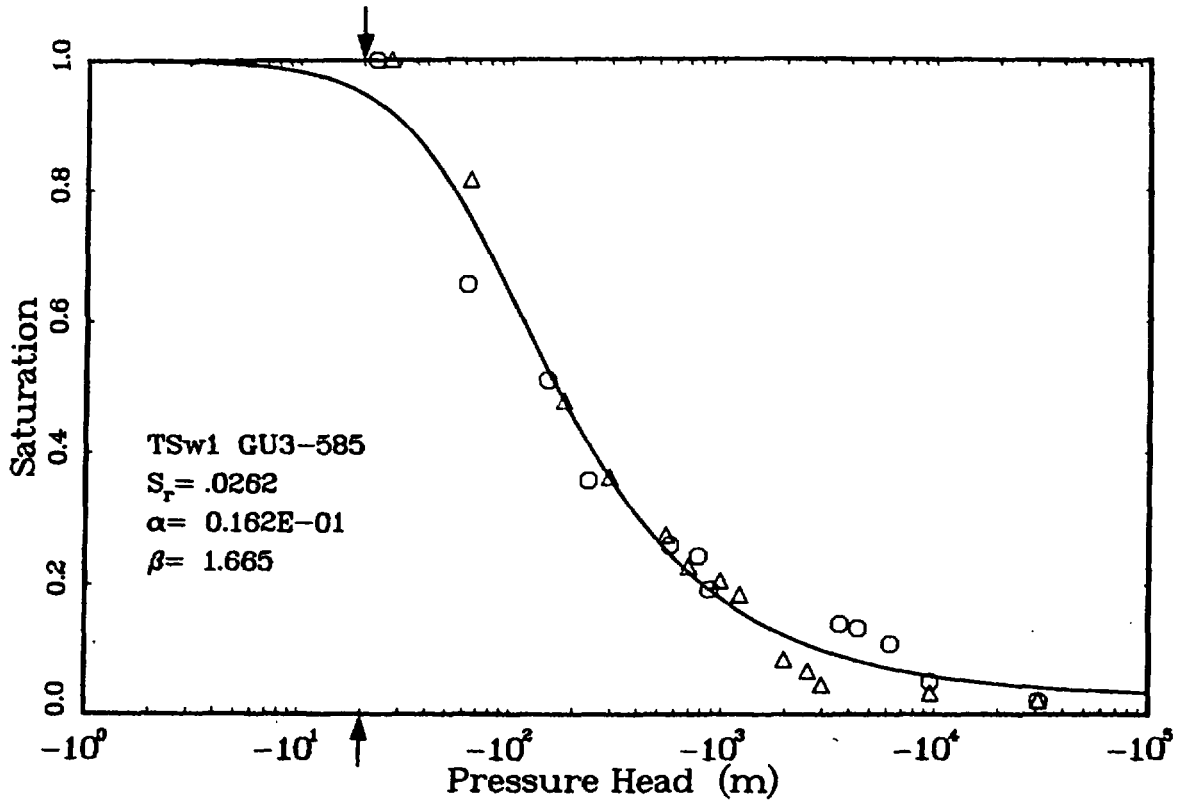

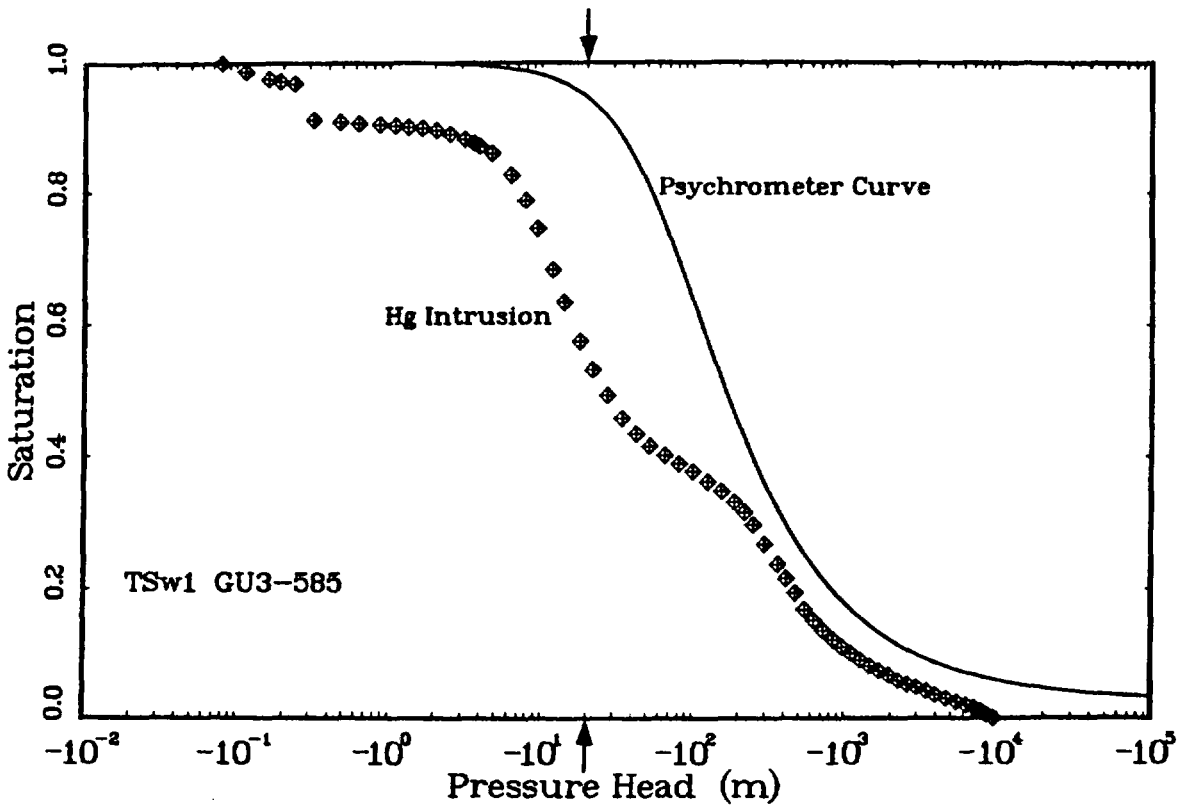

Figure B.17 Saturation as a Function of Pressure Head for Sample GU3-585

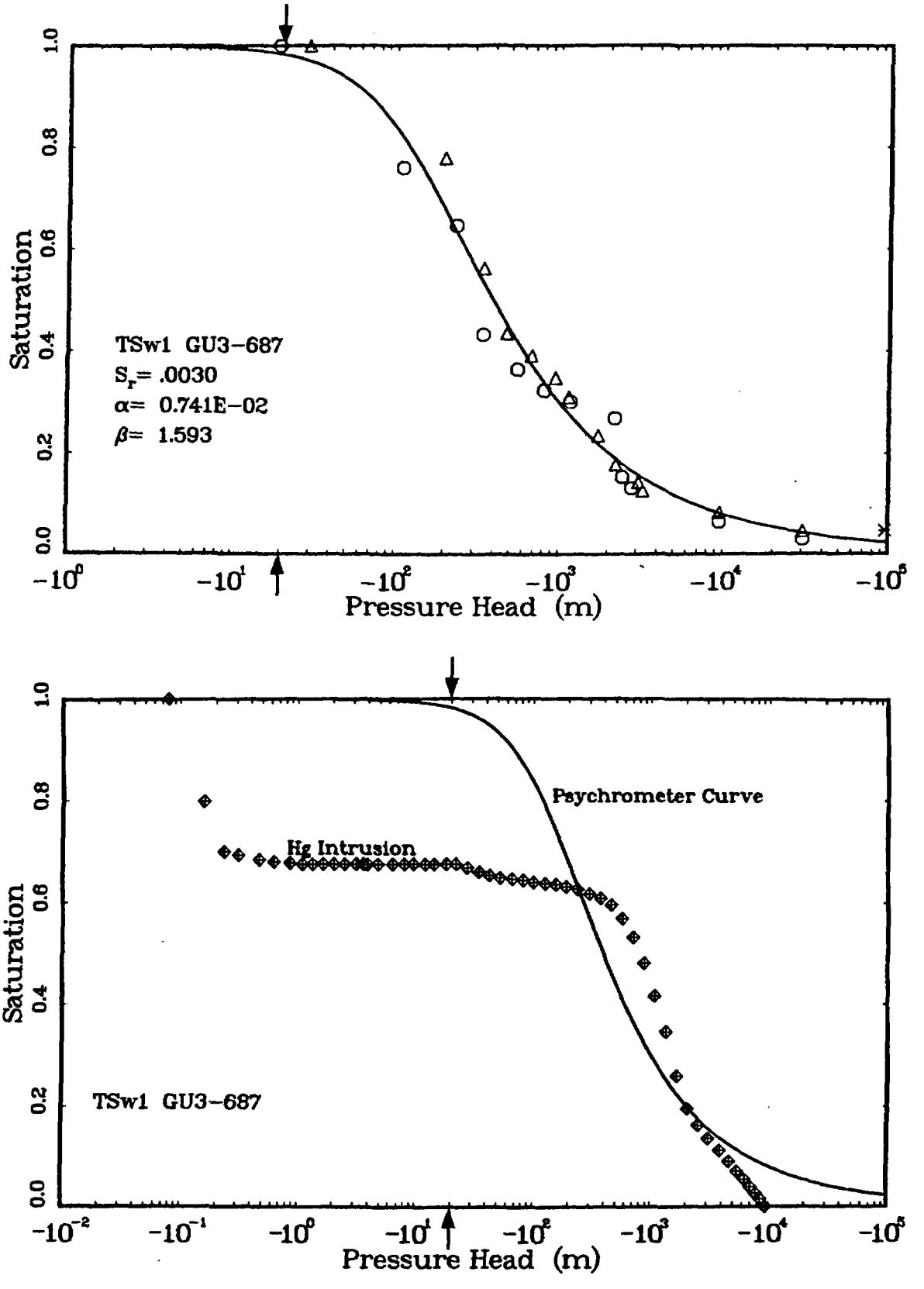

Figure B.18 Saturation as a Function of Pressure Head for Sample GU3-687

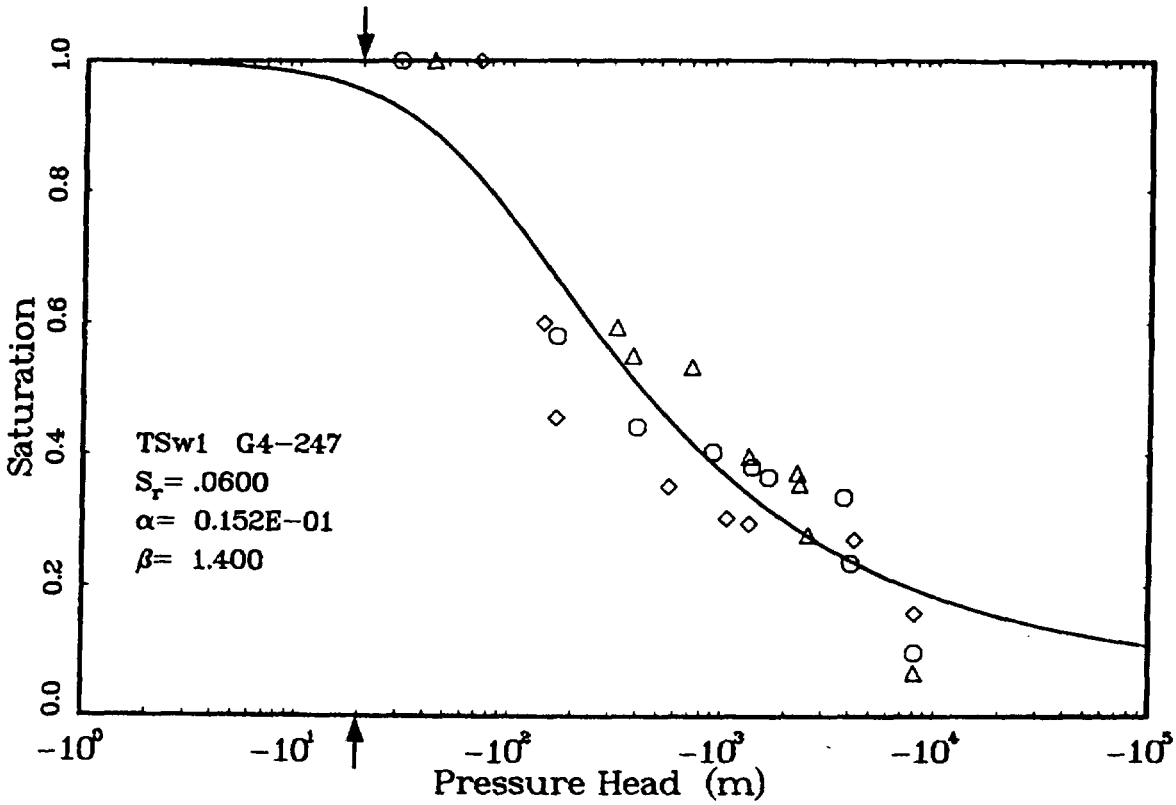

Figure B.19 Saturation as a Function of Pressure Head for Sample G4-247 (Psychrometer Only)

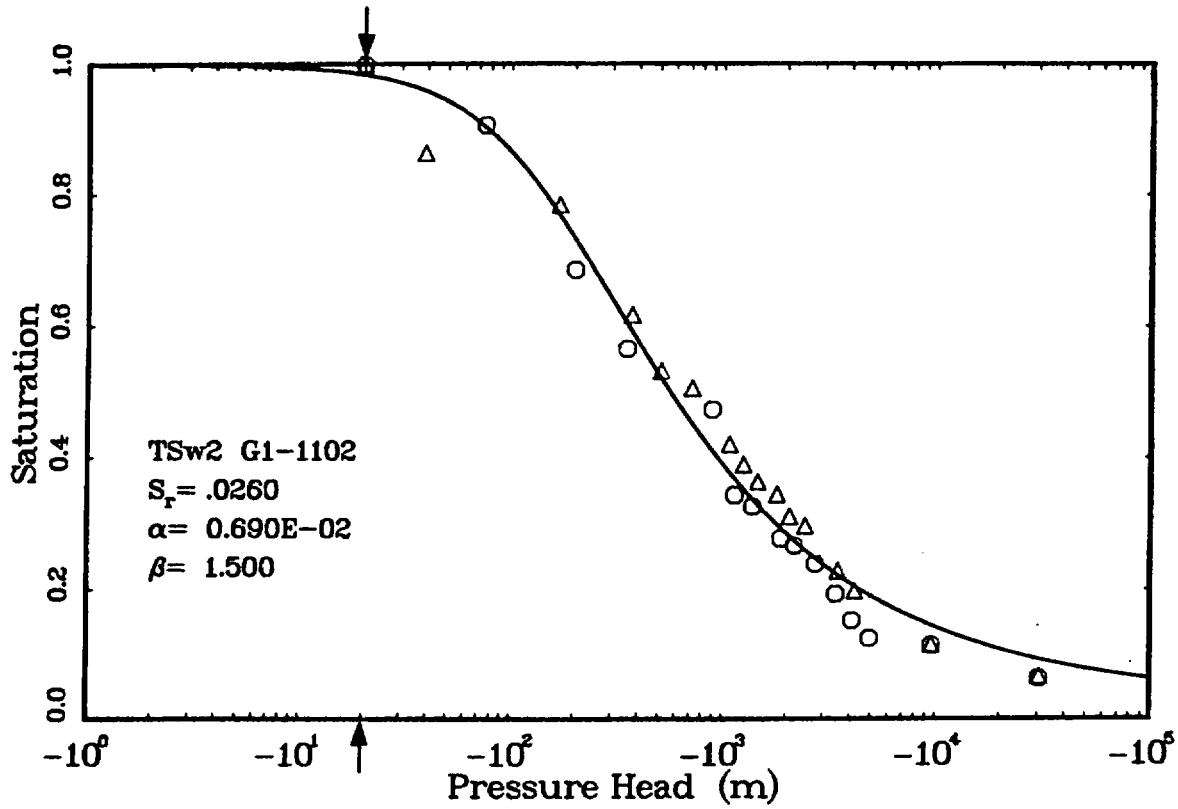

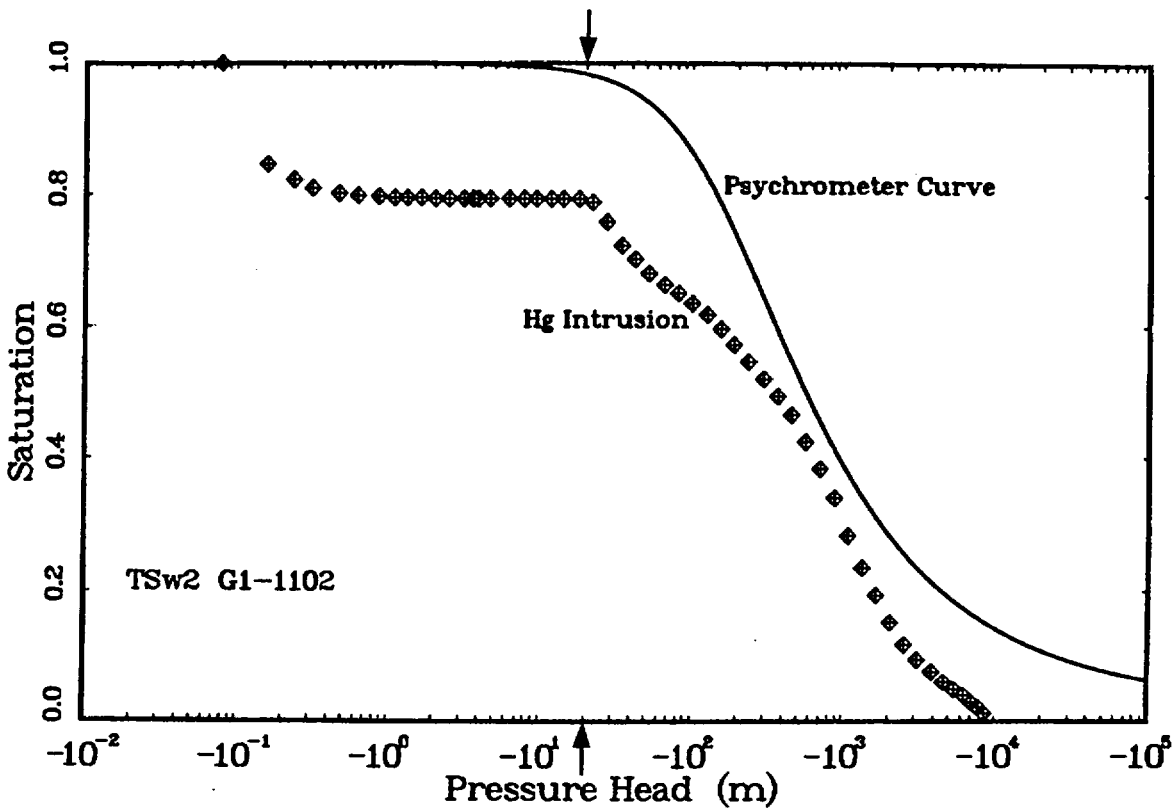

Figure B.20 Saturation as a Function of Pressure Head for Sample G1-1102

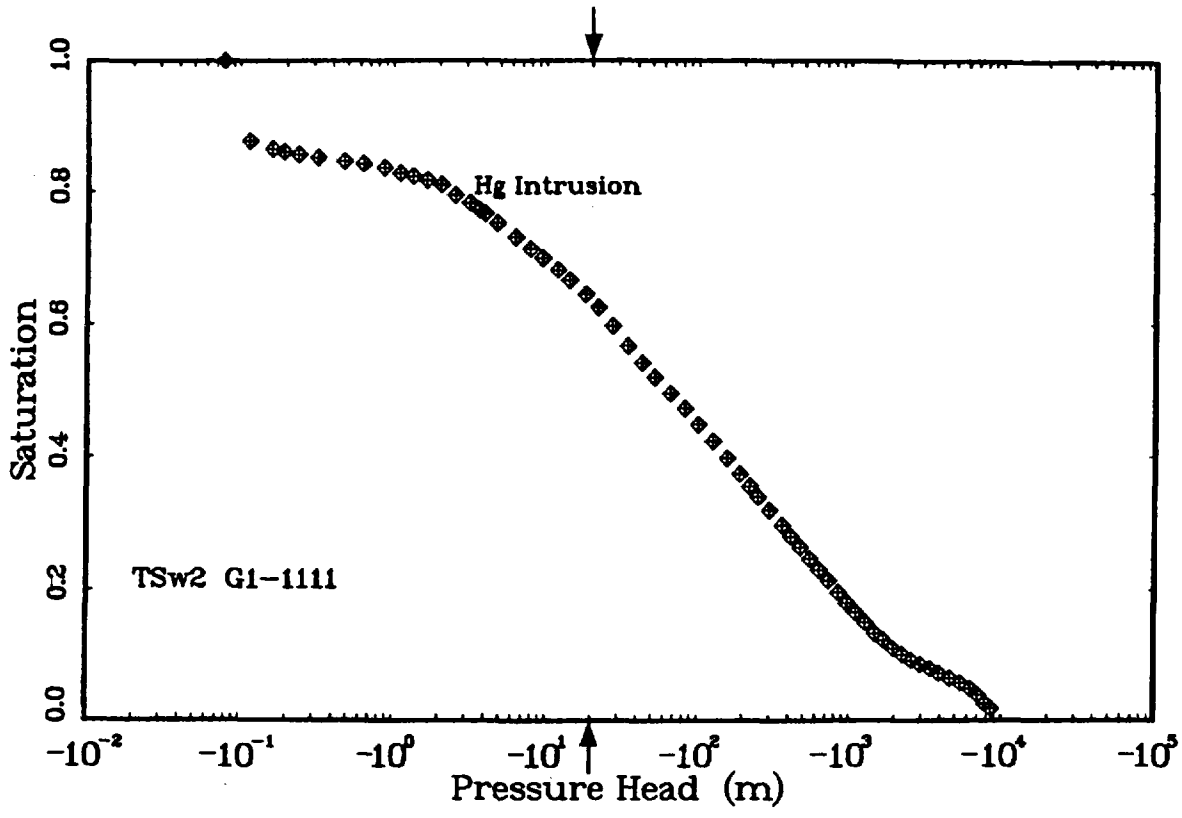

Figure B.21 Saturation as a Function of Pressure Head for Sample G1-1111 (Mercury Intrusion Only)

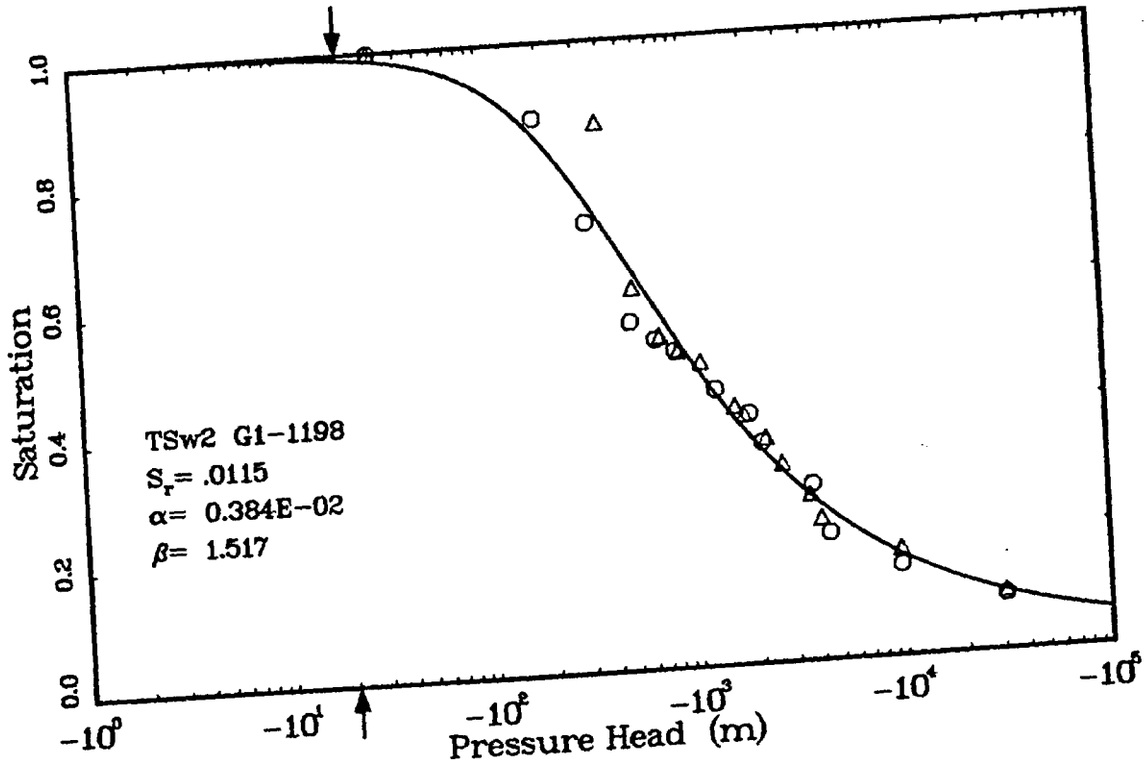

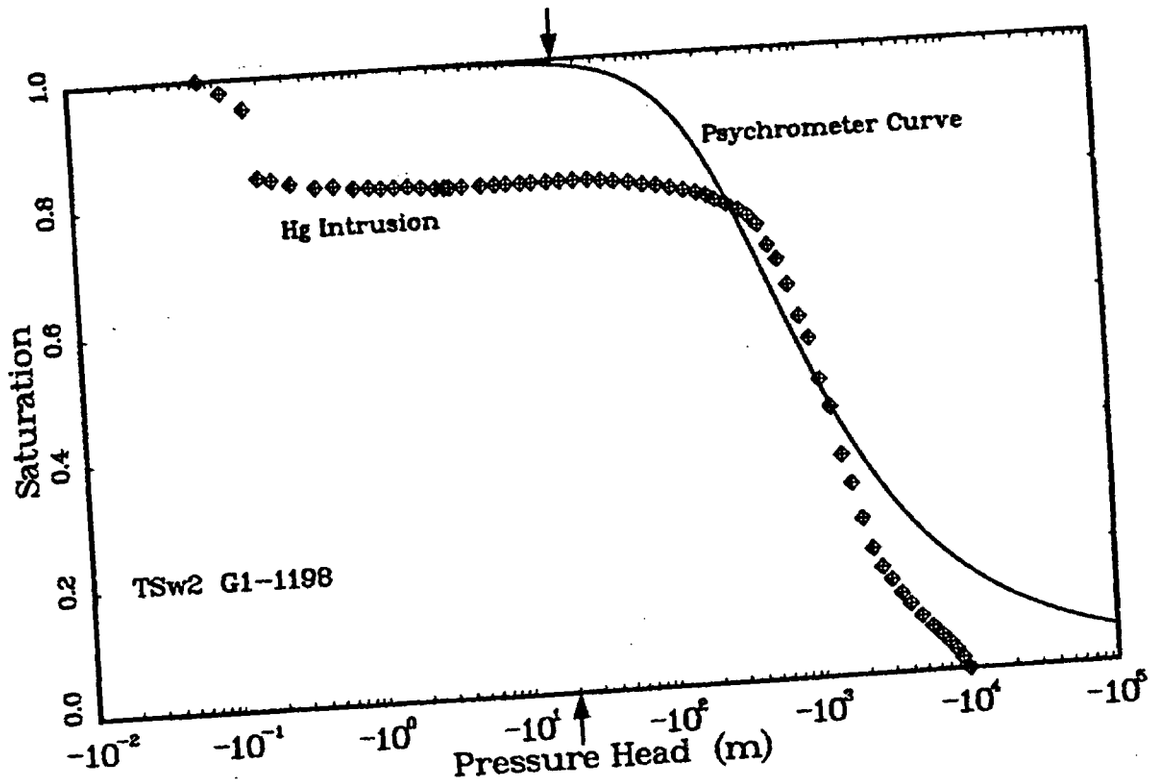

Figure B.22 Saturation as a Function of Pressure Head for Sample G1-1198

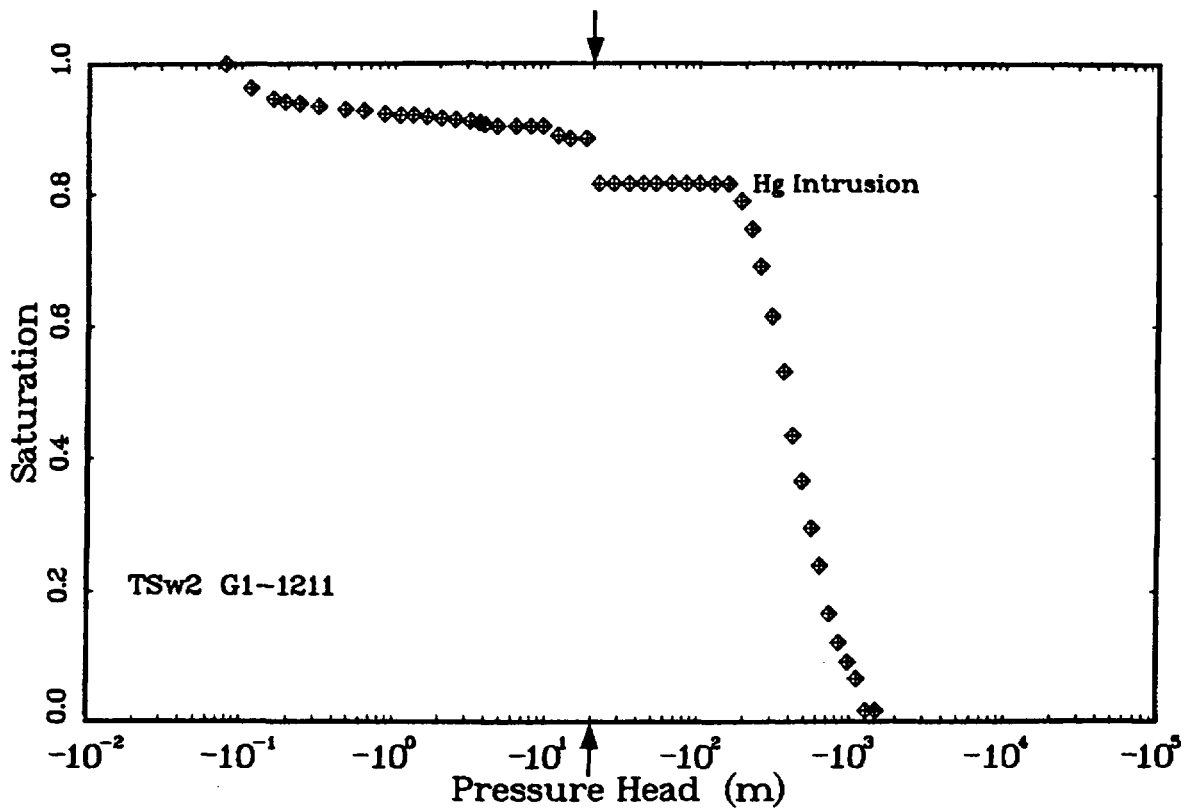

Figure B.23 Saturation as a Function of Pressure Head for Sample G1-1211 (Mercury Intrusion Only)

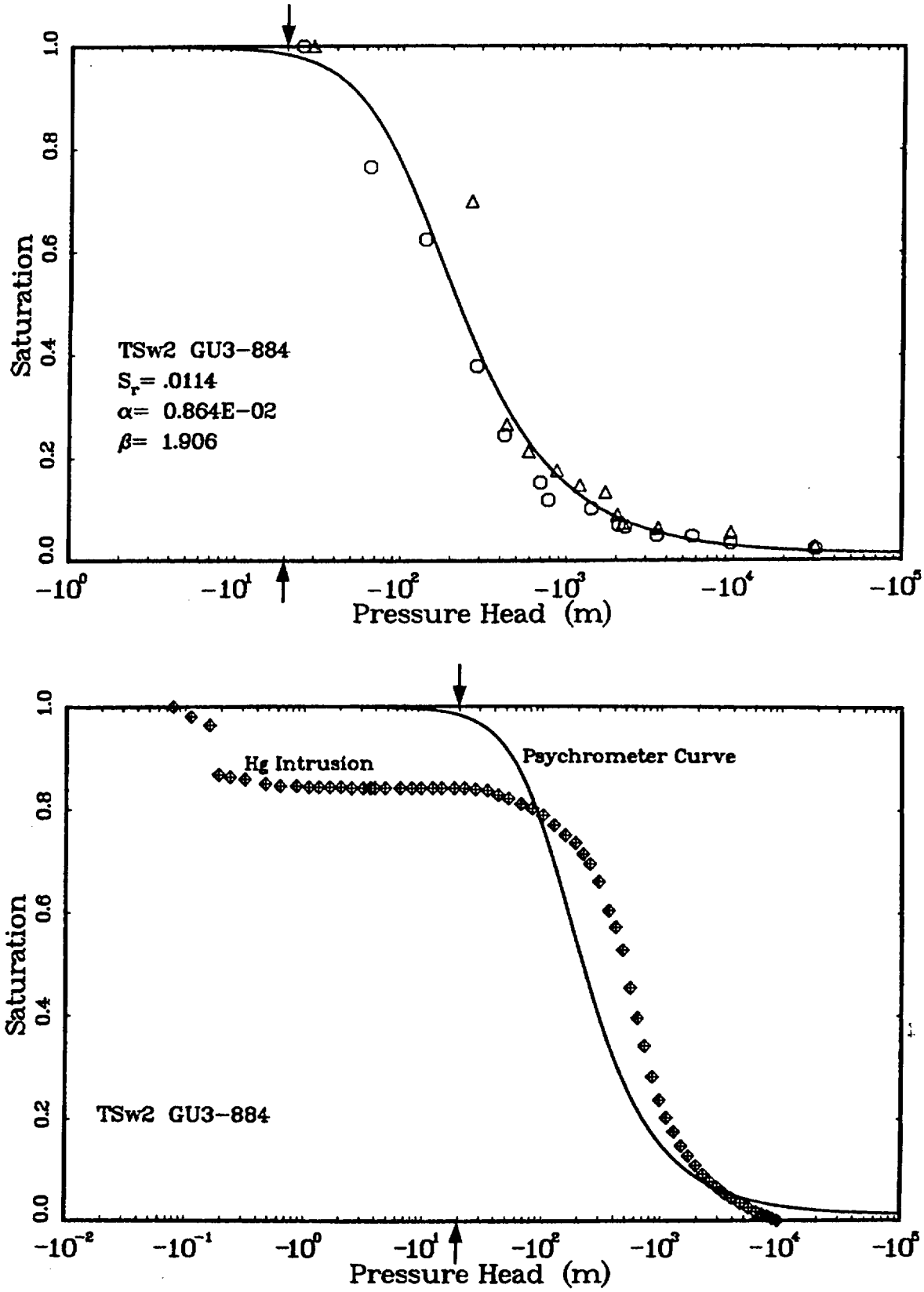

Figure B.24 Saturation as a Function of Pressure Head for Sample GU3-884

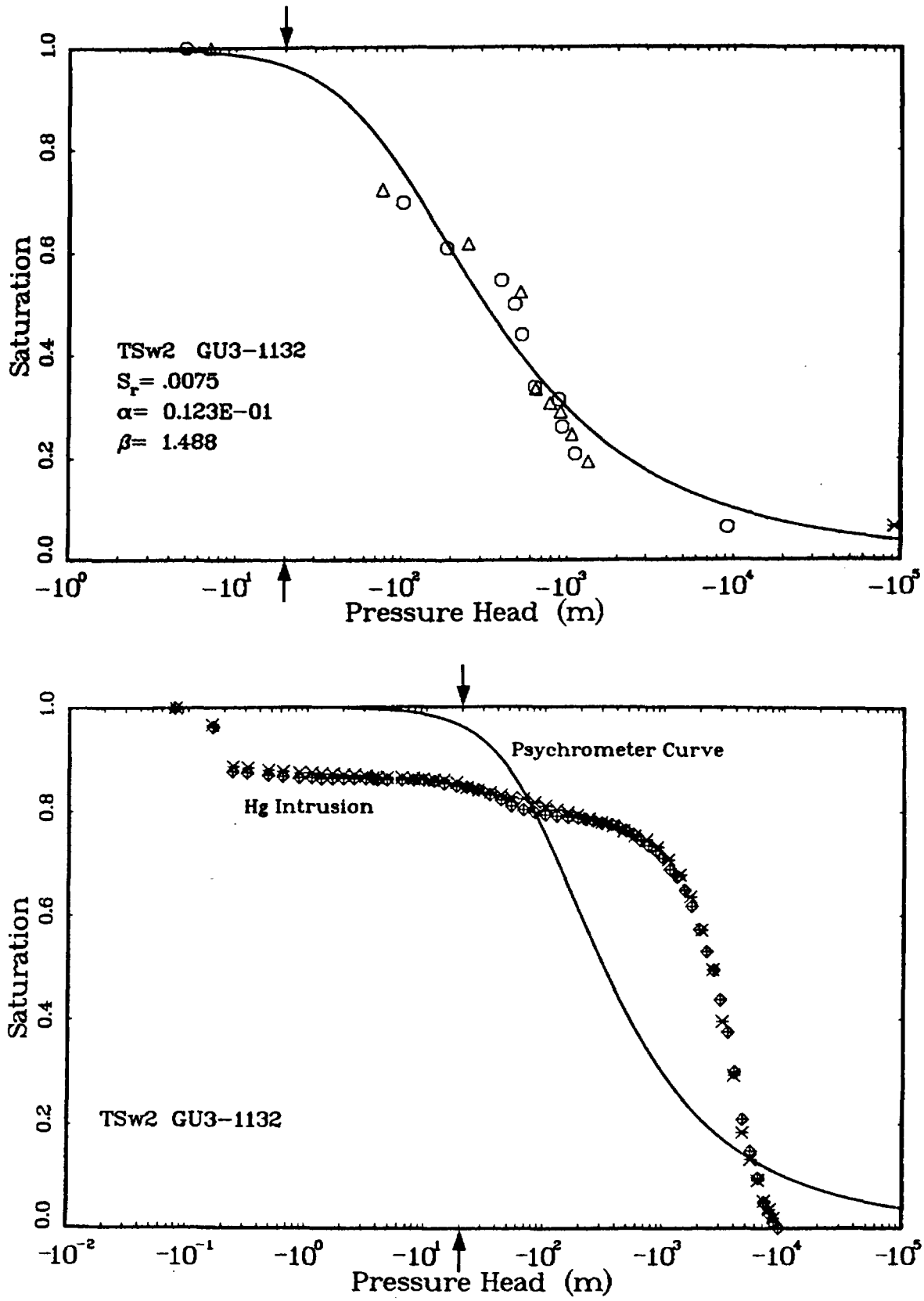

Figure B.25 Saturation as a Function of Pressure Head for Sample GU3-1132

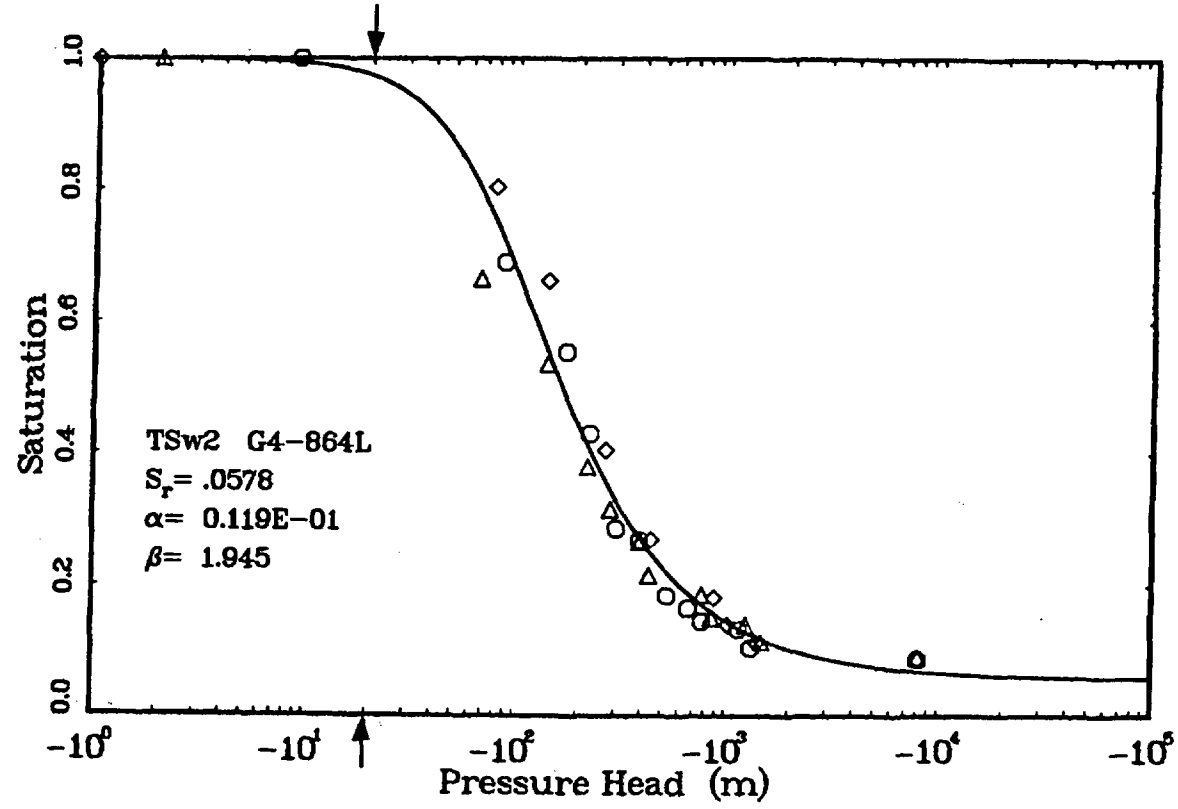

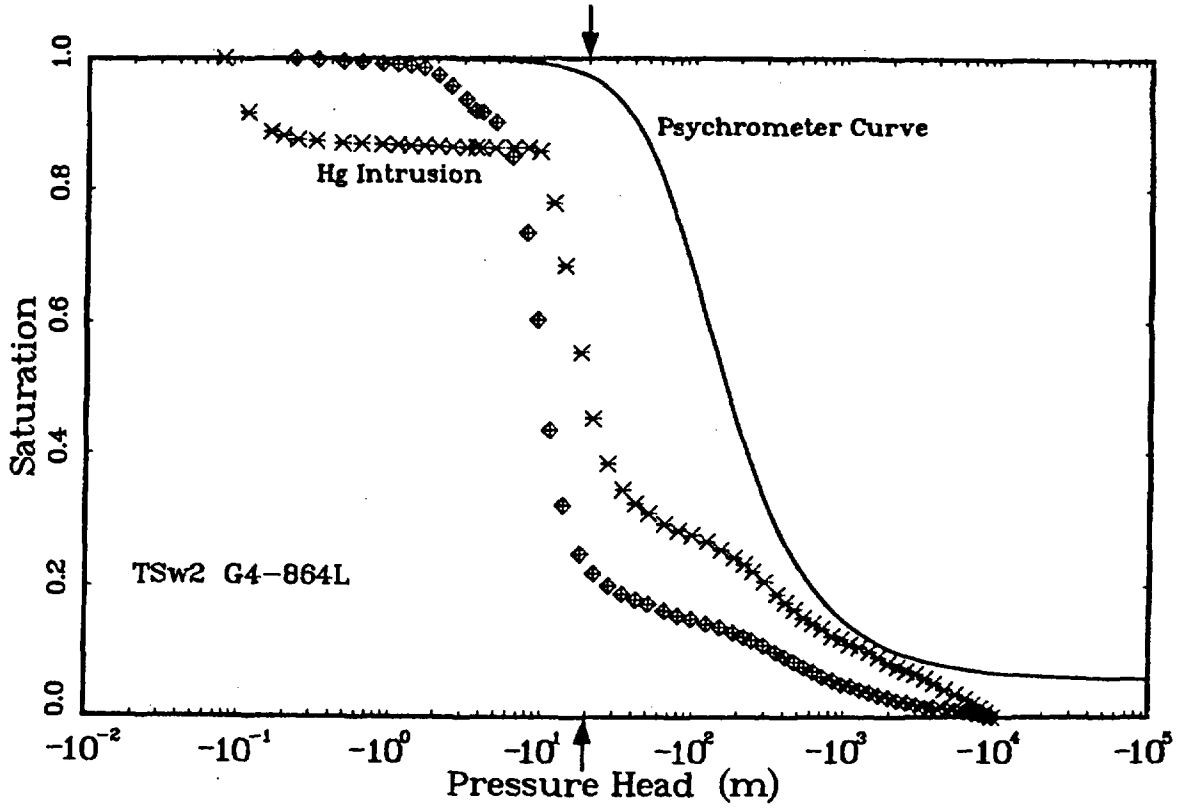

Figure B.26 Saturation as a Function of Pressure Head for Sample G4-864L

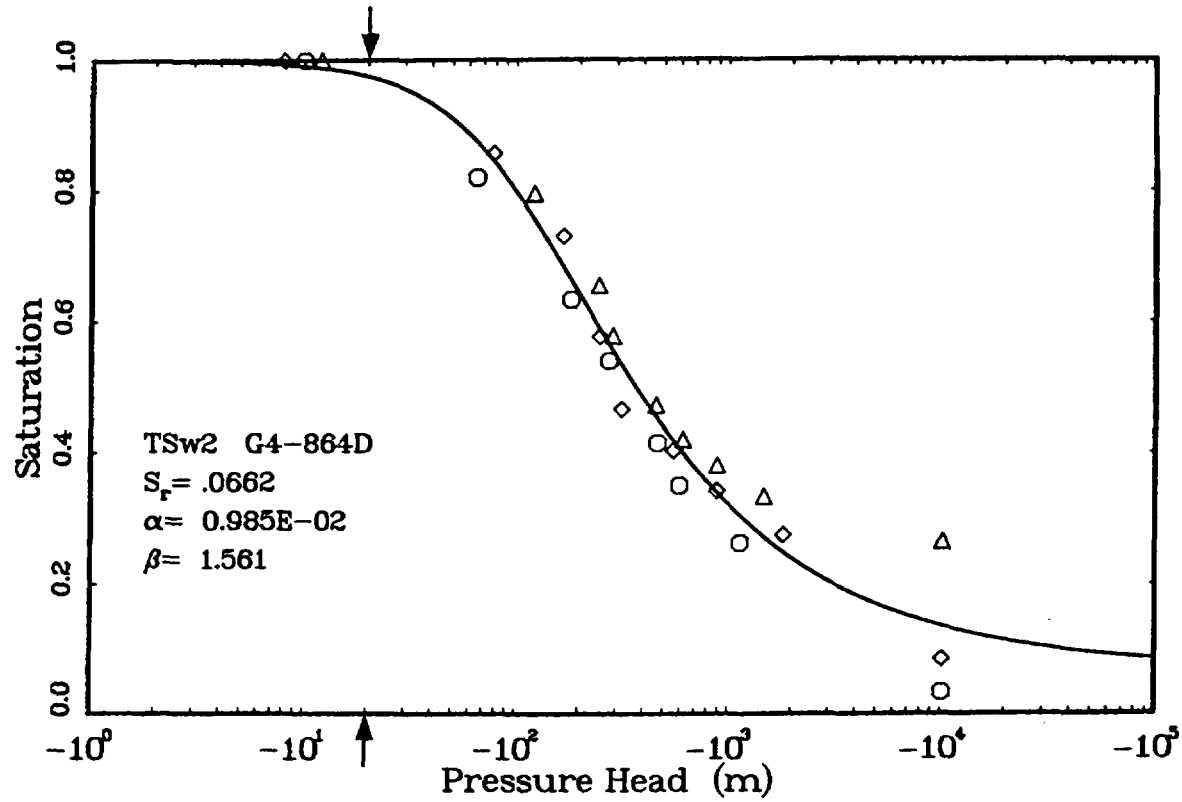

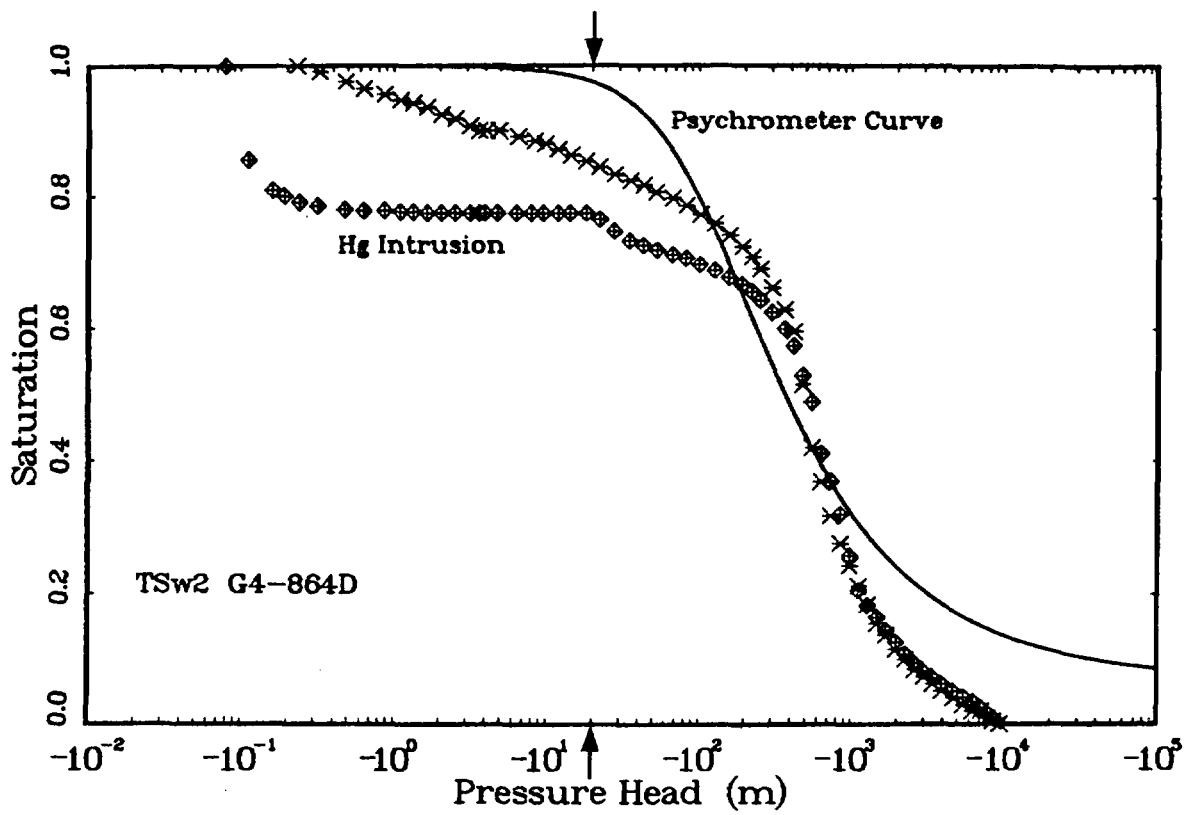

Figure B.27 Saturation as a Function of Pressure Head for Sample G4-864D

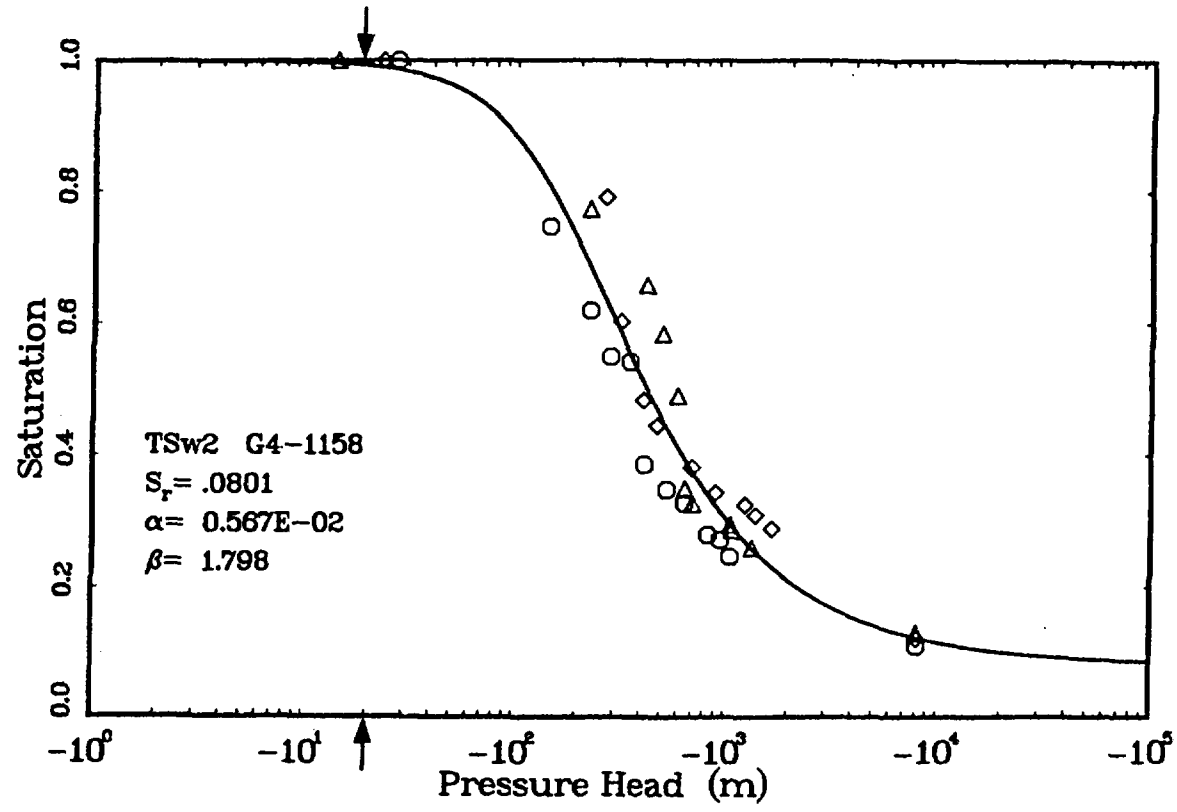

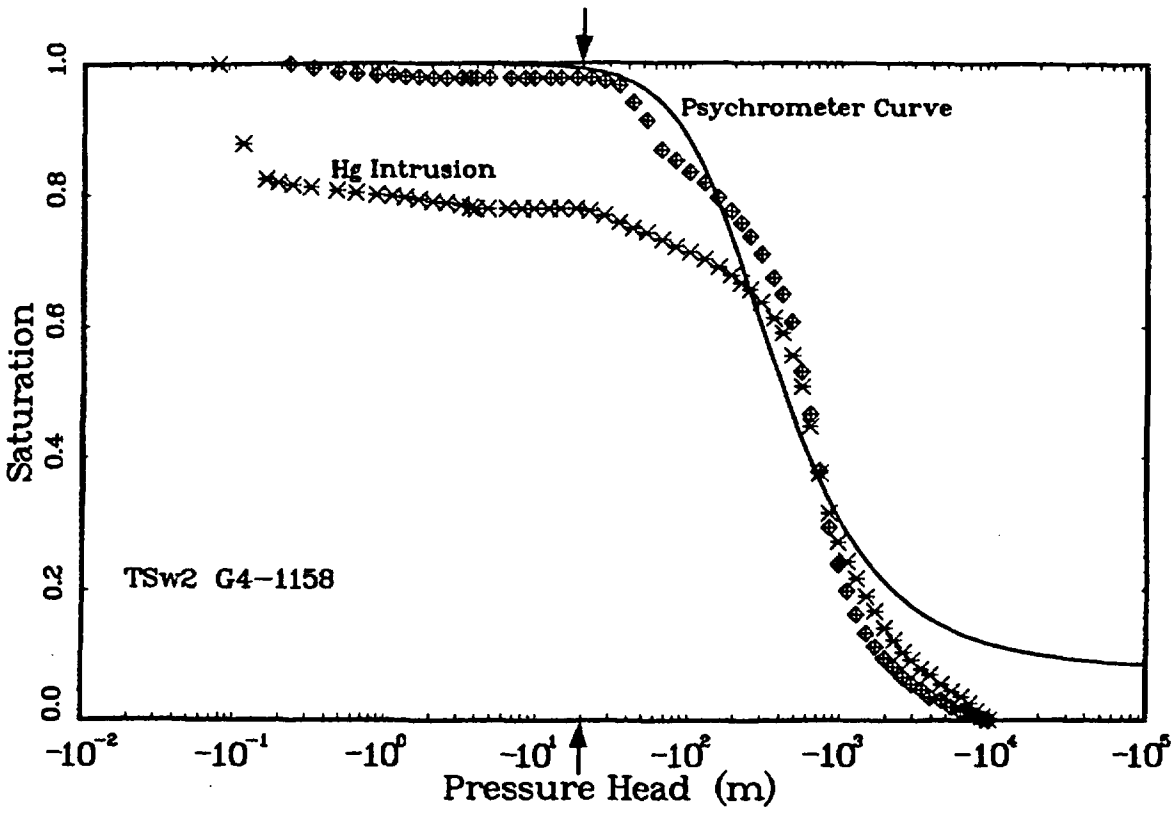

Figure B.28 Saturation as a Function of Pressure Head for Sample G4-1158 (Mercury-Intrusion Test Results from G4-1159 Added)

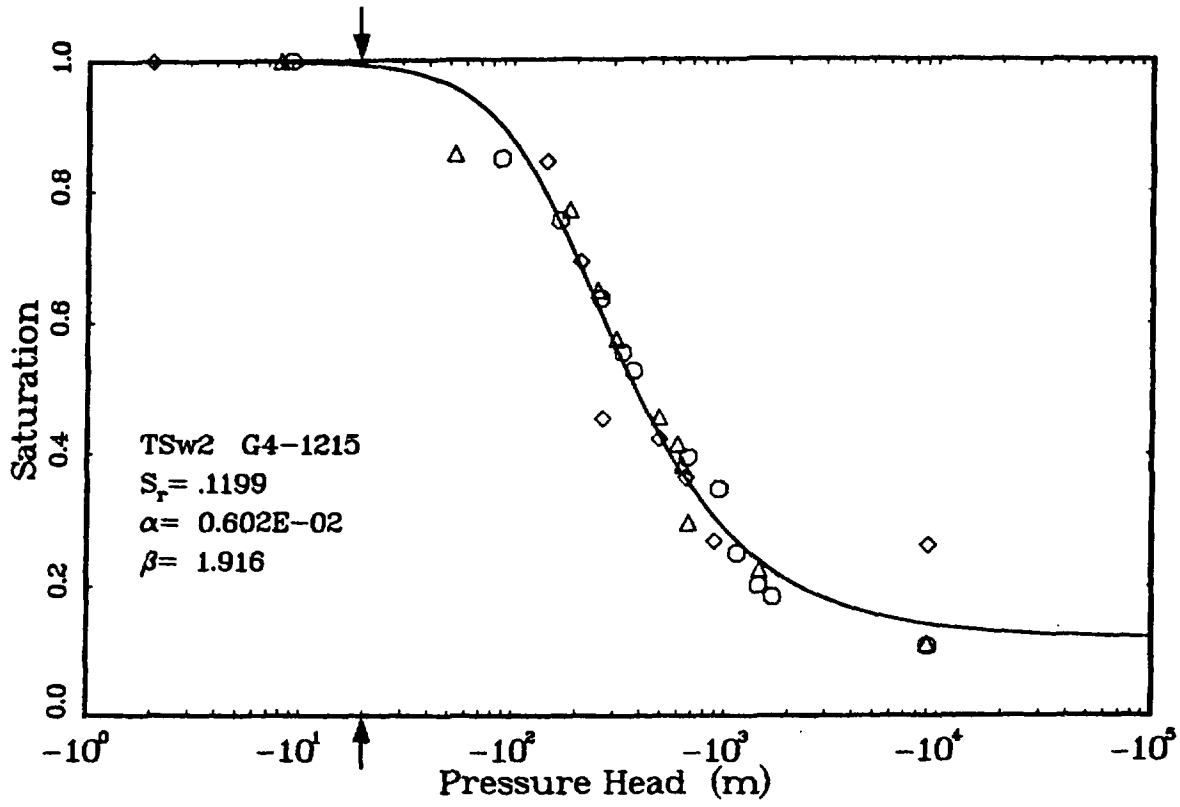

Figure B.29 Saturation as a Function of Pressure Head for Sample G4-1215 (Psychrometer Only)

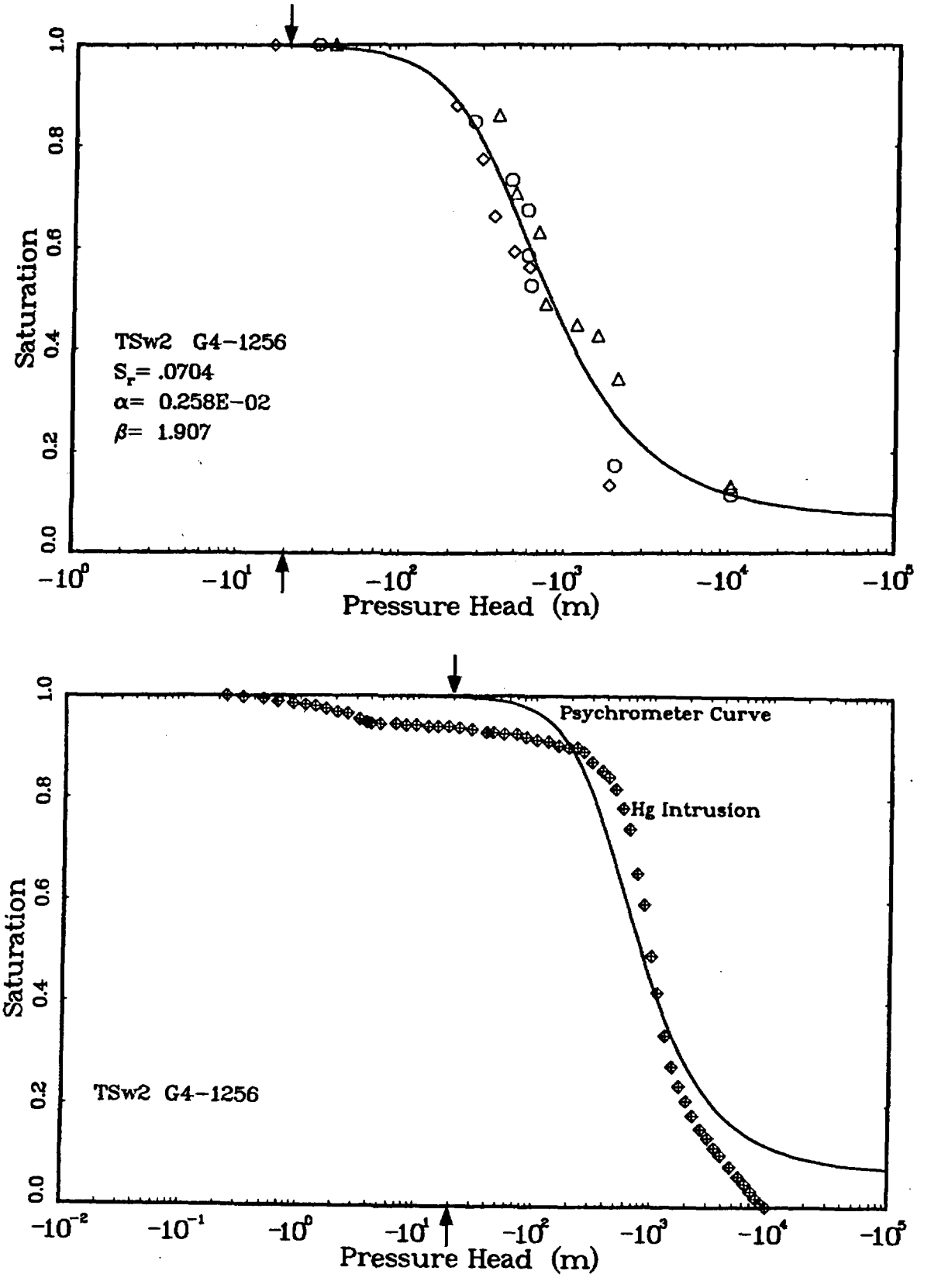

Figure B.30 Saturation as a Function of Pressure Head for Sample G4-1256

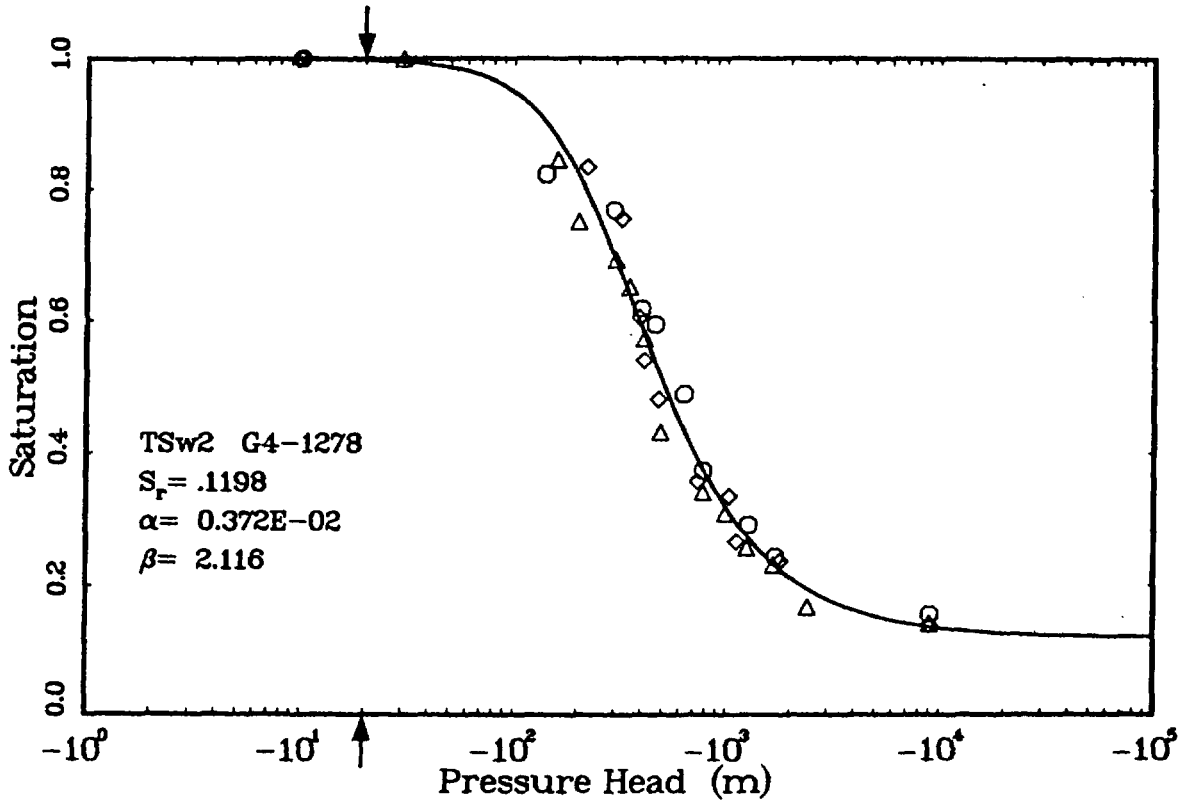

Figure B.31 Saturation as a Function of Pressure Head for Sample G4-1278 (Psychrometer Only)

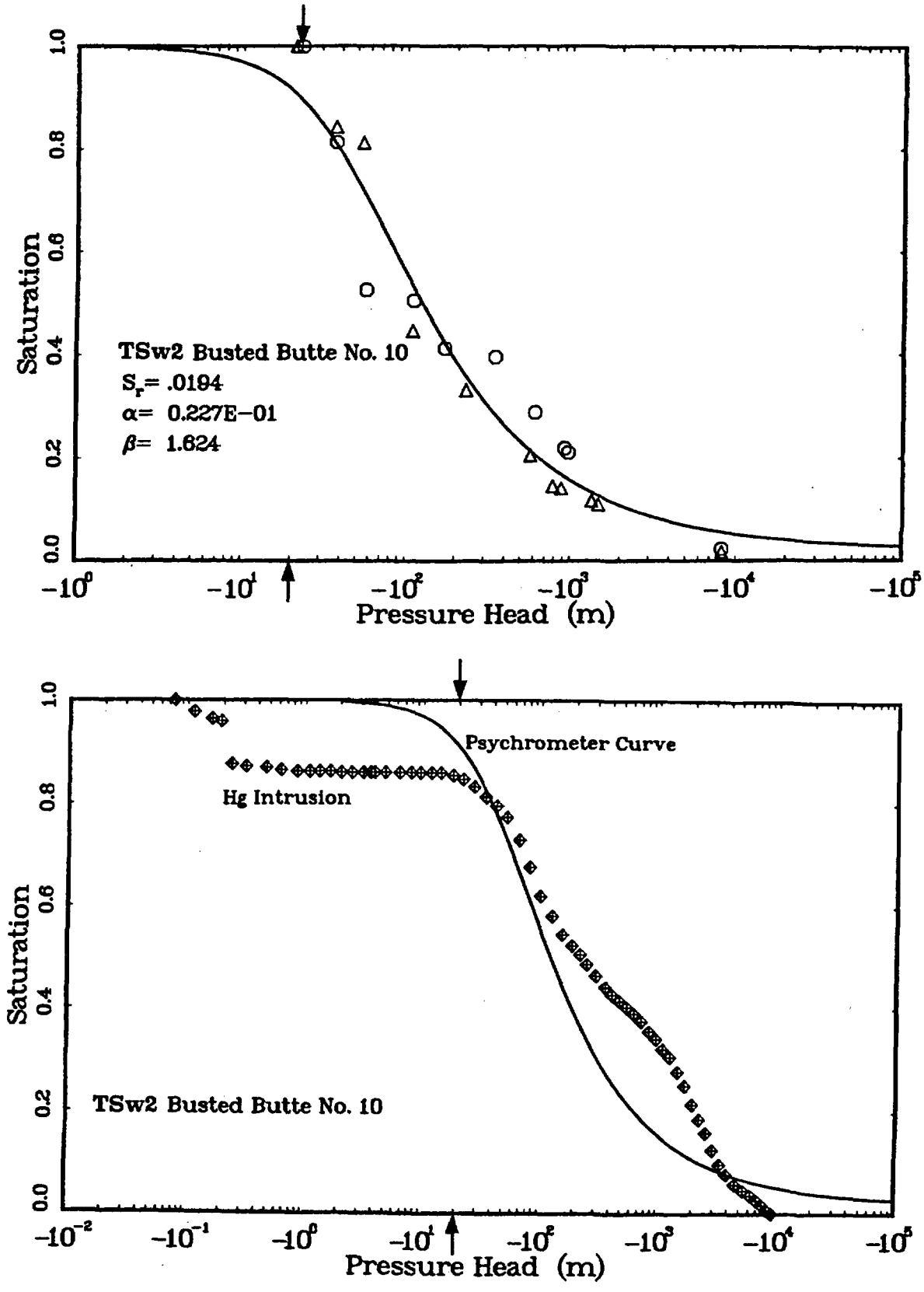

Figure B.32 Saturation as a Function of Pressure Head for Sample B.B. #10

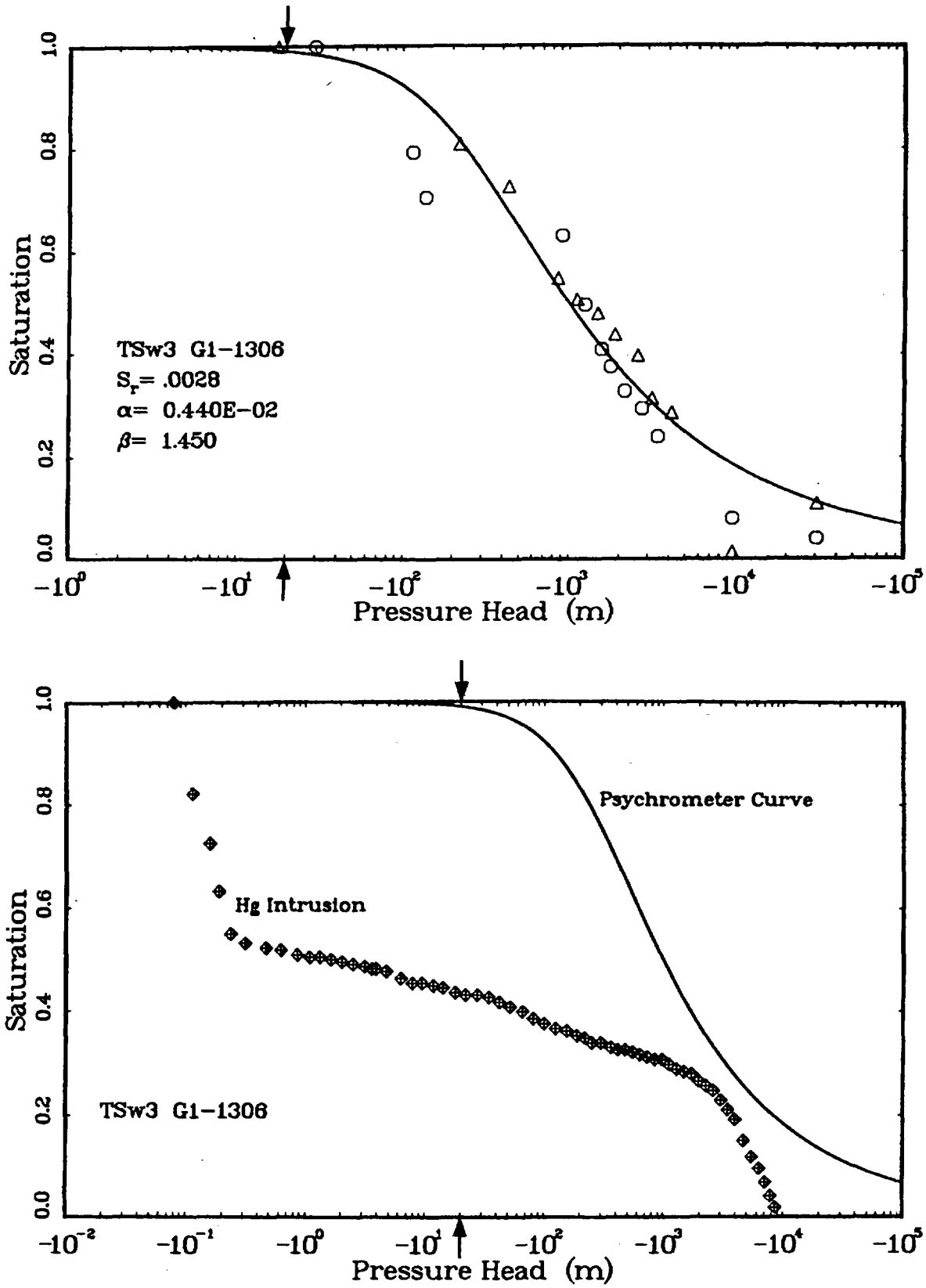

Figure B.33 Saturation as a Function of Pressure Head for Sample G1-1306

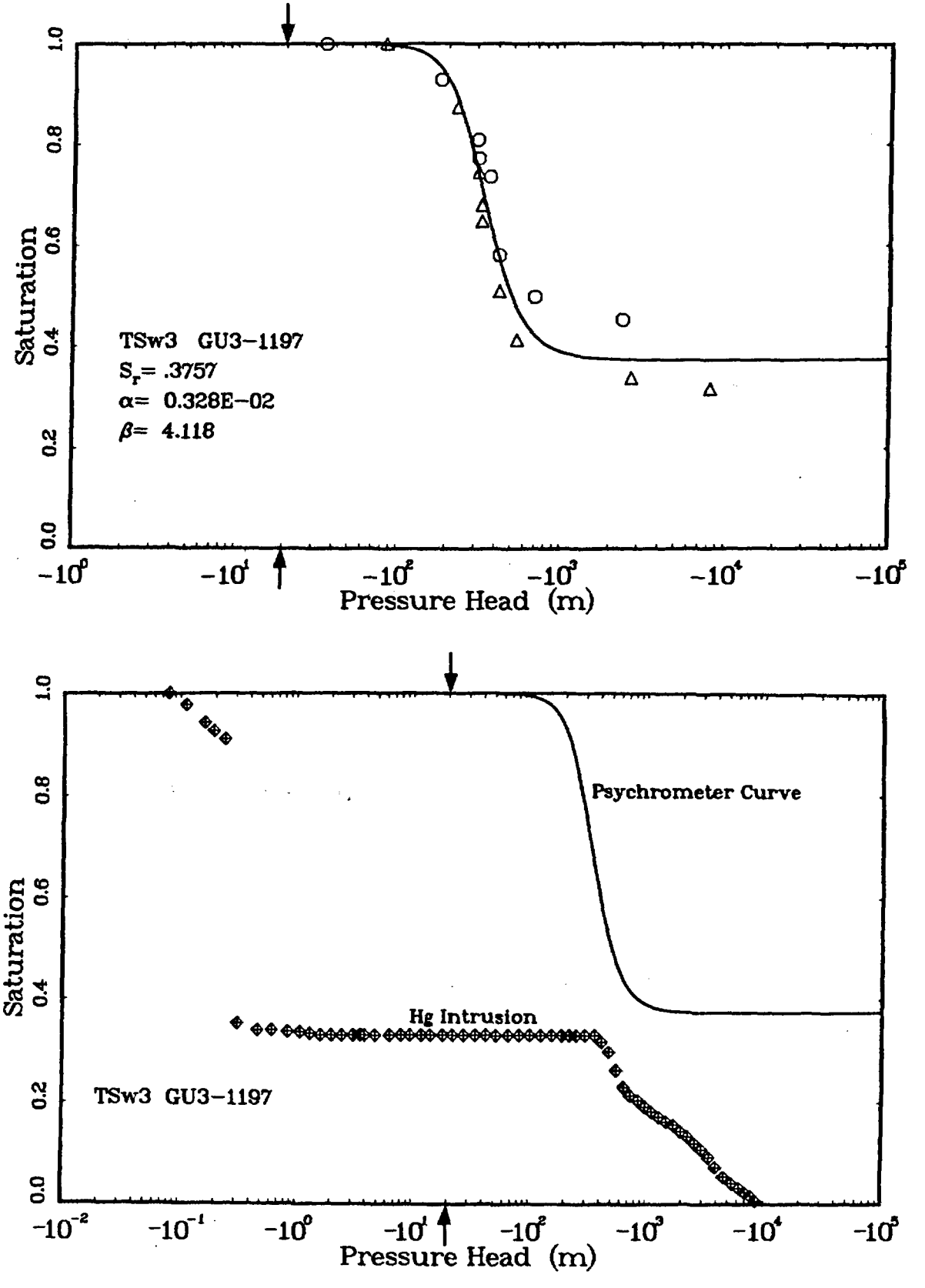

Figure B.34 Saturation as a Function of Pressure Head for Sample GU3-1197

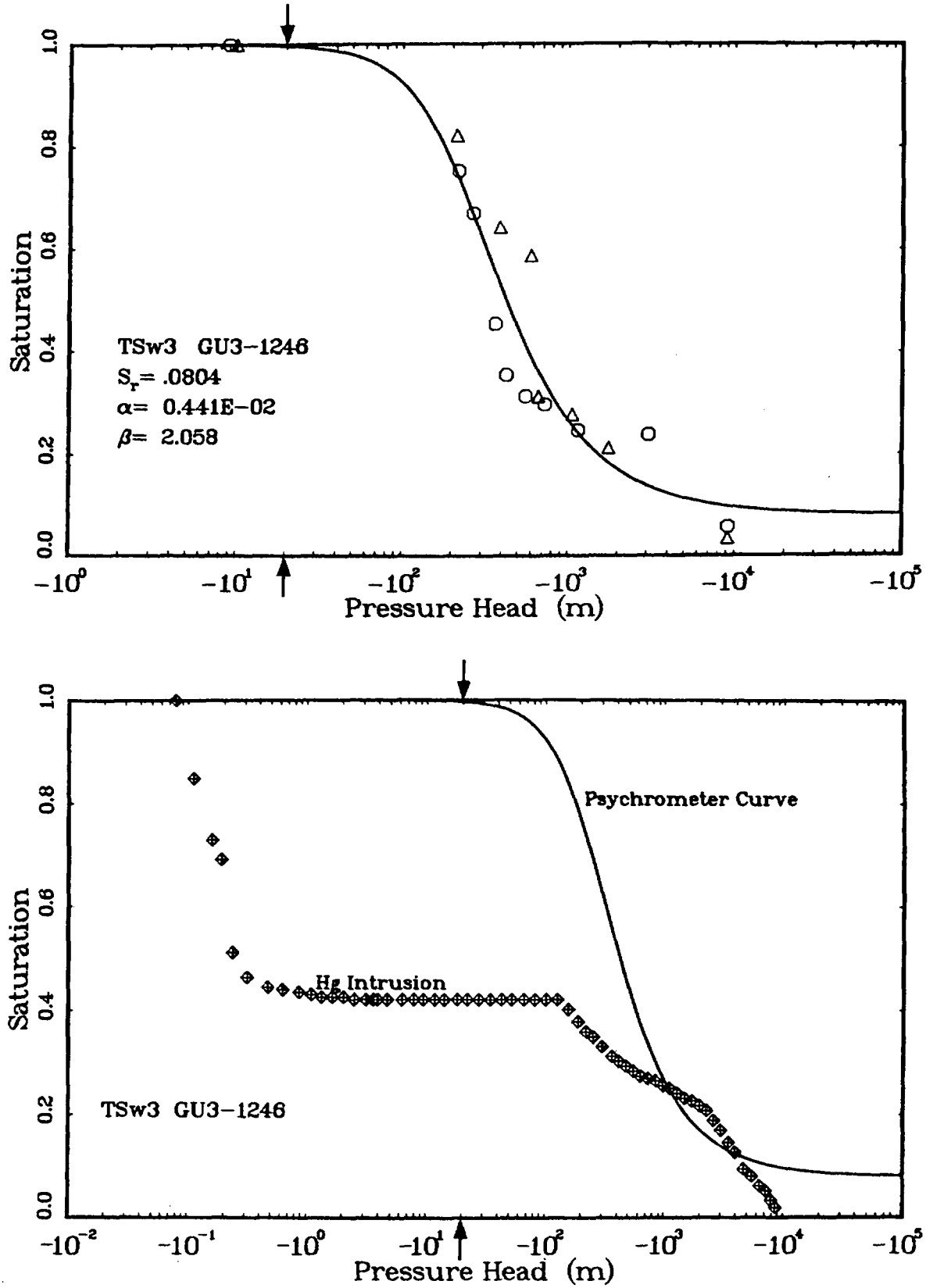

Figure B.35 Saturation as a Function of Pressure Head for Sample GU3-1246

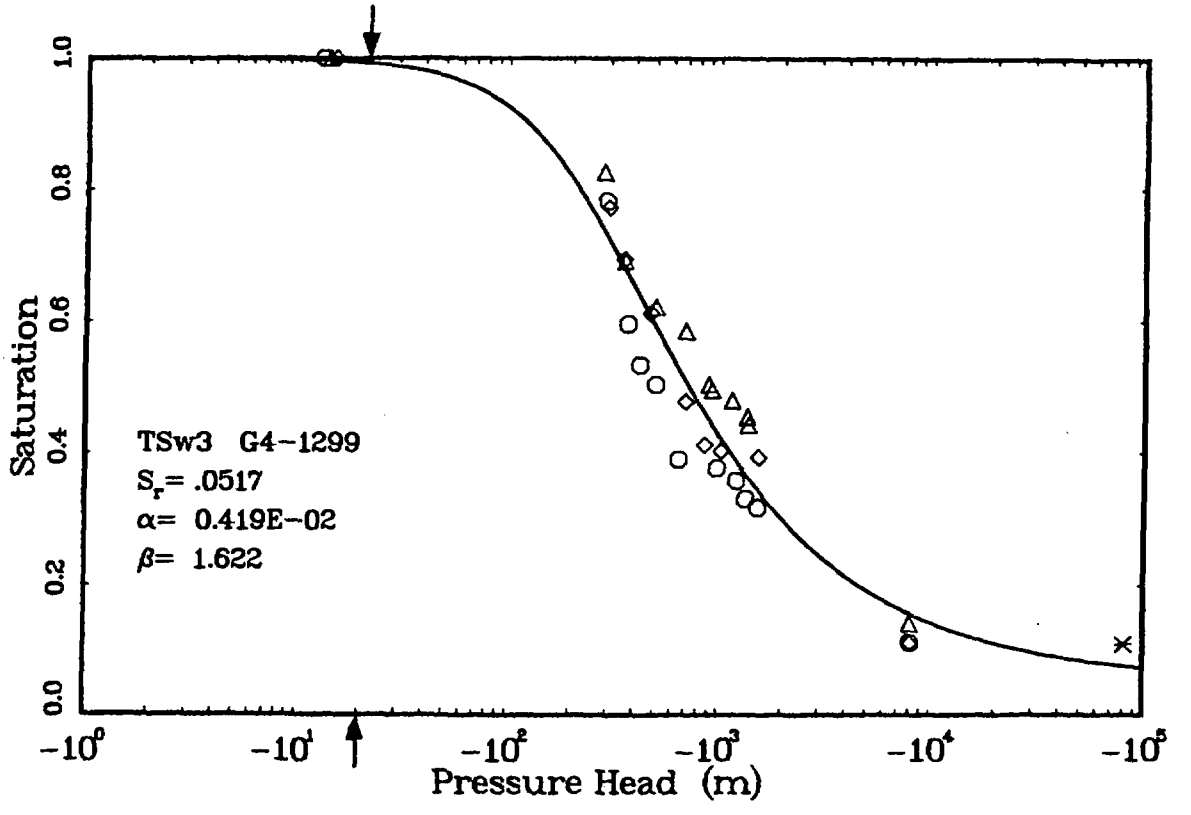

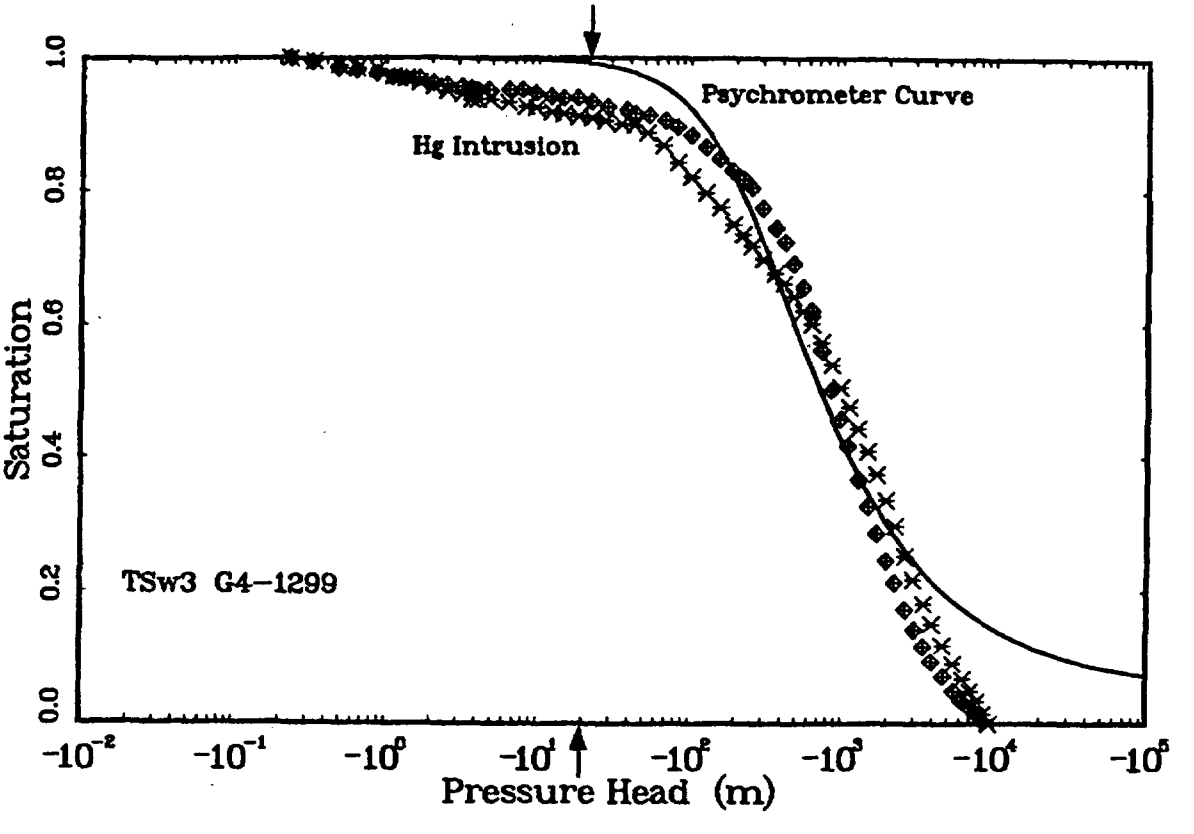

Figure B.36 Saturation as a Function of Pressure Head for Sample G4-1299

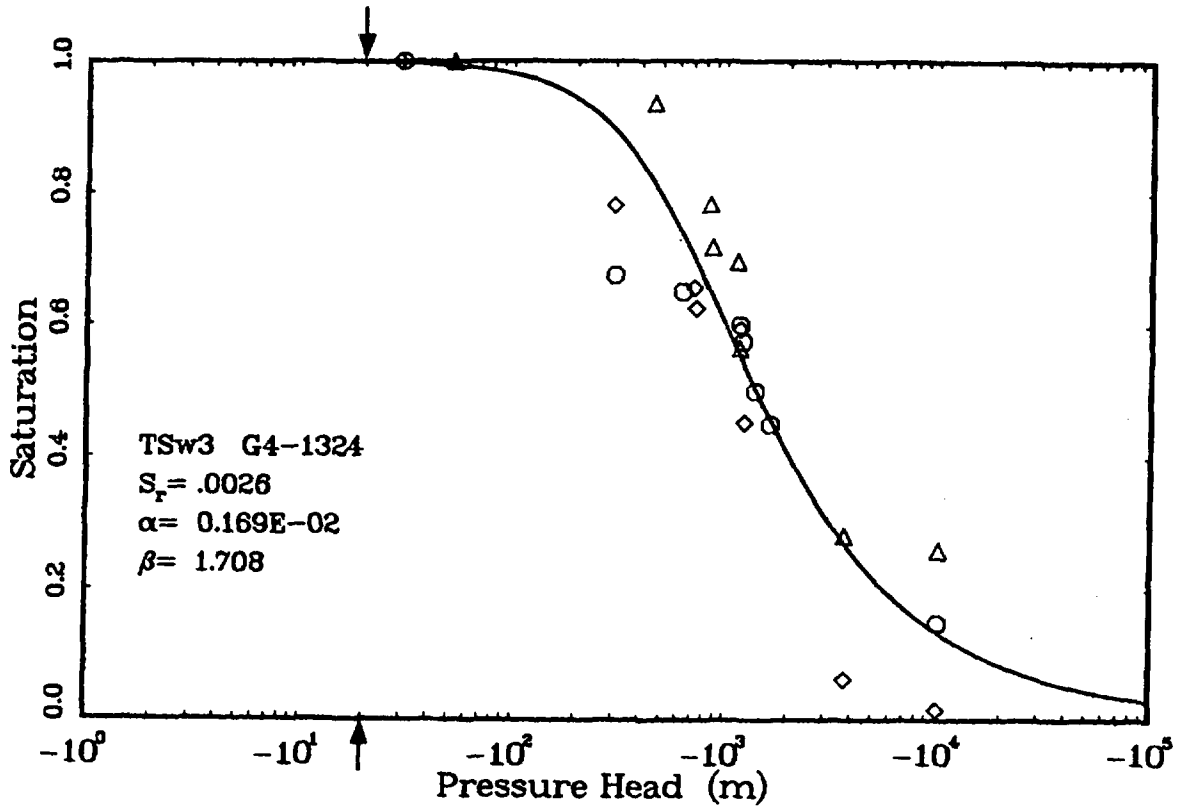

Figure B.37 Saturation as a Function of Pressure Head for Sample G4-1324 (Psychrometer Only)

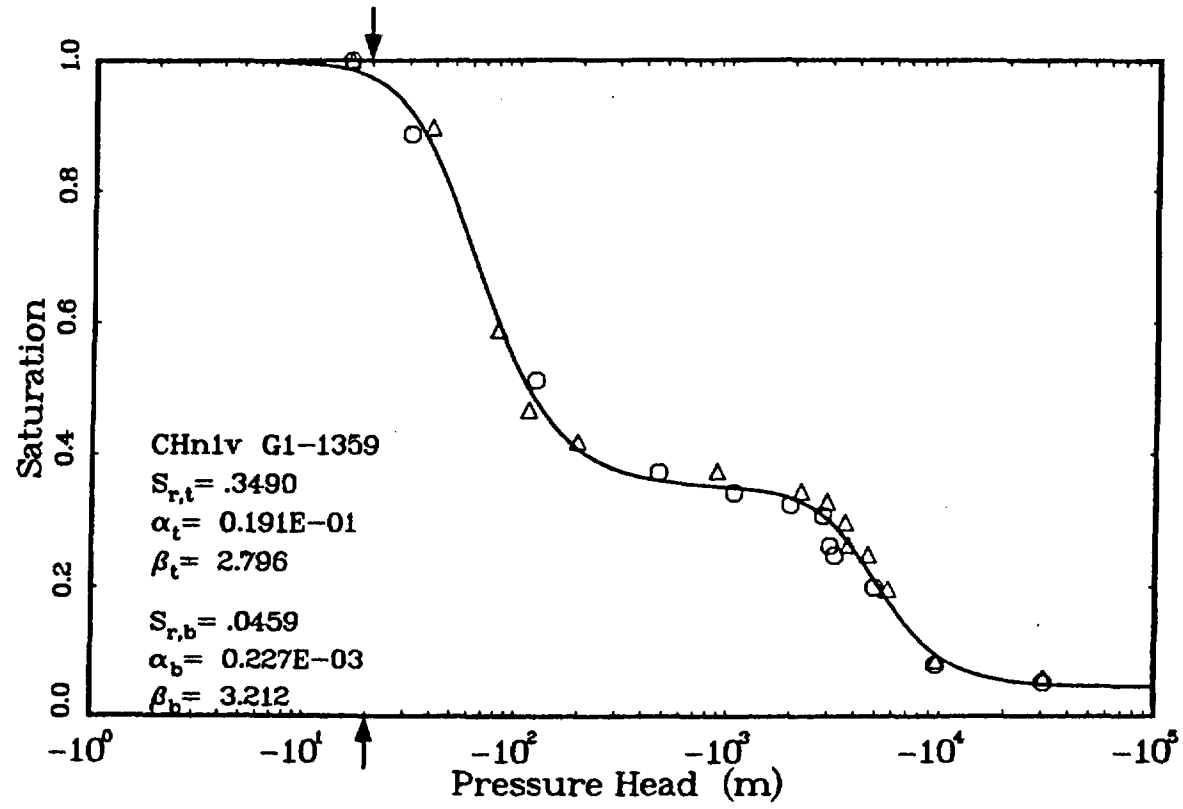

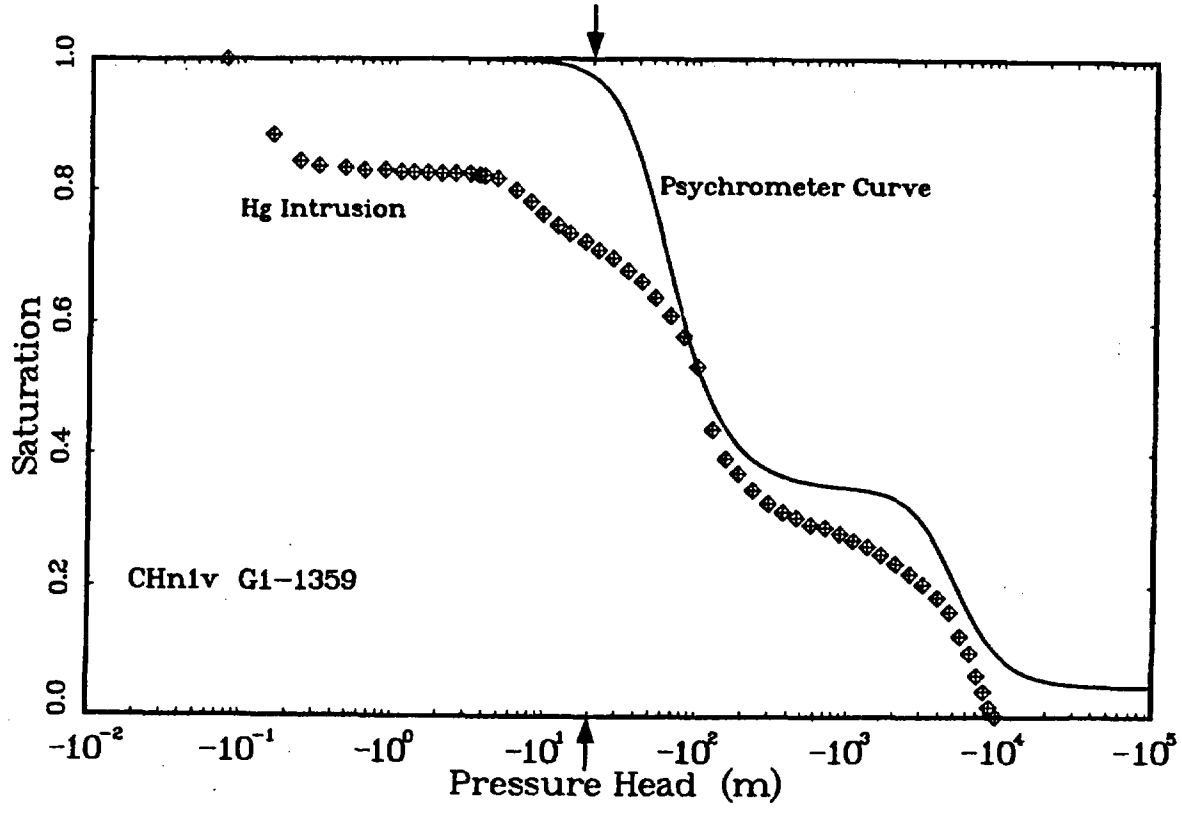

Figure B.38 Saturation as a Function of Pressure Head for Sample G1-1359

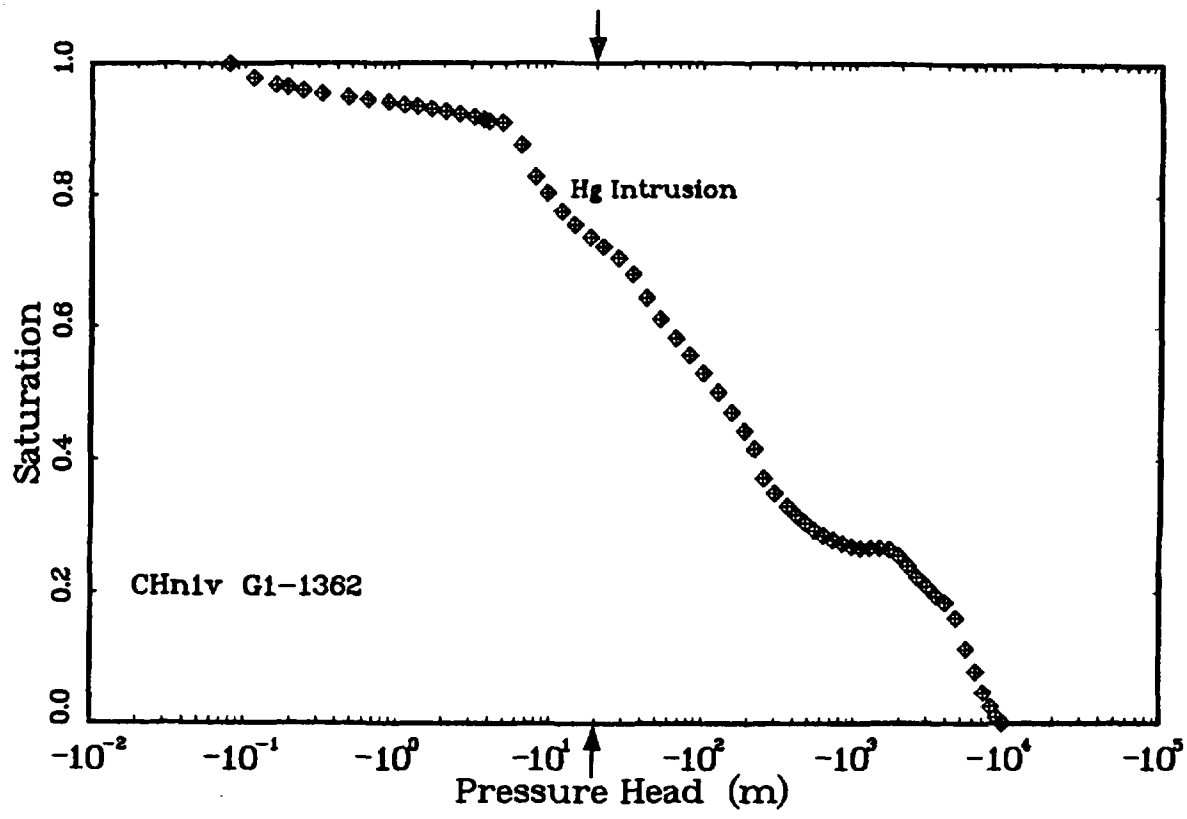

Figure B.39 Saturation as a Function of Pressure Head for Sample G1-1362 (Mercury Intrusion Only)

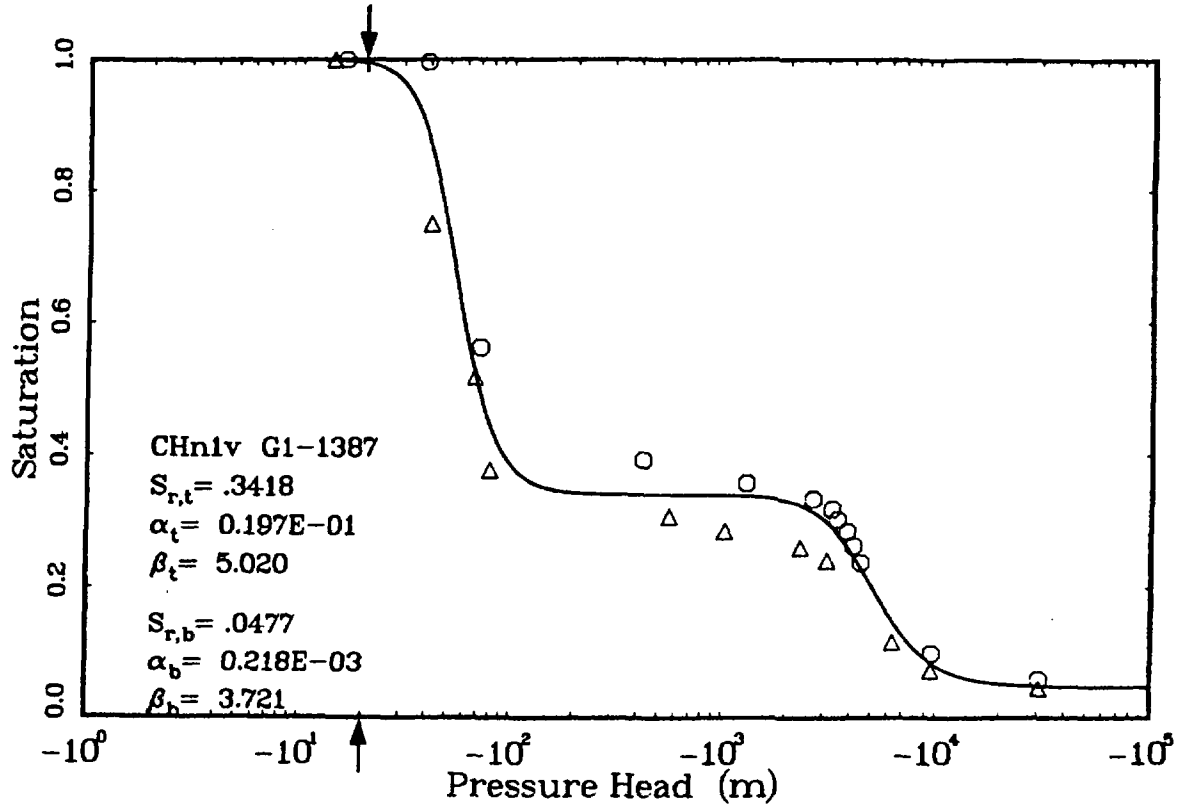

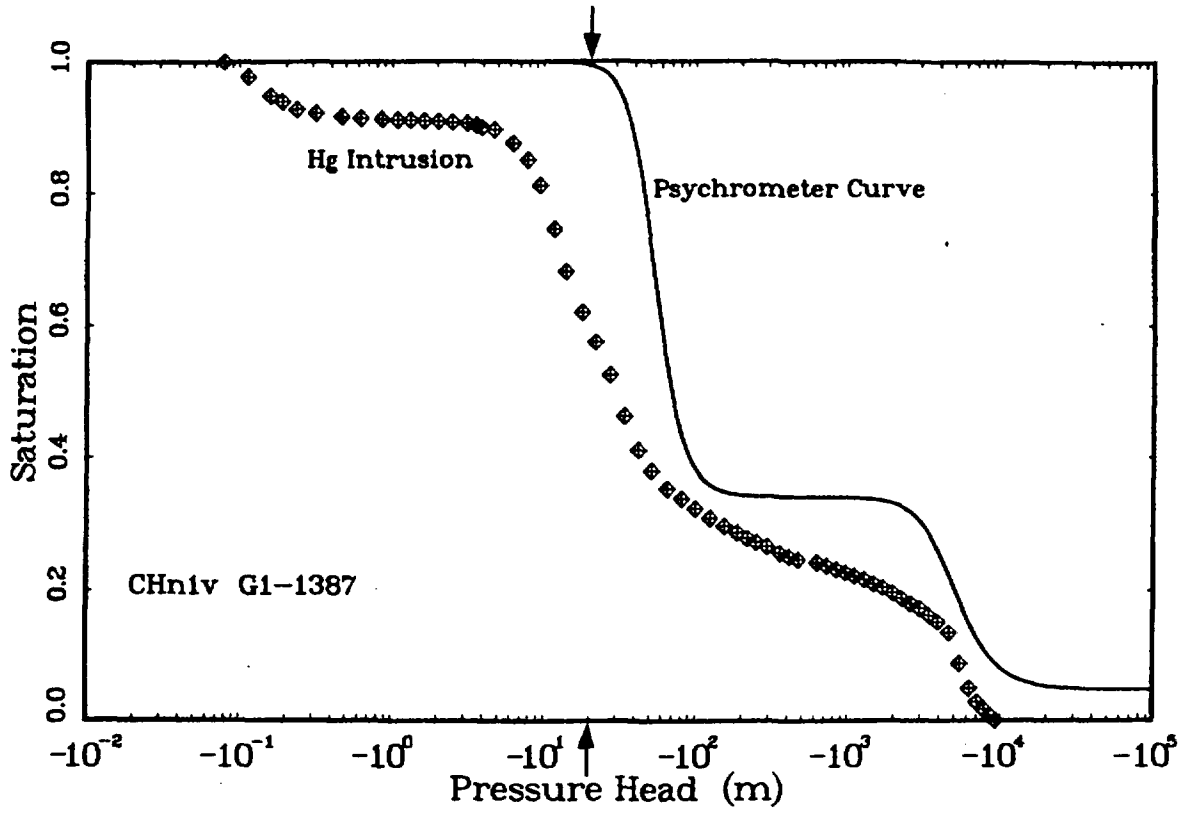

Figure B.40 Saturation as a Function of Pressure Head for Sample G1-1387

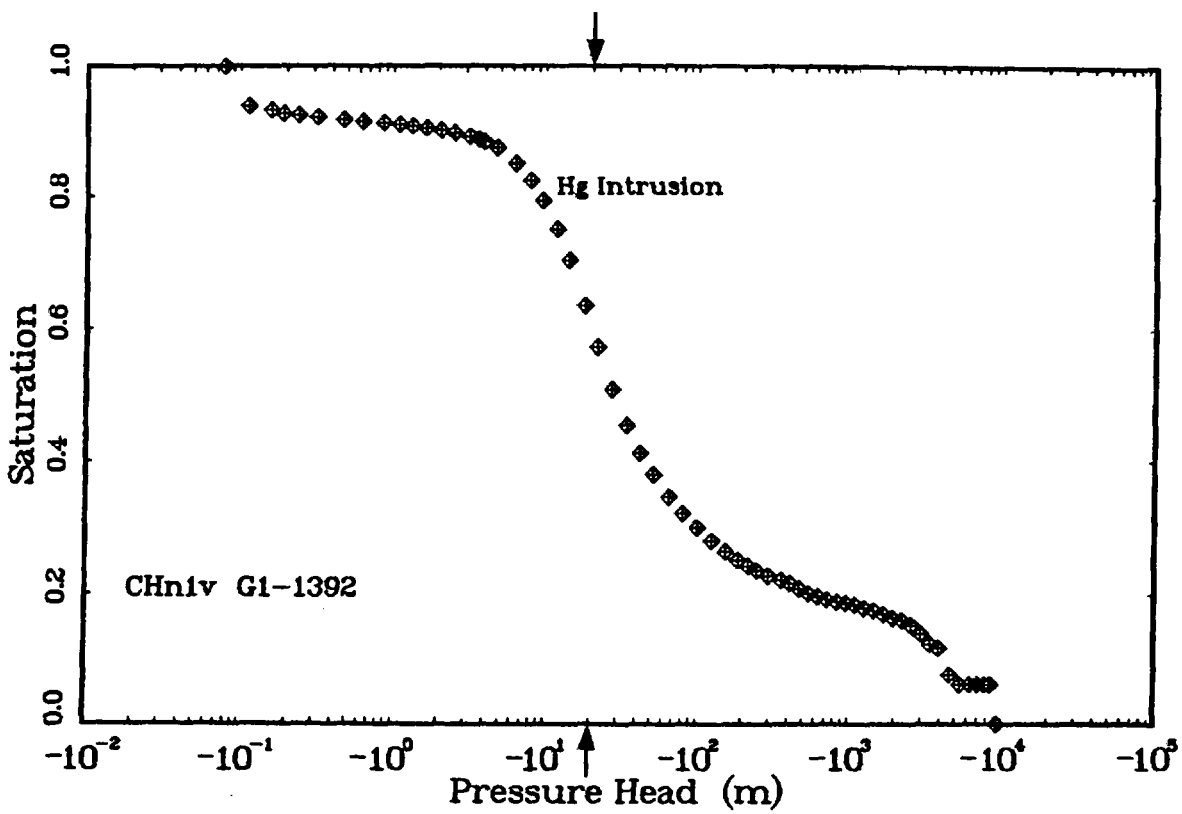

Figure B.41 Saturation as a Function of Pressure Head for Sample G1-1392 (Mercury Intrusion Only)

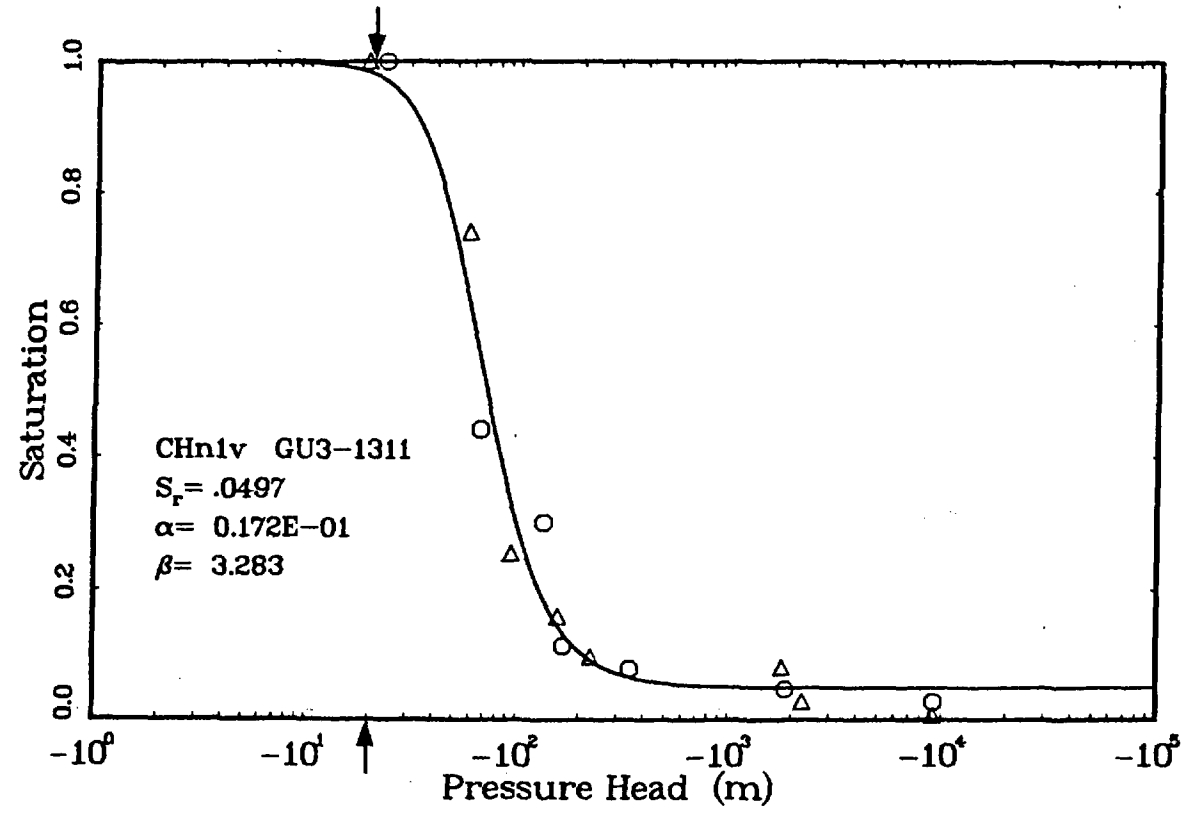

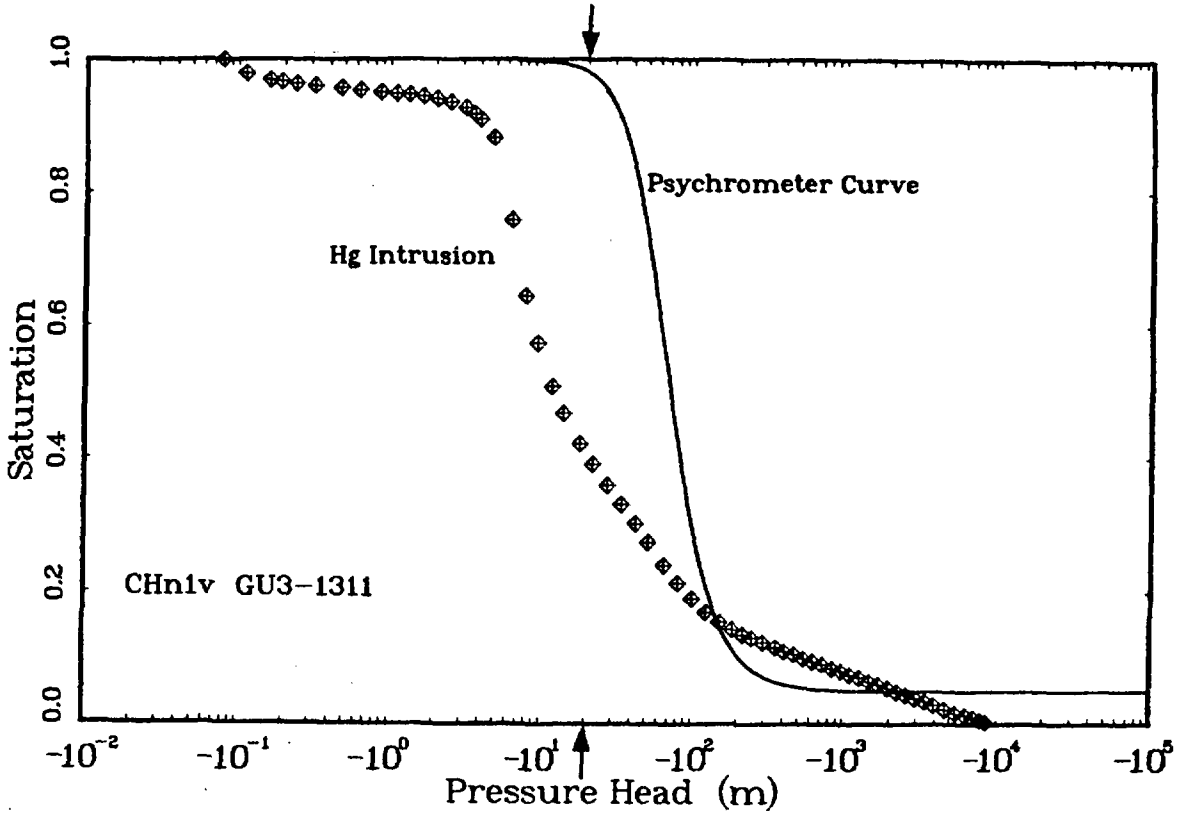

Figure B.42 Saturation as a Function of Pressure Head for Sample GU3-1311

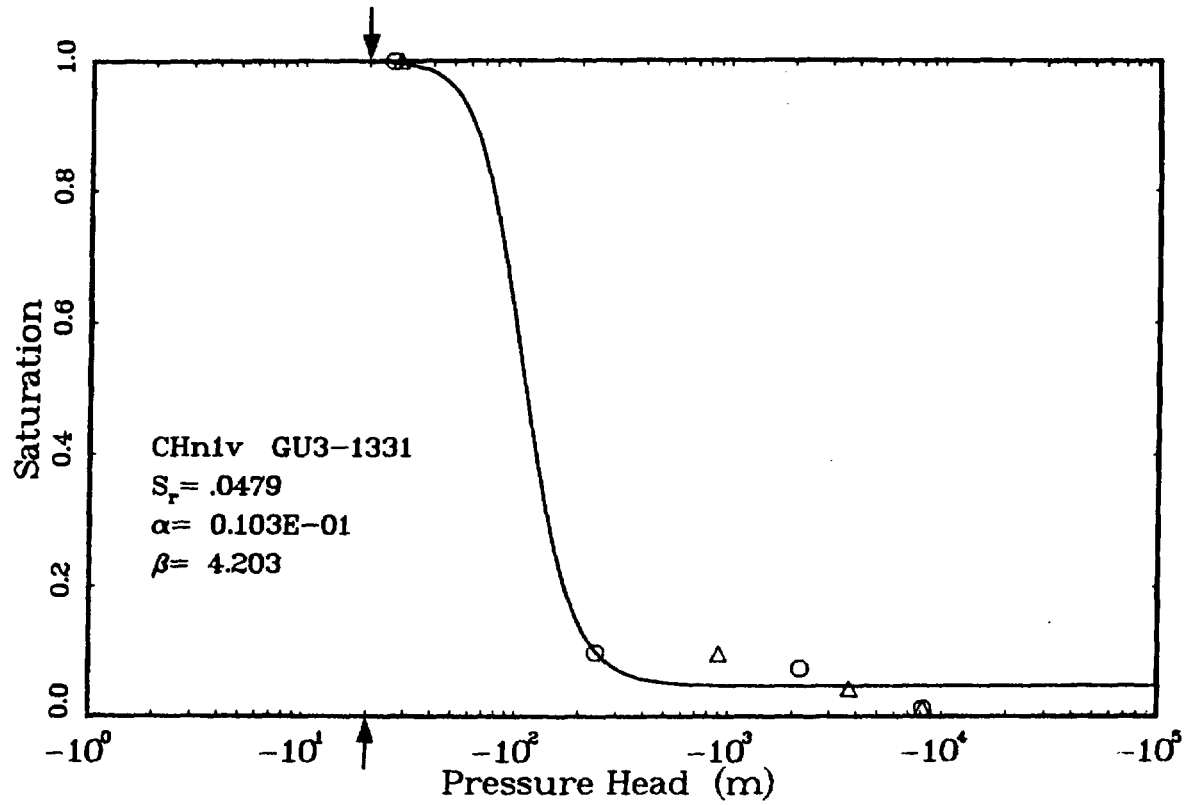

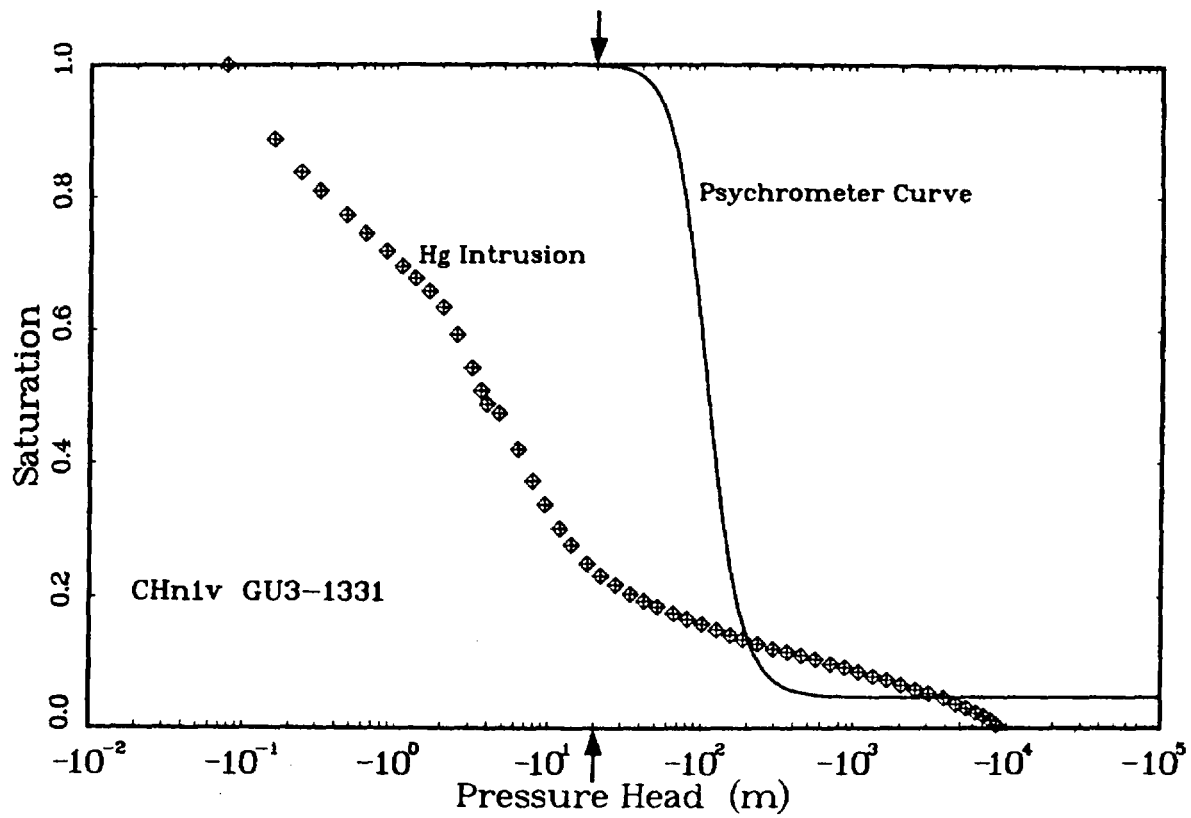

Figure B.43 Saturation as a Function of Pressure Head for Sample GU3-1331

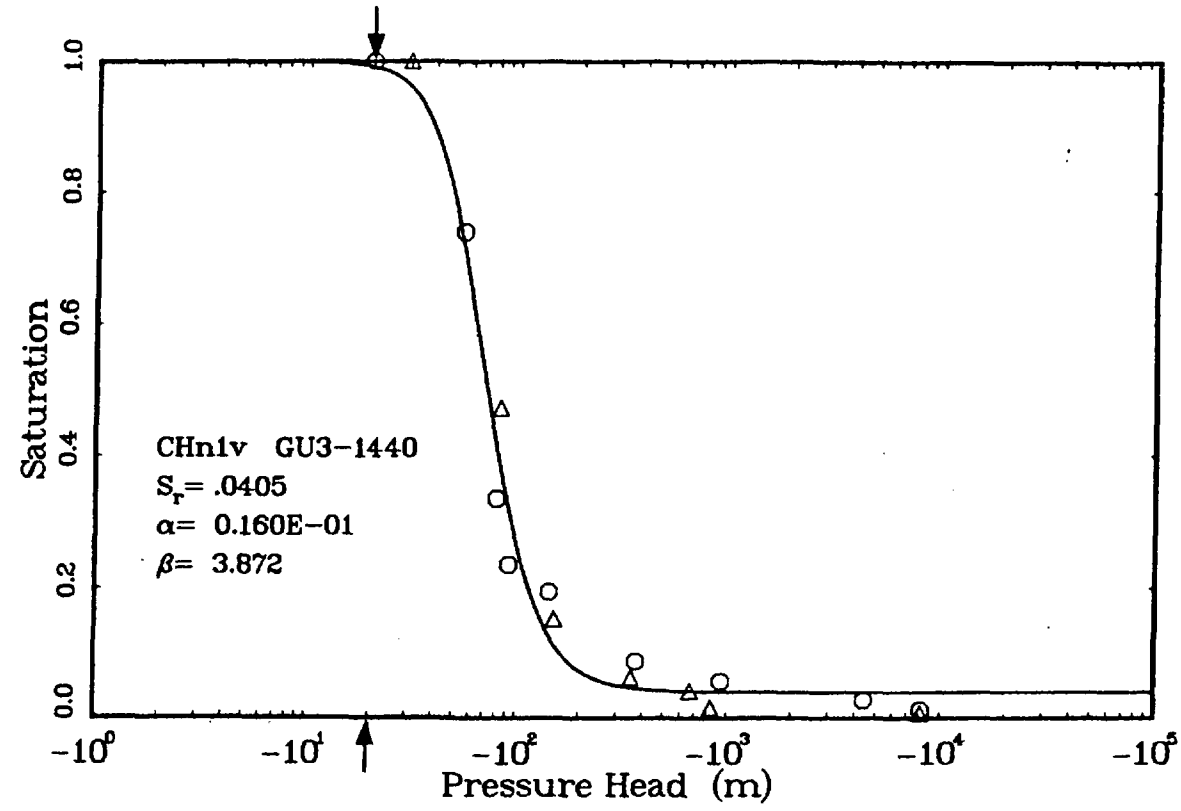

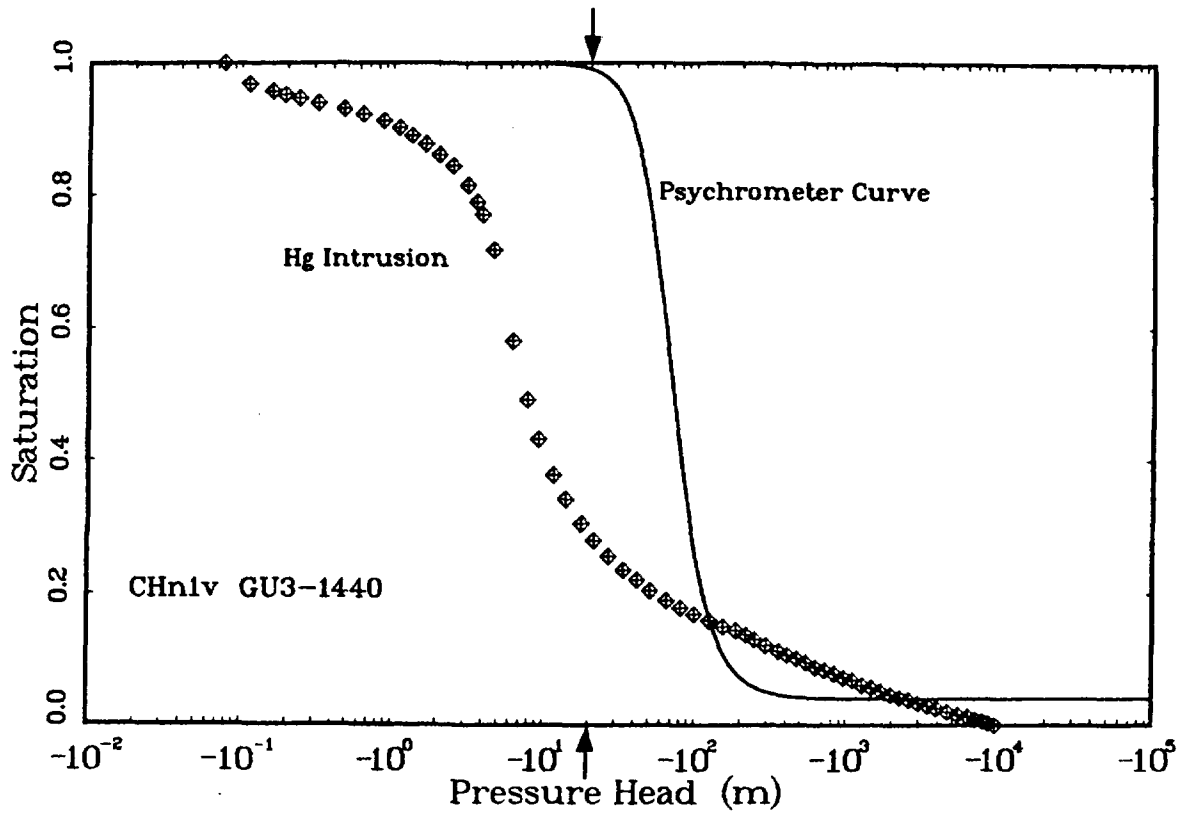

Figure B.44 Saturation as a Function of Pressure Head for Sample GU3-1440

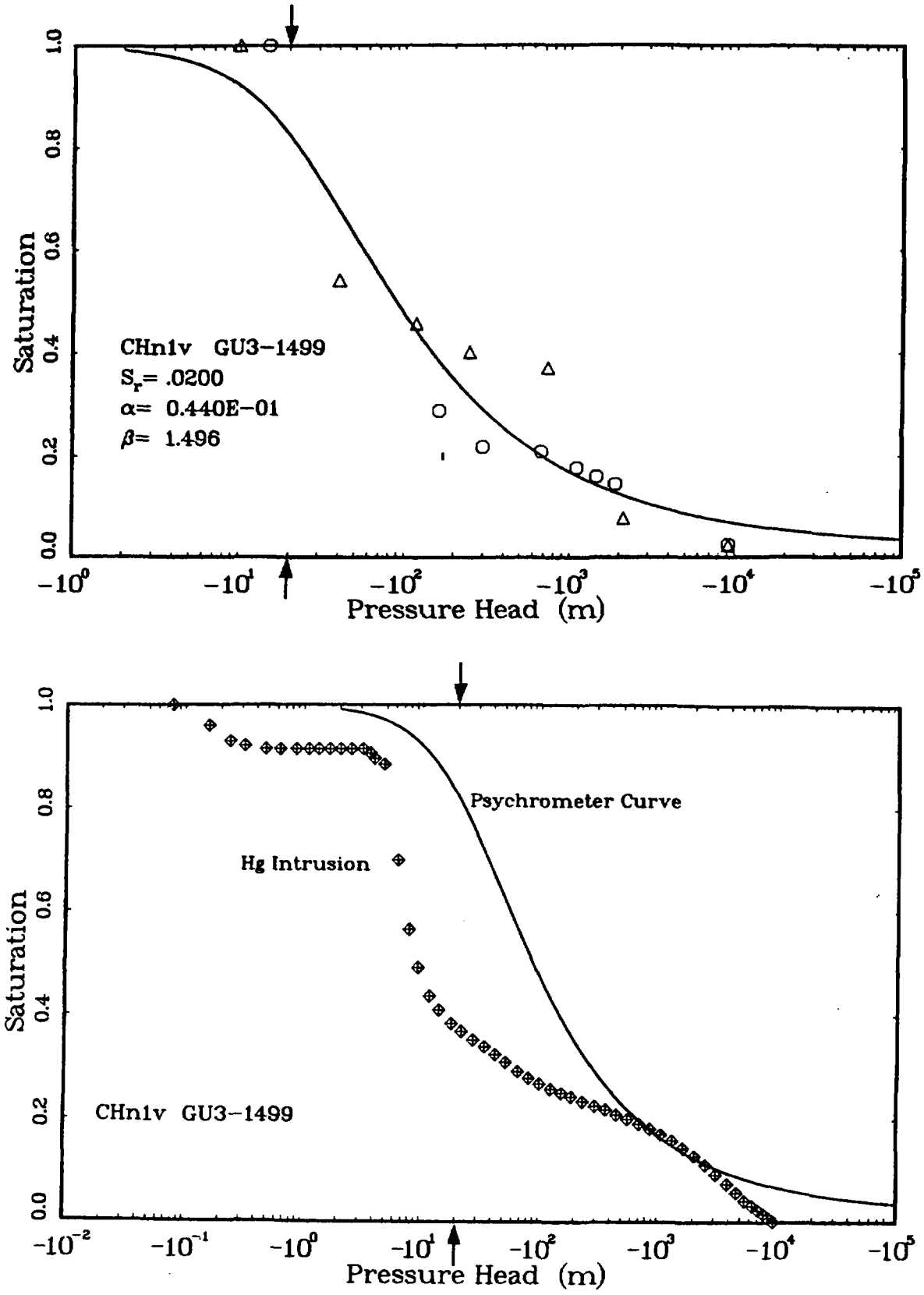

Figure B.45 Saturation as a Function of Pressure Head for Sample GU3-1499

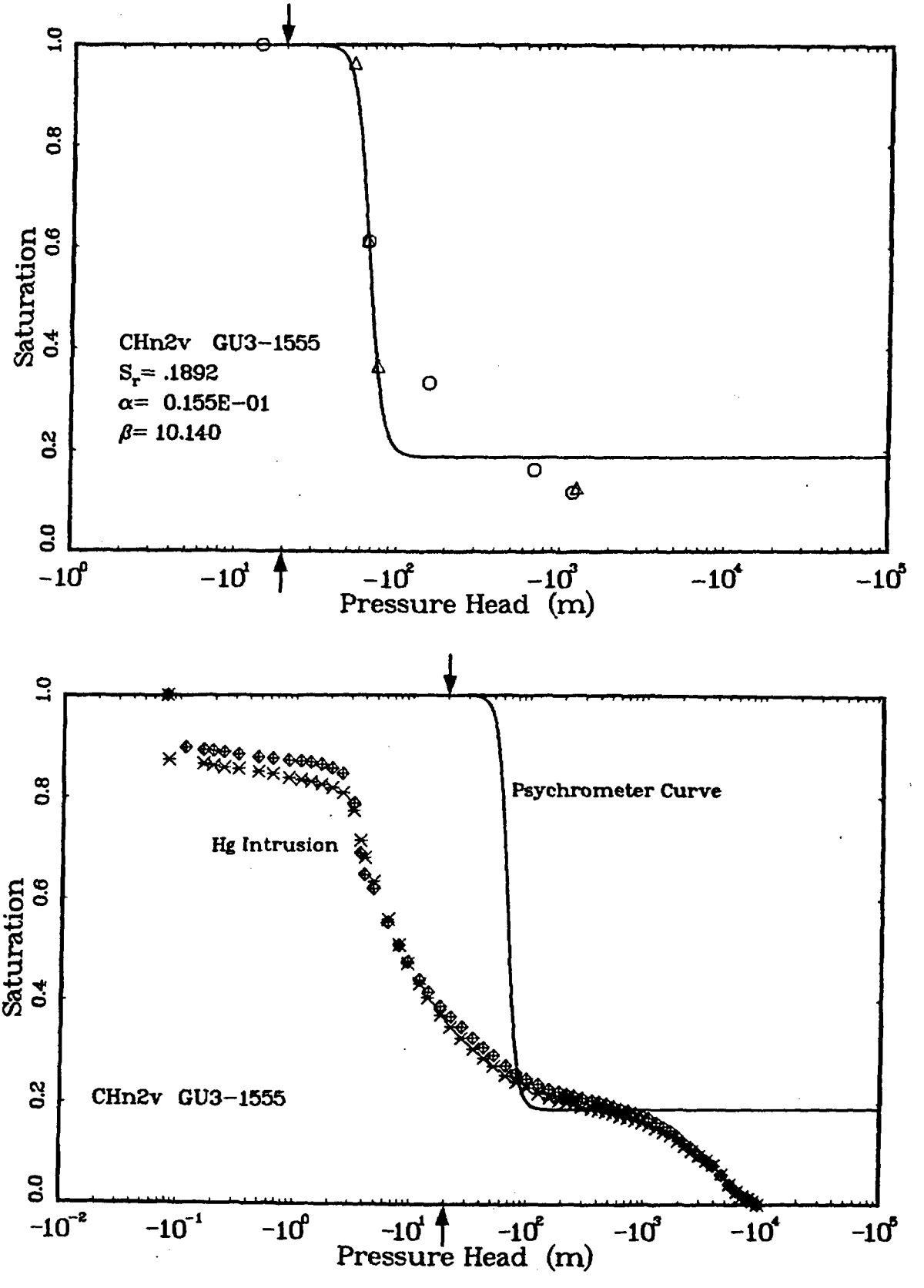

Figure B.46 Saturation as a Function of Pressure Head for Sample GU3-1555

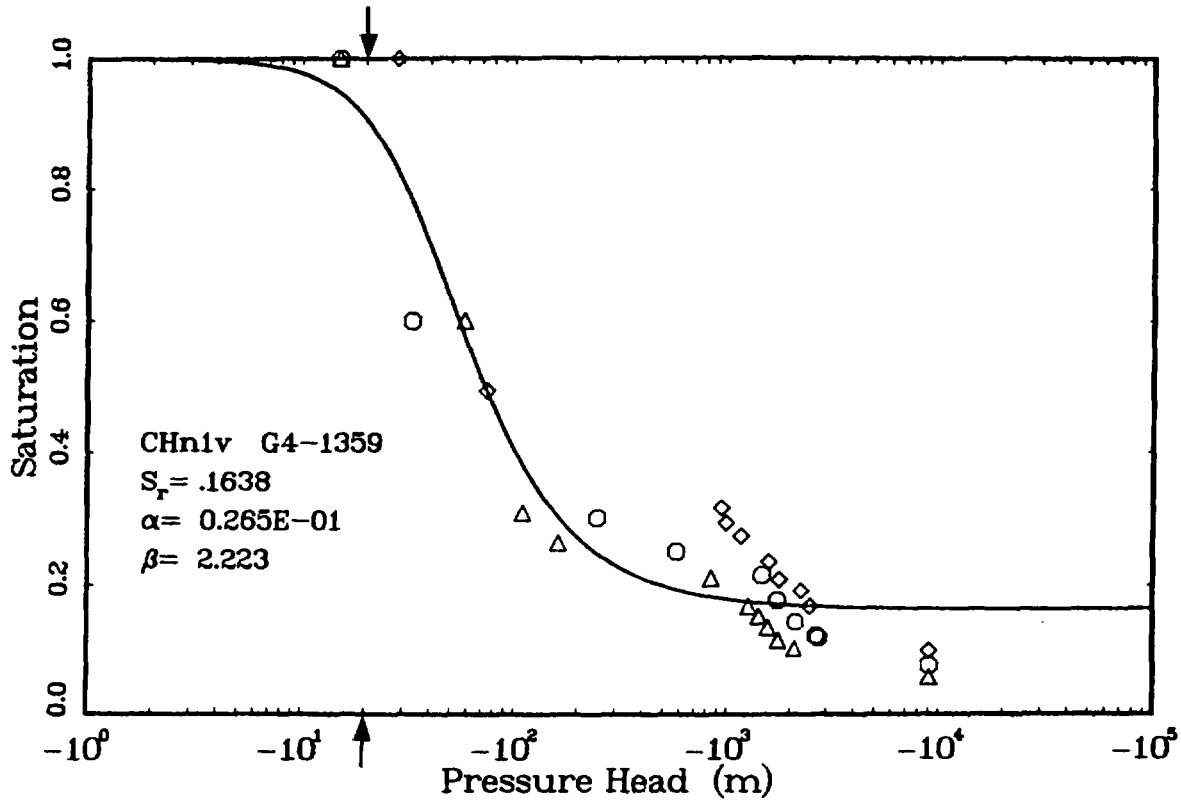

Figure B.47 Saturation as a Function of Pressure Head for Sample G4-1359 (Psychrometer Only)

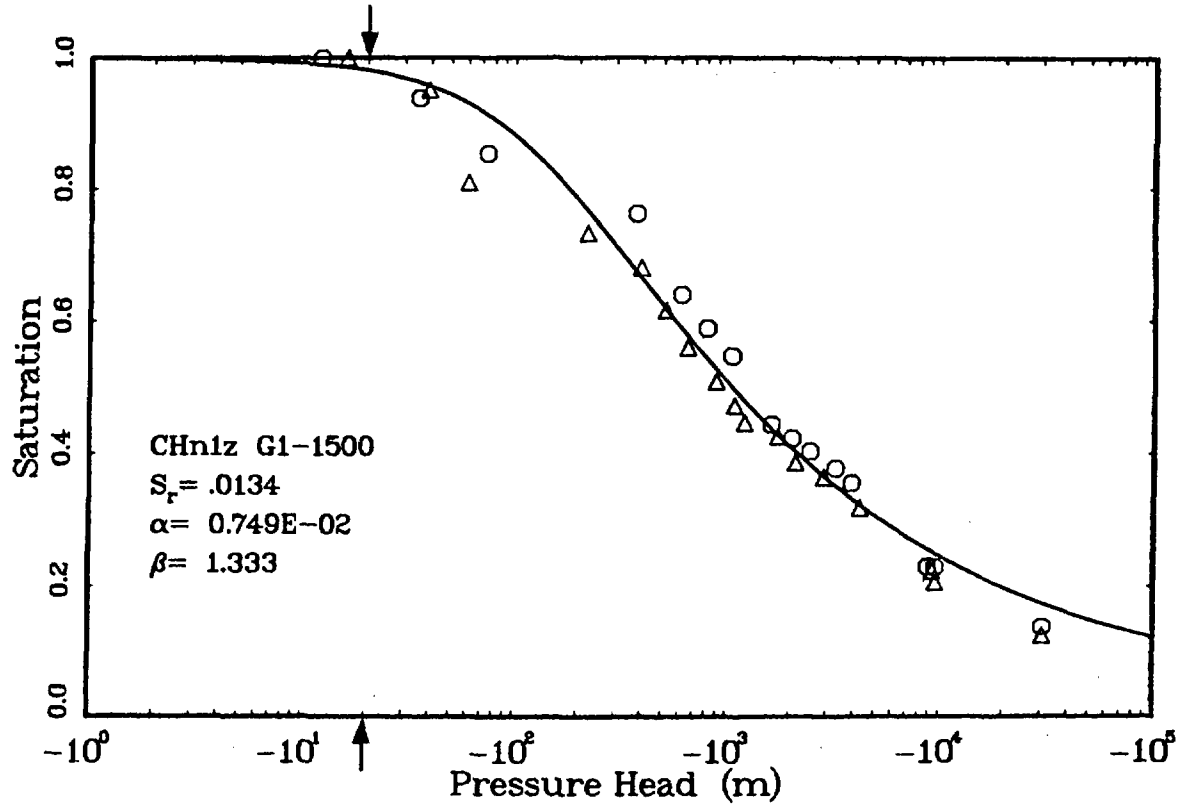

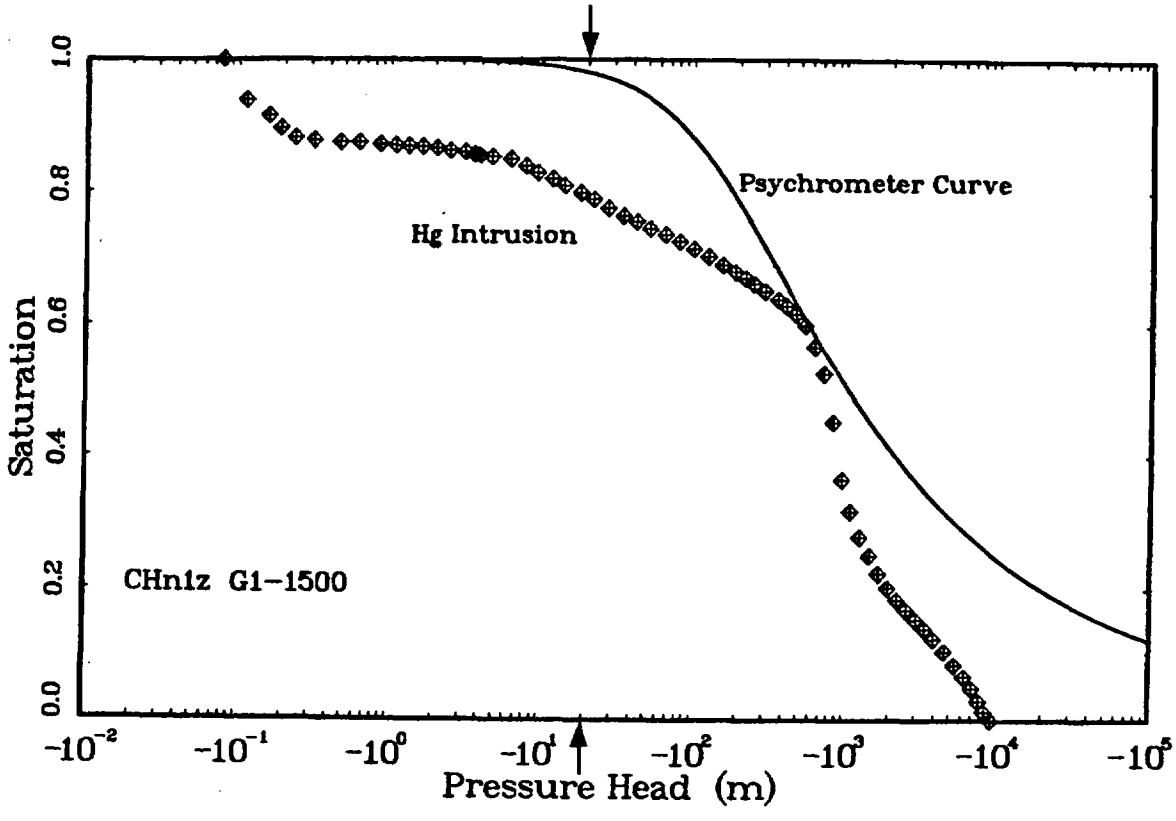

Figure B.48 Saturation as a Function of Pressure Head for Sample G1-1500

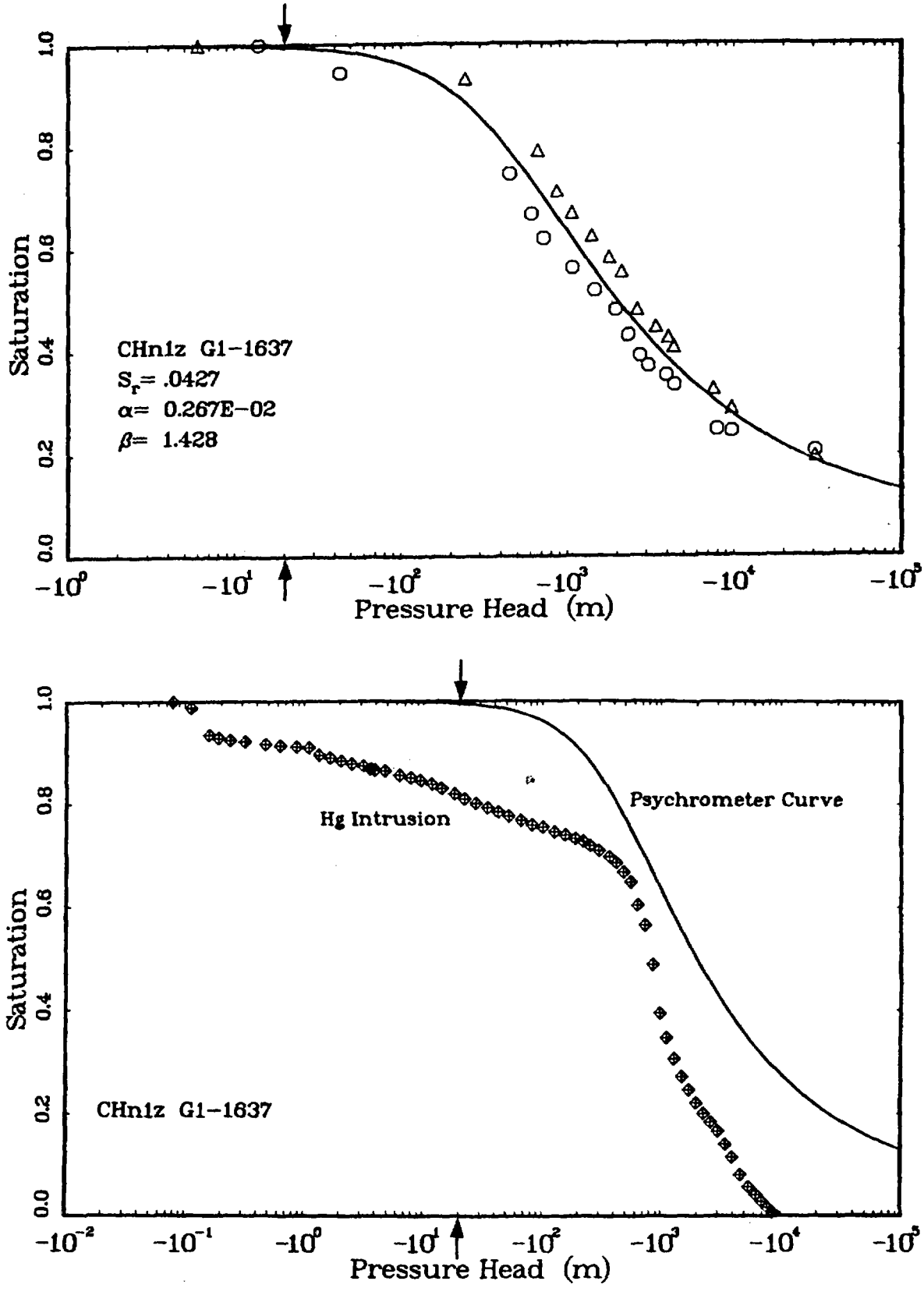

Figure B.49 Saturation as a Function of Pressure Head for Sample G1-1637

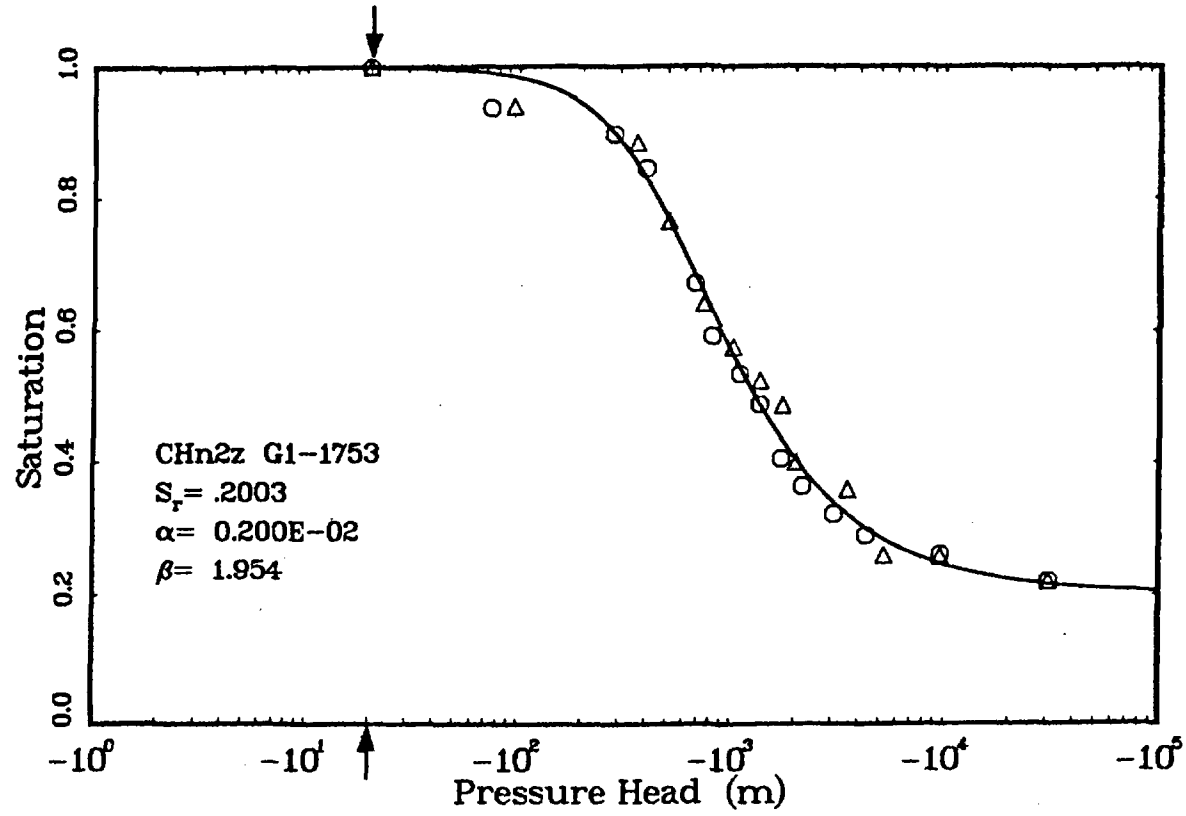

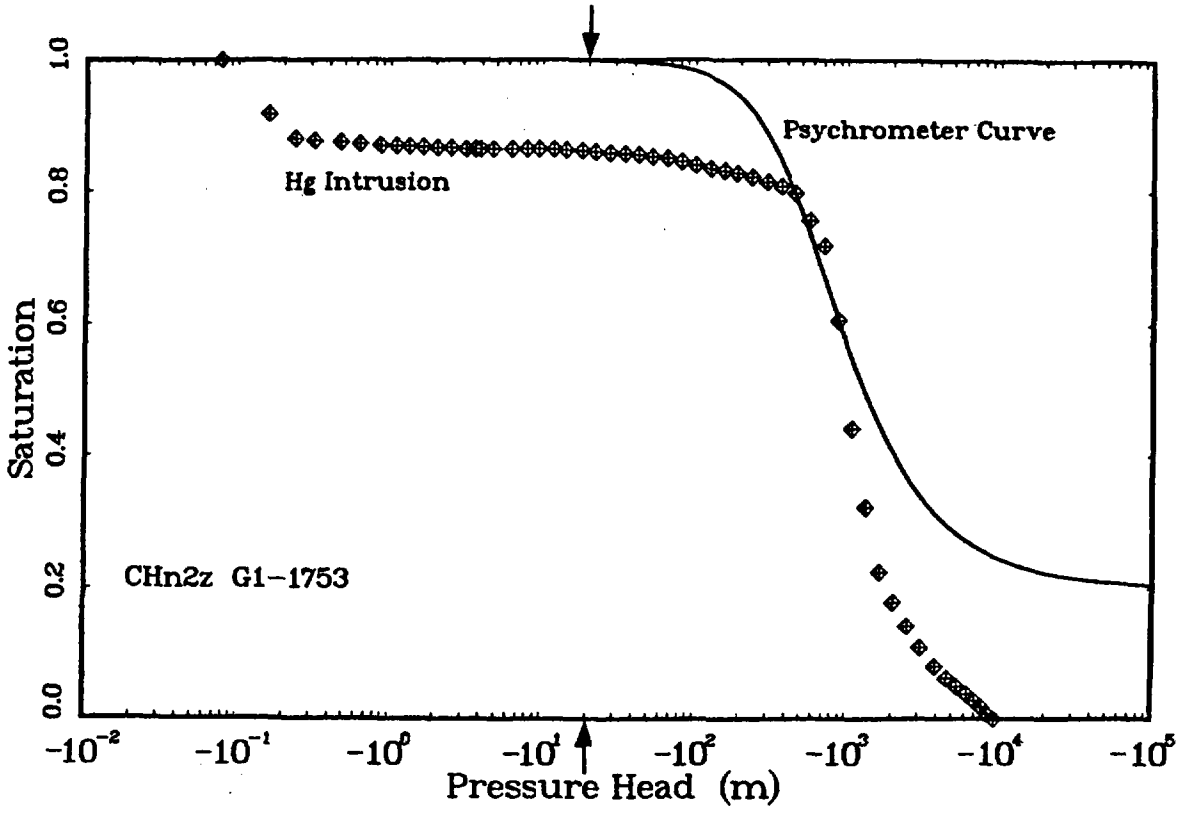

Figure B.50 Saturation as a Function of Pressure Head for Sample G1-1753

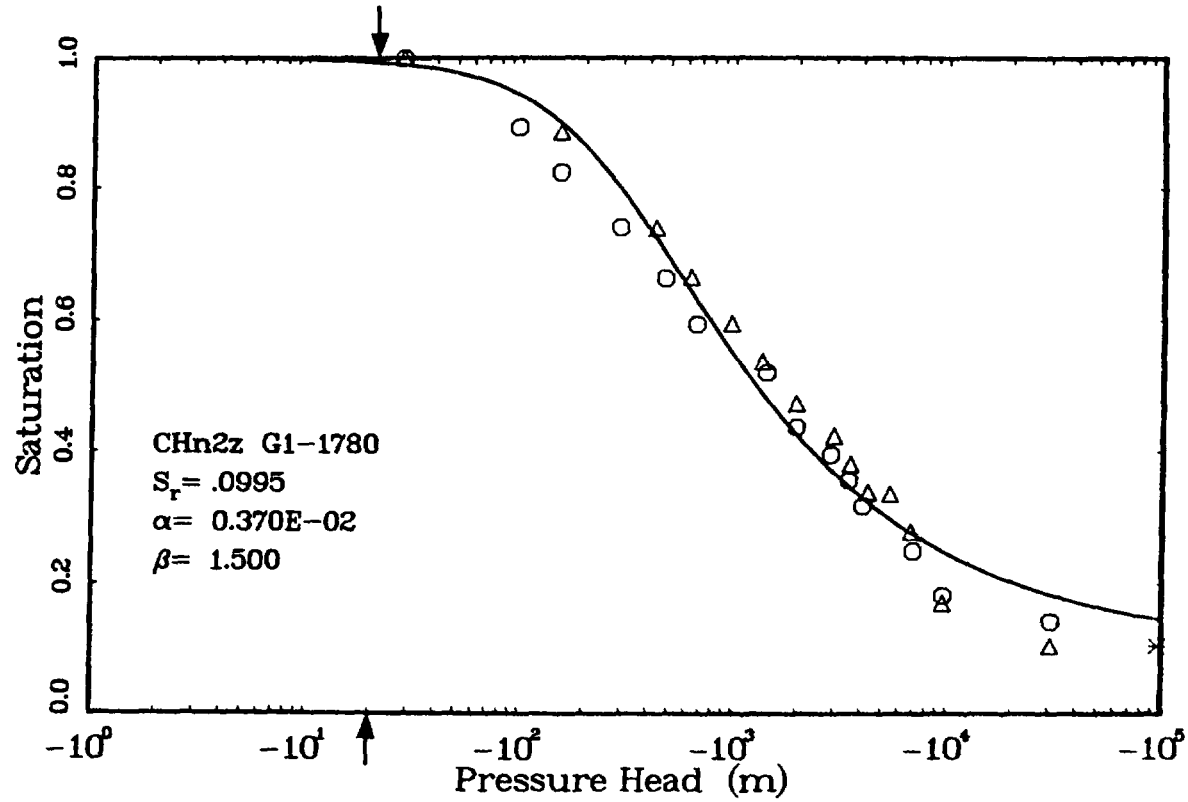

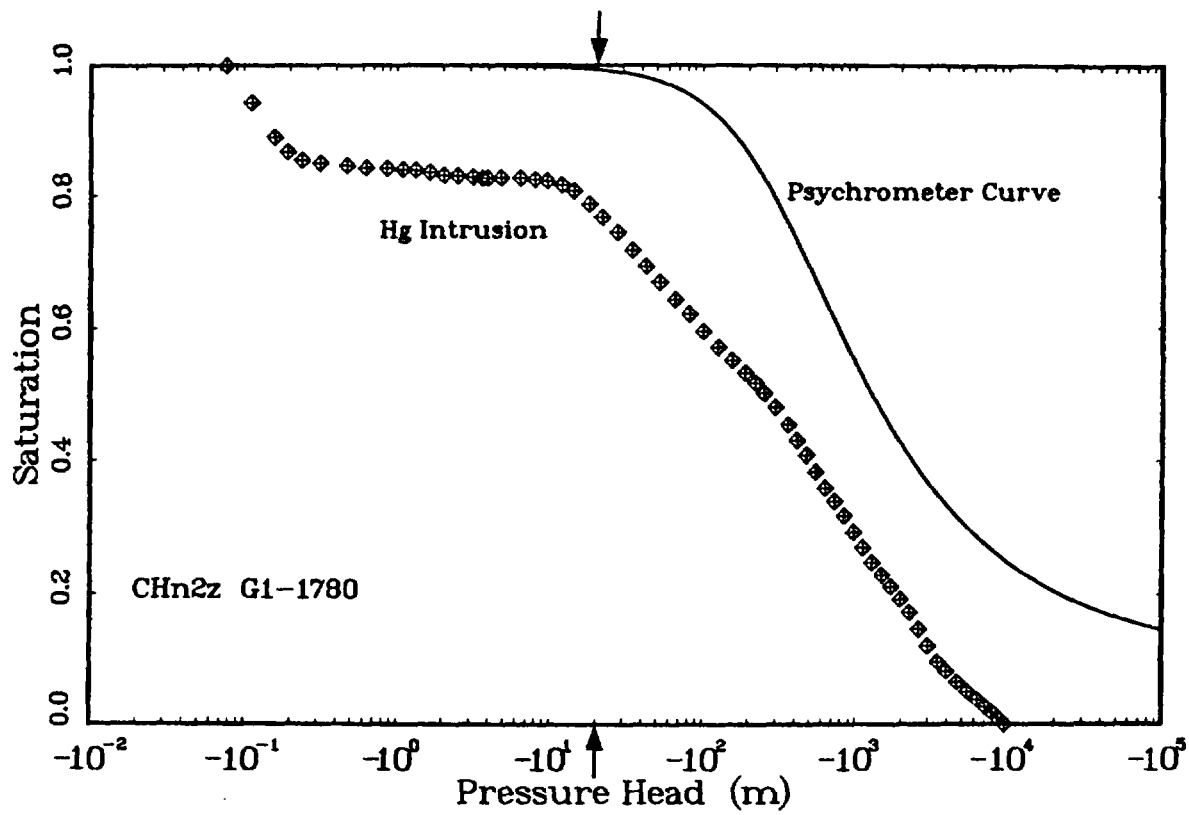

Figure B.51 Saturation as a Function of Pressure Head for Sample G1-1780

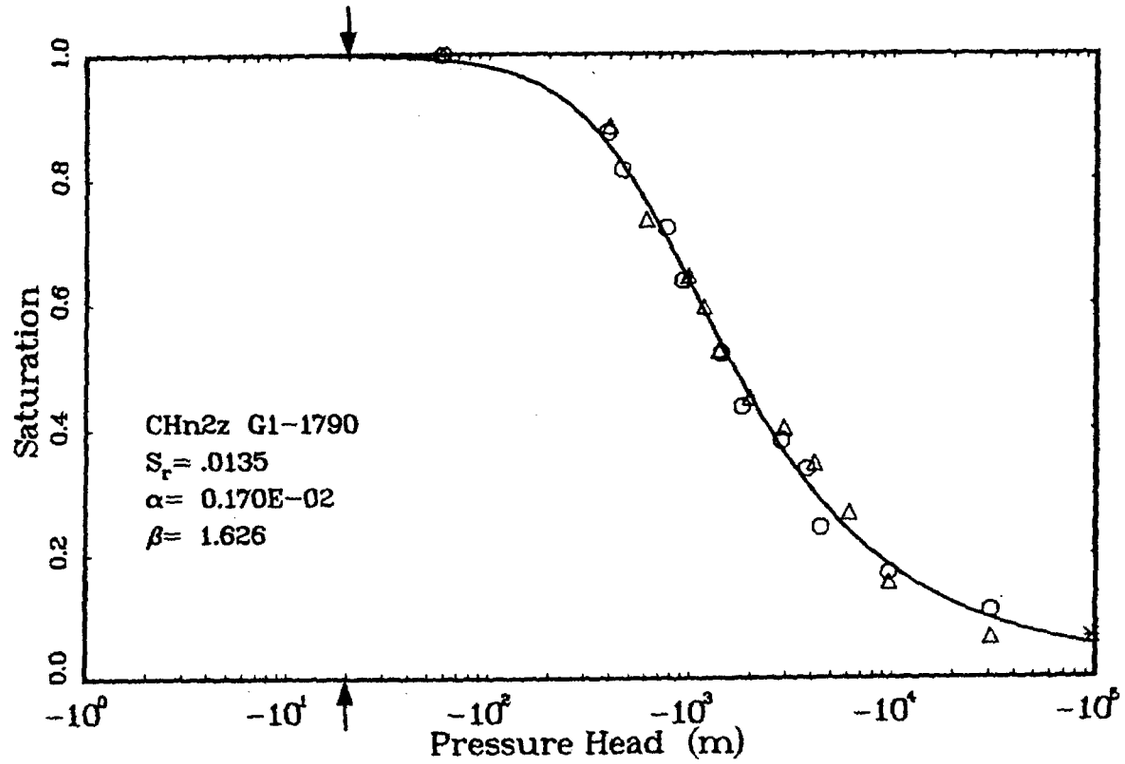

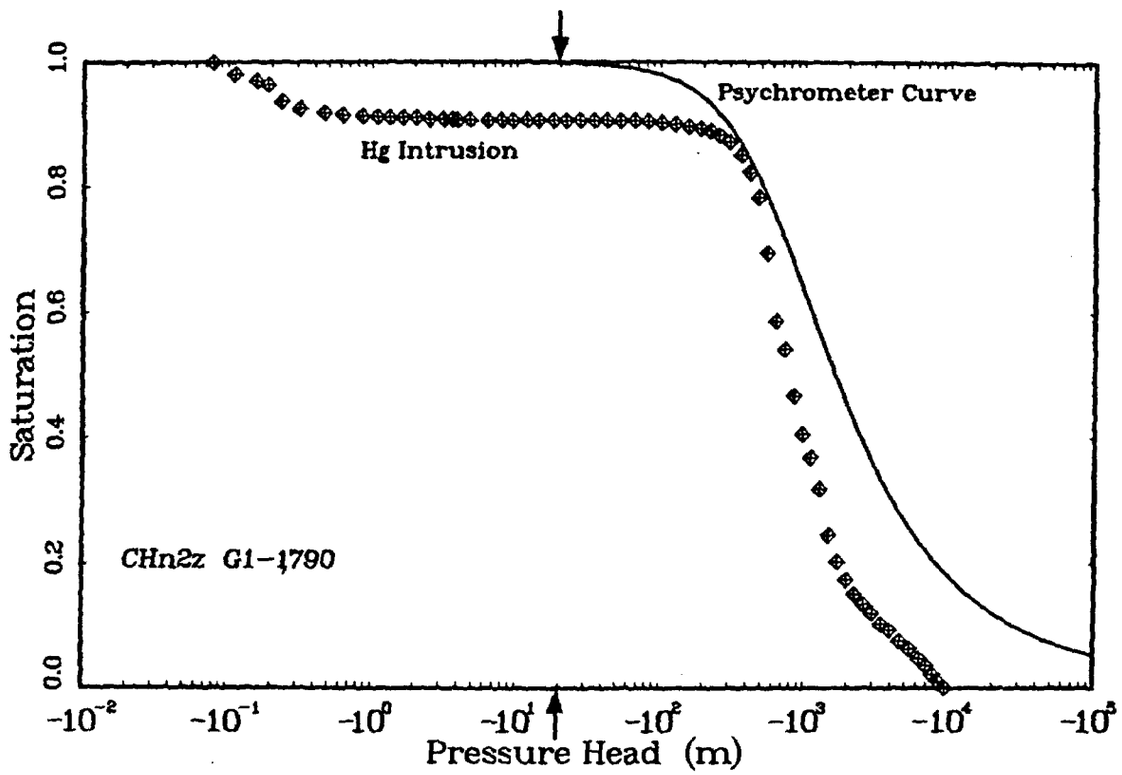

Figure B.52 Saturation as a Function of Pressure Head for Sample G1-1790

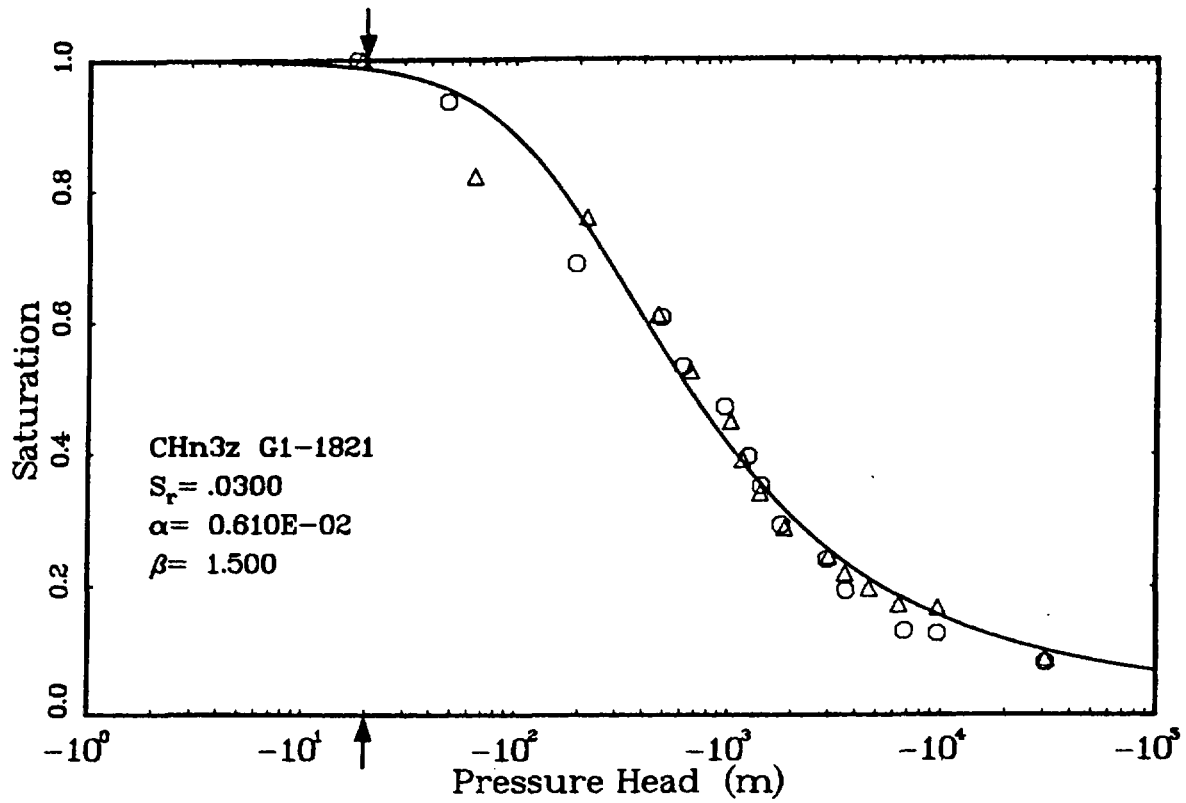

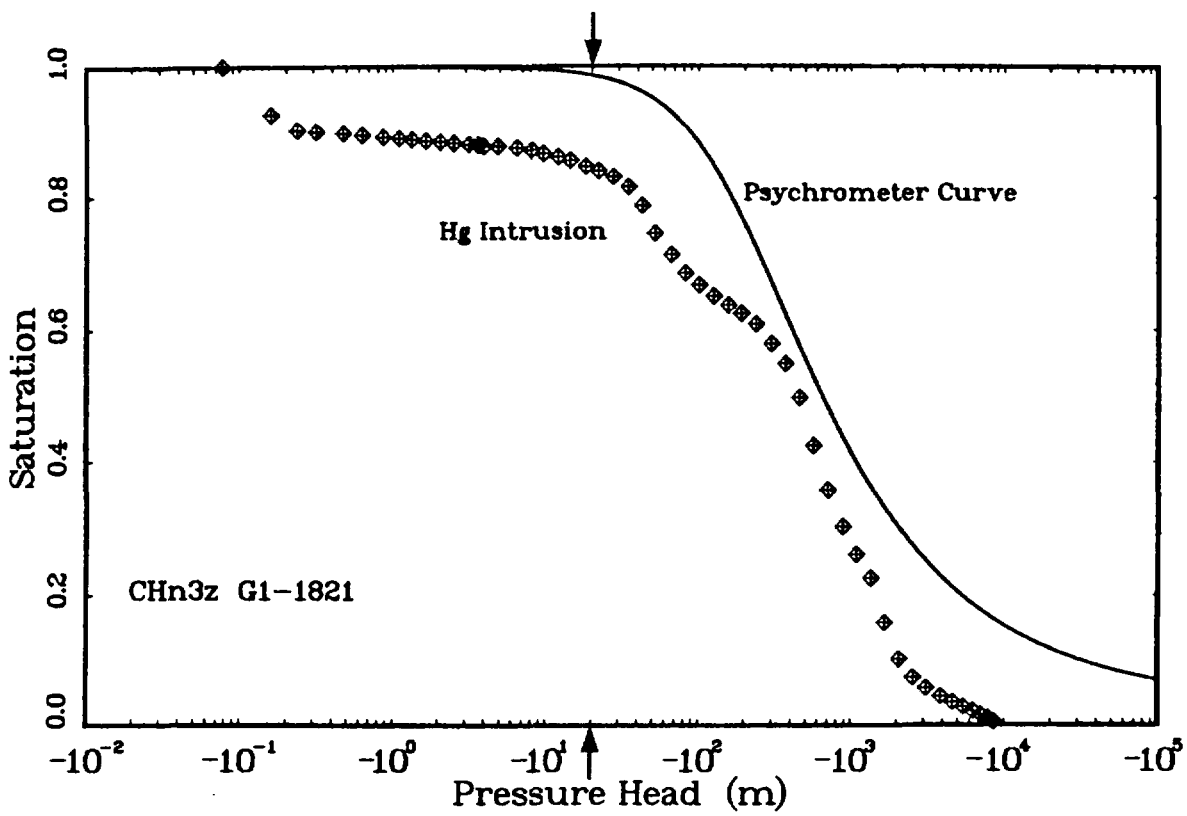

Figure B.53 Saturation as a Function of Pressure Head for Sample G1-1821

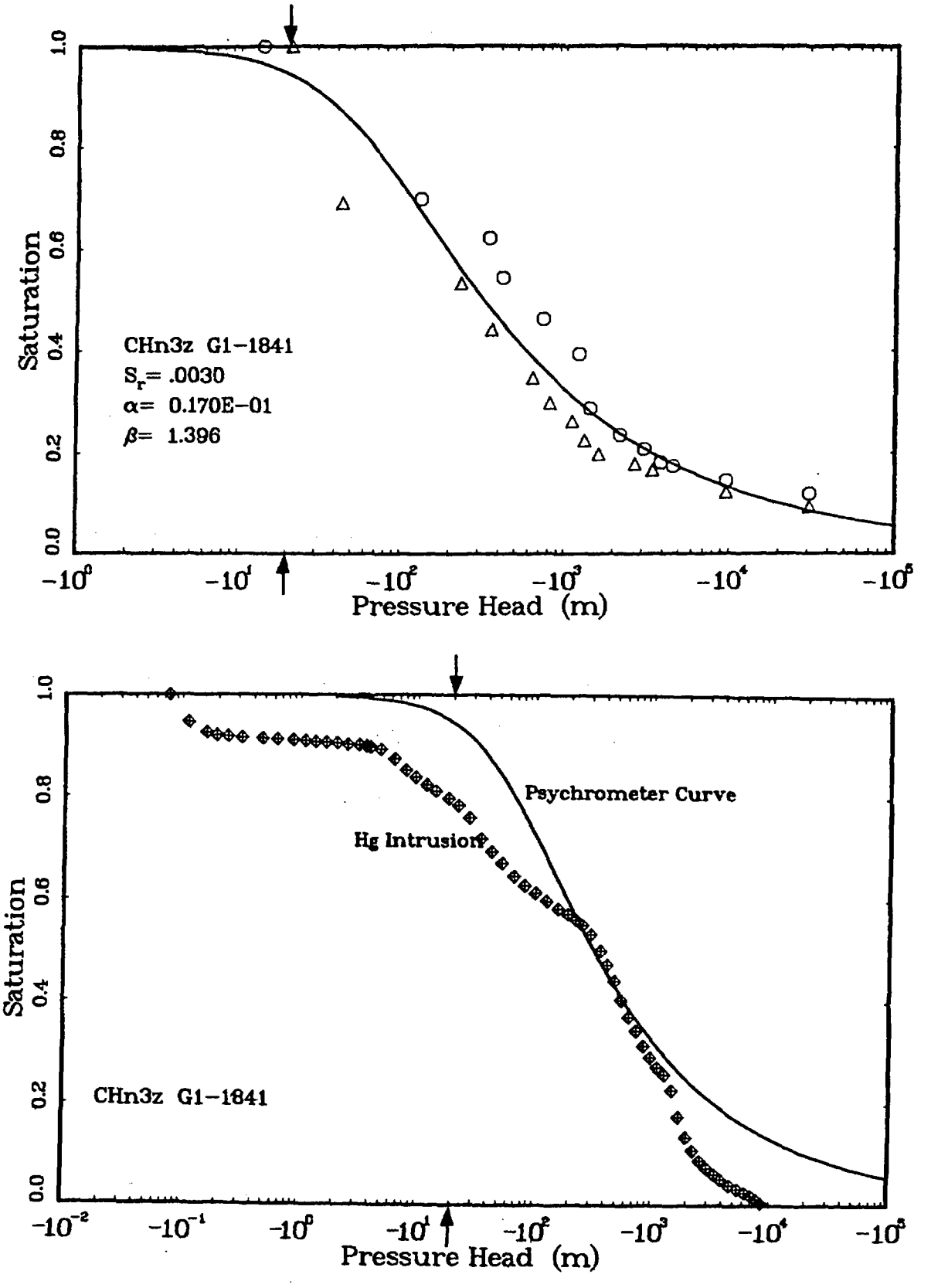

Figure B.54 Saturation as a Function of Pressure Head for Sample G1-1841

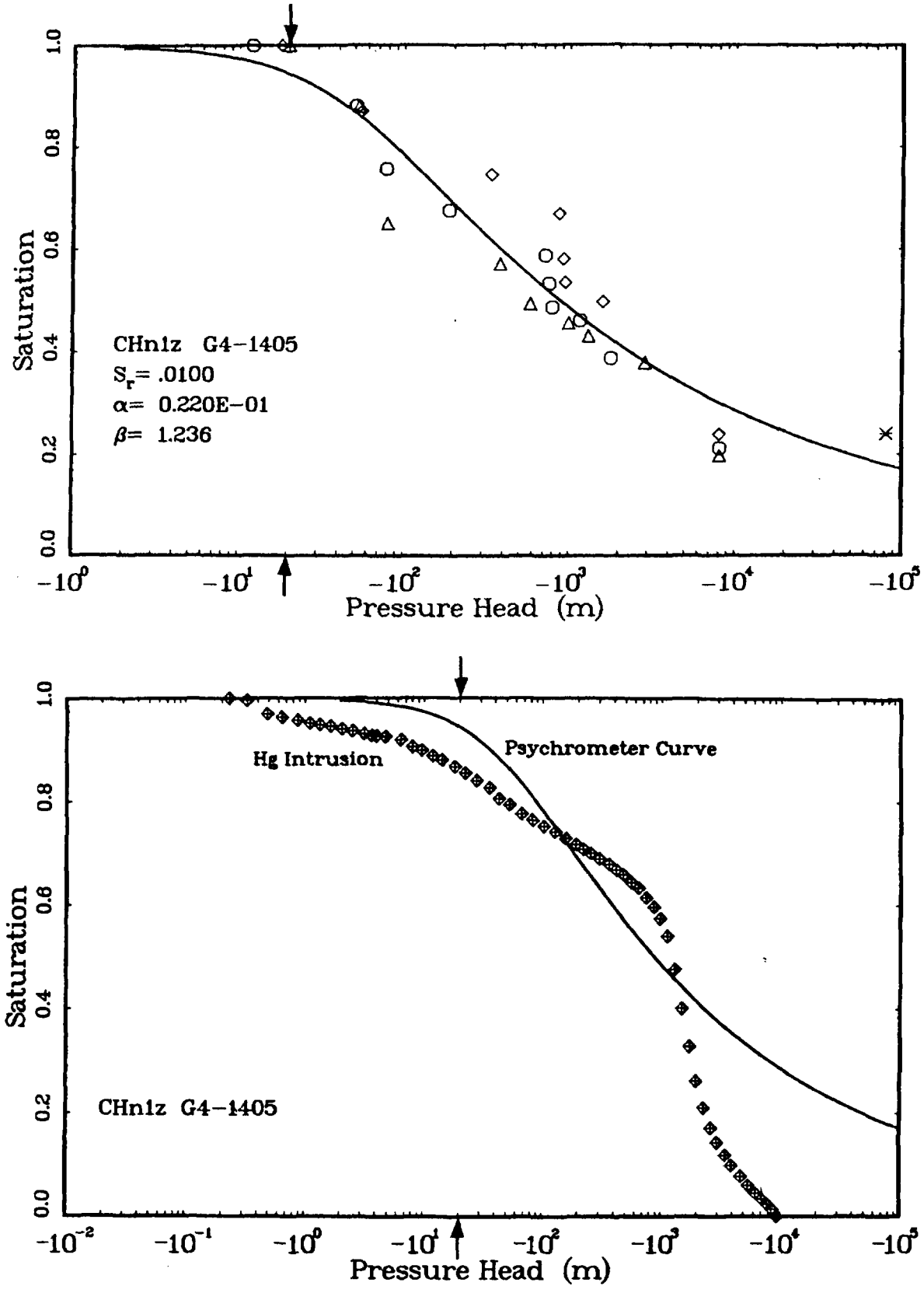

Figure B.55 Saturation as a Function of Pressure Head for Sample G4-1405

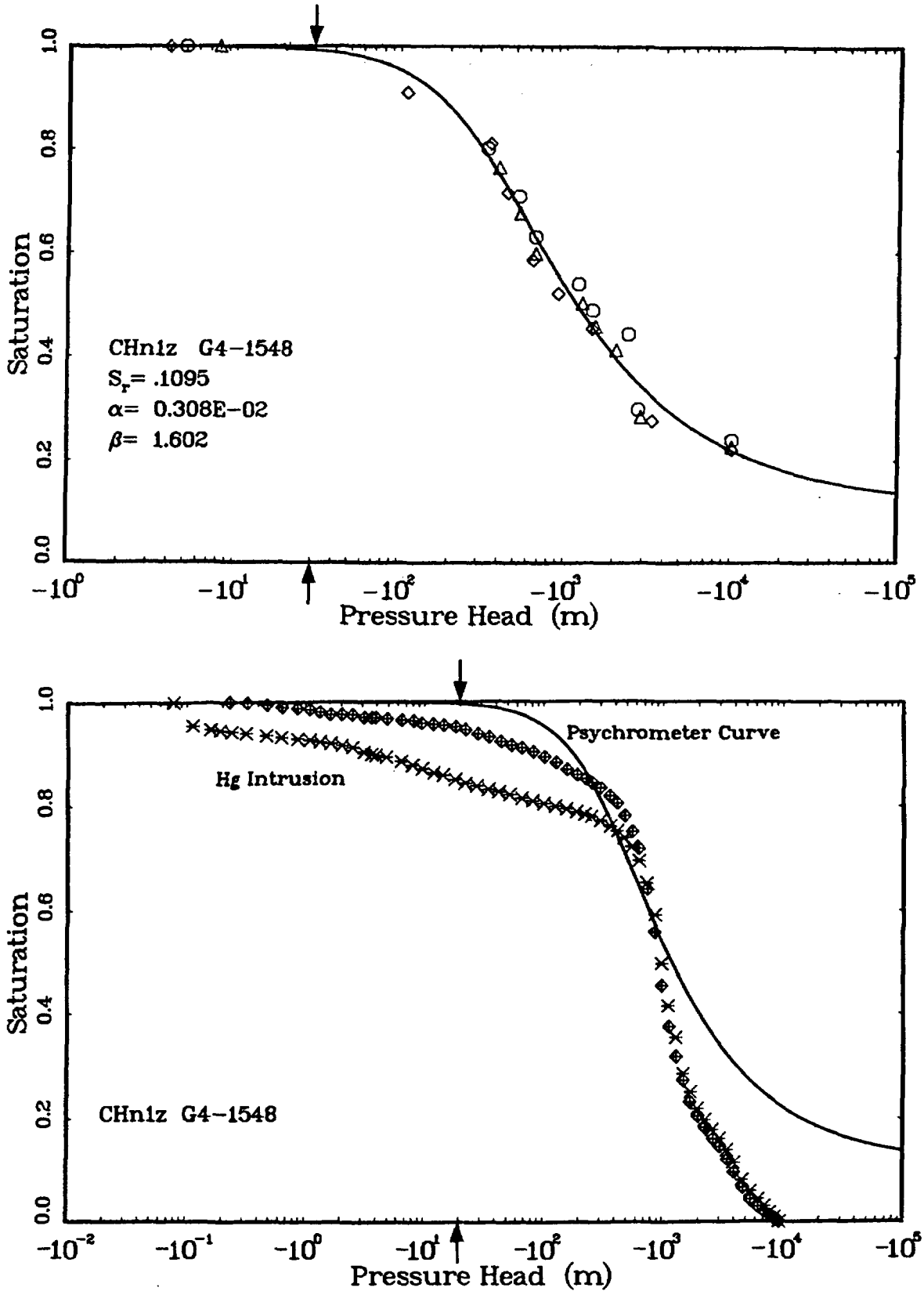

Figure B.56 Saturation as a Function of Pressure Head for Sample G4-1548 (Mercury-Intrusion Test Results from G4-1547 Added)

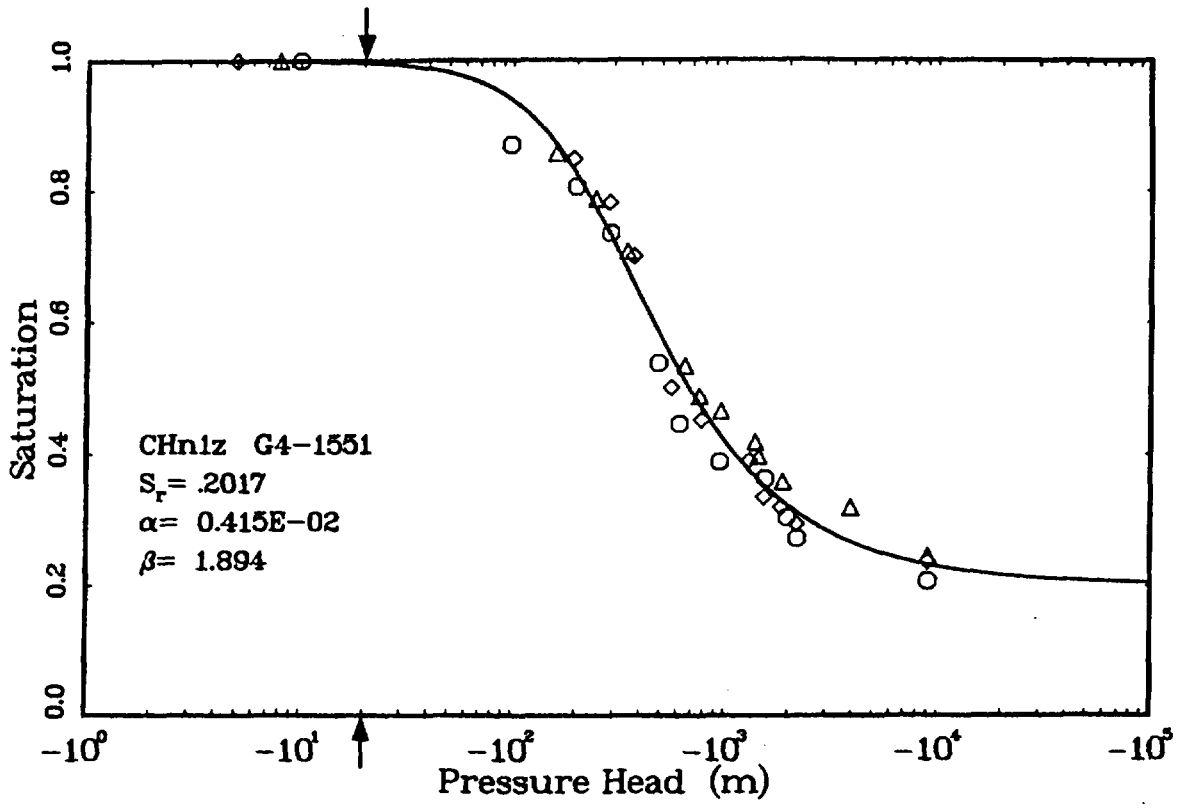

Figure B.57 Saturation as a Function of Pressure Head for Sample G4-1551 (Psychrometer Only)

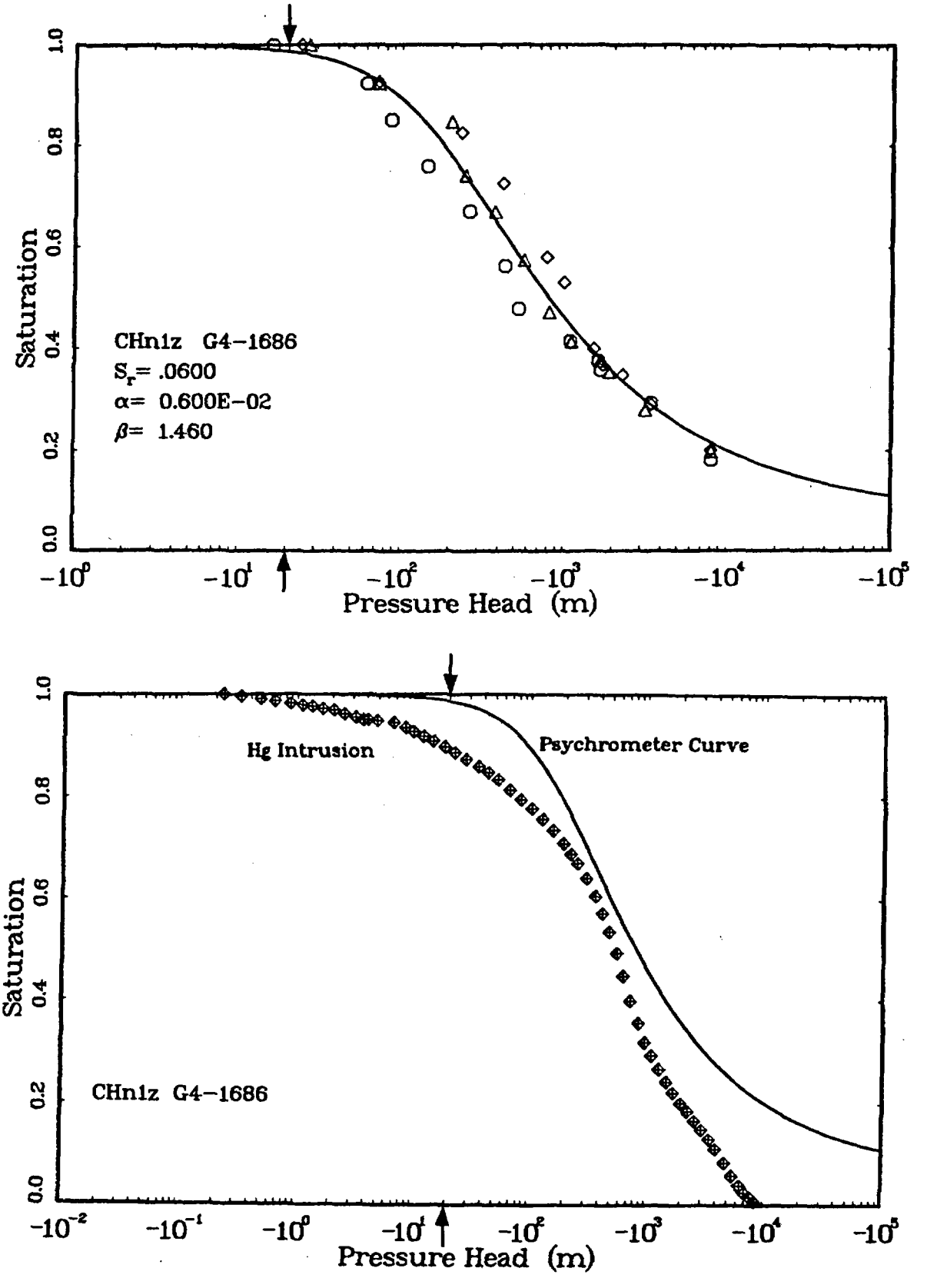

Figure B.58 Saturation as a Function of Pressure Head for Sample G4-1686

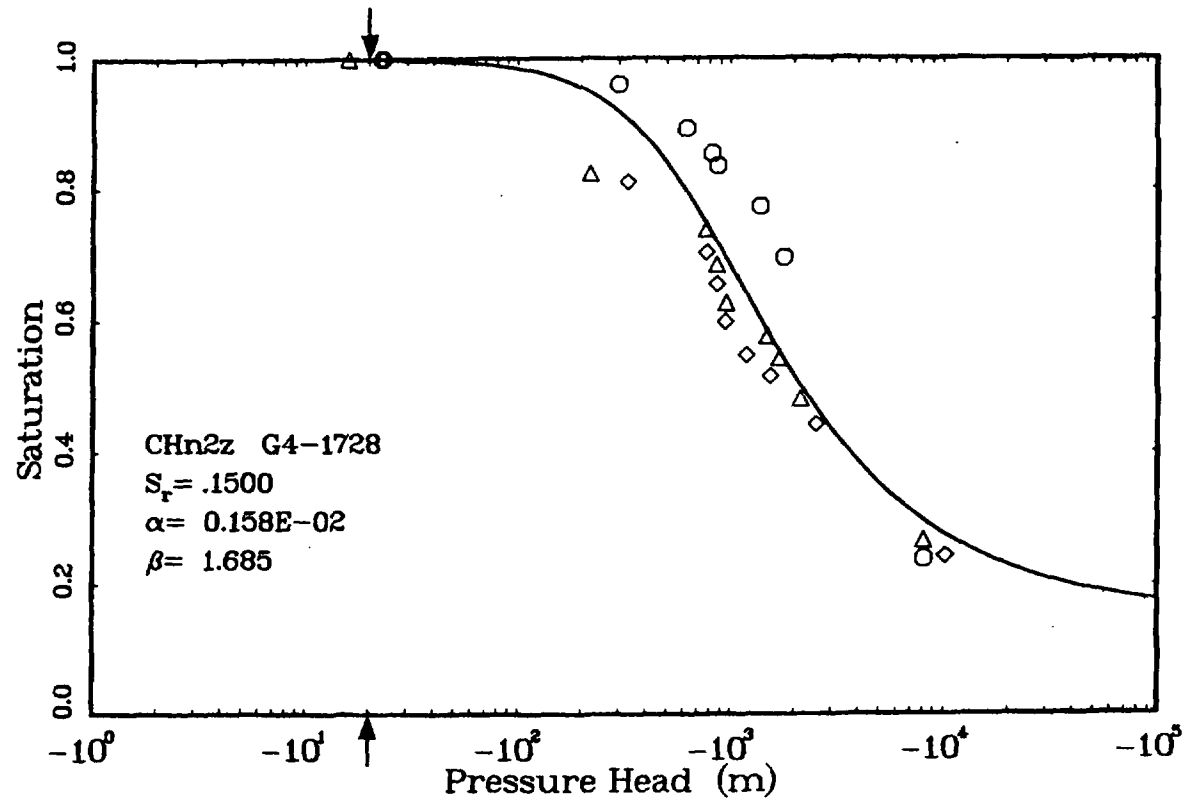

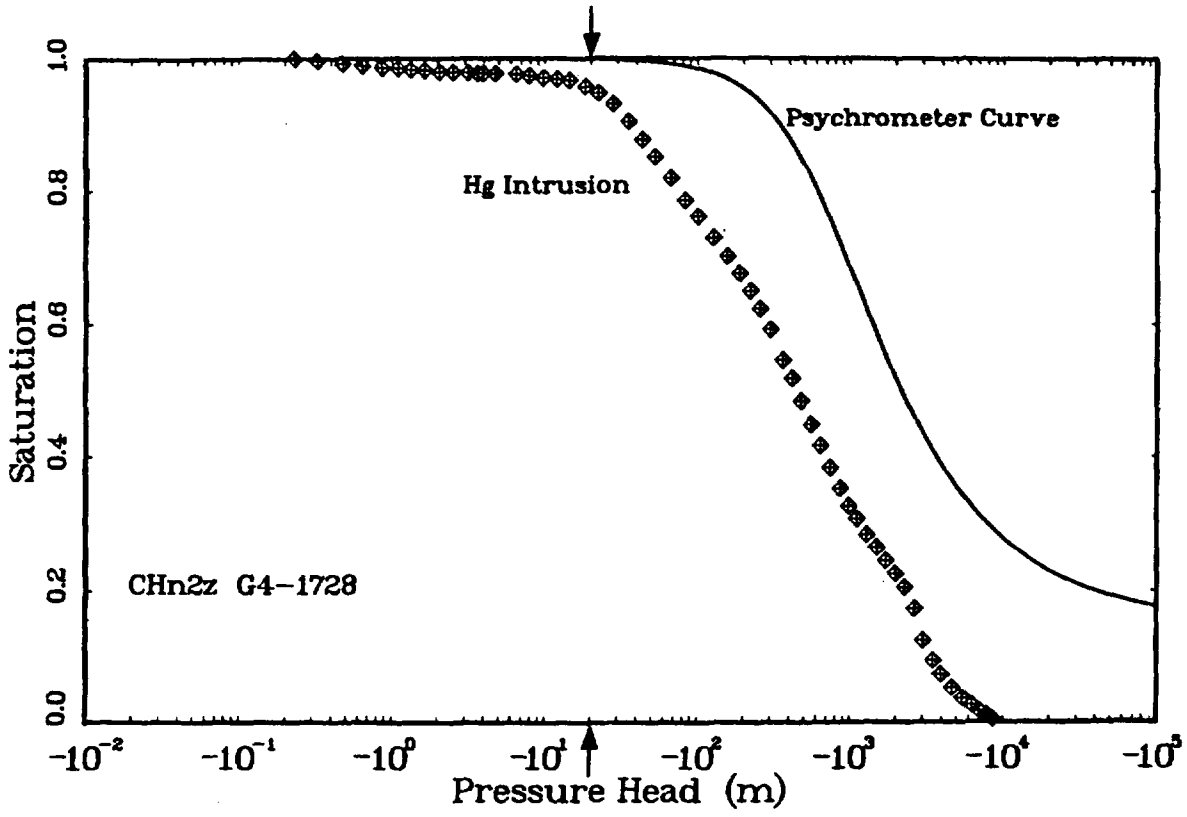

Figure B.59 Saturation as a Function of Pressure Head for Sample G4-1728

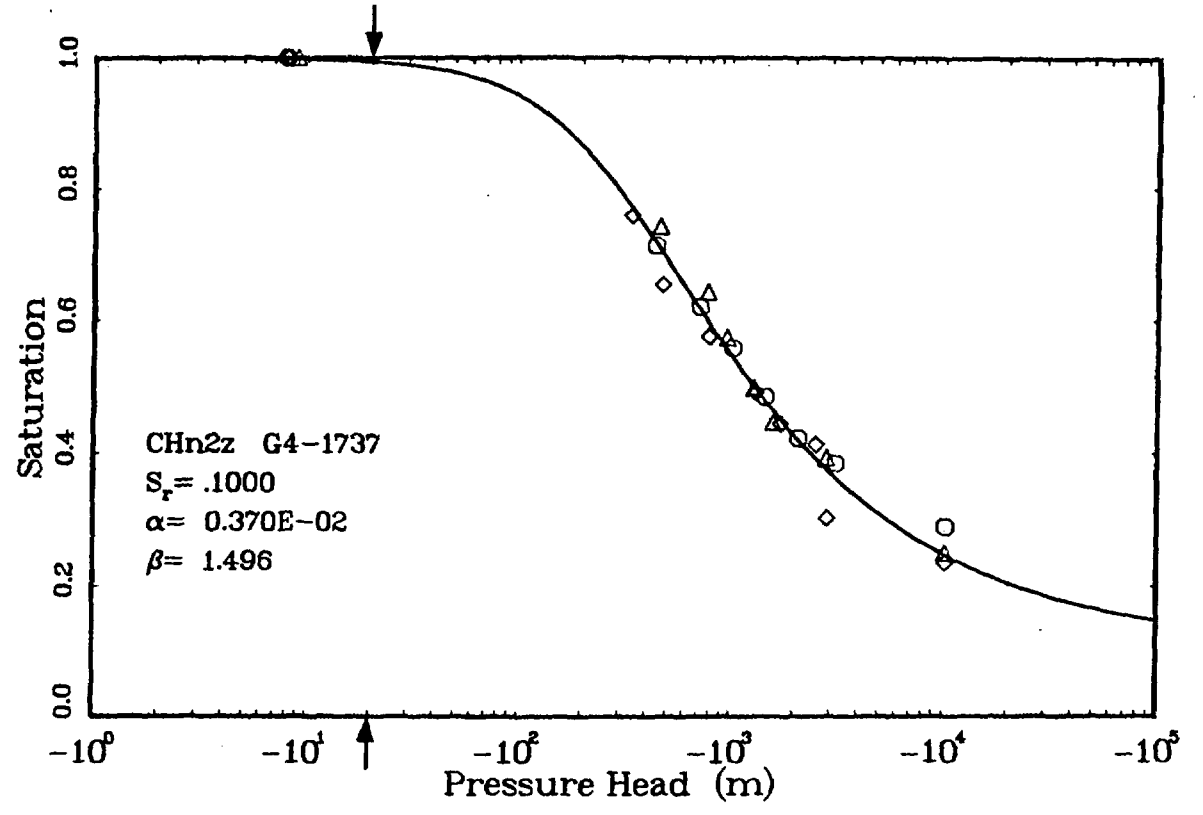

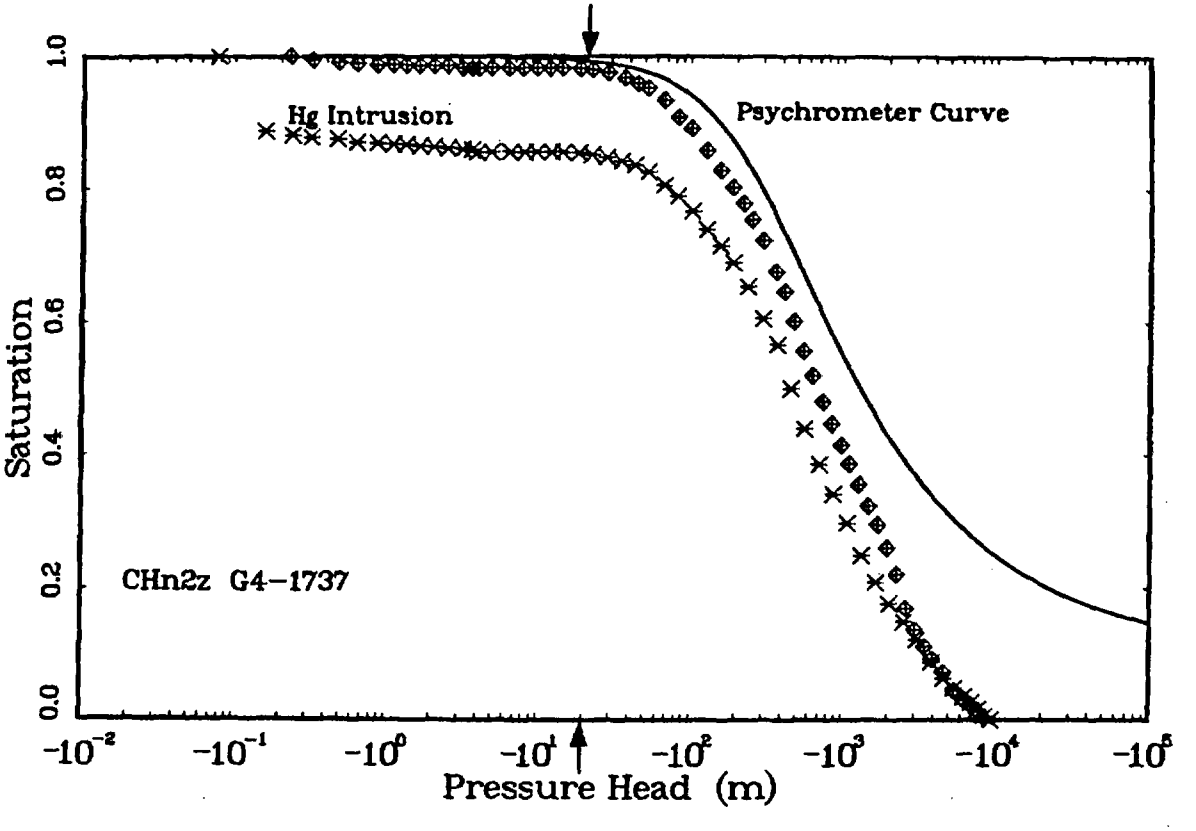

Figure B.60 Saturation as a Function of Pressure Head for Sample G4-1737 (Mercury-Intrusion Test Results from G4-1736 Added)

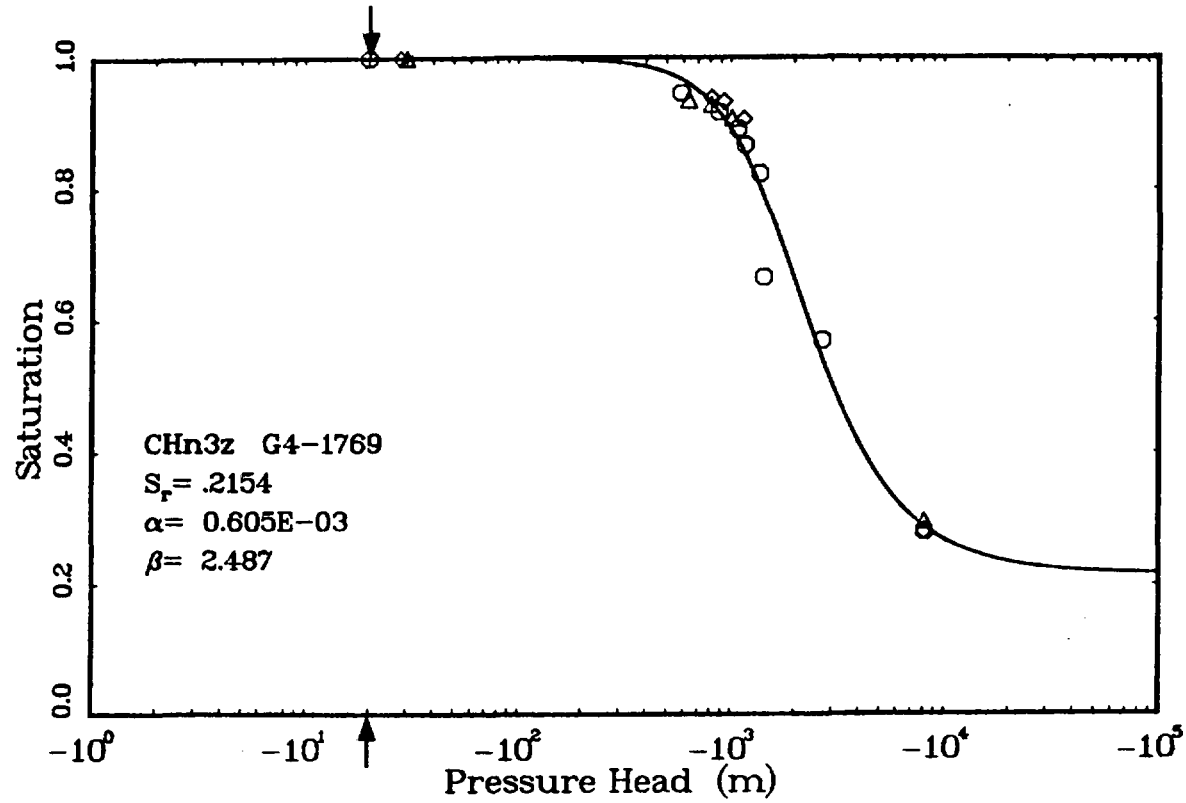

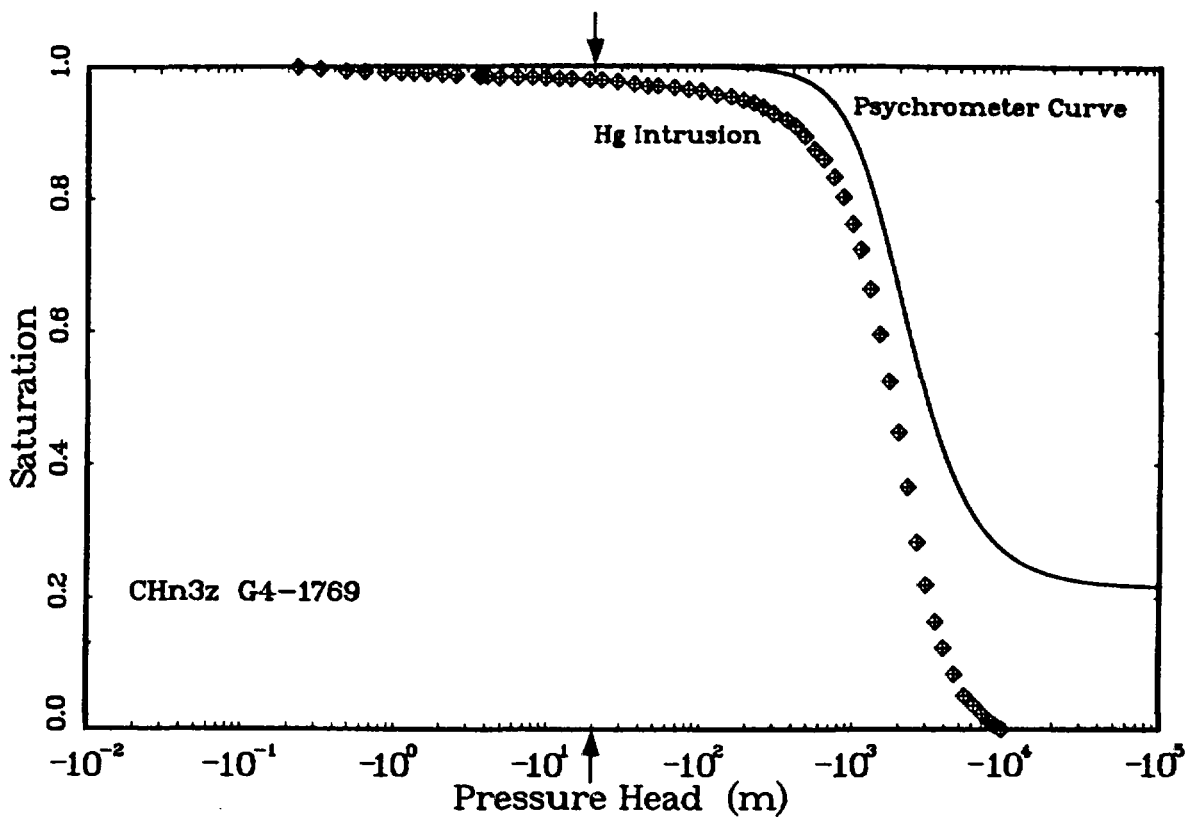

Figure B.61 Saturation as a Function of Pressure Head for Sample G4-1769

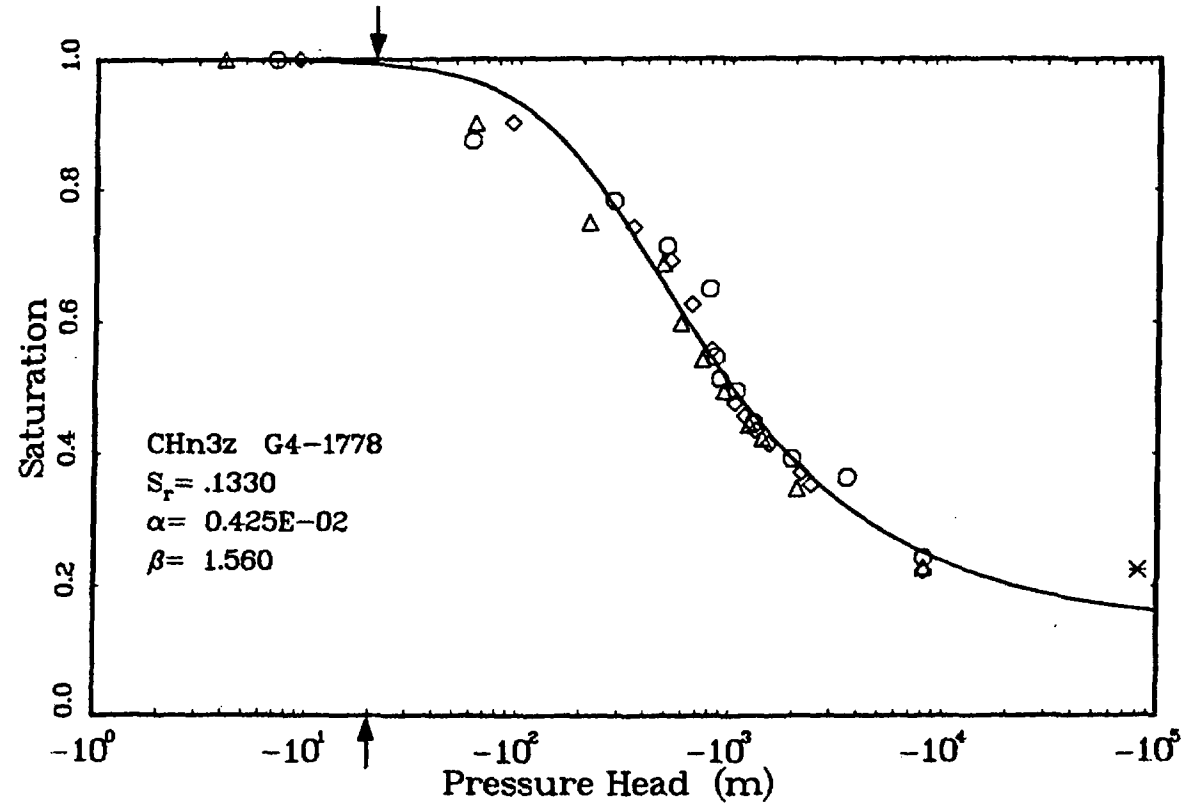

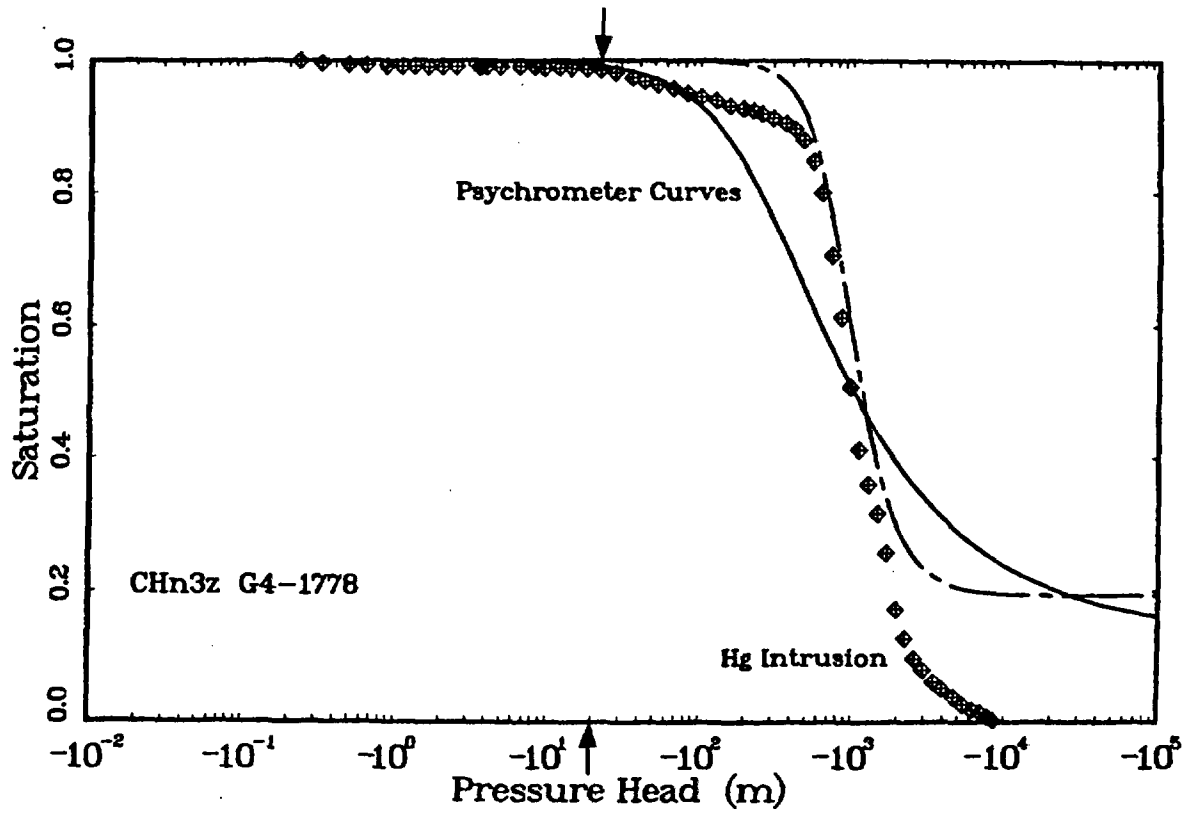

Figure B.62 Saturation as a Function of Pressure Head for Sample G4-1778 (Thermocouple-Psychrometer Curve-Fit from G4-1778-F Added)

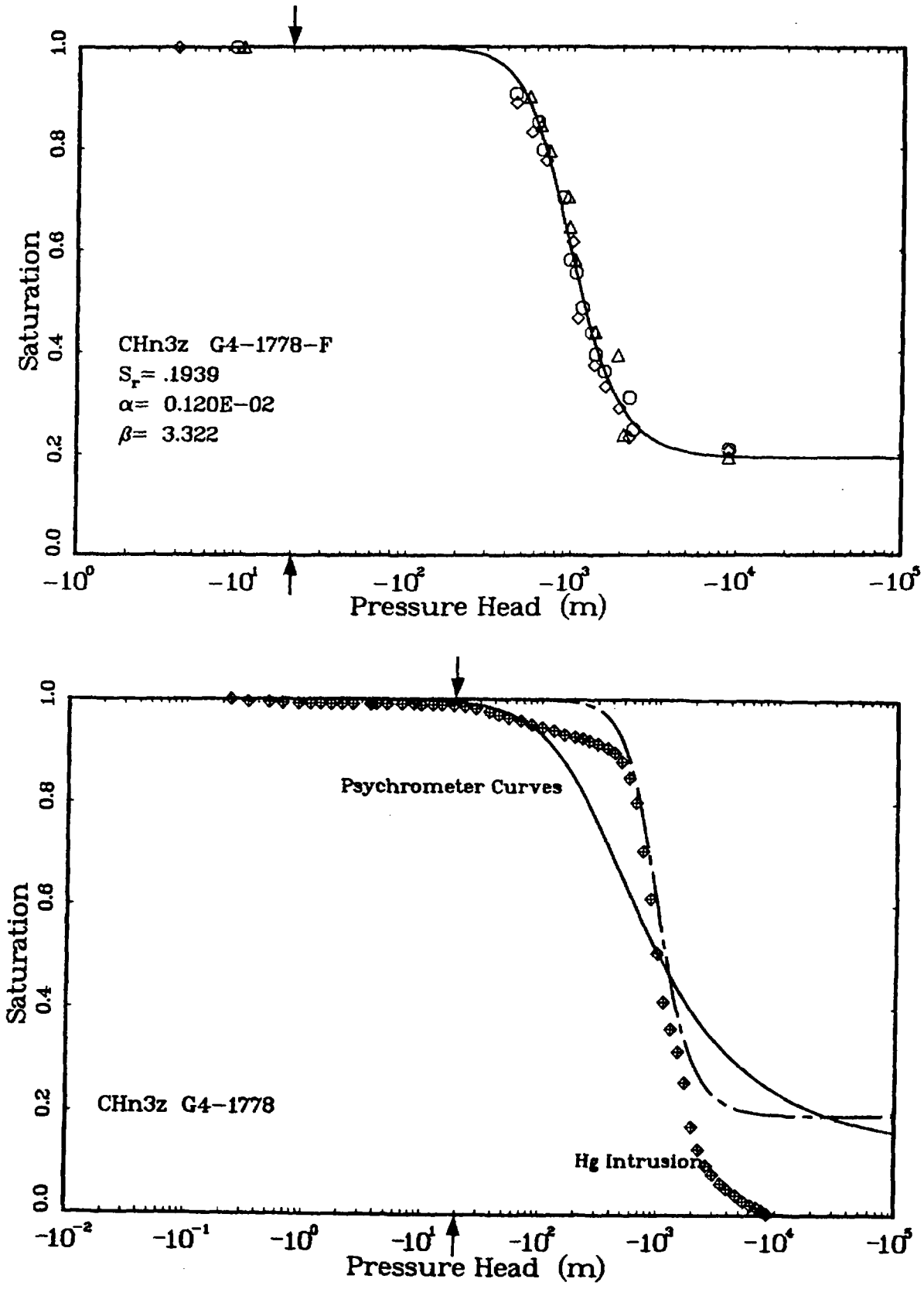

Figure B.63 Saturation as a Function of Pressure Head for Sample G4-1778-F (Thermocouple-Psychrometer Curve-Fit from G4-1778 Added)

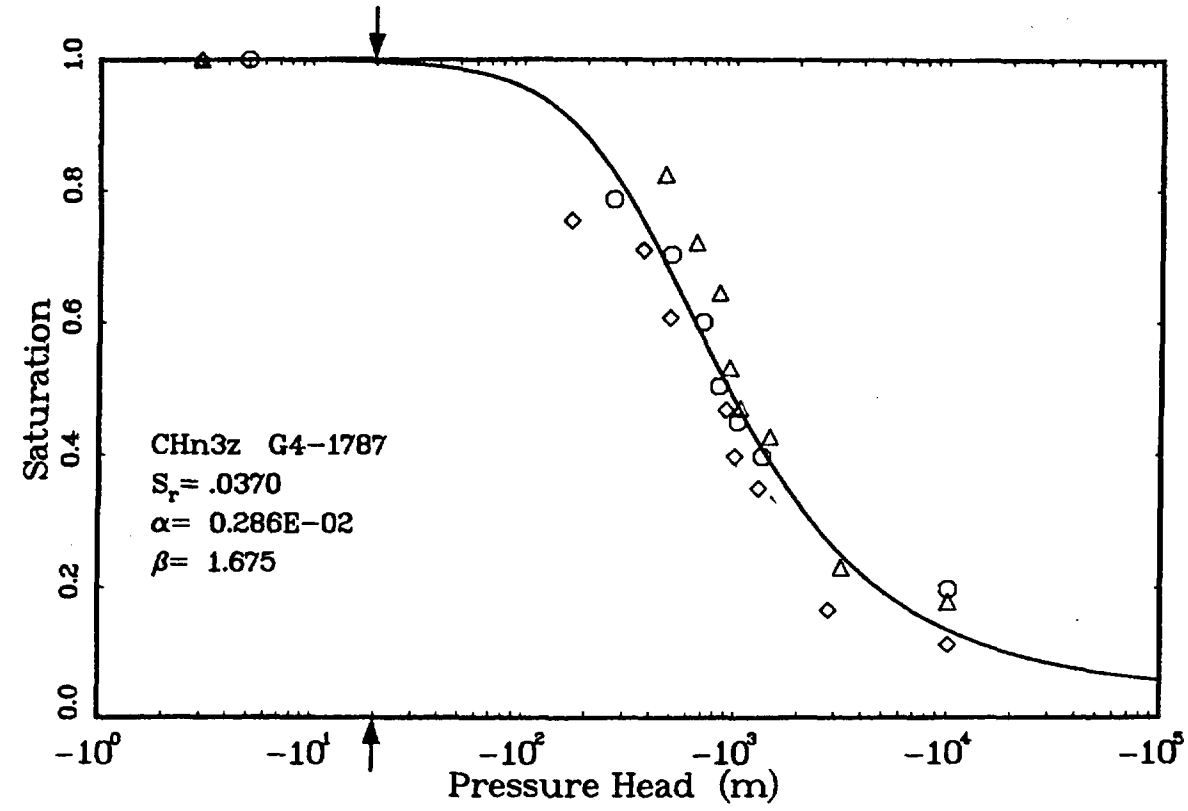

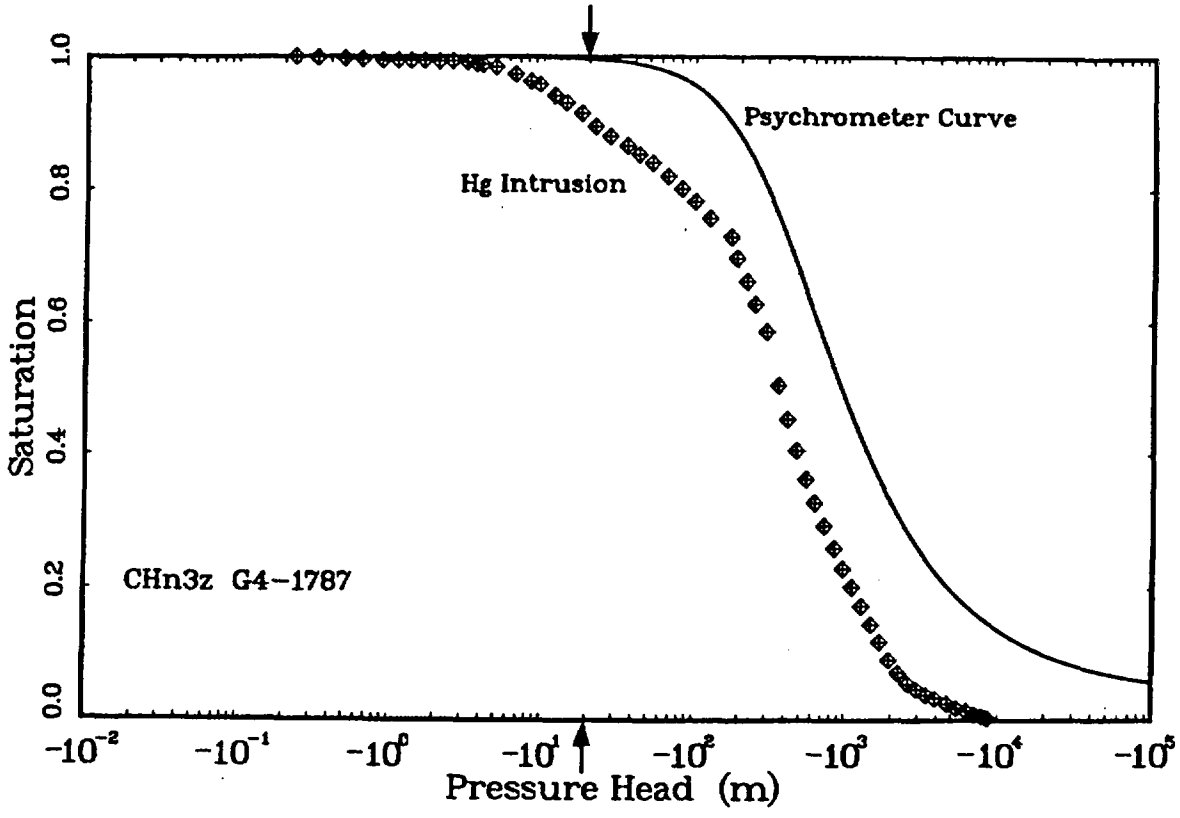

Figure B.64 Saturation as a Function of Pressure Head for Sample G4-1787

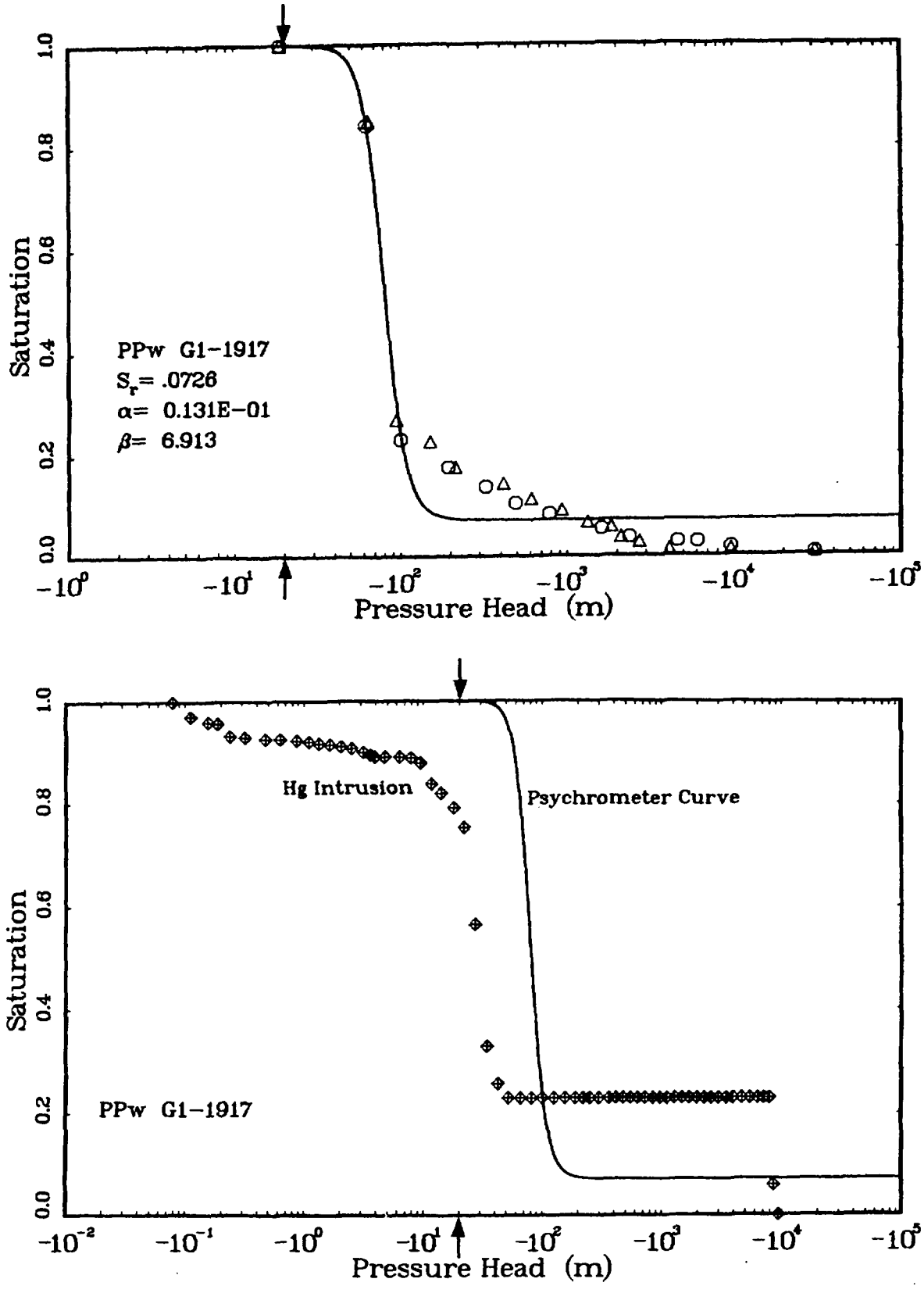

Figure B.65 Saturation as a Function of Pressure Head for Sample G1-1917

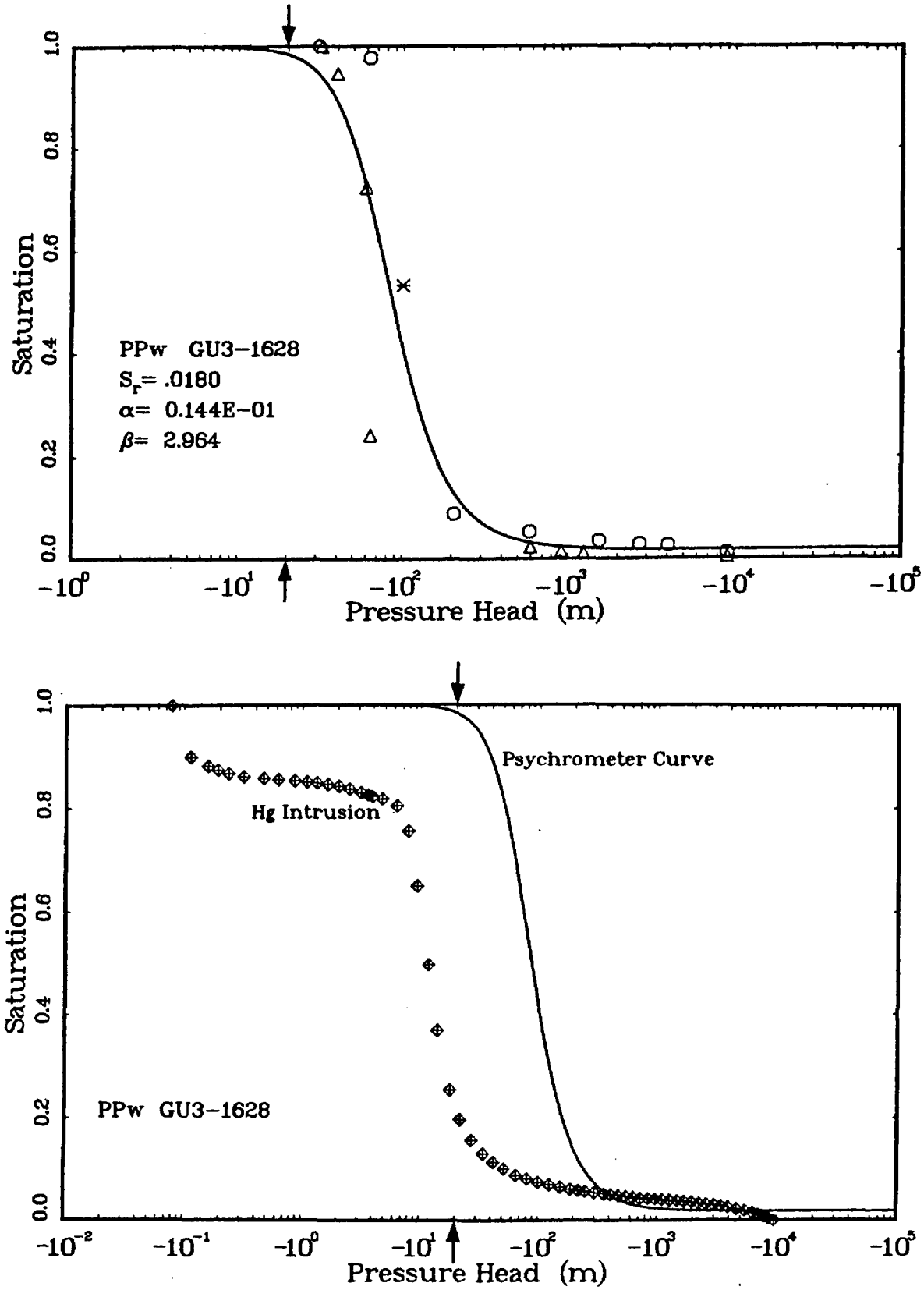

Figure B.66 Saturation as a Function of Pressure Head for Sample GU3-1628

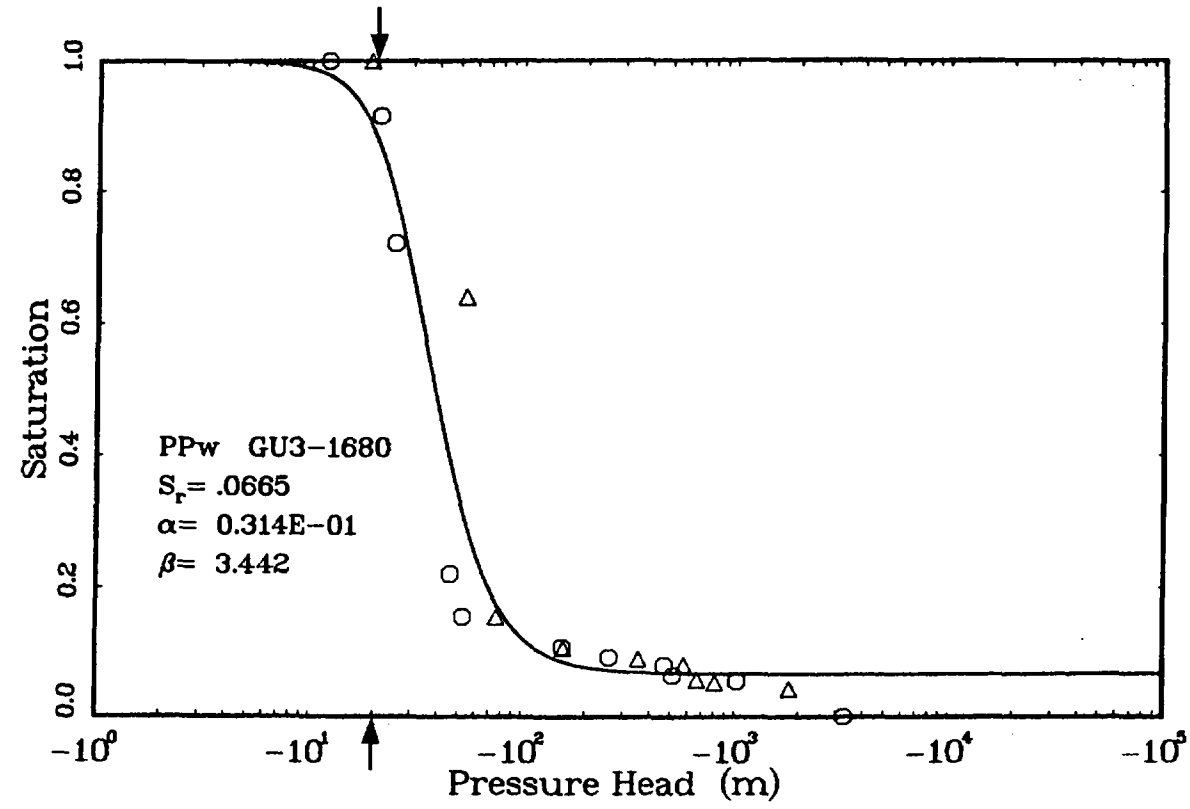

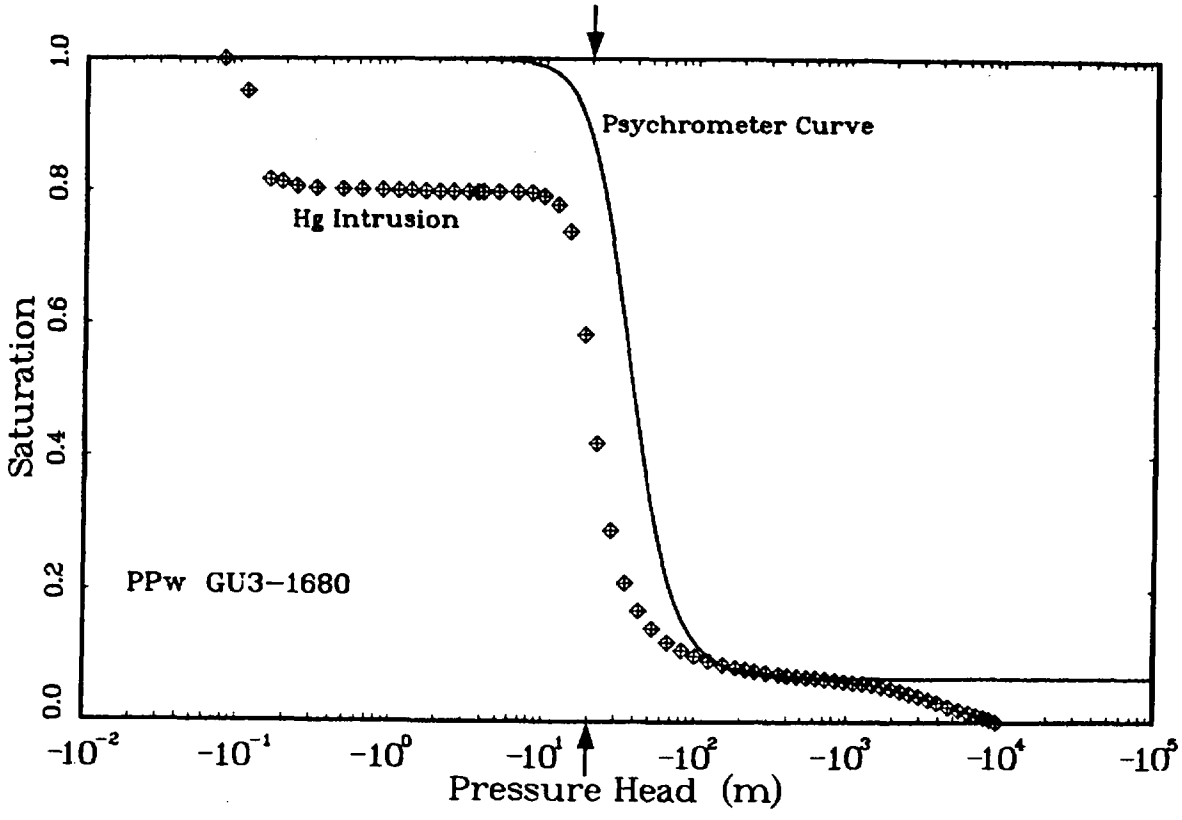

Figure B.67 Saturation as a Function of Pressure Head for Sample GU3-1680

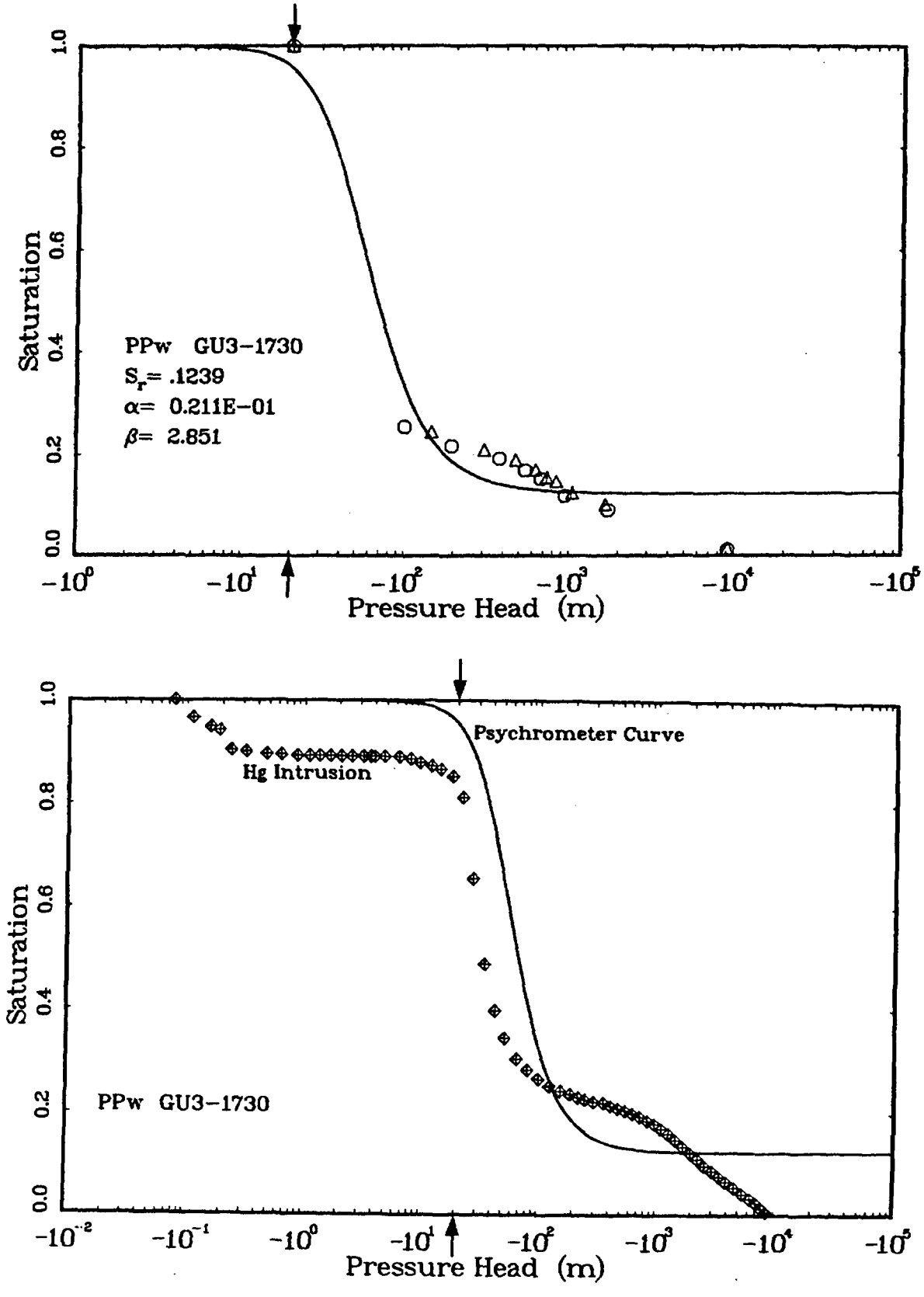

Figure B.68 Saturation as a Function of Pressure Head for Sample GU3-1730

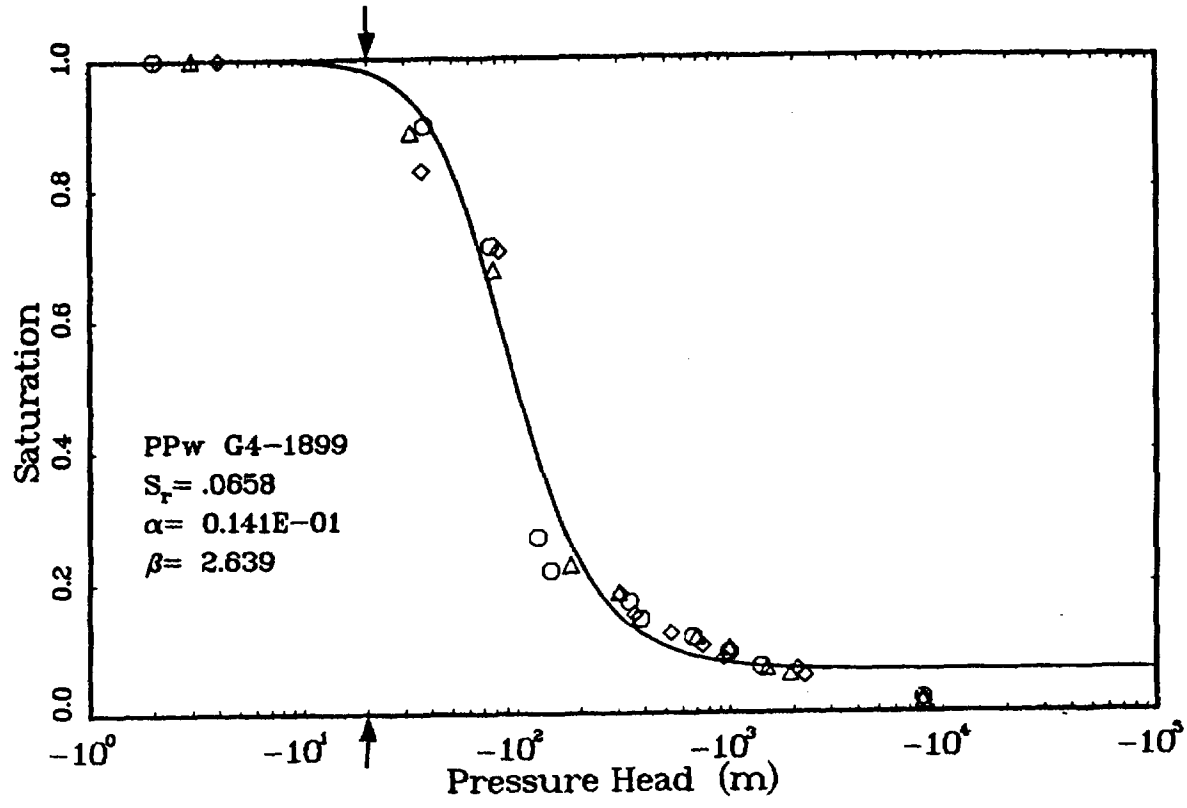

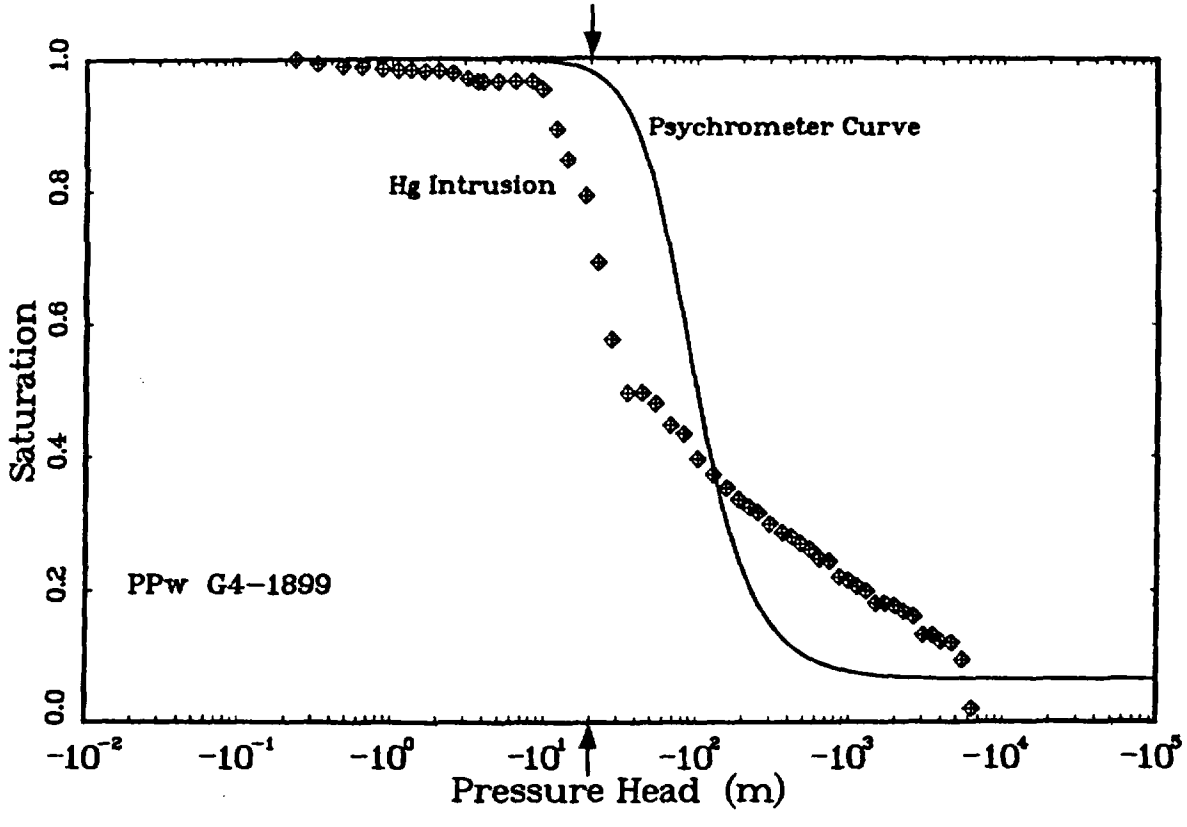

Figure B.69 Saturation as a Function of Pressure Head for Sample G4-1899

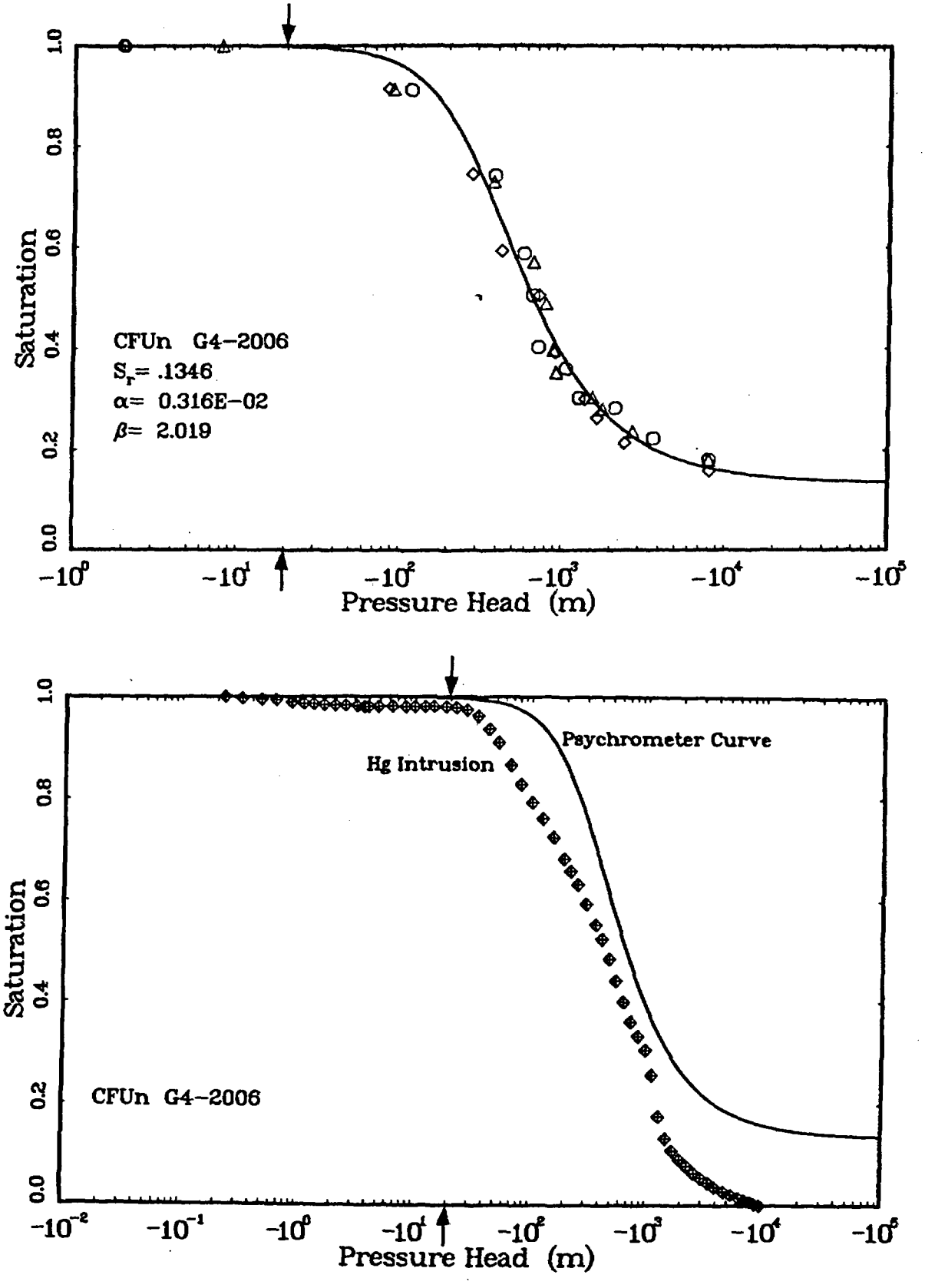

Figure B.70 Saturation as a Function of Pressure Head for Sample G4-2006

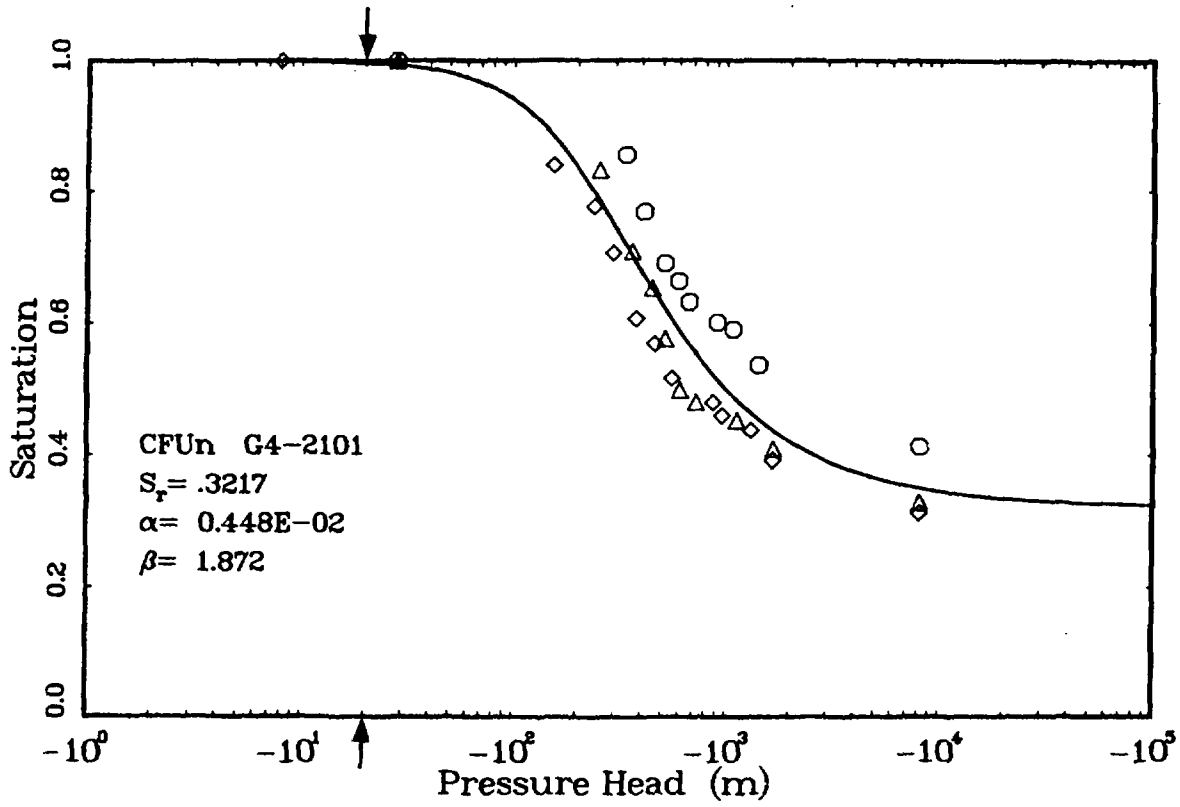

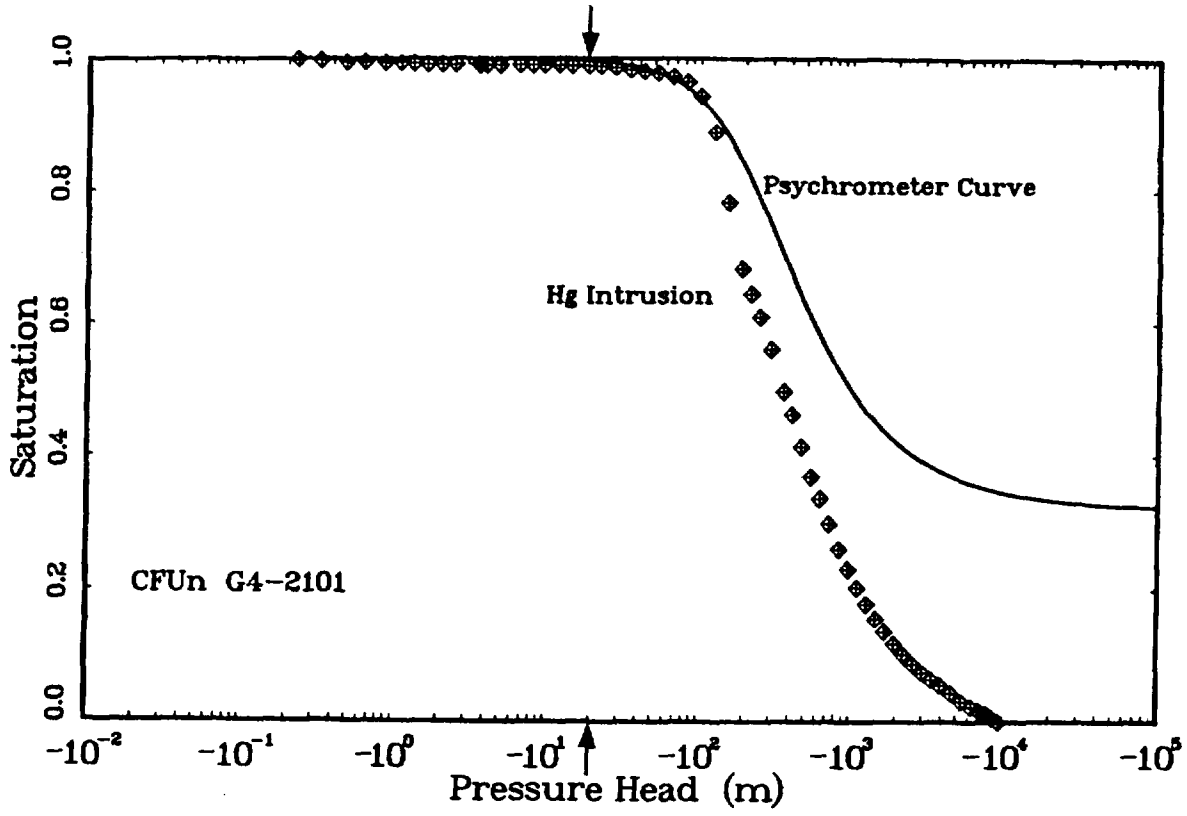

Figure B.71 Saturation as a Function of Pressure Head for Sample G4-2101

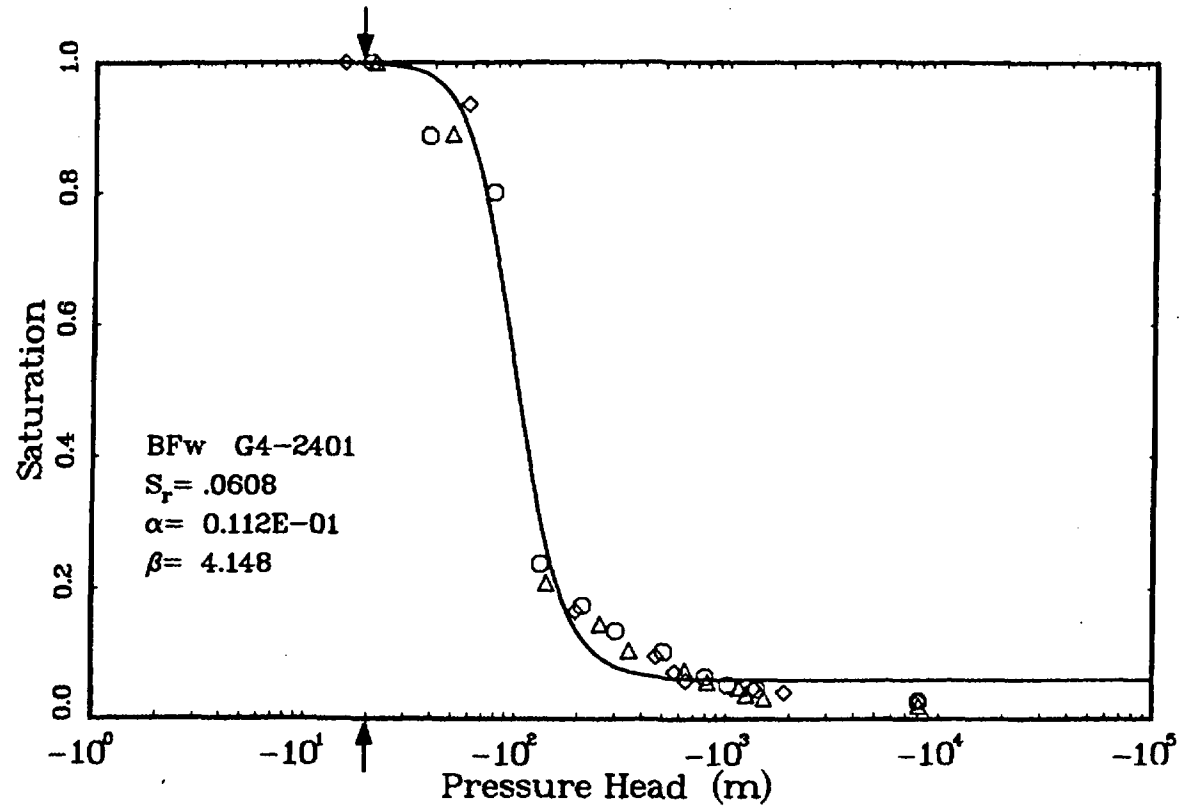

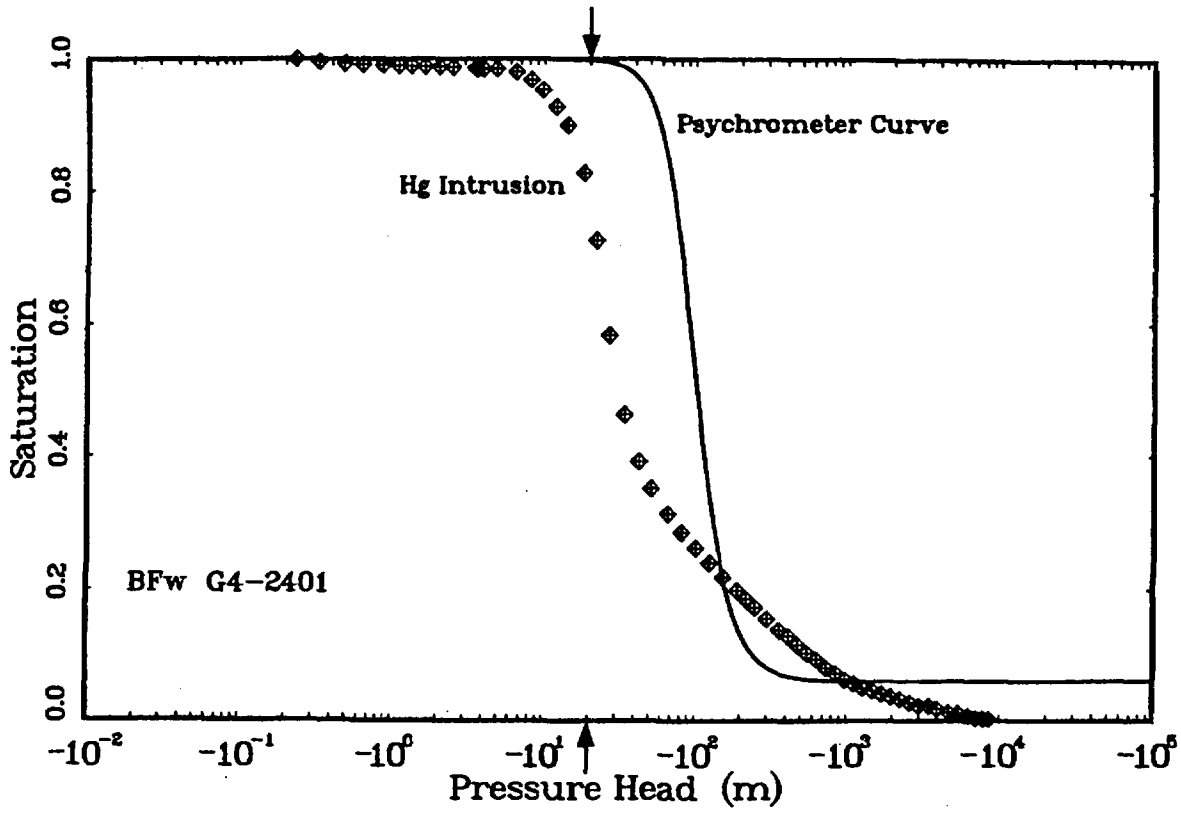

Figure B.72 Saturation as a Function of Pressure Head for Sample G4-2401

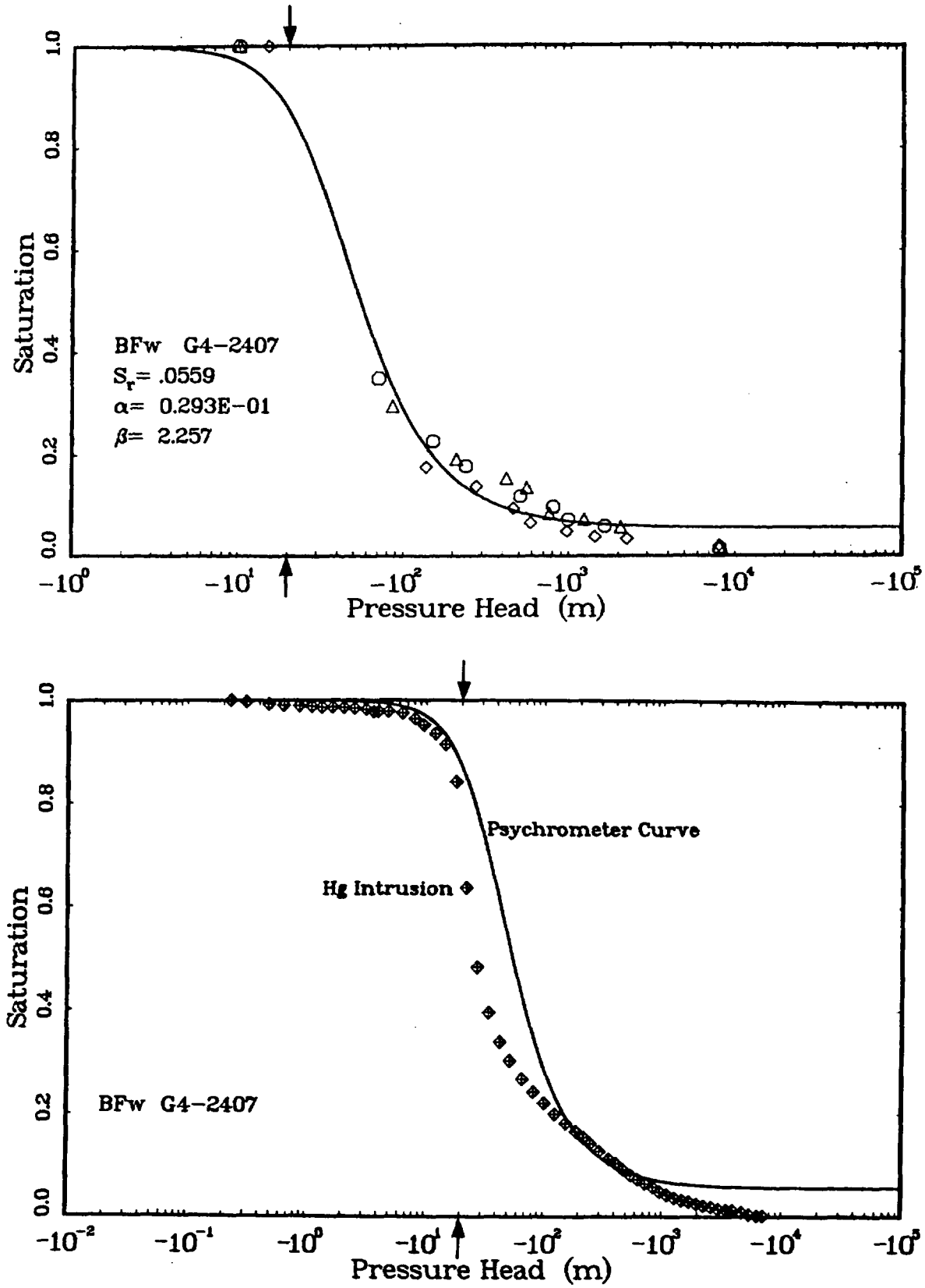

Figure B.73 Saturation as a Function of Pressure Head for Sample G4-2407

DISTRIBUTION LIST

B. C. Rusche (RW-1)
Director
Office of Civilian Radioactive
Waste Management
U.S. Department of Energy
Forrestal Building
Washington, DC 20585

Ralph Stein (RW-23)
Office of Civilian Radioactive
Waste Management
U.S. Department of Energy
Forrestal Building
Washington, DC 20585

J. J. Fiore, (RW-221)
Office of Civilian Radioactive
Waste Management
U.S. Department of Energy
Forrestal Building
Washington, DC 20585

M. W. Frei (RW-231)
Office of Civilian Radioactive
Waste Management
U.S. Department of Energy
Forrestal Building
Washington, DC 20585

E. S. Burton (RW-25)
Siting Division
Office of Geologic Repositories
U.S. Department of Energy
Forrestal Building
Washington, D.C. 20585

C. R. Cooley (RW-24)
Geosciences & Technology Division
Office of Geologic Repositories
U.S. Department of Energy
Forrestal Building
Washington, DC 20585

V. J. Cassella (RW-222)
Office of Civilian Radioactive
Waste Management
U.S. Department of Energy
Forrestal Building
Washington, DC 20585

T. P. Longo (RW-25)
Program Management Division
Office of Geologic Repositories
U.S. Department of Energy
Forrestal Building
Washington, DC 20585

Cy Klingsberg (RW-24)
Geosciences and Technology Division
Office of Geologic Repositories
U. S. Department of Energy
Forrestal Building
Washington, DC 20585

B. G. Gale (RW-223)
Office of Civilian Radioactive
Waste Management
U.S. Department of Energy
Forrestal Building
Washington, DC 20585

R. J. Blaney (RW-22)
Program Management Division
Office of Geologic Repositories
U.S. Department of Energy
Forrestal Building
Washington, DC 20585

R. W. Gale (RW-40)
Office of Civilian Radioactive
Waste Management
U.S. Department of Energy
Forrestal Building
Washington, D.C. 20585

J. E. Shaheen (RW-44)
Outreach Programs
Office of Policy, Integration and
Outreach
U.S. Department of Energy
Forrestal Building
Washington, DC 20585

J. O. Neff, Manager
Salt Repository Project Office
U.S. Department of Energy
505 King Avenue
Columbus, OH 43201

D. C. Newton (RW-23)
Engineering & Licensing Division
Office of Geologic Repositories
U.S. Department of Energy
Forrestal Building
Washington, DC 20585

O. L. Olson, Manager
Basalt Waste Isolation Project Office
Richland Operations Office
U.S. Department of Energy
Post Office Box 550
Richland, WA 99352

D. L. Vieth, Director (4)
Waste Management Project Office
U.S. Department of Energy
Post Office Box 14100
Las Vegas, NV 89114

D. F. Miller, Director
Office of Public Affairs
U.S. Department of Energy
Post Office Box 14100
U.S. Department of Energy
Las Vegas, NV 89114

P. M. Bodin (12)
Office of Public Affairs
U.S. Department of Energy
Post Office Box 14100
Las Vegas, NV 89114

B. W. Church, Director
Health Physics Division
U.S. Department of Energy
Post Office Box 14100
Las Vegas, NV 89114

Chief, Repository Projects Branch
Division of Waste Management
U.S. Nuclear Regulatory Commission
Washington, D.C. 20555

Document Control Center
Division of Waste Management
U.S. Nuclear Regulatory Commission
Washington, D.C. 20555

S. A. Mann, Manager
Crystalline Rock Project Office
U.S. Department of Energy
9800 South Cass Avenue
Argonne, IL 60439

K. Street, Jr.
Lawrence Livermore National
Laboratory
Post Office Box 808
Mail Stop L-209
Livermore, CA 94550

L. D. Ramspott (3)
Technical Project Officer for NNWSI
Lawrence Livermore National
Laboratory
P.O. Box 808
Mail Stop L-204
Livermore, CA 94550

W. J. Purcell (RW-20)
Associate Director
Office of Civilian Radioactive
Waste Management
U.S. Department of Energy
Forrestal Building
Washington, DC 20585

D. T. Oakley (4)
Technical Project Officer for NNWSI
Los Alamos National Laboratory
P.O. Box 1663
Mail Stop F-619
Los Alamos, NM 87545

L. R. Hayes (3)
Technical Project Officer for NNWSI
U.S. Geological Survey
Post Office Box 25046
421 Federal Center
Denver, CO 80225

NTS Section Leader
Repository Project Branch
Division of Waste Management
U.S. Nuclear Regulatory Commission
Washington, D.C. 20555

V. M. Glanzman
U.S. Geological Survey
Post Office Box 25046
913 Federal Center
Denver, CO 80225

P. T. Prestholt
NRC Site Representative
1050 East Flamingo Road
Suite 319
Las Vegas, NV 89109

M. E. Spaeth
Technical Project Officer for NNWSI
Science Applications
International Corporation
Suite 407
101 Convention Center Drive
Las Vegas, NV 89109

SAIC-T&MSS Library (2)
Science Applications
International Corporation
Suite 407
101 Convention Center Drive
Las Vegas, NV 89109

W. S. Twenhofel, Consultant
Science Applications
International Corp.
820 Estes Street
Lakewood, CO 89215

A. E. Gurrola
General Manager
Energy Support Division
Holmes & Narver, Inc.
Mail Stop 580
Post Office Box 14340
Las Vegas, NV 89114

J. A. Cross, Manager
Las Vegas Branch
Fenix & Scisson, Inc.
Mail Stop 514
Post Office Box 14308
Las Vegas, NV 89114

Neal Duncan (RW-44)
Office of Policy, Integration, and
Outreach
U.S. Department of Energy
Forrestal Building
Washington, DC 20585

J. S. Wright
Technical Project Officer for NNWSI
Westinghouse Electric Corporation
Waste Technology Services Division
Nevada Operations
Post Office Box 708
Mail Stop 703
Mercury, NV 89023

ONWI Library
Battelle Columbus Laboratory
Office of Nuclear Waste Isolation
505 King Avenue
Columbus, OH 43201

W. M. Hewitt, Program Manager
Roy F. Weston, Inc.
955 L'Enfant Plaza, Southwest, Suite 800
Washington, DC 20024

H. D. Cunningham
General Manager
Reynolds Electrical &
Engineering Co., Inc.
Post Office Box 14400
Mail Stop 555
Las Vegas, NV 89114

T. Hay, Executive Assistant
Office of the Governor
State of Nevada
Capitol Complex
Carson City, NV 89710

R. R. Loux, Jr., Executive Director (3)
Nuclear Waste Project Office
State of Nevada
Evergreen Center, Suite 252
1802 North Carson Street
Carson City, NV 89701

C. H. Johnson, Technical
Program Manager
Nuclear Waste Project Office
State of Nevada
Evergreen Center, Suite 252
1802 North Carson Street
Carson City, NV 89701

John Fordham
Desert Research Institute
Water Resources Center
Post Office Box 60220
Reno, NV 89506

Dr. Martin Mifflin
Desert Research Institute
Water Resources Center
Suite 1
2505 Chandler Avenue
Las Vegas, NV 89120

Department of Comprehensive
Planning
Clark County
225 Bridger Avenue, 7th Floor
Las Vegas, NV 89155

Planning Department
Nye County
Post Office Box 153
Tonopah, NV 89049

Lincoln County Commission
Lincoln County
Post Office Box 90
Pioche, NV 89043

Economic Development
Department
City of Las Vegas
400 East Stewart Avenue
Las Vegas, NV 89101

Community Planning and
Development
City of North Las Vegas
Post Office Box 4086
North Las Vegas, NV 89030

Director of Community
Planning
City of Boulder City
Post Office Box 367
Boulder City, NV 89005

City Manager
City of Henderson
Henderson, NV 89015

Commission of the
European Communities
200 Rue de la Loi
B-1049 Brussels
BELGIUM

N. A. Norman
Project Manager
Bechtel National Inc.
P. O. Box 3965
San Francisco, CA 94119

Technical Information Center
Roy F. Weston, Inc.
955 L'Enfant Plaza, Southwest, Suite 800
Washington, DC 20024

Flo Butler
Los Alamos Technical Associates
1650 Trinity Drive
Los Alamos, New Mexico 87544

R. Harig
Parsons Brinkerhoff Quade &
Douglas, Inc.
1625 Van Ness Ave.
San Francisco, CA 94109-3678

Timothy G. Barbour
Science Applications
International Corporation
1626 Cole Boulevard, Suite 270
Golden, CO 80401

Dr. Madan M. Singh, President
Engineers International, Inc.
98 East Naperville Road
Westmont, IL 60559-1595

E. P. Binnall
Field Systems Group Leader
Building 50B/4235
Lawrence Berkeley Laboratory
Berkeley, CA 94720

Roger Hart
Itasca Consulting Group, Inc.
P.O. Box 14806
Minneapolis, Minnesota 55414

T. H. Isaacs (RW-22)
Office of Civilian Radioactive
Waste Management
U.S. Department of Energy
Forrestal Building
Washington, DC 20585

J. P. Knight (RW-24)
Office of Civilian Radioactive
Waste Management
U.S. Department of Energy
Forrestal Building
Washington, DC 20585

D. H. Alexander (RW-232)
Office of Civilian Radioactive
Waste Management
U.S. Department of Energy
Forrestal Building
Washington, DC 20585

Allen Jelacic (RW-233)
Office of Civilian Radioactive
Waste Management
U.S. Department of Energy
Forrestal Building
Washington, DC 20585

B. J. King, Librarian (2)
Basalt Waste Isolation Project
Library
Rockwell Hanford Operations
Post Office Box 800
Richland, WA 99352

J. R. Rollo
Deputy Assistant Director
for Engineering Geology
U.S. Geological Survey
106 National Center
12201 Sunrise Valley Drive
Reston, VA 22092

David K. Parrish
RE/SPEC Inc.
3815 Eubank, N.E.
Albuquerque, NM 87191

R. Lindsay Hundell
United States Bureau of Mines
P.O. Box 25086
Building 20
Denver Federal Center
Denver, Colorado 80225

D. L. Fraser, General Manager
Reynolds Electrical & Engineering
Co., Inc.
Mail Stop 555
Post Office Box 14400
Las Vegas, NV 89114-4400

Vincent Gong
Technical Project Officer for NNWSI
Reynolds Electrical & Engineering
Co., Inc.
Mail Stop 615
Post Office Box 14400
Las Vegas, NV 89114-4400

Gerald Parker (RW-241)
Office of Civilian Radioactive
Waste Management
U.S. Department of Energy
Forrestal Building
Washington, DC 20585

Christopher M. St. John
J. F. T. Agapito Associates, Inc.
27520 Hawthorne Blvd., Suite 137
Rolling Hills Estates, CA 90274

J. P. Pedalino
Technical Project Officer for NNWSI
Holmes & Narver, Inc.
Mail Stop 605
Post Office Box 14340
Las Vegas, NV 89114

S. D. Murphy
Technical Project Officer for NNWSI
Fenix & Scisson, Inc.
Mail Stop 514
Post Office Box 15408
Las Vegas, NV 89114

Eric Anderson
Mountain West Research-Southwest, Inc.
398 South Mill Avenue, Suite 300
Tempe, AZ 85281

S. H. Kale (RW-20)
Office of Civilian Radioactive
Waste Management
U.S. Department of Energy
Forrestal Building
Washington, DC 20585

Judy Foremaster (5)
City of Caliente
Post Office Box 158
Caliente, NV 89008

J. H. Anttonen, Deputy Assistant
Manager for Commercial
Nuclear Waste
Basalt Waste Isolation Project
Office
U.S. Department of Energy
P.O. Box 550
Richland, WA 99352

D. Hodgkinson
Theoretical Physics Div.
AERE Harwell
Oxfordshire OX11 ORA
United Kingdom

J. R. Connolly
Dept. of Geology
Institute of Meteoritics
Univ. of New Mexico
Albuquerque, NM 87104

K. Eggert
Lawrence Livermore National Laboratories
P.O. Box 808 L206
Livermore, CA 94550

D. Evans
Dept. of Hydrology and Water Res.
Univ. of Arizona
Tucson, AZ 85719

G. W. Gee
Pacific Northwest Laboratory
P.O. Box 999
Richland, WA 99352

D. Hammermeister
USGS-WRD, MS 416
Federal Center
Denver, CO 80225

D. Hoxie
USGS-WRD, MS 416
Federal Center
Denver, CO 80225

P. Montazer
USGS-WRD, MS 416
Federal Center
Denver, CO 80225

W. E. Wilson
USGS-WRD, MS 416
Federal Center
Denver, CO 80225

P. Kelsall
IT Corporation
2340 S. Alamo
Albuquerque, NM 87106

T. N. Narasimhan
Lawrence Berkeley Laboratory
Berkeley, CA 97420

D. Stevens
Dept. of Soil Sciences
N.M. Tech.
Socorro, NM 87801

J. Cullen
Science Applications International
Corp.
2769 South Highland
Las Vegas, NV 89190

S. Tyler
DRI
2505 Chandler Ave., Suite 1
Las Vegas, NV 89120

T. J. Nicholson
Earth Science Branch
USNRC MS 1130-55
Washington, D.C. 20815

M. Teubner
Science Applications International
Corp.
2769 South Highlands
Las Vegas, NV 89190

B. J. Travis
Los Alamos National Laboratory
P.O. Box 1663
Los Alamos, NM 87545

E. Weeks
USG-WRD, MS 416
Federal Center
Denver, CO 80225

1511 N. E. Bixler
1511 R. R. Eaton
1511 P. Hopkins
6300 R. W. Lynch
6310 T. O. Hunter
6311 C. Mora
6312 F. W. Bingham
6312 G. E. Barr
6312 A. L. Dudley
6312 J. H. Gauthier
6312 M. L. Green
6312 B. S. Langkopf
6312 R. R. Peters (10)
6312 R. W. Prindle
6312 M. S. Tierney
6312 M. Wilson
6313 T. E. Blejwas
6313 R. Finley
6313 E. A. Klavetter (10)
6313 F. B. Nimick
6313 L. E. Shephard
6313 R. M. Zimmerman
6314 J. R. Tillerson
6315 S. Sinnock
6315 P. C. Kaplan
6315 C. A. Rautman
6313 B. M. Schwartz (2)

6310 51/L08A.A-4/1/83
6310 51/L08A.A-10/7/85
6331 A. R. Lappin
6332 R. Beraum
6332 WMT Library (20)
6430 N. R. Ortiz
6431 R. M. Cranwell
6431 E. J. Bonano
6431 R. Guzowski
7223 R. G. Easterling
7223 I. J. Hall
3141 S. A. Landenberger (5)
3151 W. L. Garner (3)
8024 P. W. Dean
3154-3 C.H. Dalin (28)
for DOE/OSTI

Item Description:	An Evaluation of the Use of Mercury Porosimetry in Calculating Hydrologic Properties of Tuffs From Yucca Mountain, Nevada
Availability:	X Publicly Available ☐ Non-Publicly Available
Sensitivity:	X Non-Sensitive ☐ Non-Sensitive–Copyright ☐ Sensitive ☐ Sensitive–Copyright
Electronic Media Type: (If applicable)	Microfiche
Contact:	US Nuclear Regulatory Commission Office of Nuclear Materials Safety and Safeguards Yucca Mountain Project Manager
Storage/File Location:	US Nuclear Regulatory Commission Office of Nuclear Materials Safety and Safeguards Two White Flint North Room T7- E34 11545 Rockville Pike Rockville, Maryland 20852-2738

Org	Bldg.	Name	Rec'd by	Org.	Bldg.	Name	Rec'd by

Sandia National Laboratories